WIDEBAND SPECTROPOLARIMETRY OF EXTRAGALACTIC RADIO SOURCES WITH KAT 7 AND COMMISSIONING PHASE MEERKAT

Mr. Letjatji S. Legodi

Advisor:
Prof. A. R. Taylor (UCT/IDIA)

Astronomy Department
University of Cape Town (UCT)

A dissertation submitted in fulfilment of the requirements for the degree of Doctor of Philosophy in the Astronomy Department of the University of Cape Town (UCT).

January 2019

This work is funded, to a large degree, by the South African National Research Foundation (SA NRF) and the Square Kilometre Array South Africa (SKA SA) project through their postgraduate student scholarship programme. Opinions expressed and conclusions made, are those of the author and not necessarily those of the SA NRF, SKA SA, and/or the University of Cape Town.

Declaration of Authorship

I, Letjatji Samuel Legodi, know the meaning of plagiarism and hereby declare that all of the work in this document, save for that which is properly acknowledged, is my own.

Signature:

Signed by candidate

Date: 31 January 2019

Abstract

The study of cosmic magnetism is vital in fully understanding the role that magnetic fields play in the evolution of cosmological objects such as galaxies. The exact role played by magnetism in galaxy evolution is still not fully understood. This work aims to use wide band radio polarimetry to probe the frequency dependent polarization properties in a small sample of unresolved known disc and AGN powered radio galaxies and also in a larger faint radio source sample from a deep blind survey. The second sample is composed of lesser known faint radio sources spanning ~ 4 square degrees. We also aim to develop broad band radio polarimetry techniques that can be utilised in the future.

We observed six radio galaxies at frequencies spanning $1200 - 1900$ MHz – divided into three 256 MHz bands centred on 1350, 1600, and 1850 MHz. We also analysed deeper wide band and wide field observations from the commissioning phase of the South African SKA precursor, MeerKAT. The MeerKAT observations are of the DEEP field, a radio quiet region in the southern sky. These observations were made at frequencies 890 MHz to 1702 MHz. Following data calibrations, we made sensitive (down to ~ 7 μJy/beam) high resolution (6”) total intensity image maps for DEEP field source finding and characterization, as well as lower resolution (14”) IQU image cubes. We analysed sources with total flux density greater than one milliJy.

The technique of Faraday rotation measure synthesis (RM synthesis) was employed through a python based algorithm to probe the broad band structure of the polarisation spectra. RM synthesis has the power to resolve individual contributions to the overall observed spectropolarimetric features along a line of sight.

We found agreement with literature with regard to total radio intensities and the expected polarisation levels of order 1%. Our polarisation detection rate in the wide field case was estimated to be $24 \pm 9\%$ per square degree. This translates to 30 ± 13 polarised sources per square degree, in agreement with projections from the literature. The results confirm two main categories of polarised radio sources. These are: (1) sources with simple polarisation profiles, theoretically resulting from a scenario where incident polarised emission is Faraday rotated by a foreground region of coherent magnetic field such as in the case of a radio bright galactic nucleus emitting synchrotron radiation that then traverses disk and halo regions filled with a uniform magnetic field; (2) sources with complex Faraday spectra, indicating depolarisation and/or repolarisation suggesting other complex behaviour originating from several combinations of Faraday rotating and synchrotron emitting regions along the line of sight. We found that the most complex polarisation profiles emanate from the most polarised radio sources.

From the sample of known sources observed with KAT 7, we found that unresolved disk dominated galaxies tended to be less polarised than compact sources suggesting a morphological dependence of the polarisation spectrum where disk galaxies may tend to have more regions within them, such as pockets of turbulent magnetic fields in the material disk, that may cause depolarisation to a larger degree as compared to earlier type non-disk dominated galaxies. Steep spectrum sources of different types (radio lobes and most polarised compact sources) show the most complexity with multiple Faraday emission components, depolarisation, and repolarisation.

The more sensitive MeerKAT data allowed us to probe the broad band polarimetric properties of faint never observed radio sources. Our study is an early step to future campaigns with MeerKAT to explore relations between polarimetry and source properties, probing the correlations of magnetism with galaxy evolution and the evolution of large-scale fields in galaxies, galaxy groups and clusters.

Acknowledgements

To my parents who have always shown faith in me and steered me in the right directions, I would like to express a depth of gratitude beyond words. To my grandmother, who has always been a pillar of strength, gentleness and firmness I say *ke a leboga Noko monyela sediba!* To my brothers and cousins, I hope to encourage unbound faith in your own limitless potential.
My sincere thanks also goes to Professor Russ Taylor for always giving me support amid his many obligations and responsibilities. To my friends, officemates and colleagues Precious, Brenda, Liz, Iniyan, Narges, Mokhine, Nikki, Riona, and Hannes who have always been such a pleasure to work alongside and who have also pushed me to work harder. To my volunteer team leaders at church, Dillon, Lynn, and Cecile, for always encouraging and celebrating everyone on the host team. To my friends Violet and Azwi for always being sources of laughter amid the seemingly enduring stresses of PhD student life. I would like to also thank Dr Nadeem Oozeer for his help and guidance during the earlier stages of my thesis while I was beginning radio interferometry reductions on KAT 7 observations. Your basic introductions were invaluable. To Nicky Walker and Roslyn Daniels, thank you for always being there to listen and advise with everything from flights and accommodations for conferences to general life problems.

This work was funded, to a large degree, by the South African National Research Foundation (SA NRF) and the South African Radio Astronomy Observatory (SARAO - formerly “SKA SA”) through their doctoral student scholarship programme. Additional funding was provided by the Inter-University Institute for Data Intensive Astronomy (IDIA), the lions share of the analysis is done on the IDIA cloud computing facility.

Data Sources

Radio observations are from the SARAO SKA precursor, MeerKAT synthesis array and the Karoo Array Telescope, KAT 7. Data storage, calibration, and imaging are performed on IDIA cloud computing facilities.

Contents

List of Figures

List of Tables

Chapter 1

Introduction

1.1 Magnetic fields in astronomy

The gyration of electrons along magnetic field lines produces some of the most spectacular displays of physics that can be observed with the naked eye such as the aurora above the Earth's poles. The same magnetic field guides certain migratory animals along to greener pastures amid unfavourable seasonal conditions. Still the same field shields organic life on Earth from harmful extra-terrestrial radiation. The same physical phenomenon, that is magnetism, results in the 22 year sunspot cycle observed on the solar surface. This same magnetism is responsible for spectacular behaviour in stellar objects such as pulsars, rapidly rotating and beaming magnetically generated signals at the Earth that a young Jocelyn Bell and contemporaries initially thought to be the work of little green men on a far away planet. Magnetic fields are also known to influence the formation of new stars as they influence the collapse of star-forming regions, exerting pressure to counteract gravitational collapse in stellar nurseries. On still larger scales, these magnetic fields have been observed to mysteriously form spiral arm patterns in the regions between the observed material spiral arms of disk galaxies (e.g Scarrott et al., 1987; Fletcher et al., 2011; Chamandy et al., 2014a; Moss et al., 2015). Still other mysterious patterns are observed in disk galaxies where magnetic vertical structures are seen in the galactic haloes of edge-on disk galaxies (e.g Hummel et al., 1988; Beck et al., 1994; Fendt et al., 1996; Beck, 2015). The vertical components observed do not geometrically follow the material disk as is the case for large scale fields in the disk. This field morphology may be driven by stellar winds arising from star formation as large actively star forming galaxies have been observed to show this geometry, however, the true origins are yet unknown (Soida et al., 2011; Klein and Fletcher, 2015).

A large fraction of the radiation observed as long wavelength radio waves, *radio synchrotron*, emanates from emission of electrons as they gyrate along magnetic fields and the study of integrated polarised emission, in addition to knowledge of magneto-ionic material densities, along a line of sight sheds light on large-scale coherent/ordered magnetic fields along that line of sight. The emitted synchrotron light encodes magnetic details of the environment from the emission point, through intervening media, up to the point where the signal is observed. This chapter introduces the topics involved with this endeavour of using radio polarimetry to probe magnetic fields in extra-galactic sources – that is coherent magnetic fields in galaxies, active-galactic nuclei (AGN) sources, AGN jets, and radio lobes. We disentangle, in this thesis, the various components emitting polarised light and those magnetic field components that may alter the incident radio synchrotron emission along a line of sight.

1.1.1 Synchrotron radiation

The main probe for magnetism in the cosmos is synchrotron radiation resulting from relativistic cosmic-ray electrons spiralling along magnetic field lines. This is non-thermal radiation with an energy distribution that follows a power law. This is a form of continuum radiation, emitted over a broad range of wavelengths, prominently detected at radio wavelengths ($\sim$ centimetres to metres) and forms the primary component in radio astronomy observations. Radiation at the same radio wavelengths can also have a thermal component from an ensemble of electrons that have Maxwellian energy distributions. The relativistic electrons posses much higher energies and tend to dominate the overall emission observed in distant radio sources. These relativistic energies result from processes such as supernova explosions, AGN activity, and collisions of galaxy groups and clusters. Synchrotron radiation has a characteristic frequency and is linearly polarised to maximum theoretical levels of $\sim 70\%$ of the observed total intensity, with negligible levels of circular polarisation (e.g Beck, 2004; Klein and Fletcher, 2015). Some astronomical sources such as masers (Microwave Amplification by Stimulated Emission of Radiation), the sun, planets such as Jupiter, and highly magnetic stellar remnants such as pulsars do emit appreciable levels of circular polarisation (e.g Vlemmings et al., 2001; Sarma et al., 2001; Watson and Wyld, 2001; Assaf et al., 2013; Kato and Soda, 2016; Fassett et al., 2018). It is also a powerful probe of magnetism in diffuse media where the linear polarisation fraction undergoes Faraday rotation (rotation of the electric field vector as the radiation traverses a magnetic field). The Faraday rotation signatures (see Section 1.3) can probe the magnetic field strengths and orientations in the space between us and the radio sources, making them invaluable in understanding the magnetic cosmos.

An ensemble of relativistic electrons has electrons of energies in the range $[E,\ E + dE]$, and an energy distribution, $N(E)$, with power law

$$N(E)dE \sim E^{-g}, \tag{1.1}$$

where E denotes energy and g is the power law index. Following the theoretical derivations underpinning synchrotron radiation (e.g. Klein and Fletcher, 2015), the radio intensity at a certain frequency, I_ν, also follows a power law:

$$I_\nu \sim B_\perp^{1+\alpha} \nu^{-\alpha}, \tag{1.2}$$

where $B_\perp$ is the perpendicular component (relative to the line of sight) of the magnetic field in the region occupied by the electrons and the spectral index, $\alpha = (g-1)/2$. Given a maximum energy, E_{max}, the ensemble will have a critical radiation frequency, ν_c (beyond which the energy decreases exponentially), for the electron energy distribution given by:

$$\nu_c \propto \frac{eB_\perp}{m_e c} \gamma_{max}^2, \tag{1.3}$$

where $\gamma = (1 - \beta^2)^{-1}$ is the Lorentz factor with $\beta = v/c$ (v is the speed of an electron and c that of light in a vacuum). The electron mass and charge are m_e and e, respectively. Figure 1.1 displays such a spectrum.

The complete polarisation state of synchrotron radiation can be represented by Stokes parameters I, Q, U, and V, where I is the total intensity and

$$I_{pol} = \sqrt{U^2 + Q^2 + V^2}, \tag{1.4}$$

is the total polarised intensity. Here, V is the circularly polarised intensity.

$$P = \sqrt{U^2 + Q^2} \tag{1.5}$$

is the total linearly polarised intensity which dominates the polarised emission from most astrophysical scenarios (Klein and Fletcher, 2015). The degree of linear polarisation is given by

$$p = \frac{P}{I}. \tag{1.6}$$

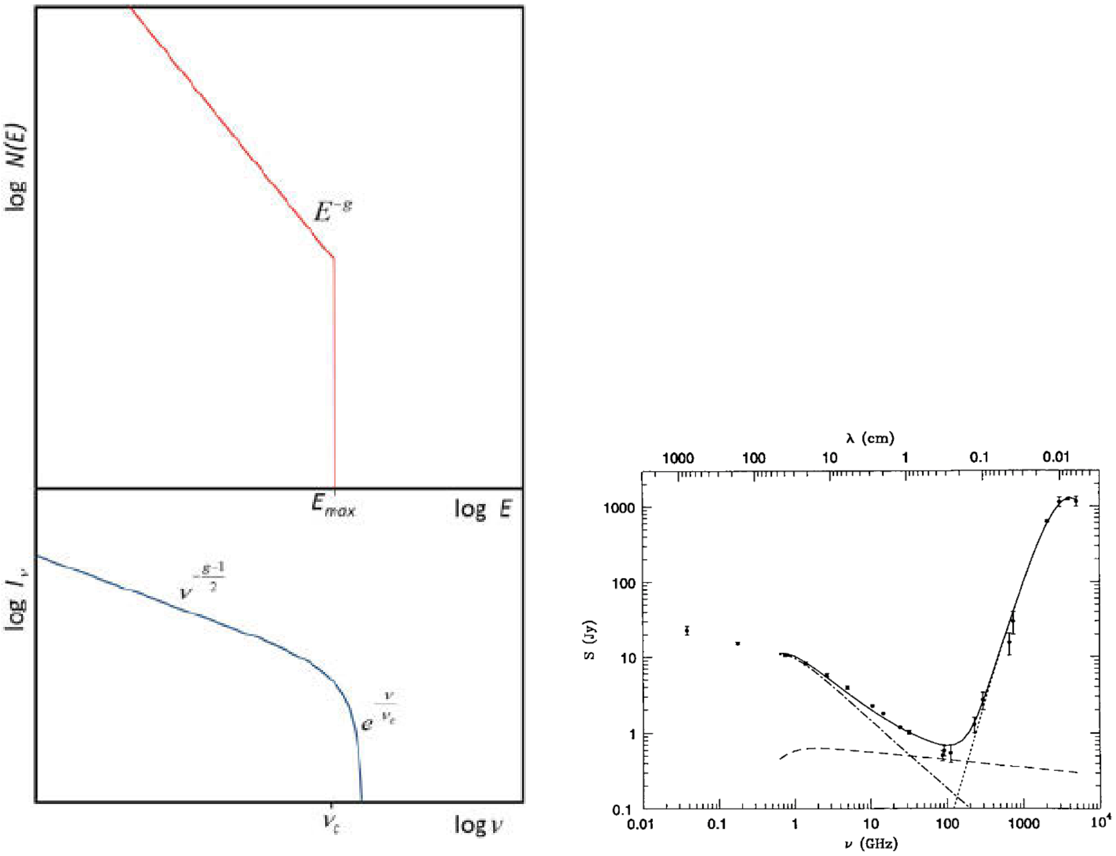

Figure 1.1: Synchrotron radiation spectrum with energy distribution cut-off E_{max} (left panel). Adapted from Figure 2.19 of (Klein and Fletcher, 2015). Right panel: synchrotron flux density spectrum displaying the spectral shape near $\nu \sim 1$ GHz. The dot-dashed line shows cosmic-ray electron emission dominant at $\nu < 30$ GHz, dashed line shows thermal emission from ionised HII regions. Free-free absorption dominates the $\nu < 1$ GHz regime.

As per equation 1.1 and 1.2, the total intensity radiated depends on the density of cosmic-ray electrons within an energy range and also the total field strength of the orthogonal component – that is the component in the plane of the sky. Polarised emission results from ordered fields – that is non-turbulent fields, with a preferred vector orientation. However, polarization angles intrinsic to synchrotron emission have an $n\pi$ ambiguity (e.g Farnsworth et al., 2011), and as such do not carry enough information to distinguish regular ordered fields with a well-defined direction within the telescope resolving element (the telescope *beam* – see Section 1.2) from anisotropic turbulent fields, resulting from the superposition of small-scale (scales below the coherence/"ordering" scale of the ordered component) isotropic turbulent magnetic fields. The superposition of the small scale turbulent fields can be "ordered" by compression or shear of gas flows, which have a preferred flow orientation, but these flows and shearing motions can reverse their direction on these small scales. Unpolarised synchrotron emission results from small scale isotropic turbulent fields whose random directions results in a diminished field on larger scales (Beck and Wielebinski, 2013).

The component of the large scale field that is orthogonal to the sky plane and along the line of sight is encoded in the Faraday depth, which measures the amount by which the polarisation vector of incident radiation is rotated by a foreground magneto-ionic medium consisting of a coherent large scale magnetic field and a population of thermal electrons (see Section 1.3).

1.1.2 Magnetic fields in galaxies

The total synchrotron intensity carries information about the total magnetic field of the emitter – both the small scale field, on the scales of turbulent gas clouds in the environments of starforming regions, and the large scale field. The large scale component manifests on scales of galactic spiral arms. Polarised synchrotron emission encodes the complex combination of large scale fields along a certain line of sight between the emitter and the observer. In the sections that follow, I give a basic introduction of the large scale field component observed through linearly polarised radio emission that is emitted by different constituents of galaxies.

Fields in galaxy disks and halos

Polarised synchrotron radiation (Section 1.1.1) traces large-scale ordered/coherent magnetic fields observed to form spiral structures that are geometrically similar to material spiral arms in disk galaxies (Krause et al., 1993; Beck et al., 1996; Beck, 2012). An example is the case of the Whirlpool galaxy (M51), displayed in Figure 1.2 (Fletcher et al., 2011). These spiral field morphologies are also observed in other disk galaxy morphologies such as ringed galaxies as observed by Chyży and Buta (2008), flocculent galaxies without spiral structure (Soida et al., 2002), and disk galaxies with circum-nuclear starburst regions (Beck and Wielebinski, 2013). Due to the emission mechanism of synchrotron radiation – requiring cosmic ray electrons to be accelerated by magnetic fields such that they emit, early type morphologies such as Sa, S0, and ellipticals display no such spiral fields (Beck and Wielebinski, 2013). Early type galaxies that are quiescent and with no star formation (sometimes referred to as *red and dead*) cannot support the cosmic ray particle populations required to produce polarisation detections. More active galaxies can sometimes be detected in polarisation.

The formation of these field patterns is a subject of debate as the spiral structure should, for example, eventually dissipate and present a wound up structure following the circular gas flows in disk galaxies that have no bar, significant tidal interactions, or strong density waves. This is not observed and instead the large scale fields maintain the spiral structure with maximum field strengths found in the inter-arm regions of spiral galaxies (Fletcher, 2010; Chamandy et al., 2014a). The magnetic *dynamo*, converting mechanical energy into magnetic energy, is the most successful model in explaining the observed structures (e.g Beck et al., 1996; Moss, 1998; Lou and Fan, 1998; Beck, 2012; Chamandy et al., 2016). A dynamo converts kinetic energy into electro-magnetic (EM) energy and in the case of galaxies this is theorised to arise from galactic rotation (on large scales) and turbulent motions (on small scales) that provide ionised populations of the ISM with kinetic energy which then

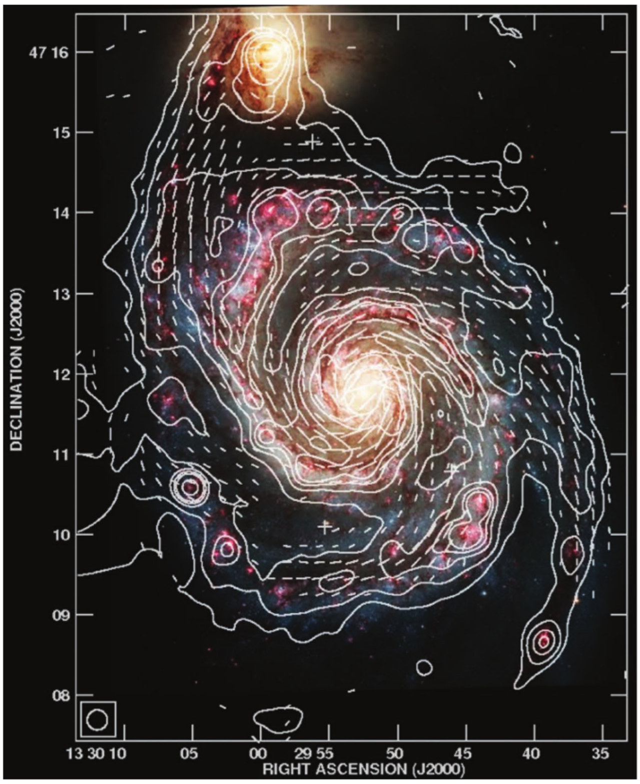

Figure 1.2: Optical image (Hubble Space Telescope [NASA, ESA, S. Beckwith (STScI)]) of the spiral galaxy M51 (RGB image), overlaid with $\lambda = 3$ cm $15''$ resolution VLA and Effelsberg radio total intensity contours at 6, 12, 24, 36, 48, 96, 192 times the noise levels of 20µJy/beam. Vectors show the polarisation of the observed electric field rotated by 90° *(Fletcher et al., 2011).*

generates the magnetic field (Klein and Fletcher, 2015).

Ordered large scale fields in disk galaxies are observed to have vertical structures that, in some cases, resemble an X-shape (e.g Heesen et al., 2009a,b; Krause, 2009, 2014). The origin of this structure is also another puzzle with possible solutions that involve galactic winds as indicated by magneto-hydrodynamic (MHD) simulations (Gressel et al., 2008a,b; Hanasz et al., 2009; Krause, 2014). The dynamo mechanism driven by outflows may hold some answers (Moss et al., 2010) but these structures so far remain shrouded in mystery (Klein and Fletcher, 2015).

Fields in AGN cores, jets, and lobes

The brightest radio sources tend to be radio galaxies, which are bright AGN sources with distinctive large scale structures. The typical radio galaxy displays an unresolved point-like core (resolved by VLBI at scales of milli-arcseconds), narrow elongated emission (in a pair of radio jets) which appear to be in opposite directions from the core, large scale diffuse plumes of emission situated at the ends of the jets (radio lobes), and bright radio hot-spots either on the leading edges of the lobes (the so-called FRII[1] radio galaxy morphology (Fanaroff and Riley, 1974)) or along the jets themselves (the so-called FRI morphology). The latter tend to be less powerful radio emitters than the former.

The AGN cores of these strong radio emitters tend to be polarised at levels of order 1% while the jets are highly polarised at levels an order of magnitude higher at $\nu \sim 1$ GHz. These radio bright sources dominate the

---

[1] A classification of lobed radio galaxies by B.L. Fanaroff and J.M. Riley (Fanaroff and Riley, 1974), where these sources are placed into two classes viz, FR I and FR II, based on the brightness of the peripheral components (extended structures such as radio lobes) relative to the central regions. FR I sources have lower surface brightness in their peripheral regions relative to their central regions while the FR II class has higher surface brightness in the extremities (lobes).

micro-Jy radio sky and require broad band and deep high resolution polarisation observations to probe their complex magnetic fields (e.g Agudo et al., 2010; O'Sullivan et al., 2012, 2015; Pasetto et al., 2018).

1.2 Introduction to radio interferometry

Radio astronomy offers a view of the cosmos, invisible to our eyes but revealing some of the most significant and fundamental aspects of our universe. This section briefly outlines the theory behind this branch of observational astronomy and the development of the next generation of radio observation facilities. Particular emphasis is made for the case of cosmic magnetism, probed through polarisation studies using these facilities.

1.2.1 Introduction to radio astronomy

The curiosity and ingenuity of one Karl G. Jansky ignited the flame for radio astronomy back in 1932 when he made the first radio observations of a mysterious and persistent radio signal that interfered with telephone transmissions at the time. Jansky was a radio engineer employed by the Bell Telephone Laboratory, and he confirmed the radio signal at 20.5 MHz to be originating from the Galactic center (Jansky, 1932, 1933). Jansky's work made front page news in the New York Times (May 5th, 1933) but the work of this novice radio astronomer was not recognised by the astronomy community until Grote Reber, also a radio engineer and novice astronomer, discovered significant emission in the directions of Sagittarius, Cygnus, and Cassiopeia (Reber, 1940, 1944) – spiking the interest of the community, given that the most prominent emission came from a region removed by 30° from what was then thought to be the Galactic center. With the many negative consequences of the second world war, came expertise and technology seminal to the establishment of radio astronomy – a new probe of the cosmos.

Radio astronomy complements astronomy at higher frequencies since radio waves permeate much farther in space as they are not vulnerable to extinction to the same levels as higher frequency light. Extinction diminishes the incident light by scattering light from the line of sight of an observer and thus conceals the emitter. This scattering is correlated to the scattering particle sizes in relation to the wavelength of the incident light – the closer the wavelengths are to the size of the particles in the intervening media, the more extinction the incident light will undergo. This effect causes the sky to appear blue as the shorter blue wavelengths, closer in size to molecules in the Earth's atmosphere, scatter more significantly than their longer wavelength counterparts in the red end of the EM spectrum. The loss of information on astronomical scales is quite severe as interesting objects such as star-forming regions, the Galactic center are shrouded in an amalgamation of simple and complex molecules and also minute *dust* particles. Radio waves penetrate such obscured regions. Some physical processes in galaxy-galaxy interactions (galaxy mergers, the intergalactic medium, galaxy groups and clusters), galaxies themselves (active galactic nuclei (AGN), extended galaxy emission such jets and lobes), inter-stellar medium (ISM – e.g. Galactic maser objects and H1 regions) and stars (e.g pulsar phenomena) may also emit prominently in the radio regime with minimal emissions at higher frequencies.

My first astronomy lecturer, Dr Sarah Blyth [2], introduced the telescope using the analogy of a bucket to collect water. Telescopes are light *buckets* commissioned to capture as many of the cosmic photons *raining* down on us as possible. The analogy translates very well to optical telescopes where observed wavelengths span one to two orders of magnitude but in radio astronomy the *buckets* vary significantly among each other as the observable radio spectrum spans many orders of magnitude (from wavelengths of ~ 10 m to ~ 0.01 m, see Figure 1.3) and thus radio telescopes have to be very specialised to detect only a fraction of it. The flux unit used in radio astronomy is the so called *flux density* and is expressed as the Jansky, Jy, where 1 Jy $= 10^{-26}$ W m^{-2} Hz^{-1}. This unit sufficiently represents compact unresolved sources, that is a source smaller than the *beamwidth* of the telescope but in the case of a resolved source spanning a region of sky beyond the beamwidth,

---

[2] Astronomy Department, University of Cape Town.

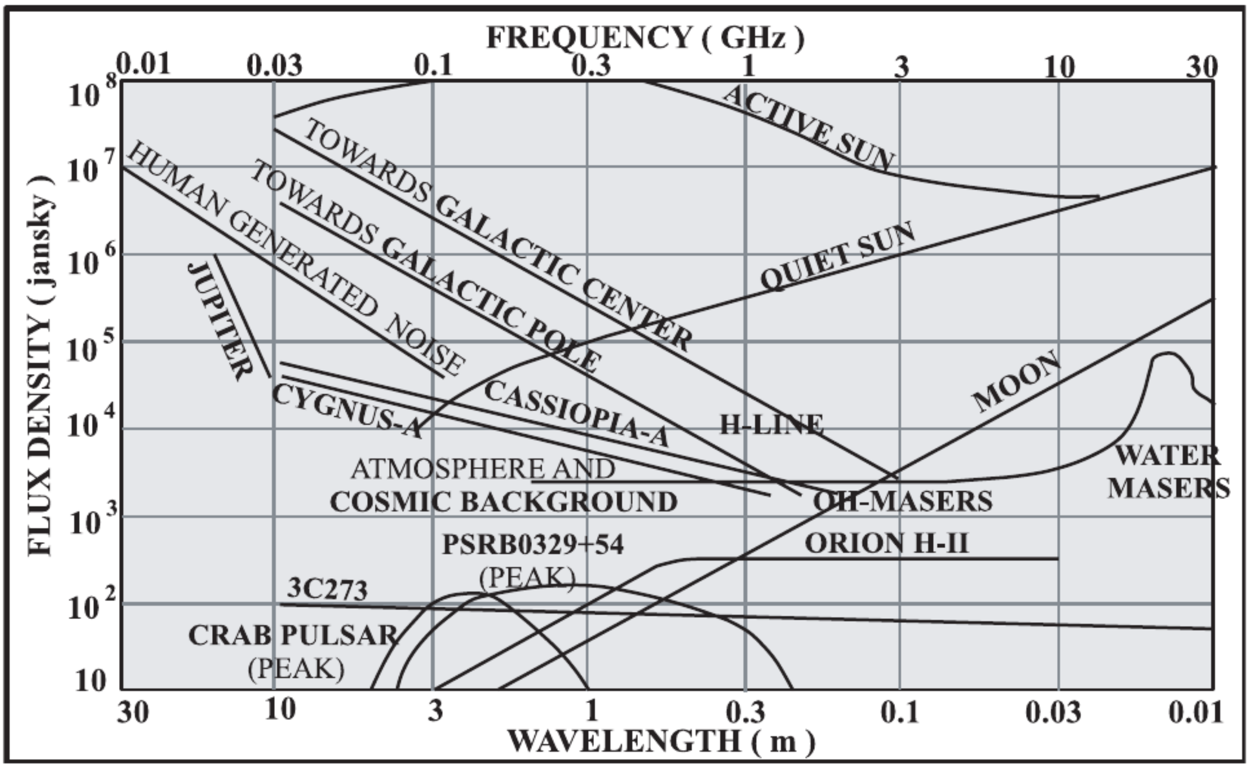

Figure 1.3: From Joardar et al. (2010) displaying emission from the myriad of radio sources detectable across radio wavelengths observable from the surface of the Earth.

the surface brightness is reported. The surface brightness is given in units of Jy sterad^{-1} (W. N. Christiansen, 1985).

The simplest radio telescope, the *dipole antenna*, can be made with two collinear conductors of some length l. In simple terms, an antenna is a device that converts electromagnetic radiation into electric signals which can then be amplified/correlated and analysed further [3]. Dipole antennas are ideal for long wavelengths where $l \ll \lambda$. They can be combined to form *arrays* to increase their *effective collecting area* but such arrays are not feasible for short wavelengths – i.e. $\lambda \lesssim 1$m. Conventional short wavelength radio telescopes tend to have large diameters ($D \sim 10$ m) with paraboloid reflectors (dishes) that focus incident radiation onto feed antennas which can then make the conversion to electrical signals. The *beamwidth* or the angular resolution relates to the size of the dish by $\theta \sim \lambda/D$. Single dishes are built up to $D \sim 100$ m to achieve high resolutions and sensitivity e.g the world's largest steerable single dish radio telescope, the Green Bank Telescope with $D = 100$ m, the Arecibo Telescope with $D = 305$ m, and the Chinese Five Hundred Meter Aperture Spherical Telescope (FAST) with $D = 500$ m. Beyond these large sizes it becomes impractical to build and operate single dish telescopes and thus interferometers become much more suitable. An interferometer combines the collecting area of a number of N individual telescopes (often referred to simply as antennas or elements) into a single telescope array whose diameter is defined by the largest distance between any two antennas. A single antenna has a geometric area limited to $\pi D^2/4$, while an interferometer can have an arbitrarily large area defined by $N\pi D^2/4$. In this way a much larger telescope is synthesised. The angular resolution of an instrument can be made intrinsically large by increasing the distance between antennas.

A radio interferometer samples the sky brightness in a discrete and convoluted manner. The instrument samples the visibility function $V(u, v)$, which is the Fourier transform of the actual sky brightness distribution $I(\boldsymbol{s})$. Figure 1.4 displays the position vectors associated with a simple two element interferometer response to a radio source. Here $\boldsymbol{s}$ is a unit vector pointing in the direction of the radio source, and (u, v, w) are the

---

[3] `https://www.cv.nrao.edu/courses/astr534`

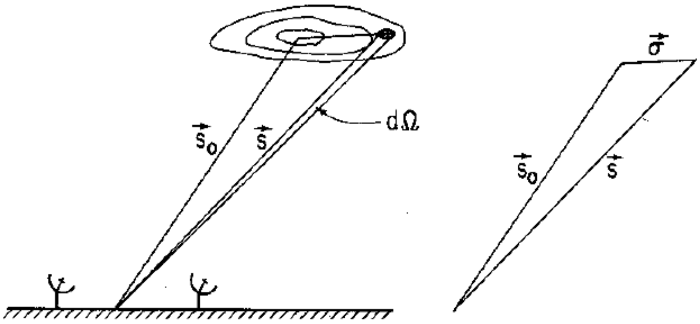

Figure 1.4: A simple representation used by Taylor et al. (1999) displaying the position vectors associated with a two element interferometer response to a radio source.

coordinates in the u-v plane – the plane on the sky where (u, v, w) are the vector separation of the interferometer elements (i.e the projected baseline coordinates) measured in units of wavelengths. w is in the plane orthogonal to the sky plane containing (u, v) and thus points along $\boldsymbol{s}_0$. The notation l, m, and n is used to denote the directional cosines used to define the spherical sky coordinate system in which $I(\boldsymbol{s})$ is measured. Some arrays will have antennas that are coplanar and so $n - 1$ becomes negligible. This is also the case for small field imaging – where the region of the sky being observed is flat, i.e $n \approx 1$, making V and I just functions of (u, v) and (l, m), respectively (Taylor et al. (1999); (Rau et al., 2009)). For the sake of simplicity we will, where possible, omit the coordinate labels (u, v) and (l, m) in equations that follow. Observing a radio source on the sky in the direction given by $\boldsymbol{s}$ with two interferometer elements with a projected baseline length $\boldsymbol{b}$, we can define

$$V(u, v) = |V|e^{i\phi_V} = \int_S \boldsymbol{\mathcal{A}}(\boldsymbol{\sigma})I(\boldsymbol{\sigma})e^{-2\pi i\nu\boldsymbol{b}\cdot\boldsymbol{\sigma}/c}d\Omega \tag{1.7}$$

as the complex visibility of the radio emission over some angular size, Ω, on the sky (with subscript S denoting the integral evaluated over the entire sky). Equation 1.7 follows from the derivation by Taylor et al. (1999) where the authors give the technical details of radio calibrations and synthesis imaging. $\boldsymbol{\mathcal{A}}(\boldsymbol{\sigma}) = \boldsymbol{A}(\boldsymbol{\sigma})/A_0$ is the normalised antenna reception pattern, commonly referred to as the primary beam pattern. $\boldsymbol{A}(\boldsymbol{\sigma})$ is the effective collecting area of an antenna in the direction $\boldsymbol{s} = \boldsymbol{s}_0 + \boldsymbol{\sigma}$, and A_0 is the response at $\boldsymbol{s}_0$. The unit vector $\boldsymbol{s}_0$ represents the position on which the synthesised field of view is centred and c is the speed of light in a vacuum. $V(u, v)$ and $I(\boldsymbol{\sigma})$ are measured at some frequency ν.

In the most ideal case, equation 1.7 would fully represent reality but in practice radio observations are plagued by unwanted signals that limit sensitivity. Such signals have contributions from the telescope electronics, terrestrial sources such as the ground and man made tools (spark plugs in cars, mobile phones, blue-tooth devices, etc.) and signals from satellites in the Earth's orbit. A well known, but challenging to predict and localise, manifestation of this *noise* is the so called Radio Frequency Interference (RFI). "RFI" tends to be used as an umbrella term for unwanted radio frequency (RF) signals. Electronics designed to operate with minimal noise contribution, can mitigate contributions of random processes to the errors produced. Knowledge of the portions of RF bands that are affected by RFI is also used to remove unwanted signals during the data reduction process. Section 2.2 gives details of how we minimise the noise contribution to our data.

1.2.2 The Square Kilometre Array and MeerKAT

The upcoming Square Kilometre Array (SKA) is envisioned to set a new paradigm in radio astronomy observations, reaching new levels of sensitivity, speed and sizes of areas surveyed on the sky. The SKA is an international effort and will initially be located in the Karoo semi-desert of South Africa and another portion of it will be located in Australia's outback. The construction is divided into two phases, with Phase 1 comprising of SKA1 LOW ($\nu \sim 50 - 350$ MHz) and SKA1 MID ($\nu \sim 350 - 1760$ MHz) and Phase 2 comprised of SKA2 that is planned to expand across Australia, South Africa, and eventually to other African countries[4].

The SKA and precursor arrays, MeerKAT (Karoo Array Telescope, South Africa) and ASKAP (Australian Square Kilometre Array Pathfinder), are the new generation of radio telescopes set to revolutionise the current state of radio astronomy observations. Significant upgrades are or have already been commissioned for the leading current generation facilities such as the Jansky Very Large Array (JVLA, located near the town of Socorro, New Mexico, USA), upgraded Giant Metrewave Radio Telescope (uGMRT, located near the town of Pune, India). These updates increase the observed instantaneous bandwidths, featuring improved electronics such as correlators[5], reaching sensitivities of $\sim 1\ \mu$Jy (Rudnick and Owen, 2014; Taylor et al., 2014, 2015). The new upgrades to current generation facilities improve prospects for deep (sensitive) broadband polarisation studies but with limited sky coverage of ~ 1 square-degree and long observing times. MeerKAT will survey the sky significantly faster thereby improving the statistical significance of detections made. SKA1 MID will reach sensitivities improved by an order of magnitude with higher resolution and over larger areas, enabling the detection of large numbers of faint polarised sources at high redshifts – $z \gtrsim 2.5$ in the case of disk galaxies and $z \gtrsim 7.0$ for AGN sources (Taylor et al., 2015).

The study of the origin and evolution of cosmic magnetism is one of the five SKA key science goals (Carilli and Rawlings, 2004). The SKA will be capable of detecting high redshift polarised sources and thus improve on current foreground magnetic field studies[6] such as those based on Faraday Synthesis (see Section 1.3) of polarised synchrotron radiation (see Section 1.1.1) from grids on the sky of bright polarised background sources (Xu et al., 2006; Oppermann et al., 2012; Oppermann et al., 2014). The polarisation state of polarised radio emission from high redshift sources will be altered when passing through foreground magnetic fields and as such a statistical study of the polarised light of a grid of these background sources can be used to probe magnetic environments in the foreground (such as mapping the magnetic analogy to the cosmic microwave background (CMB – Penzias and Wilson (1965); Dicke et al. (1965))). Beck and Gaensler (2004) proposed such a study, where a 1.4 GHz polarisation study with the SKA would be conducted to map 10 000 square-degrees of sky resulting in a gridded dataset of rotation measures (see Section 1.3.1) across a large area of the sky. This data set can then be used to study global magnetic properties of foreground structures and phenomena in the Galaxy, the inter-galactic medium, other galaxies, galaxy groups and galaxy clusters. The cosmic evolution of magnetic fields and their relation to galaxy evolution for example, will also be probed with current low redshift studies (Beck et al., 2002; Vollmer et al., 2013; Beck, 2015) complemented with statistically significant high redshift work, enriching with observational evidence, current theories (e.g Sokoloff et al., 1998; Moss et al., 2012; Moss et al., 2013; Chamandy et al., 2014b,a; Moss et al., 2015) of our understanding of how magnetic fields emerge and evolve on cosmic time scales.

The key cosmic magnetism science[7] that is planned to leverage the capabilities of SKA1 rely on sensitive wideband spectro-polarimetry at $\nu \sim 1$ GHz. New understanding will be pursued regarding the Galactic field structure, the galactic cosmic web, foreground extragalactic fields, fields in individual galaxies, the role of fields in galaxy evolution, field formation and evolution as well as their structures and roles in galaxy clusters, groups, and the intergalactic medium. The following specific aspects pertaining to the current observational and theoretical cosmic magnetism puzzles, form part of the SKA key science areas and will be further investigated:

- *Properties of fields in AGN and physical properties of foreground environments*: Large scale AGN jet emission is significantly linearly polarised, typically reaching radio polarisation degrees of order 10% (Agudo et al., 2010). There are open questions regarding the field structures producing such levels of

---

[4] https://www.skatelescope.org

[5] A radio telescope's correlator, in the simplest terms, takes the voltage outputs from a pair of interferometer antennas and correlates them (multiplied and averaged).

[6] Where *magneto-ionised* media are distinct from the radio polarisation emitter.

[7] https://www.skatelescope.org/magnetism/

polarisation, how these fields interact with the jet, and how the fields themselves form and evolve. Probing the jet environment will require ultra-high resolution observations requiring SKA1 to be used in a very large baseline interferometer array (VLBI) with other radio observatories around the world (Paragi et al., 2015). Improved understanding of AGN magnetism also improves prospects for mapping foreground field structures where faint foreground structures can be mapped with bright background sources (e.g Taylor et al., 2009; Stil et al., 2011; Bernet et al., 2012; Schnitzeler et al., 2015).

- *The role of fields in galaxy evolution and magnetic field origins*: Broad band polarisation structure carries information about the magneto-ionised media in and around galaxy cores and a disentanglement of this information will reveal the roles of magnetism in galaxy evolution processes such as star-formation, feedback and triggering mechanisms. Polarisation purity at high sensitivities will help resolve these effects at even earlier cosmic times improving our understanding of the cosmic evolution of the roles of fields in galaxy evolution. Such depth will also allow for observational evidence to be contrasted with current field formation histories. Field strengths determine synchrotron intensity and at very large redshifts, radio emission from accelerated electrons will be shifted to lower energies leading to deep detections placing stricter constraints on field strengths of early galaxies (Beck, 2012).

SKA1 MID/survey will cover broad instantaneous bandwidths of ~ 1 GHz with sensitivities of ~ 1 μJy/beam at the widest field of view (30 000 square-deg) with $2''$ resolution while reaching higher sensitivities (~ 0.01 μJy/beam) and resolutions ($1''$) over 30 square-deg. The South African SKA precursor, MeerKAT (see Section 3.1), is already constructed and currently in the science commissioning phase. This work will utilise the initial science commissioning observations made with 16 antennas, with the initial array sometimes dubbed "MeerKAT (16)"[8]. MeerKAT (16) can achieve ~ 800 MHz instantaneous bandwidth, survey a square degree on the sky, with a resolution of $\sim 6''$, and sensitivity of order ~ 10 μJy/beam. These capabilities allow us to start to disentangle complex frequency dependent polarisation behaviour (see Section 1.3.1) in faint extragalactic sources and also spatially resolve them.

1.3 Faraday rotation

This section introduces the concepts involved in the Faraday Rotation of broad band radio emission and, a powerful technique that resolves the Faraday structure, and some physical origins of the Faraday structure.

1.3.1 Rotation Measure synthesis

The electric field vector of linearly polarised electro-magnetic waves is rotated and it's amplitude altered via the Faraday process, as the waves pass through magnetic fields. The component of the magnetic field along our line of sight (LoS) can be probed through observations of this emission. Burn (1966) presented a technique which can resolve the different components of magnetic fields that alter the polarisation of the incident radiation along the line of sight. The technique was later expanded and dubbed Rotation Measure synthesis (RM-synthesis, for short) by Brentjens and de Bruyn (2005). The technique transforms the observed Stokes parameters $q(\lambda^2)$ and $u(\lambda^2)$ to synthesised $q(\phi)$ and $u(\phi)$ via a Fourier transform . The parameter ϕ is the Faraday depth, which is defined as a product of the line of sight integral (the LoS displacement $\boldsymbol{r}$, measured in parsecs) of the thermal electron number density (often denoted as n_e, with units cm^{-3}) and coherent magnetic field component in the plane parallel to the observer's line of sight (sometimes denoted as $B_{\|} = \boldsymbol{B} \cdot d\hat{\boldsymbol{r}}$, in units of μGauss):

$$\phi(\boldsymbol{r}) = 0.81 \int_{source}^{observer} n_e \boldsymbol{B} \cdot d\boldsymbol{r} \ [\text{rad m}^{-2}]. \tag{1.8}$$

---

[8] The initial 16 antenna array used for initial commissioning.

The electric field vector of radiation can be rotated by a certain amount during Faraday rotation and the quantity which measures this rotation is called the Rotation Measure (RM, for short). The RM is defined by the change in polarisation angle $\chi(\lambda^2)$ as a function of the square of the wavelength, λ^2:

$$\mathrm{RM} = \frac{d\chi(\lambda^2)}{d\lambda^2}\ [\mathrm{rad\ m}^{-2}], \tag{1.9}$$

with the polarisation angle given by

$$\chi = \frac{1}{2}\arctan\frac{u}{q}. \tag{1.10}$$

The Faraday depth and the rotation measure are the same in the simplest case where there is only a single source of non-varying Faraday rotation. This is the so called Faraday simple case (Brown et al., 2017, eg), where the phase of the complex valued polarisation intensity, that is the angle characterising the rotation of the electric field vector (polarization angle, χ) is related to the Faraday depth by

$$\chi = \chi_0 + \phi\lambda^2. \tag{1.11}$$

This, however, is rarely the case observed with most polarised sources and cannot be assumed (Farnsworth et al., 2011). The complex valued synthesised Faraday spectrum, denoted as $F(\phi)$ (Sun et al., 2015), previously referred to as the Faraday dispersion function (Burn, 1966; Brentjens and de Bruyn, 2005), must be investigated at all possible values of ϕ to show the dependence of the intrinsic linear polarisation intensity on ϕ and thus resolve the different magnetic field components that altered the incident radiation. The observed polarisation intensity, $P(\lambda^2)$ is related to the Faraday spectrum $F(\phi)$ by:

$$P(\lambda^2) = |p|Ie^{2i\chi} = \int_{-\infty}^{\infty} F(\phi)e^{2i\phi\lambda^2}\, d\phi. \tag{1.12}$$

Equation 1.12 assumes λ^2 to be continuous and also both positive and negative, which is not physical. In real world observations, λ is positive, finite and discontinuous, and so we approximate the Fourier transform with a summation viz.,

$$P(\lambda^2) \approx \sum_j F(\phi)_j e^{2i\phi_j\lambda^2}. \tag{1.13}$$

In real observations, λ^2 is sampled discretely around a central value, λ_0^2, and to account for this Brentjens and de Bruyn (2005) define sampling function $W(\lambda^2)$ which is zero everywhere beyond the limits of the observed λ^2 range but non-zero where the range is sampled. This re-defines the observed polarised intensity $\tilde{P}(\lambda^2)$ in terms of the true intensity $P(\lambda^2)$:

$$\tilde{P}(\lambda^2) = W(\lambda^2)P(\lambda^2) = W(\lambda^2)\int_{-\infty}^{\infty} F(\phi)e^{2i\phi(\lambda^2-\lambda_0^2)}\, d\phi. \tag{1.14}$$

Thus, we have that the reconstructed intensity $\tilde{F}(\phi)$ is a convolution (denoted by $*$) of the true $F(\phi)$ with the Fourier transform of the sampling function, $W(\lambda^2)$. Inversion of equation 1.14 gives:

$$\begin{aligned}\tilde{F}(\phi) &= K\int_{-\infty}^{\infty} \tilde{P}(\lambda^2)e^{-2i\phi(\lambda^2-\lambda_0^2)}\, d\lambda^2. && (1.15)\\ &= F(\phi) * R(\phi). && (1.16)\end{aligned}$$

Here we have K as the multiplicative inverse of the λ^2 integral of $W(\lambda^2)$:

$$K = \left(\int_{-\infty}^{\infty} W(\lambda^2)\, d\lambda^2 \right)^{-1}, \tag{1.17}$$

and

$$R(\phi) = K \int_{-\infty}^{\infty} W(\lambda^2) e^{-2i\phi\lambda^2}\, d\lambda^2 \tag{1.18}$$

is the RM transfer function (RMTF) (Brentjens and de Bruyn, 2005), which is analogous to the synthesised beam in radio interferometry (see Section 1.2) and thus more appropriately renamed to "rotation measure spread function" (RMSF) (Heald et al., 2009). The $RMSF$ is unit-less with a peak equal to unity. The amount of errors in the synthesised quantities is governed by the sampling function. For instance, the widest λ^2 range increases the accuracy with which ϕ-components can be resolved in ϕ-space, and the more continuous the λ^2 range the lower the amplitude of side lobes of the the RMSF (Brentjens and de Bruyn, 2005).

Looking back to the real world approximations introduced in equation 1.13, we have

$$\tilde{P}(\lambda^2) \approx W(\lambda^2) \sum F(\phi_j) e^{2i\phi_j(\lambda^2-\lambda_0^2)} \tag{1.19}$$
$$\tilde{F}(\phi) \approx K \sum_k \tilde{P}(\lambda_k^2) e^{-2i\phi(\lambda_k^2-\lambda_0^2)} \tag{1.20}$$
$$R(\phi) \approx K \sum_k W(\lambda_k^2) e^{-2i\phi(\lambda_k^2-\lambda_0^2)} \tag{1.21}$$
$$K \approx \left(\sum_k W(\lambda_k^2) \right)^{-1}. \tag{1.22}$$

The conversion of the observed polarised signal into the Faraday spectrum is possible only for a constant spectral dependence along the line of sight (Brentjens and de Bruyn, 2005) and thus equations 1.19 and 1.20 are evaluated using the observed fractional quantities $p \equiv P/I, q \equiv Q/I$, and $u \equiv U/I$, so as to eliminate effects of a variable spectral index. Brentjens and de Bruyn (2005) define three important parameters that constrain a RM-synthesis experiment. Given the observed channel width ($\delta\lambda^2$), observed λ^2 range ($\Delta\lambda^2$), and the smallest λ^2 observed (λ^2_{min}):

- The resolution of ϕ-components, i.e the FWHM of the RMSF (denoted as $\delta\phi$ or $\delta\phi_{RMTF}$) is inversely proportional to $\Delta\lambda^2$:

$$\delta\phi \approx \frac{2\sqrt{3}}{\Delta\lambda^2}. \tag{1.23}$$

- The largest scale in ϕ-space to which an experiment can make detections is inversely proportional to λ^2_{min}:

$$\phi_{\text{max-scale}} \approx \frac{\pi}{\lambda^2_{\text{min}}}. \tag{1.24}$$

- The maximum observable Faraday depth is inversely proportional to $\delta\lambda^2$:

$$||\phi_{\text{max}}|| \approx \frac{\sqrt{3}}{\delta\lambda^2}. \tag{1.25}$$

The channel width, observed λ^2 range, and minimum observed λ^2 are calculated from frequency via

$$\delta\lambda^2 = \frac{2c^2}{\nu_{\rm max}^3}\delta\nu, \tag{1.26}$$

$$\Delta\lambda^2 = \frac{2c^2}{\nu_{\rm min}^3}\Delta\nu, \tag{1.27}$$

$$\lambda_{\rm min}^2 = \left(\frac{c}{\nu_{\rm max}}\right)^2. \tag{1.28}$$

The minimum frequency, maximum frequency, frequency channel width, and bandwidth are given by $\nu_{\rm min}$, $\nu_{\rm max}$, $\delta\nu$, and $\Delta\nu$, respectively.

1.3.2 RM synthesis in practice

RM-synthesis has the power to resolve the different magnetic field components that contribute to Faraday rotation along the line of sight. These different components are a result of magneto-ionic media located anywhere along the line of sight, and when thermal electron densities are known, field strengths can be quantified. The technique also remedies the effects of having ambiguous solutions to models of the polarisation angle as a function of wavelength, the so-called $n\pi$-ambiguity, where n is an integer. This ambiguity arises when a ϕ value is determined through a linear fit to equation 1.11 using data with very limited λ^2 sampling. The primary cause of the ambiguity is the fact that the response of a linear polarisation detector to linearly polarised radiation is unchanged by a 180° rotation of the detector's dipole (Klein and Fletcher, 2015). The ambiguity is exacerbated when attempts to determine ϕ make the assumption that equation 1.11 contains all the information about the Faraday structure of radiation for the entire LoS path[9], which applies only when there is a single Faraday rotating foreground screen (a non-emitting medium containing an ordered magnetic field and thermal electrons that is distinct from the source of emission) along the LoS, the so-called Faraday simple case (Farnsworth et al., 2011). In the Faraday simple case, a synchrotron source with a negligible thermal emission component results in a single peaked Faraday spectrum (Beck et al., 2012). Equation 1.11 can then be used to constrain the Faraday depth. In Faraday complex cases the ambiguities are minimised with RM-synthesis, where increasing the λ^2 range and its sampling rate produces less ambiguous results and thus lead to less erroneous conclusions.

The polarisation angle rotates as a function of bandwidth and the amount of rotation is increased with the larger bandwidths of modern radio interferometers. The average $Q(\lambda^2)$ and $U(\lambda^2)$ are thus reduced as they are rotated from positive to negative and vice versa. This effect, called *bandwidth depolarisation*, decreases the polarisation amplitude as a function of bandwidth and is most severe for high RM and sources that have complex Faraday structures, with multiple ϕ values along the LoS, that significantly rotate the polarisation angle (Brentjens and de Bruyn, 2005). Faraday complex cases can occur in such situations as when we observe radiation that has passed through a medium that further polarises the incident radiation and also injects polarised photons into the incident radiation along the LoS. The co-additive nature of the RM-synthesis technique (equations 1.19 - 1.22) overcomes bandwidth depolarisation by adding up all the polarisation intensities measured across the band. The approach we follow evaluates equation 1.20 over an array of ϕ values to determine those ϕ values that maximise the intrinsic polarisation flux. The peaks in the Faraday spectrum will occur at component values of ϕ along the LoS.

Bandwidth depolarisation is also minimised, but not completely removed, by finer λ^2 sampling, but this minimisation decreases for very large ϕ values that rotate the polarisation angles by at least π radians between two adjacent λ^2 samples (Heald et al., 2009). A large gap in the λ^2 range (due to reasons such as unavailability of data in the gap due to RFI contamination or physical limitations on the observations) will introduce significant effects in the form of increased side lobes in the RMSF. Bandwidth depolarisation can be characterised (e.g

---

[9] i.e that the polarisation angle is completely linear w.r.t λ^2 all along the LoS path.

Klein and Fletcher, 2015) by

$$\Delta\psi = -2\lambda_0^2 \cdot RM \cdot \frac{\Delta\nu}{\nu_0}, \tag{1.29}$$

where $\Delta\psi$ is the resulting rotation to the electric field vector, λ_0 is the wavelength corresponding to the center frequency ν_0, and $\Delta\nu$ is the width of each frequency channel. Thus for a rotation of 1 radian at $\Delta\nu = 5$ MHz, one would have $RM = 0.04$ rad/m^2 (or 6.25×10^{-4} rad/m^2 for $\Delta\psi = 1°$).

Weighting can be used to shape the sampling function, $W(\lambda)$, in order to mitigate these uncertainties. One can approximate $W(\lambda)$ by

$$W(\lambda_k) \approx \sigma_k^{-2}, \tag{1.30}$$

where σ_j^{-2} is the error in the j-th value of the measured polarisation intensity, $P(\lambda_k)$. $W(\lambda)$ has the effect of decreasing the uncertainties in estimated ϕ values but at the cost of the resolution of Faraday structures as weighting broadens the RMSF. Different weighting schemes must be used to achieve different goals so that the advantages of each scheme are optimally leveraged to achieve the best results (Heald et al., 2009).

RM-synthesis is a powerful technique, especially when used in the most optimal conditions where observations from a wide, densely sampled λ^2 range are available. The analysis of polarisation degree p, and both Stokes q and u spectra is most useful, as opposed to just the degree of polarisation and polarisation angle, in utilising the strengths of RM-synthesis (Farnsworth et al., 2011).

1.3.3 Physical origins of Faraday structure

Burn (1966) presents several physical scenarios that may produce the observed Faraday structures observed towards polarised sources. These are briefly reviewed in Klein and Fletcher (2015) with idealised examples given in Heald et al. (2009). We briefly introduce some of these below.

1.3.3.1 No intervening magneto-ionic media

This is the most physically simple case where the incident polarised signal is unobstructed and passes through no foreground magneto-ionic media and thus experiences no Faraday rotation. The incident polarised intensity, $P(\lambda^2)$, remains constant along with both $Q(\lambda^2)$ and $U(\lambda^2)$. The Faraday spectrum is a Dirac-delta function that is non-zero only at $\phi_{peak} = 0$ rad m^{-2}. The incident emission will still, however, be coupled to ionospheric effects (e.g W. D. Cotton, 2018). The RM contribution of the ionosphere can be derived if TEC (total electron content) measurements are available.

1.3.3.2 Resolved foreground screen

This is the so called Faraday simple case introduced above where there exists only a single Faraday rotating screen of material. In this case the Faraday spectrum is Dirac-δ function

$$F(\phi) = \delta(\phi - \phi_0). \tag{1.31}$$

The polarisation angle is then given by equation 1.11 with $\chi_0 = \chi(\lambda = 0)$. This allows for equation 1.8 to be evaluated given that the rest of the parameters are known or can be reasonably approximated.

1.3.3.3 Unresolved foreground screen

This is the case where several foreground cells of different Faraday depths within the observing beam are not resolved by the beam. Each of the Faraday depths rotates the incident radiation by a different amount resulting in a diminished signal due to superposition of the cells when the signal is integrated across the beam width.

This is beam depolarisation, in which equation 1.11 no longer applicable. These cells can be created in a region of turbulent magnetic fields where the turbulence scales are smaller than the observing beam. The polarisation plane of the incident wave can be thought of as undergoing a random walk process as the different cells rotate it in random directions (Sokoloff et al., 1998). Depolarisation with frequency/wavelength in this case is significant with an exponential dependence on the wavelength (Klein and Fletcher, 2015):

$$P(\lambda^2) \propto p_0 e^{-\lambda^4}. \tag{1.32}$$

1.3.3.4 Internal Faraday rotation

In this scenario, the Faraday rotation that occurs is intrinsic to the source. This is due to an emitting region which also contains thermal electrons and ordered/coherent magnetic fields. This causes polarised emission from the far-side of the region to undergo Faraday rotation more than the near-side of the region. This process is called differential Faraday rotation. In the simplest case where the emitting medium has a single rotation measure, the wavelength-dependent depolarisation is given by Arshakian and Beck (2011):

$$P(\lambda^2) = p_0 \left(\frac{\sin(2RM\lambda^2)}{2RM\lambda^2} \right) e^{2i(\chi_0 + 0.5RM\lambda^2)}, \tag{1.33}$$

where

$$RM \simeq 0.81 \langle n_e \rangle \langle B_{ord,\parallel} \rangle L, \tag{1.34}$$

is the average rotation measure in rad m^{-2} and $B_{ord,\parallel}$ is the ordered magnetic field component in the plane parallel to the observer's line of sight. This is the *Burn slab* approximation, where the magneto-ionic medium within the source is uniform and the resulting Faraday spectrum is a tophat function, the observed polarisation degree takes on the form of a sinc function – the Fourier inverse of a top-hat function (Burn, 1966; Heald, 2008; Klein and Fletcher, 2015). Internal Faraday rotation can also occur in cases where the emitting region contains a turbulent magnetic field instead of the ordered field considered above. A simple approximation of this case, which also applies for the case of mixed turbulent and ordered fields of comparable field strengths (Sokoloff et al., 1998; Arshakian and Beck, 2011), a uniform slab with a constant linear path, L, of the incident light along the LoS. In this case,the polarisation intensity is modelled as (Burn, 1966):

$$P(\lambda^2) = p_0 \frac{1 - e^{-S}}{S}, \tag{1.35}$$

where S is a complex quadratic function of λ^2:

$$S = (K n_e B_r)^2 d L \lambda^4 - i 2 K n_e B_{o,\parallel} L \lambda^2. \tag{1.36}$$

Here K is the constant in front of the integral in equation 1.8, d is the scale of the fluctuations in the turbulent magnetic field component B_r, and $B_{o,\parallel}$ is the LoS component of the ordered magnetic field. A uniform spherical geometry is also modelled by Burn (1966) where:

$$P(\lambda^2) = p_0 \frac{3[(S+1)e^{-S} + 0.5S^2 - 1]}{S^3}, \tag{1.37}$$

with L now representing the sphere's diameter. The depolarisation behaviours of the two models are displayed in Figure 1.5 (Gardner and Whiteoak, 1966).

1.3.3.5 Bandwidth depolarisation

Beam width depolarisation is introduced in the previous subsection describing the case of an unresolved foreground screen. In addition to the superposition of randomly oriented Faraday rotations across the beam, the physical fact that the beam width, the resolution, is frequency dependent also adds to the apparent change of the measured polarisation (Gardner and Whiteoak, 1966). This is the so called bandwidth depolarisation effect

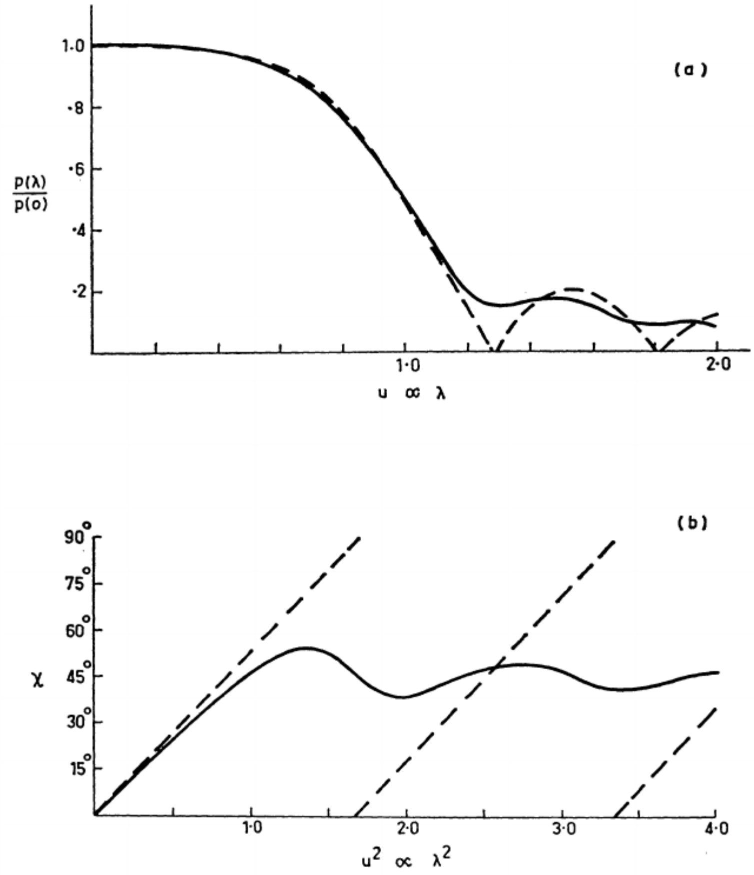

Figure 1.5: Internal depolarisation models (top panels) for a Burn slab (dashed) along with a spherical model (solid line). Bottom panel: polarisation angle as a function of λ^2 (the plot line styles follow the same convention as the top panel). The plots are from Figure 6 of Gardner and Whiteoak (1966)

which can also diminish the observed degree of polarisation. The effect is strongest at large wavelengths. To overcome this, the fine channelisation of broad band observations by modern radio interferometers, like KAT 7 and MeerKAT, is particularly useful in RM-synthesis where the fine sampling of the band adds to the quality of the results (Heald et al., 2009).

1.3.4 RM Clean

Section 1.3.1 introduces the constraint encountered in RM-synthesis where the reconstructed intrinsic polarisation signal, the Faraday spectrum $\tilde{F}(\phi)$, is the true spectrum convolved with the RMSF, $R(\phi)$. In low signal-to-noise cases or when there may be multiple features in $\tilde{F}(\phi)$ that are not initially resolved by the reconstruction, the interpretation of the results becomes more uncertain. Depolarisation models, introduced in Section 1.3.3, can be fitted to polarisation spectra so as to best approximate the true broad band properties and also to narrow down the most likely physical origins of these properties (e.g Farnsworth et al., 2011; O'Sullivan et al., 2012; Sun et al., 2015; O'Sullivan et al., 2015; Anderson et al., 2015, 2016). Current available algorithms tend to model the observed polarisation behaviour with degenerate models (Sun et al., 2015). We use the deconvolution of the measured broad band spectra to extract the true spectra $F(\phi)$. This deconvolution is commonly called RM clean (Heald et al., 2009) due to it's analogy to the CLEAN algorithm in radio synthesis imaging (Högbom, 1974). Without making assumptions regarding the physical scenario responsible for observed polarimetry, RM-clean generally produces Faraday spectra with reduced contributions from Faraday components that may be noise. The largest λ^2 coverage, the most sensitive, and high resolution observations are required for the best clean model of the observed $q(\lambda^2), u(\lambda^2)$ to be produced (Farnsworth et al., 2011). We developed a Python[10] based algorithm to perform RM clean on the IDIA HPC facilities. The process of RM clean consists of the following steps:

1. The location ϕ_j of the peak in $\tilde{F}(\phi)$ is found and $\tilde{F}(\phi_j)$ is recorded.

2. Next $\tilde{F}(\phi_j)$ is multiplied by a constant factor, γ called the loop gain – with the most optimal value being typically 0.1 (Heald et al., 2009; Farnsworth et al., 2011). $\gamma\tilde{F}(\phi_j)$, ϕ_j, and the polarisation angle $\chi_{0,j}$ (defined by equation 1.10) are then stored as a "clean ϕ-component" (Faraday component).

3. Then $R(\phi_j)$ is scaled and shifted to equal $\gamma\tilde{F}(\phi_j)$ and then subtracted from $\tilde{F}(\phi)$.

4. Steps 1 - 3 are repeated on the residual spectrum, $\tilde{F}(\phi)$ until a certain threshold in $\tilde{F}(\phi)$ is reached (e.g relative to the level of noise) or a certain number of iterations (usually obtained by trial and error) have been performed.

5. The final step is the reconstruction of the cleaned spectrum, $F(\phi)$, by convolving the ϕ-components with a real valued function such as a Gaussian with full-width-half-maximum (FWHM) equal to that of the main lobe of the RMSF. This reconstruction is then added to the residuals with the result being a closer approximation of $F(\phi)$ (Heald et al., 2009). We, however, make no such approximation but instead reconstruct the $\tilde{q}(\lambda^2), \tilde{u}(\lambda^2)$ spectra from the cleaned components and then calculate the cleaned Faraday spectrum from the reconstructed spectra. The reconstruction from ϕ-space to λ^2-space is done through the following relations, for the j-th component:

$$\chi_j(\lambda^2) = \phi_j\lambda^2 + \chi_{0,j} \tag{1.38}$$

$$\tilde{q}(\lambda^2) = \sum_j |\tilde{F}(\phi_j)| \cos(2\chi_j) \tag{1.39}$$

$$\tilde{u}(\lambda^2) = \sum_j |\tilde{F}(\phi_j)| \sin(2\chi_j). \tag{1.40}$$

---

[10] `https://www.python.org/`

In the rest of this work we use the notation of $F(\phi)$ in place of $\tilde{F}(\phi)$ for simplicity.

1.4 Motivation

1.4.1 The literature so far

The study of cosmic magnetism is vital in fully understanding the role that magnetic fields play in the evolution of cosmological objects such as galaxies and their large-scale components such as radio lobes and jets. Magnetic fields in galaxies influence star-formation and properties of the ISM such as gas pressure, cosmic ray densities and flows (Beck et al., 1999; Beck and Gaensler, 2004; Beck, 2015). The exact role played by magnetism in galaxy evolution is, however, still a puzzle. Some theoretical work has been done (e.g. Lou and Fan, 1998) but empirical constraints from extensive polarisation campaigns are still lacking (e.g. Chamandy et al., 2016). Works such as Eichendorf and Reinhardt (1979), Beck et al. (2002), Beck (2004), O'Sullivan et al. (2012), Beck et al. (2012), Farnes (2014) have provided some insight into the workings of magnetism in galaxies. Eichendorf and Reinhardt (1979) provide some of the earliest catalogs of polarimetry data across several wavelengths for radio sources that were observed between 1965 and the middle of 1974, while the more recent work by Farnes (2014) presents a catalog of polarimetry data, across a very wide range of wavelengths (400 MHz to 100 GHz) as a result of cross-matching the NRAO VLA Sky Survey (NVSS (Condon et al., 1998)) data base with other polarimetry and total intensity studies. Beck et al. (2002) present a study of polarised and total intensities for 20 barred galaxies with radio observations from the VLA at 3, 6, 18, 22, and Australian Telescope Compact Array (ATCA) at 6, and 13 cm. O'Sullivan et al. (2012) present a broad-band ($1.1 - 3.1$ GHz) polarimetry study on bright (> 1 Jy) strongly polarised radio-loud quasars with ATCA while O'Sullivan et al. (2015) present a narrow band study (NVSS observations at $\nu = 1.4$ GHz) of AGN dominated radio galaxies (high-excitation radio galaxies (HERGS), radio-loud quasi-stellar objects (QSOs), and low-excitation radio galaxies (LERGs)) in different accretion phases. The biggest hurdles in all these studies, however, have been radio frequency bandwidth coverage and/or radio flux sensitivity – where reported work has been done only on bright and highly polarised radio sources. High resolution (at resolutions of $2''$ - $15''$ and $9''$ - $25''$) narrow-band imaging observations of nearby disk galaxies have been made (e.g. Beck et al., 2005), showing large scale magnetic fields related to spiral structure. For galaxies that remain unresolved by current radio imaging telescopes we must rely on the frequency dependence of polarization as our primary probe of magnetic properties (Stil et al., 2009). However, the relatively narrow instantaneous bandwidths typical of most past studies of radio polarization limit both the resolution of Faraday spectral features and the ability to characterize the broad band properties of polarised intensity such as depolarisation.

Recent studies are beginning to probe polarized radio emission over broader bands. O'Sullivan et al. (2012), for example, presented a broad-band spectro-polarimetric study of four radio bright and highly polarized AGN sources, for which, Faraday rotation features could be resolved. Anderson et al. (2015) report a wide band ($1.3 - 2.0$ GHz) and wide field (30 square degree) study of extragalactic sources, and Anderson et al. (2016) observed 36 strongly polarized sources over a very wide, non-contiguous band from $\sim 1 - 10$ GHz, finding Faraday complexity in most of them, asserting that complex features and properties of Faraday spectra are common among strongly polarised sources.

1.4.2 Open questions

At the heart of polarimetry is the desire to fully understand magnetic fields and their roles in cosmic evolution. Important properties of the fields, such as the field observed strengths and field origins, are not fully understood (Beck and Wielebinski, 2013). Some theoretical models such as the mean-field dynamo (e.g. Ruzmaikin et al., 1988; Beck et al., 1996; Brandenburg and Subramanian, 2004; Moss et al., 2012; Chamandy et al., 2014b) have been successful in predicting the observed field strengths but questions still remain. Examples of the missing information pertain to how and when the first fields were generated and amplified to the levels observed, what effect these fields had on early galaxy evolution, what the origin of intergalactic fields is, understanding the structure and strength of intergalactic fields and also the structure and properties of the large scale field in our own galaxy (Beck and Wielebinski, 2013).

1.5 This thesis

Below I outline the objectives, scope, and structure of this thesis.

Aims and objectives

The main aims of this work relate to the SKA Radio Astronomy Science areas, in that the overall goal of the project is to study the presence and properties of coherent magnetic fields in radio sources by observing the linear polarisation of faint objects. This work also relates to SKA techniques areas in that since the basic observational data will be broad band polarimetry secured with the Karoo Array Telescope (KAT 7) and the SKA SA precursor, MeerKAT (e.g Carilli, 2015). Techniques for polarization calibration and RM synthesis of data taken over broad bands are explored and developed both in direct pointing mode using several sufficiently bright radio galaxies, and also in wide-field imaging mode for faint sources in ~ 1 square-degree field populated by several thousand radio sources, most of which have not been studied yet. We explore the spectropolarimetric properties of radio sources and report on the results of this analysis.

The useful technique of RM synthesis (see Section 1.3.1 and 1.3.4) is applied to broad band polarisation data as recent results have shown that integrated polarization properties of disk galaxies can be used to explore the presence and properties of coherent large-scale disk fields (e.g. Stil et al., 2009; Arshakian et al., 2011; Beck et al., 2012; Gaensler et al., 2015; Heald et al., 2015). This is only now beginning to be extended to include Faraday synthesis information owing to technical advances of current and next generation radio interferometers (such as broad instantaneous observing bands with high resolution of the band and high flux sensitivity). Large-scale magnetic fields within galaxies should create a frequency dependent polarisation signature and as such, this study uses the RM synthesis technique to first explore signatures of coherent fields in a sample of low redshift radio sources. The full polarisation radio observations used are acquired with KAT 7 at frequencies $\nu \sim 1.20 - 1.95$ GHz. Subsequent analyses then extend this to interpret the spectropolarimetric signatures of faint radio sources at higher redshift through high angular resolution ($\sim 14''$), wide-field ($\sim$ 1-square degree), broad band ($\nu \sim 0.80 - 1.70$ GHz), and deep (rms noise ~ 70 μJy/beam) observations from the first 16 MeerKAT antennas.

Structure of this thesis

This dissertation is structured follows: Chapter **2** presents our spectropolarimetric study of six radio galaxies observed with KAT 7. Chapter **3** presents our study of a ~ 4 square degree field using observations from the 16 antenna commissioning MeerKAT array. The MeerKAT study builds upon the basic techniques and tools for RM synthesis and RM clean developed and introduced in the KAT 7 study, and also includes additions and considerations that are pertinent issues in cases of survey-style wide field studies, such as source finding. Chapter **4** presents our discussions of the main results of both our KAT 7 (Section **4.1**) and MeerKAT (Section **4.2**) studies. We present our conclusions and suggestions for related future studies in Chapter **5**. Appendix **A** presents our appendices.

Chapter 2

Broadband Polarimetry with KAT 7

2.1 Sample and Observations

2.1.1 Sample

We selected our sample of disk galaxies from the source list for the MHONGOOSE survey (MeerKAT HI Observations of Nearby Galactic Objects: Observing Southern Emitters[1]). MHONGOOSE will secure very high sensitivity atomic hydrogen images of a sample of nearby galaxies. A further criterion was that our sources be sufficiently bright with an integrated total power intensity greater than 200 mJy. This resulted in a sample of two disk galaxies. We also observed four AGN dominated emitters, including a flat-spectrum source, a steep spectrum source, and a GigaHertz Peak Spectrum (GPS) source. Two of the AGN served also as calibrators for the remaining targets.

2.1.1.1 Disk Galaxies

NGC1097 is identified as a Sy1 galaxy (Storchi-Bergmann et al., 1997) with a circumnuclear star-burst ring (Gerin et al., 1988). It is a barred spiral, SBb, with it's radio emission dominated by the circumstellar ring and nucleus (Beck et al., 2005). The magnetic properties of NGC1097 have been studied by Beck et al. (2005) with narrow band (~ 50 MHz) high resolution radio data, at 4.8 and 8.4 GHz and with resolutions of $2'' - 15''$, with the NRAO Very Large Array, VLA. The galactic magnetic field was observed to control the ISM gas flow at kpc scales and found to have a regular component that follows the shape of the spiral arms (Beck et al., 2005). The galaxy has a redshift of 0.0042.

NGC1808 is identified as a Sy2 galaxy (Tacconi-Garman (1996); Galliano et al. (2008)) with a low luminosity AGN (Véron-Cetty and Véron (1985); Dahlem et al. (1990); González-Martín et al. (2013); Esquej et al. (2013)). It was classified as a peculiar Sbc galaxy (Véron-Cetty and Véron (1985)). It also has a star-burst region in the inner ~ 750 pc dominating the infrared emission (Sengupta and Balasubramanyam (2006)). From observations at 6 and 20 cm wavelength with the VLA in DnC configuration, Dahlem et al. (1990) found linear polarization degrees of up to 30% and a steep ($\alpha = -0.88$) radio spectrum from outside the central region of the galaxy. The galaxy has a redshift of 0.0033.

2.1.1.2 AGN

J0240-231 has been identified to be a quasi-stellar object (QSO) and also a Gigahertz-peaked spectrum (GPS) source (Kuehr et al. (1981); O'Dea (1998a); Véron-Cetty and Véron (2006)). It is located at z = 2.22 (Hewitt and Burbidge, 1989). The source has been observed to show significant linear polarization at 4.8 GHz where $p = 3.47\%$ (Edwards and Tingay, 2004). VLBI studies show that it has some structure resembling two lobes that are separated by 12 mas (Dallacasa et al., 1998).

---

[1] `http://mhongoose.astron.nl/`

Table 2.1: Summary of the KAT 7 observations. The table lists the radio source observed during each run, the observation dates, central frequency, number of antennas available, and the total recovered bandwidth.

Sources Observed	Date	ν_c (GHz)	$N_{\rm ant}$	$\Delta\nu$ (MHz)
NGC1808, PKA1934-683, J0538-440, PKSB0407-658	29/07/2016	1.894	6	152
NGC1808, PKS1934-638, J0538-440, PKSB0407-658	31/07/2016	1.394	6	148
NGC1097, PKS1934-638, J0240-231, PKSB0407-658	09/06/2015	1.850	7	223
NCG1097, PKS1934-638, J0240-231, PKSB0407-658	15/06/2015	1.350	7	211

J0538-440 is reported to be a BL Lac, GPS object and also a variable γ-ray source located at redshift 0.896 (Impey and Tapia (1988); Romero et al. (2000); Tornikoski et al. (2001); Romero et al. (2002); Andruchow et al. (2005); Torniainen et al. (2005)). It has also been identified as a potential gravitational lens (Surpi et al., 1996).

PKS1934-638 and PKSB0407-658 are both QSO and GPS sources (O'Dea et al., 1991). VLBI imaging of PKS1934-638 shows that it has a double lobed structure (Tzioumis et al., 1989). PKS1934-638 and PKSB0407-658 have redshifts of 0.18 and 0.96, respectively.

2.1.2 Observations

The Karoo Array Telescope (KAT 7) is a synthesis array telescope located adjacent to the MeerKAT and SKA phase 1 site in the Karoo plateau in South Africa. It was built as an engineering test-bed preceding the SKA mid-frequency precursor array, MeerKAT, which is currently under construction. The initial design had KAT as a 20 antenna array which was later expanded to 64 dishes. The construction of KAT 7 was then commissioned to be the test bed for the 64 dish array, now called MeerKAT (Foley et al., 2016). KAT 7 consists of seven 12-metre, centre-fed parabolic antennas in a fixed configuration with baselines ranging from 26 to 185 metres (Carignan et al., 2013). It has a maximum instantaneous bandwidth of 256 MHz within the RF range 1200 - 1950 MHz. Two components of linear polarisation are detected with prime-focus feeds on each antenna. We observed in wide-band, full-polarisation mode, providing four polarisation correlation products sampling the 256 MHz band in 1024 spectral channels of width 390.625 kHz. Our observations covered the entire 750 MHz RF band using three separate observing runs for each source with the 256 MHz centred on 1350, 1600, and 1850 MHz.

Each observation consisted of 12-hours tracks during which on-source observations of 4 minutes of either NGC 1097 or NGC 1808 were alternated with either J0240-231 (for NGC 1097) or J0538-440 (for NGC 1808). Several integrations were made on PKSB0407-658 during each run. The 12 hour tracks provided a good range of parallactic angle variations for polarisation calibration. For all observing sessions PKS1934-638 was observed approximately every hour for primary flux density and bandpass calibration.

2.2 Calibration and imaging

In this section we explain our data reduction methods, that is editing and calibration, and also how the reduced data is then imaged into the desired products for analysis.

2.2.1 Calibration

The sections than follow introduce the basic relations that govern different stages of radio frequency calibration applied and the results acquired in this work.

2.2.1.1 Gain calibration

The observed visibilities, introduced in Section 1.2, are most often not equal to the true visibilities of the sky. This is due to the imperfect response of the telescope and results in the convolution of the true signal with the telescope response. Calibration of the data aims to undo this convolution so that we regain the true visibilities. The observed visibilities $\widetilde{V}_{ij}$ from the baseline made up of antennas i and j can be written as

$$\widetilde{V}_{ij} = \mathcal{G}_{ij} V_{ij} + \epsilon_{ij} + \eta_{ij}, \tag{2.1}$$

here we have $\mathcal{G}_{ij}$, ϵ_{ij}, and η_{ij} as the baseline based gain, offset, and random noise, respectively. The visibility sampling is discrete in time and so Equation 2.1 is also a function of time.

Observing non-variable sources of known flux and astrometry can help us determine the true visibilities. These are calibrator sources whose observations are interwoven into those of the target source. These are usually very bright and observed for short periods in comparison to the target and their observation help determine

$$\mathcal{G}_{ij} = g_i g_j^*, \tag{2.2}$$

where $g_i$and g_j are the complex antenna gains (the star represents the complex conjugate), whose amplitudes and phases are to be determined through calibration. Given N antennas, we will have $N(N-1)/2$ baselines with $\mathcal{G}_{ij}$ for each of the baselines and $g_i g_j$ for each of the antennas. The process of determining the complex gains is sometimes referred to as gain calibration. Figures 2.1 and 2.2 show our gain solutions plotted for secondary calibrator J0538-440.

2.2.1.2 Calibrator sources

Radio sources that are used as calibrators are not point sources physically and if the resolution of the observations is high enough, such as in VLBI, their complex structure will be revealed. For the frequency bands observed with KAT 7 and the array's resolving power, most common calibrator sources are indeed observed to be point sources making them ideal for calibration purposes. These sources are required not to vary on time scales of the observations, be isolated on the sky, and also with known and simple spectral behaviour. This implies that, for these sources, the true visibility is known. These properties help in determining the true visibilities of the target observations but they do have limitations such as the inability to use calibrators to calibrate any variations that are on time scales shorter than the time it takes to switch between observing a target and observing the calibrator. This is due solely to practical reasons that the calibrators are often not located very near the target. In the cases where the target is sufficiently bright, it can be used to calibrate itself through the process of self-calibration where the target visibilities are used to determine the complex gains in equation 2.2, see e.g Taylor et al. (1999). During self-calibration: an initial rough model of the source is made, then that model is used to convert the source to a point source, following this a solution for the complex gains is determined and applied to the observed visibilities, a new model is then formed using the newly corrected visibilities. This process is iterated until a certain user defined number of cycles is reached. The solutions converge fairly quickly requiring just several iterations. We decrease our solution intervals each iteration to better resolve the gain solutions with respect to time.

2.2.1.3 Bandpass calibration

The spectral behaviour of sources is also a vital property that requires to be accurately determined and thus calibrated accordingly. This is achieved through bandpass calibration where the frequency dependence of the complex gains $\mathcal{G}_{ij}(\nu)$ is determined. This calibration is stage is where the simple and preferably well understood

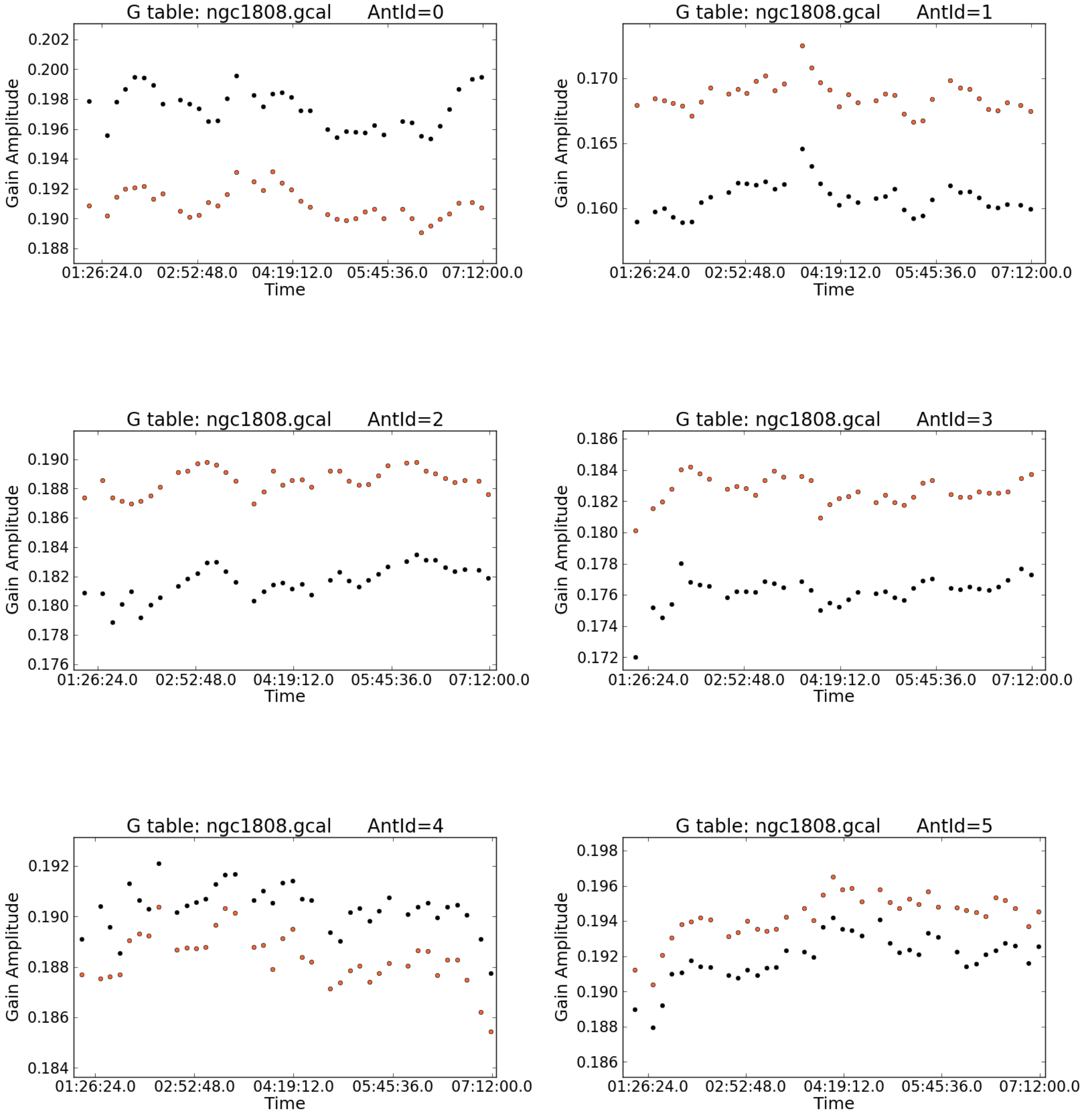

Figure 2.1: Gain solutions showing gain amplitude against frequency for our secondary calibrator, J0538-440. The observations are those made at the high band with 6 antennas. The solutions are for the parallel hand correlations XX and YY shown by different colours.

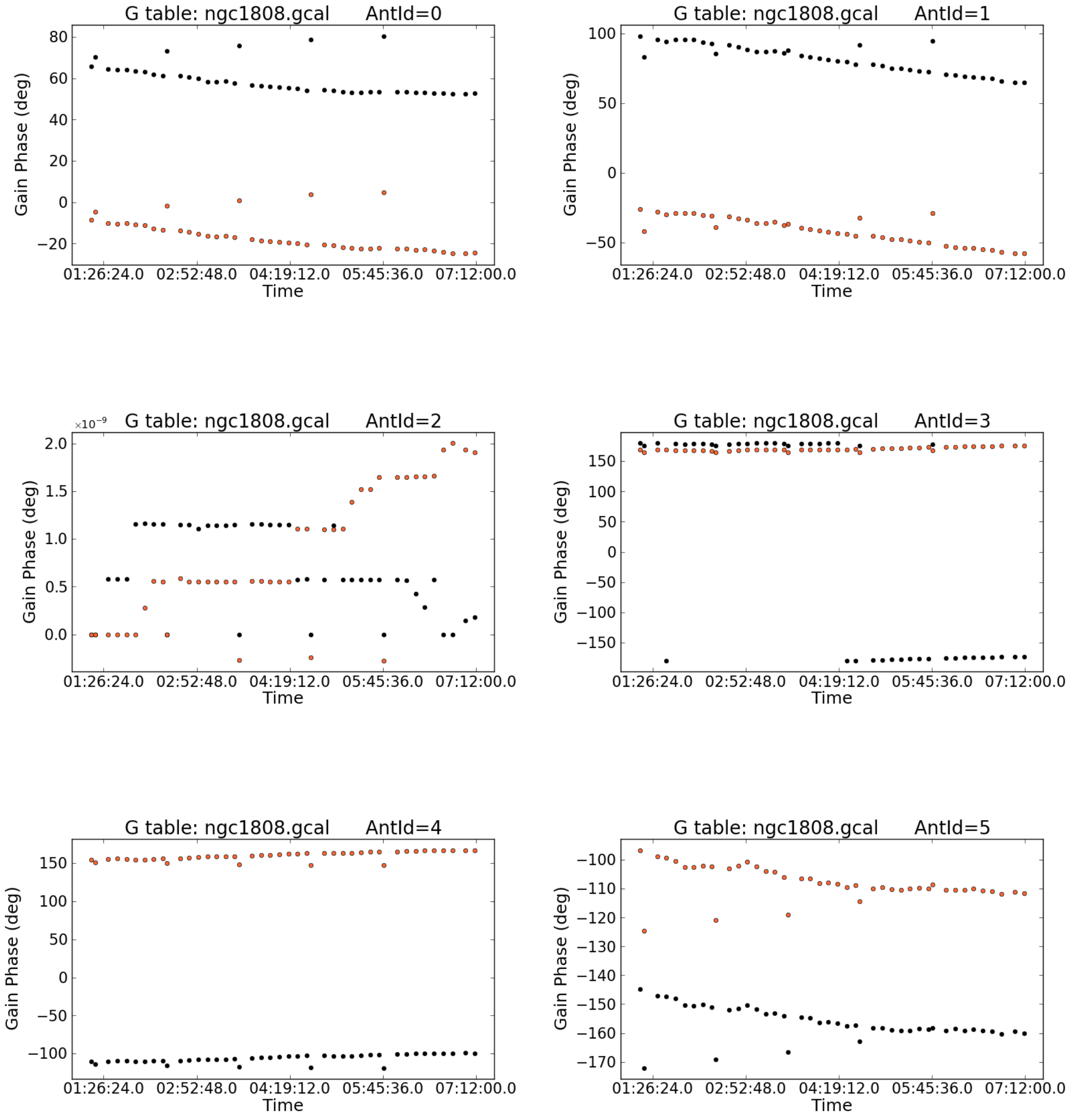

Figure 2.2: Gain solutions showing gain phases against frequency for our secondary calibrator, J0538-440. The observations are those made at the high band with 6 antennas corresponding to Figure 2.1. Antenna 3 was used as the reference antenna. The solutions are for the parallel hand correlations XX and YY shown by different colours.

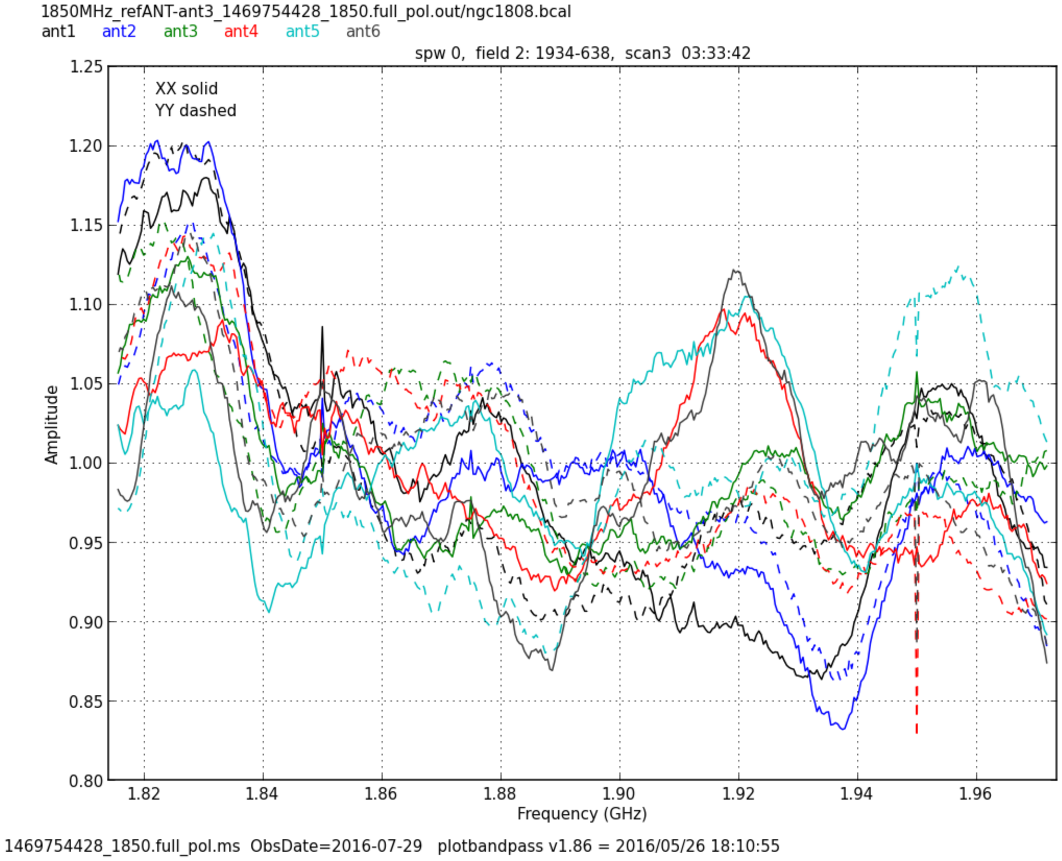

Figure 2.3: Bandpass solutions showing gain amplitude against frequency for our primary calibrator, PKS1934-638. The observations are those made at the high band for 6 antennas. The solutions are for the parallel hand correlations XX (solid lines) and YY (dashed lines) with different antennas shown by different colours.

spectral behaviour of the calibrator is most evidently required. Bandpass solutions for this work are displayed in Figure 2.3. We find that the bandpass response is stable over the observing periods.

2.2.1.4 Delay calibration

The physical nature of interferometers also introduces a time difference of radio signals received by different elements in the array, causing the signal to reach one antenna sooner than the other in a baseline. This *delay* comes from the geometry of the array but also has a contribution from signal propagation differences internal to each antenna. The *geometric delay* can be defined as

$$\tau_g = \boldsymbol{b} \cdot \boldsymbol{s}/c, \tag{2.3}$$

where the vectors are as defined in Figure 1.4 and the associated text. This delay can be determined by taking the geometry of the array into consideration but the internal antenna based delay will need to be calibrated. This is what, in practice, is called delay calibration. This *delay* so far, has only considered parallel-hand polarisation channels, that is XX, YY in linear polarisation terms or RR, LL in circular polarisation terms. Cross-hand calibration is a related calibration step where the time differences between orthogonal polarisation channels (XY, YX or RL, LR) are also calibrated so as to correctly determine polarisation signals from the source. The details of polarisation calibration are discussed below.

2.2.1.5 Polarisation calibration

The four correlations of the two orthogonal polarisations, mentioned briefly in the text above, fully express the radiation field of a source. The polarisation procedures discussed so far, mostly account for calibration of the parallel-hand correlations XX, YY (in the case of KAT 7 and MeerKAT which have linear feeds). The calibration of signals in the cross-hand correlations, XY and YX, is vital if one is to discern the full polarisation state of the source. Looking back at the Stokes parameters I, Q, U, and V, we can label the visibilities of each component of the Stokes vector as V_I, V_Q, V_U, and V_V. In practice, these visibilities are coupled in linear combinations contained in the visibilities of the four correlations XX, YY, XY, and YX; and are only separated after the observation stage. Denoting the observed visibilities of each of the four correlations in the fashion $V(XY)$, we can implicitly express V_I, V_Q, V_U, and V_V through the following:

$$V(XX) = V_I + V_Q \cos 2\psi + V_U \sin 2\psi, \tag{2.4}$$
$$V(YY) = V_I - V_Q \cos 2\psi - V_U \sin 2\psi, \tag{2.5}$$
$$V(XY) = -V_Q \sin 2\psi + V_U \cos 2\psi + iV_V, \tag{2.6}$$
$$V(YX) = -V_Q \sin 2\psi + V_U \cos 2\psi - iV_V, \tag{2.7}$$

where ψ is the antenna polarisation position angle (Thompson et al., 2017).

Polarisation calibration comprises of two main stages viz: correcting for the polarisation leakage (instrumental polarisation) and correcting for differences in phase between the two polarisation channels in each of the two cross-hand correlations. Polarisation leakage results from the fact that in reality, the two "orthogonal" polarisation channels are not *fully* orthogonal and thus signals from one channel *leak* into the other and are detected as part of that channel giving spurious detections. We can reveal the contribution of the complex leakage terms D_X and D_Y to the *orthogonal* channel voltages v_X and v_R through

$$v_X = E_X e^{-i\chi} + D_X E_Y e^{i\chi}, \tag{2.8}$$
$$v_Y = E_Y e^{i\chi} + D_Y E_X e^{-i\chi}, \tag{2.9}$$

where the E_X and E_Y are the unaltered electric fields in each channel. The leakage terms are in general small compared to the true signals, save for strongly polarised sources, and so rewriting equations 2.4 - 2.7 we can ignore products of the leakage terms, including those with Q, U and V. Thus

$$V(XX) = V_I + V_Q(\cos 2\psi - D^+_{XX} \sin 2\psi) + V_U(\sin 2\psi + D^+_{XX} \cos 2\psi) - iV_V D^-_{XX}, \tag{2.10}$$
$$V(YY) = V_I - V_Q(\cos 2\psi + D^+_{YY} \sin 2\psi) - V_U(\sin 2\psi - D^+_{YY} \cos 2\psi) + iV_V D^-_{YY}, \tag{2.11}$$
$$V(XY) = -V_Q \sin 2\psi + V_U \cos 2\psi + iV_V + (D_{X1} + D^*_{Y2})V_I, \tag{2.12}$$
$$V(YX) = -V_Q \sin 2\psi + V_U \cos 2\psi - iV_V + (D_{Y1} + D^*_{X2})V_I, \tag{2.13}$$

where D_{Xj} represents the leakage term contribution from antenna j in channel X and similarly for the leakage term contribution in the other channel and the other antenna. D^+_{XX} and D^-_{XX} are defined as

$$D^+_{XX} = D_{X1} + D^*_{X2}, \tag{2.14}$$
$$D^-_{XX} = D_{X1} - D^*_{X2}. \tag{2.15}$$

D^+_{YY} and D^-_{YY} are defined in a similar manner. Equations 2.10 - 2.13 follow the derivation of (Thompson et al., 2017) where the formalism for circularly polarised feeds is also given. Also see Taylor et al. (1999).

An unpolarised calibrator can be used to determine the relative leakage terms as the cross-hand channels will *detect* non-zero polarisation due, solely, to polarisation leakage differences. With an unpolarised calibrator we do not know the absolute Q and U of the source so we cannot relate the leakage back to the source frame. A polarised calibrator will, however, determine the absolute leakages. Good parallactic angle coverage, provided by observations over long periods ($\geq$ 12 hours) following radio sources across the sky, minimizes the leakage terms as their vector sum will approach zero (Jagannathan et al., 2017) but the intrinsic leakages from the feeds will remain to be minimized during on-axis leakage calaibration. Section 3.5.1 presents our analysis of off-axis leakages in the wide field MeerKAT (16) case. Thus telescope design can also be utilized for the purpose of minimising leakage.

The gain and phase calibration discussed above neglects the phase differences in the cross-hand channels. Calibrating of these phase differences involves the calibration of residual phase differences between the cross-hands following parallel-hand phase calibrations. To this end, observations of a known calibrator (known $Q+iU$, i.e both amplitude and phase known) with a strong linearly polarised signal are required. The polarisation position angle will remain uncalibrated if a source of known polarization and position angle is not available. In these cases, only the polarisation amplitudes given by $\sqrt{q^2+u^2}$ can be calibrated. This is the case with the MeerKAT observations that we have analysed (see Section 3.3.1). Our polarisation leakage solutions for our KAT 7 observations are plotted in Figures 2.4 and 2.5

2.2.1.6 Applying calibrations

Processing of the data, both calibrations and imaging, was carried out using the Common Astronomy Software Applications[2], CASA (Mcmullin et al., 2007) package. The software is being developed for the current and next generation large synthesis arrays such as the Very Large Array (VLA) and similar facilities. CASA is a suite of C++ radio data reduction and analysis functions and tools. CASA also incorporates an interactive Python (iPython[3]) front-end and has the ability to handle both single dish and interferometric radio data. CASA is an international collaboration with development by scientists at the National Radio Astronomical Observatory (NRAO), the European Southern Observatory (ESO), the National Astronomical Observatory of Japan (NAOJ), the Academia Sinica Institute of Astronomy and Astrophysics (ASIAA), the CSIRO division for Astronomy and Space Science (CASS), and the Netherlands Institute for Radio Astronomy (ASTRON) and all guided by the NRAO. CASA provided the most flexible, capable and accessible reduction and analysis software for the student and has been in use on various studies using SKA precursor observations such as in the case of this thesis, allowing the student to learn from various experienced colleagues and other astronomers.

The un-calibrated and unedited observations from the telescope have a few artefacts and some of these are large errors at the peripheries of the observing bands. This is the roll-off due to the shape of the finite bandpass. This is caused by the telescope electronics and feed limitations. The severity of this effect varies as a function of frequency of the radiation, being larger at the shorter wavelengths characteristic of the ultra-violet end of the spectrum but less severe at the longer radio end. We remove the channels at the upper and lower ends of the band due to this effect. The visibility data was then inspected visually for other artefacts such as radio frequency interference (RFI) signals and instrumental fluctuations. The RFI generally emerge as large localised amplitudes when looking at variations of the visibilities across all channels. Figure 2.6 displays the amplitudes observed across all channels, for all baselines, and for all polarisations (XX, YY, XY, YX). This observation is that of the flux calibrator PKS1934-638. The artefacts are removed through flagging the data manually, initially, followed by automated flagging through the specialised CASA task ,“flagdata()”. The mid-band, centred at 1600 MHz, was very heavily populated with RFI occupying a large fraction of the band. Analysis in this band was severely compromised as a result and we did not include the mid-band in our subsequent analysis. The low band also had some significant RFI but still had substantial data after removal of these artefacts, while the

---

[2] `https://casa.nrao.edu/`

[3] `https://ipython.org/`

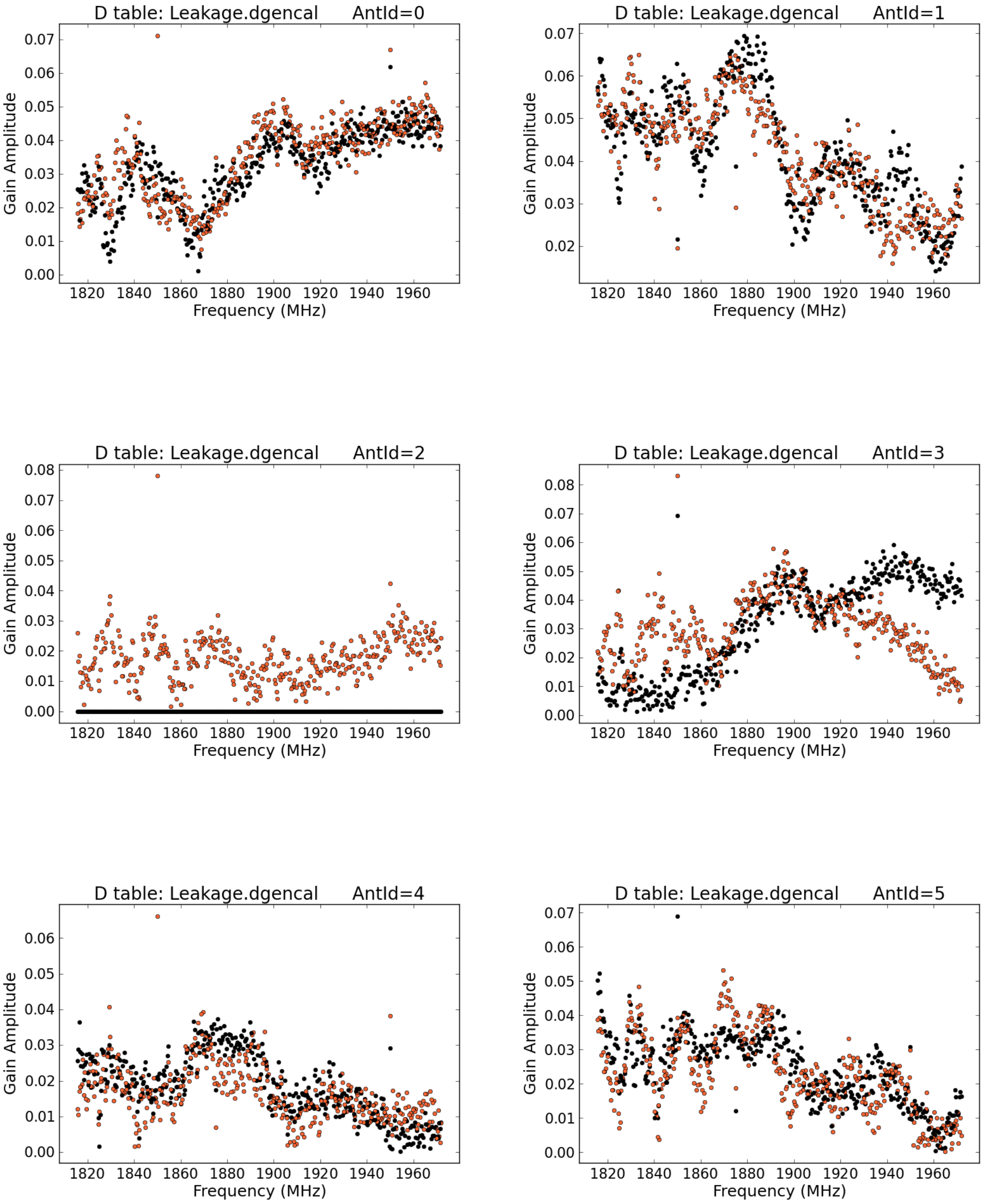

Figure 2.4: Polarisation leakage (D-terms) solutions showing amplitude against frequency for our secondary calibrator, J0538-440. The observations are those made at the high band with 6 antennas. The solutions are for the cross-hand correlations XY and YX shown by different colours. Antenna 3 (antID 2) was used as the reference antenna.

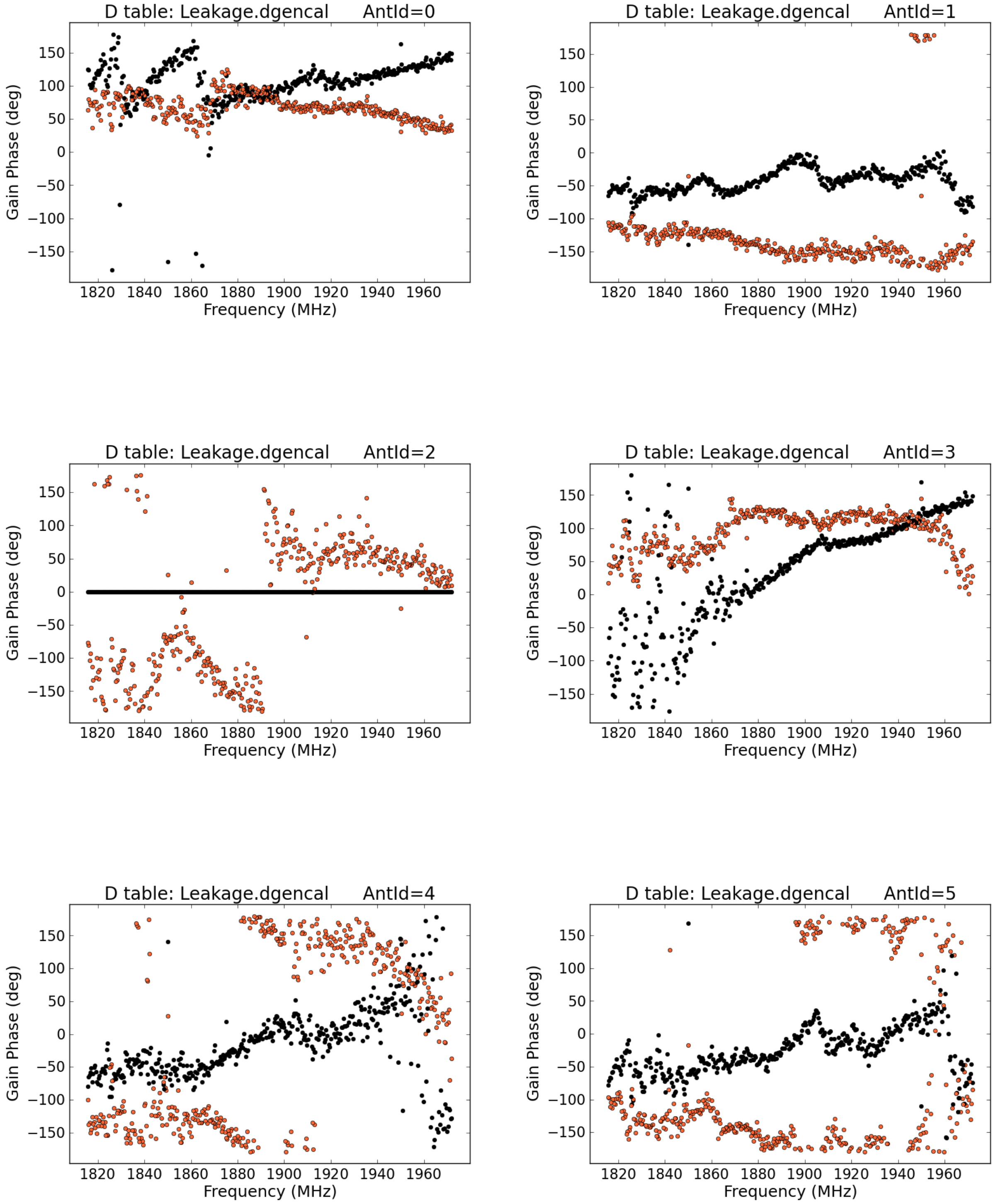

Figure 2.5: Polarisation leakage (D-terms) solutions showing phases against frequency for our secondary calibrator, J0538-440. The observations are those made at the high band with 6 antennas corresponding to Figures 2.1 - 2.4. Antenna 3 was used as the reference antenna. The solutions are for the cross-hand correlations XY and YX shown by different colours.

high band had little to no RFI. The recovered bandpass and number of operating antennas for each observing run are listed in Table 2.1.

PKS1934-638 was used primary calibrator, for absolute flux calibration (initial gain calibrations), and to measure the complex bandpass shape and cross-hand delay for all observations. The sources J0538-440 and J0240-231 were used as secondary calibrators to track time-dependent amplitude and phase calibration over the course of each observations and for polarisation calibration. The actual flux-scale of the observations is determined following calibrations of the complex gains. The determination of the gains does not determine the absolute flux of the calibrators and so a flux-scale has to established. We use the "*fluxscale*" and "*setjy*" tasks in CASA to establish correct absolute fluxes of sources, along with their uncertainties.

Along with the intrinsic linear polarisation signals, the time-dependent total intensity gain is coupled to any polarisation signal from the calibration sources. We use the task "*QUfromgain*", that is part of the ALMA[4] helper tasks, to solve for the polarisation of the calibration source by its effect on the gain solution – the effect being rotation of the source polarisation against the feed parallactic angle. The X-Y phase angle is then calibrated. The resulting source polarisation model is then used in the "*polcal*" task to solve for the polarisation leakage. We then apply calibration solutions from the initial antenna based time-dependent gain solutions and the frequency-dependent cross-hand phase calibration. Frequency dependent polarisation leakage solutions are produced and all calibration solutions are applied to all sources. We do not observe calibrators with known absolute polarisation position angle. Therefore, while the relative polarisation position angles as functions of frequency are calibrated, the absolute polarisation position angles for the polarisation solutions are not known.

2.2.2 Imaging

To produce an image from the observed visibilities, a Fourier inversion of equation 1.7 is performed, obtaining the surface brightness distribution, $I(l, m, n)$, in units of flux density per solid angle, most commonly Jy/beam. The sky coordinates (l, m, n) are directional cosines describing the deviations $\boldsymbol{\sigma}$ in the expression for the source position $\boldsymbol{s} = \boldsymbol{s}_0 + \boldsymbol{\sigma}$. An initial image, called the dirty image, can be made and is so called because of the discrete sampling of the true visibilities involved in real observations. In general, the real visibilities are multiplied by a visibility sampling function which, when Fourier inverted, becomes a convolution with the real image and is then called the *dirty beam*. The deconvolution of this image is then performed to get the real image. We use the CLEAN (Högbom, 1974) approach to do this. This approach makes the assumption that the image is a collection of point sources and in so doing, approximates *real* sources in the image as collections of point sources. The simplest form of CLEAN searches the dirty image for the location and value of the maximum flux, then subtracts a fraction of it (the maximum multiplied by a factor called the loopgain ≤ 1 – the loopgain in this work is the typical value of 0.1) from the dirty image and records the position and the fraction of the maximum flux in a model image (a model surface brightness distribution) as a point source. The process is the repeated until a predefined threshold is reached. The model image is then convolved with an idealized beam – often an elliptical Gaussian fit to the dirty beam. The CLEAN threshold is chosen as to eliminate the contribution of noise in the final image. It is usually taken as a flux that is a few times above the rms (root-mean-square) noise or as a certain number of CLEAN iterations.

The imaging and deconvolution, in this work, was done using the Clark(Clark, 1980) variant of the CLEAN algorithm implemented in the CASA through the CLEAN-based task, TCLEAN. The Clark CLEAN approach is composed of two stages/cycles called the minor and major cycles where bright points are CLEAN'ed in the minor cycles and then the collection of the points found are subtracted through a fast Fourier transform (FFT) during the major cycles. Figure 2.7 displays the results of our deconvolution with panels showing a slice through the Stokes I image cubes of each of our six sources.

---

[4] Atacama Large Millimeter/submillimeter Array

Figure 2.6: The unedited visibility amplitudes across all channels from our KAT 7 observations shown for the flux calibrator PKS1934-638. The amplitudes are from all baselines in each of the three observing bands. One can see the various artefacts that were removed during calibration. The high band had the least amount of artefacts.

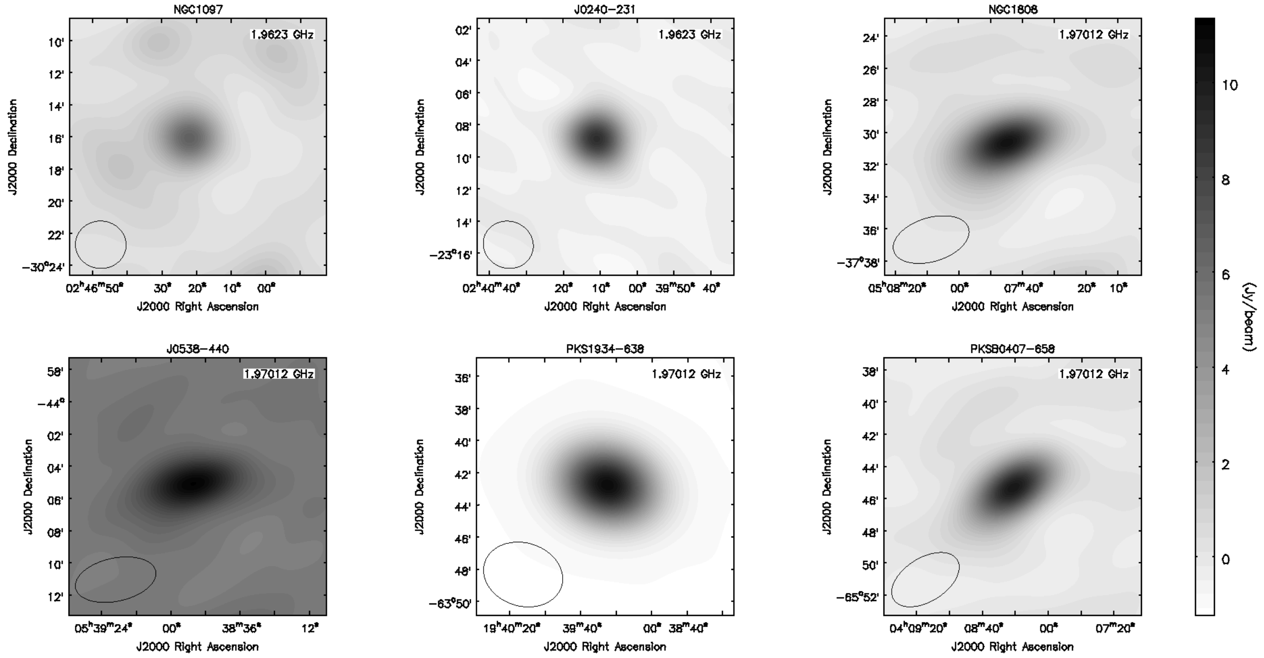

Figure 2.7: Final Stokes I images of all sources (source in each panel labelled) at the highest frequency in the high band for each observation. The $\sim 3.6'$ *synthesized beam can be seen as the black ellipse to the bottom left of each panel.*

2.3 Total and polarized intensity

Our observations allow us to analyse the total integrated Stokes I, Q, and U intensity, adding to what is already known about the sources. The sections below explore our results and compares them with the literature where possible. Integrated Stokes I, Q, and U image cubes were made for each source. We averaged every ten visibility channels into 3.9 MHz channels making up each image cube. The cubes were made to resolve the spectral behaviour of I, Q, and U. The typical synthesized beam (the interferometer response to a point-source obtained by averaging the outputs of all antenna pairs) at the low band is $\sim 4.9'$ and $\sim 3.6'$ at the high band. The observed angular size of our sources is consistent with these beams, as can be seen in Figure 2.7.

2.3.1 Total intensity

We extracted spectra in I, Q and U using the intensity of the peak values of the total integrated intensity from each Stokes cube. The error contributions from the imaging stage for each of the peak intensities are estimated by taking the rms of intensities at ~ 50 off-source locations in each frequency plane. The flux at these locations should be consistent with noise as our image fields are not crowded and these regions were chosen to be those devoid of sources. This error is then combined with the errors associated with the flux scale set by the task *fluxscale* through the simple relation

$$\sigma_I = \sqrt{\sigma_{rms}^2 + \sigma_I^2}, \tag{2.16}$$

where the rms noise is represented by σ_{rms} and σ_I is the bootstrap error derived through the *fluxscale* task during the calibration process. We then propagate these errors for derived quantities, such as linear polarisation $p = \sqrt{Q^2 + U^2}/I$, calculated from I, Q and U. The peak intensity value is a measure of the total flux density because the sources are spatially unresolved.

Per-channel Stokes I integrated flux densities for each source are shown as blue dots in Figure 2.8. For comparison we also show flux densities for each source over a broad frequency range obtained from the NED database[5]. There is very good agreement, at frequencies sampled by KAT 7 ($\sim 1-2$ GHz), between previously

---

[5] http://ned.ipac.caltech.edu/

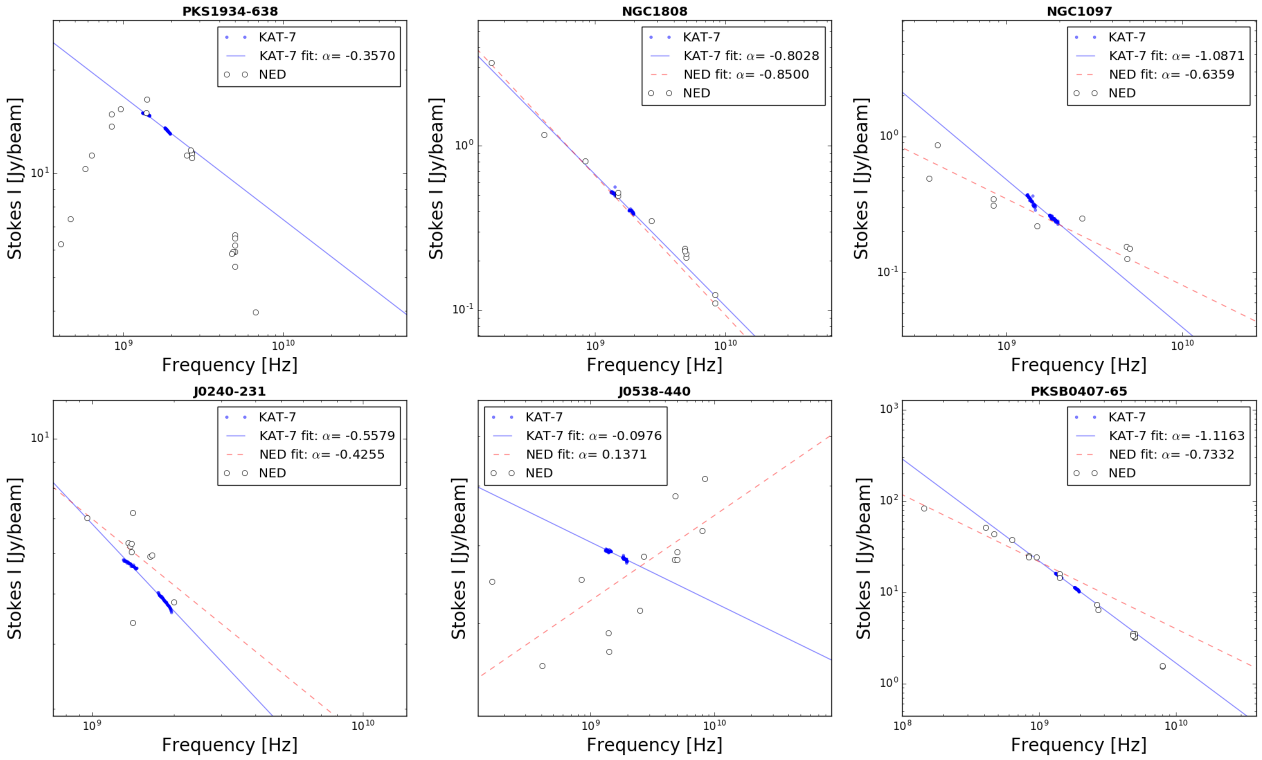

*Figure 2.8: Total integrated intensity across KAT-7 band (blue points) and corresponding literature values at frequencies overlapping with the KAT-7 band. We also display power law spectral fits of the form $I(\nu) \sim \nu^{\alpha}$ fitted to both our KAT 7 data (blue solid line) and, where possible, the NED data (red dashed line). **Top panels**: Left: The flux calibrator, PKS 1934-638. Middle: NGC 1808. Right: NGC1097. **Bottom panels**: Left: The polarization calibrators, J0538-440 and J0240-231 (middle). Right: PKSB0407-658.*

reported total intesity values and our results for PKS1934-638, NGC1808 and PKS0407-658. We fit a power law spectral behaviour of the form (see Section 1.1.1)

$$I(\nu) \sim \nu^{-\alpha}, \tag{2.17}$$

where α is the logarithmic slope of the spectrum (see e.g: de Gasperin et al. (2018))

$$\alpha = -\frac{\partial \log I(\nu)}{\partial \log \nu}. \tag{2.18}$$

The majority of radio galaxies have a linear spectrum that decreases with increasing frequency on logarithmic scales and this leads to a negative value for the spectral index (e.g. de Gasperin et al., 2018; Waldram et al., 2018). This is not always so, however for some other types of radio sources such as GPS sources which tend to have significant curvature in their spectra. This can be seen for PKS1934-638 in the top left panel of Figure 2.8, although our results agree with the literature at frequencies observed by KAT 7, we cannot make any conclusions beyond those frequencies as the power law relation also does not hold for much of the frequencies that differ from 1 GHz by about an order of magnitude.

2.3.2 Polarimetry

We introduce and discuss, in Section 1.1.1, the importance of analysing and understanding the properties of polarised radio synchrotron radiation. The KAT 7 telescope array, even with limitations that it is subject to (one being that it was built with the intent of just being an engineering test-bed for MeerKAT and the SKA (Foley et al., 2016)), has been able to provide full polarisation observations which will be able to shed some light on the polarimetric properties of radio emission from galaxies. Synchrotron theory (see e.g Klein and Fletcher,

2015) dictates that the observed linear polarisation fractions of total observed radio emission be approximately $\sim 70\%$, however, *polarisation degrees* this high are rarely seen in practice where degrees of polarisation of a few percent are deemed highly significant (e.g Vollmer et al., 2013). The alteration of the polarised signals to levels much lower than expected is due to many processes that affect the light from the moment it is emitted by the radio source to the point where the signal is converted to human discernible information at the telescope. Our goal is to disentangle some of these processes and their properties as they relate to changes in polarised emission. To this end, we explore the spectral behaviour of linear polarisation from our KAT 7 observations as one of the most apparent changes to polarised emission is depolarisation behaviour with increasing wavelength (e.g Burn, 1966; Heald et al., 2009; Braun et al., 2010; Heald et al., 2015).

The observed linear polarisation intensity

$$p = \frac{\sqrt{Q^2 + U^2}}{I}, \tag{2.19}$$

is often not an accurate representation of the true polarisation. This is due to the errors in; and also the sinusoidal nature of the complex quantities that are Q and U. As an example, take the case where the mean Q and U signal is zero within some error. Using equation 2.19 will give a non-zero degree of polarisation, which is of course wrong. This *bias* has been known early in the development of radio polarimetry (e.g Wardle and Kronberg, 1974; Simmons and Stewart, 1985) and estimators of the true polarisation degree $p_{\rm o}$ have been devised and reported on by (Simmons and Stewart, 1985), where the authors focus especially at the low signal to noise case where noise contributions to the observed polarisation intensity are significant.

We derive the bias corrected (Simmons and Stewart, 1985) integrated linear polarization degree, $p_{\rm o}$ by making use of the following relations:

$$p = \sqrt{q^2 + u^2}, \tag{2.20}$$

$$\sigma_p = \frac{\sqrt{(q \times \sigma_q)^2 + (u \times \sigma_u)^2}}{p}, \tag{2.21}$$

$$p_{\rm o} = \sqrt{p^2 - \sigma_p^2}, \tag{2.22}$$

where σ_p is the root-mean-square (rms) error in the observed linear polarization degree p and σ_q and σ_u are the equivalent quantities for q and u, respectively. $u \equiv U/I$ and $q \equiv Q/I$. Our bias correction follows the Wardle and Kronberg method (Wardle and Kronberg, 1974) which best approximates $p_{\rm o}$ for observations where $p/\sigma_p \gtrsim 0.7$. For lower signal to noise, i.e $p/\sigma_p < 0.7$ (with σ_p initially calculated via equation 2.21), we use the method outlined by Heald et al. (2009) where:

$$\sigma_p = \sqrt{\frac{4 - \pi}{2}} \sigma_{QU}. \tag{2.23}$$

We denote with σ_{QU} the noise in the fractional Stokes parameters q and u, where σ_{QU} is the rms noise of the per-channel errors in q and u. The band-averaged linear polarization intensities shown in Table 2.2 are calculated from the mean q and u (or Q and U as reported in Table 2.2) values viz

$$\overline{p} \equiv \langle p \rangle = \sqrt{\langle q \rangle^2 + \langle u \rangle^2}, \tag{2.24}$$

$$\overline{p}_{\rm o} = \sqrt{\langle p \rangle^2 - \sigma_p^2}. \tag{2.25}$$

2.4 Rotation Measure synthesis

We apply the Rotation Measure synthesis technique of Brentjens and de Bruyn (2005) to analyse the intrinsic polarization properties of our data, making use of the technique's power to resolve the different components that alter polarised radio emission (see Section 1.3.1 for an introduction and background). We use χ to transform the observed $P(\lambda^2)$ into $F(\phi)$ and then observe the behaviour of the Faraday spectrum. We use a grid of trial ϕ values, with steps of 0.1 rad/m^2 ($\phi \in [-1000, 1000]$ rad m^{-2}), to observe the behaviour of $F(\phi)$ in Faraday depth space. $F(\phi)$ is expected to peak at certain ϕ values that best approximate the intrinsic values of ϕ that are characteristic of each component, along the line of sight, that contributes to Faraday rotation of the incident radio emission. We perform RM clean following the steps explained in Section 1.3.4.

We use the entire KAT-7 radio frequency (RF) range (that is 1200 - 1950 MHz) in calculating the resolution in Faraday space, $\delta\phi$. This we do because the data that was used for rotation measure synthesis did actually cover the entire range but with large wholes in the middle where the mid-band would have been. The resolution, $\delta\phi$, is slightly worse (≈ 121 rad/m^2) in the observations of NGC1808, 0538-440, PKSB0407-65, and PKS1934-638 than in the NGC1097 and 0240-231 cases, where $\delta\phi \approx 102$ rad/m^2. This is due to the discrepancies in the wavelength sampling between these groups of observations where less sampling was achieved in the former. Table 2.4 contains the key parameters quantifying the limits of our KAT-7 data with regard to extracting polarization information from RM synthesis. KAT-7's λ^2 sampling limits us to Faraday depths of up to $|\phi_{max}| \approx 1.67 \times 10^4$ rad/m^2 ($|\phi_{max}| \approx \sqrt{3}/\delta\lambda^2$, Brentjens and de Bruyn (2005)).

Faraday complexity is wavelength dependent and Brentjens and de Bruyn (2005) define as Faraday simple/thin[6], any source where $\lambda^2\Delta\phi \ll 1$, and Faraday complex where $\lambda^2\Delta\phi \gg 1$. $\Delta\phi$ is the extend of the source in ϕ-space, a width of the source's Faraday spectral peak. Complex sources tend to be have numerous and/or broad Faraday spectral peaks, owing to a mixing of Faraday rotating and/or emitting media along the LoS, and depolarise strongly with λ^2. Simple sources have Faraday spectra that are better approximated by a single Dirac-δ function (Brentjens and de Bruyn, 2005) and polarisation angles that are modelled by the linear relation in equation 1.10. We use this definition for Faraday complex/simple source classification but also visually classify our sources after performing RM clean. A source whose reconstructed/cleaned Faraday spectra are found to have only a single peak at a certain Faraday depth, ϕ, is identified as Faraday simple and it then follows that any source whose reconstructed Faraday spectrum is found to have multiple ϕ-components/peaks or a single component whose peak is broader than the FWHM of the RMTF is identified as Faraday complex.

We sample the ϕ grid at 0.1 rad/m^2 so as to accurately look for Faraday emission components while leaving the computational requirements of our analysis as practical as possible. We then convolve the RM components arising from the RM synthesis process with a continuous MeerKAT RF range that combines the L and UHF bands – 0.55 to 2.0 GHz. This super-resolution helps to display complex components in the intrinsic Faraday spectrum that we reconstruct, see Figures 2.15 - 2.18 where the reconstructed/clean $|F(\phi)|$ is plotted to display the ϕ-components found with above the RM clean threshold.

2.5 Uncertainties

We quantify the statistical significance of ϕ-component detections by imposing a flux threshold to the RM clean algorithm. Our target confidence is set at $\gtrsim 99\%$. To this end, we select 1000 off-source positions[7] for each source image cube. We then extract the $Q(\lambda)$, $U(\lambda)$ and $I(\lambda)$ fluxes at these positions in a similar fashion as in the cases of the sources. We apply the RM clean algorithm at these off-source positions. We determine the maximum amplitude $|F|_{max}$ from the ensemble of off-source positions, above which the

---

[6] Faraday thick/thin as introduced in Section 1.3.1

[7] Positions in the image that are away from the phase centre.

Table 2.2: Band averaged values of integrated Stokes $\overline{I}_{\nu_c}$, linear polarisation intensities ($\overline{P}_{\nu_c}$), and also Q, U noise (σ_{QU}) of our KAT-7 data. The error in the averaged values are $\sigma/\sqrt{N}$, where N is the number of channels, σ is the standard deviation of the values and ν_c is the frequency associated with the band. The low and high bands are indicated by sub-/superscripts 1350 *and* 1850*, respectively indicating ν_c in MHz. The Band averaged linear polarisation intensities are ($\overline{P}$), and ($\overline{P}_0$) is the band averaged bias corrected intensity. All values are recorded in mJy/beam.*

Source	$\overline{I}_{1350}$	$\overline{P}_{1350}$	$\overline{P}_o^{1350}$	$\overline{\sigma}_{QU}^{1350}$	$\overline{I}_{1850}$	$\overline{P}_{1850}$	$\overline{P}_o^{1850}$	$\overline{\sigma}_{QU}^{1850}$
NGC1808	514.6 ± 0.2	2.4 ± 0.3	2.4 ± 0.3	0.3	400.3 ± 0.2	2.2 ± 0.3	2.2 ± 0.3	0.3
NGC1097	340.8 ± 0.3	2.6 ± 0.3	2.6 ± 0.3	0.4	248.0 ± 0.1	3.6 ± 0.02	3.5 ± 0.2	0.2
J0240-231	5727.4 ± 1.2	58.9 ± 0.7	58.9 ± 0.7	0.6	4861.1 ± 0.8	101.5 ± 0.8	101.5 ± 0.8	0.5
J0538-440	$3923.0 \pm 0.0.3$	27.6 ± 1.5	27.6 ± 1.5	0.6	3806.5 ± 1.3	10.9 ± 1.0	10.9 ± 1.0	0.4
PKS1934-638	14876.9 ± 0.5	14.6 ± 4.4	14.5 ± 4.4	1.5	13315.6 ± 0.3	5.1 ± 1.2	5.0 ± 1.2	1.0
PKSB0407-658	15130.7 ± 1.0	18.7 ± 3.1	18.7 ± 3.1	1.5	10848.2 ± 1.0	21.7 ± 1.4	21.7 ± 1.4	1.3

Probability($|F|_{max,i} \geqslant |F|_{max}$) $\leqslant 0.001$ – where $|F|_{max,i}$ is the peak $|F(\phi)|$ of the i-th ϕ-component for a position in the ensemble. This gives us a 0.999 detection probability of individual ϕ-components for each of our science targets. The RM clean threshold is then set to 3× this *noise* level. We label this threshold as $\sigma_{off,99.9}$.

We apply no weighting in our RM synthesis algorithm. We attempted the weighting function σ_p^{-2}. This gave no effect in the overall properties of the Faraday spectrum and so it was dropped for simplicity in our calculations.

2.6 Results

The subsections to follow present the results of the polarimetry and rotation measure synthesis analysis, described in sections 2.3.2 and 2.4, on our KAT 7 observations of six radio sources.

2.6.1 Radio Spectra

The results from our analysis of the total and polarised intensity spectra are presented below.

Total Intensity

Table 2.2 reports the band averaged integrated intensities derived from our dataset. Our total integrated intensities for NGC1808 and NGC1097 are in agreement with literature values of ∼ 497.0 and ∼ 219.0 mJy at 1.49 GHz, respectively (Condon et al., 1996), no errors were reported for these literature fluxes in the NED database at the time of this work, but they do serve as adequate indication for our derived values. The agreement with previous studies also holds for the total intensity of the flux calibrator, PKS1934-638, and we find agreement with several studies that together span a larger bandwidth than our KAT-7 measurements.

Total integrated flux profiles for our sample are displayed as blue dots in Figure 2.8. We also show flux densities spanning a few 100 MHz to a few GHz for each source obtained from the NED database. There is very good agreement with previously reported values in our results for PKS1934-638, NGC1808 and PKS0407-658. Power law approximations to the spectra, however show agreement for NGC1808 with discrepancies in the observed spectral curvature of the GPS sources PKS1934-638 and PKSB0407-658 caused by the limited radio frequency coverage of KAT 7. As suggested by the NED data, a larger RF coverage would better reveal more of the spectral shape and perhaps in these case more sophisticated fitting routines would be able to recover the spectra. Stanghellini et al. (1998) fit hyperbolic functions in addition to fitting the simple power law at frequencies before and after the spectral turnover/peak and this does tend to better approximate the spectra of GPS sources over larger RF ranges.

The spectrum, for NCG1097, while consistently steep, is very poorly defined by previous data. However, our data points fall within the general trend of past observations. The data for J0538-440 suggest variability with the presence of a GPS component below a few GHz and a rising spectrum at higher frequencies. The results for the flat spectrum source J0240-231 also indicate variability, with the total flux emitted in the 1.36 - 2.0 GHz frequency range has been reported to fall in the range 4.4 - 7.1 Jy (Kuehr et al. (1981); Condon et al. (1998); Stanghellini et al. (1998); Tingay (2003); Stanghellini et al. (2005)), in agreement with the total integrated fluxes we measure, see bottom-left panel of Figure 2.8. PKSB0407-65 total integrated flux is also in good agreement with literature values but, the story is different for J0538-440, where the spectral slope from our analysis seemingly differs significantly from that suggested by previous studies. There is a high probability that there is variation between our sample and that quoted in NED, and not only that, there may also be significant variation between the individual NED data points from themselves as these too come from different studies. Nevertheless, further homogenisation of ours and the NED collected data is beyond the scope of this work.

Table 2.3: Degrees of linear polarization (in percentages) from Eichendorf and Reinhardt (1979) along with corresponding values form the KAT-7 bands in this work ($\overline{p}_{0,1350}$ and $\overline{p}_{0,1850}$). Subscripts are as in Table 2.2. The last column displays the mean spectral index, $\langle\alpha\rangle^{1350}_{1850}$, over the two KAT 7 bands.

Source	p_{5000} (%)	p_{2730}, (%)	p_{1670} (%)	p_{1430} (%)	$\overline{p}_{0,1350}$ (%)	$\overline{p}_{0,1850}$ (%)	$\langle\alpha\rangle^{1350}_{1850}$
NGC1808	–	–	–	–	0.5 ± 0.06	0.5 ± 0.08	0.815 ± 0.011
NGC1097	–	–	–	–	0.8 ± 0.09	1.4 ± 0.09	1.059 ± 0.020
PKS1934-638	0.1	0.3	0.4	0.2	0.1 ± 0.03	0.04 ± 0.01	0.360 ± 0.005
PKSB0407-658	0.5	0.4	0.6	0.4	0.1 ± 0.03	0.2 ± 0.02	1.118 ± 0.003
J0240-231	5.4	3.4	1.7	1.8	1.0 ± 0.02	2.1 ± 0.02	0.562 ± 0.006
J0538-440	–	–	–	–	0.7 ± 0.04	0.3 ± 0.03	0.098 ± 0.003

Polarisation Properties

We derive integrated polarization intensities that are comparable to some found in the literature from Eichendorf and Reinhardt (1979) and Beck et al. (2002). The former present a collection of polarization properties (intensities, position angles, flux densities, and rotation measures) that were measured between 1965 and the middle of 1974 and these include data at 6, 11, 18, and 21 cm – listed in Table 2.3. Their data set contains some of our sources except for J0538-440 and the disk galaxy targets. We only have NGC1097 in common with Beck et al. (2002) – whose observations were made at 22, 18, 6, and 3 cm.

The bias correction we applied had an insignificant effect on the linear polarization intensity as σ_p was at least an order of magnitude less than the polarised intensity. Beck et al. (2002) report linear polarization degrees for NGC1097 of $p_{22cm} = 1.5 \pm 0.9\%$ and $p_{18cm} = 1.3 \pm 1\%$ in agreement, with what we find: $p_{22cm} = 0.8 \pm 0.09\%$ and $p_{16cm} = 1.4 \pm 0.09\%$ at 22 and 16 cm (1.35 and 1.85 GHz), respectively (see Table 2.3). The fractional polarization behavior in NGC1097 displays a decreasing trend across the two KAT-7 bands with a relatively large scatter of $\sigma_{QU} = 0.4$ mJy/beam at the low band and 0.2 mJy/beam at the high band. Decreasing sinusoidal behavior, representing the depolarization (internal Faraday dispersion) with λ^2, of a simple Burn slab (Burn, 1966) is suggested by the trend in the reconstructed $q(\lambda^2), u(\lambda^2)$ and $p(\lambda^2)$ which are represented as solid curves in Figures 2.9 - 2.11. The reconstructed $q(\lambda^2), u(\lambda^2)$ and $p(\lambda^2)$ are derived from detected ϕ-components (see formalism in Section 1.3.4). A similar trend is displayed in the case of NGC1808 but the Q and U fluxes are more coupled together with $\sigma_{QU} = 0.3$ mJy/beam at the low and high band (see Figure 2.10).

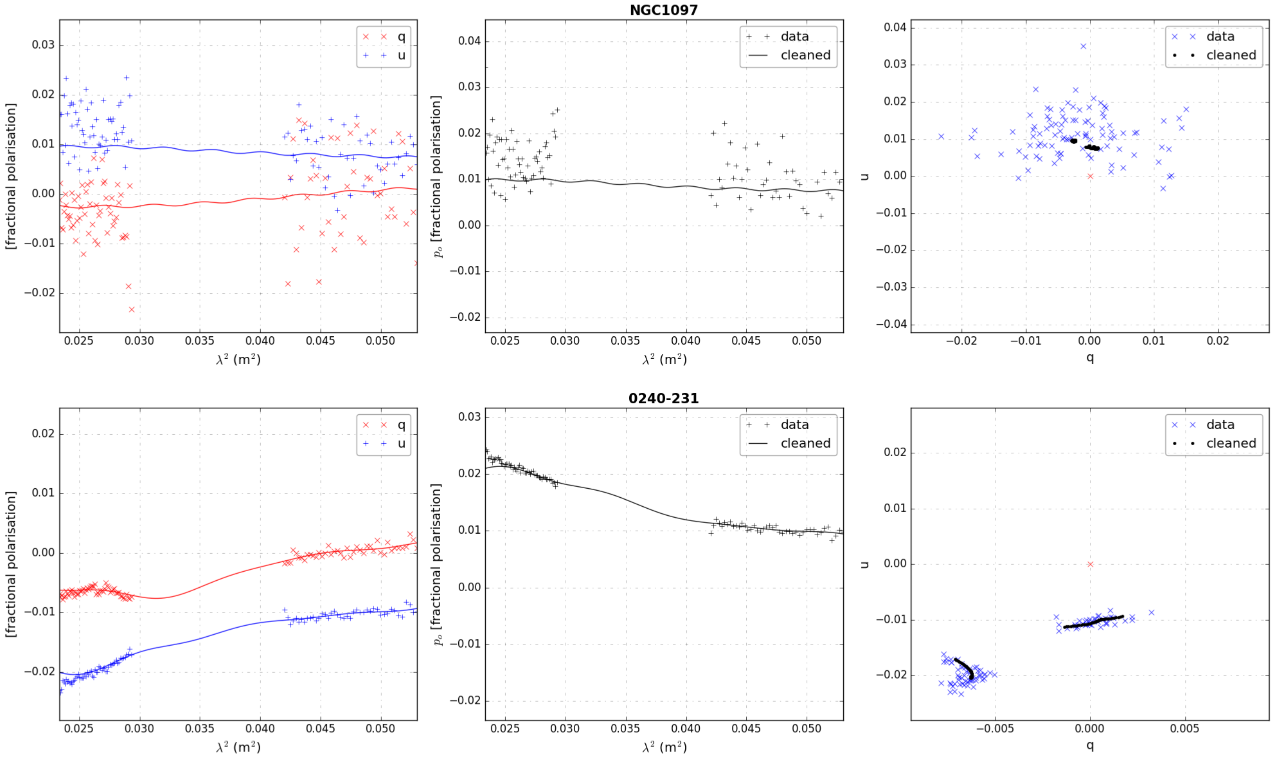

Figure 2.9: Polarization measurements across the KAT-7 band along with reconstructed $q(\lambda^2), u(\lambda^2)$ and $p(\lambda^2)$ that span the MeerKAT L and UHF bands. The plots show only the KAT-7 bands. ***Top panels****: $q(\lambda^2)$ and $u(\lambda^2)$, $p(\lambda^2)$, and q v.s u for NGC 1097.* ***Bottom panels****: Same measurements for J0240-231.*

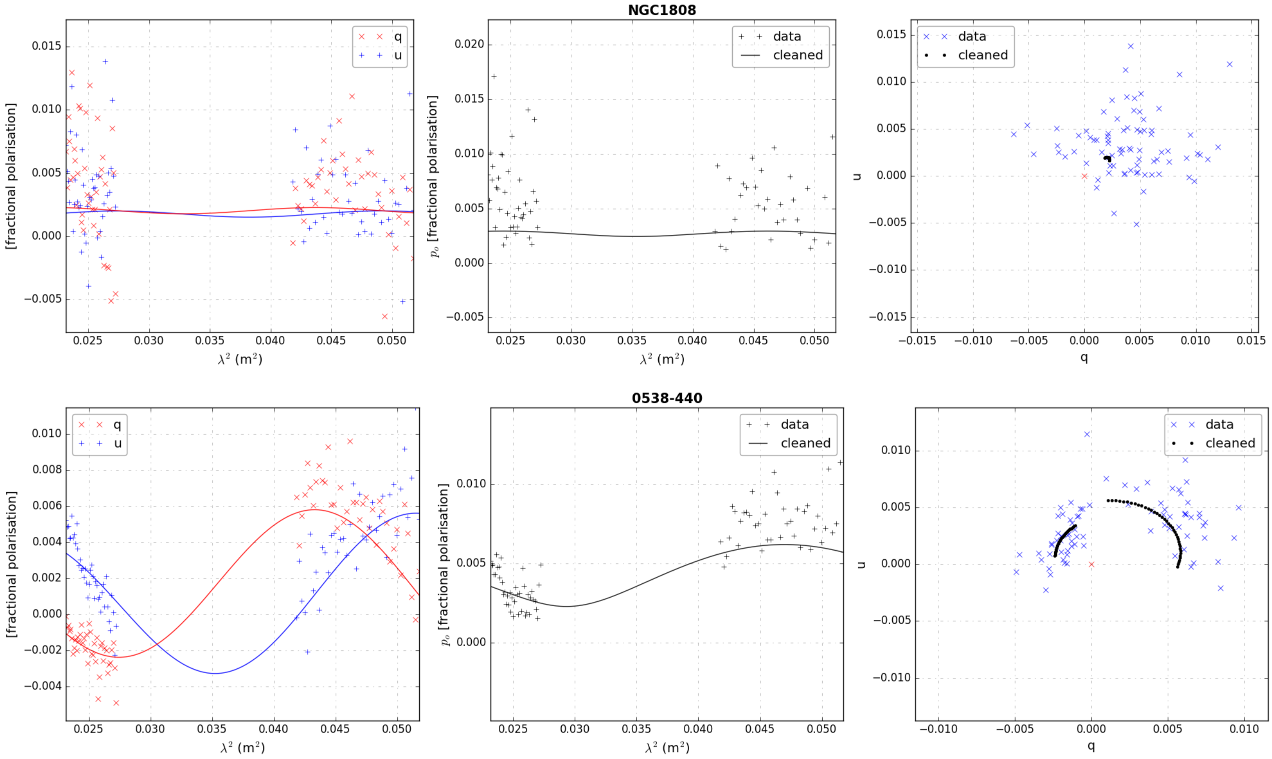

Figure 2.10: Same as in Figure 2.9, ***top panels****: Measurements for NGC 1808.* ***Bottom panels****: Same measurements for J0538-440.*

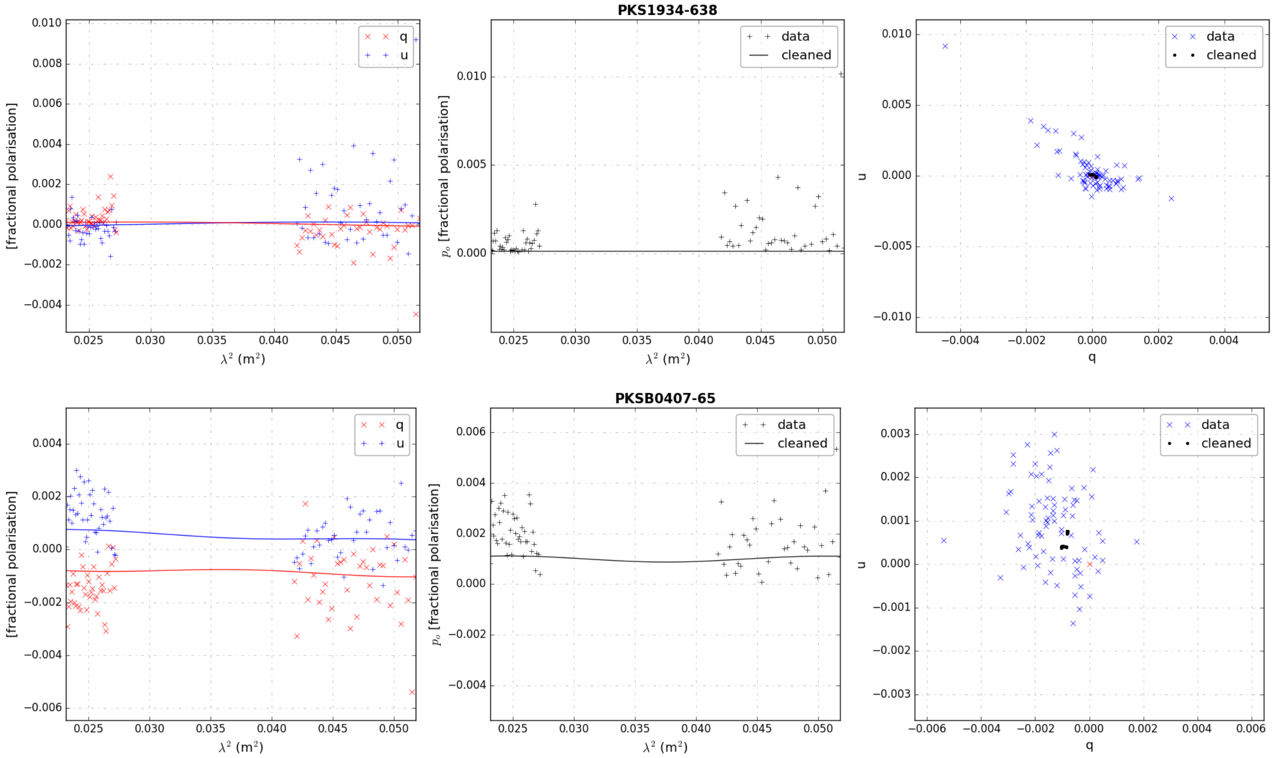

*Figure 2.11: Same as in Figure 2.9, **top panels**: PKS1934-638. **Bottom panels**: Same measurements for PKSB0407-658.*

Table 2.4: Key parameters in our RM synthesis analysis. f_c *is the frequency range covered, "Target" refers to the disk galaxy target's observation run from which the quantities in the table are derived,* $\delta\lambda^2$ *is the spacing in* λ^2, λ^2_{min} *and* λ^2_{max} *are the minimum and maximum values, respectively, of* λ^2 *corresponding to each band.* $\phi_{max\text{-}scale}$ *is the largest Faraday depth scale to which our RM synthesis analysis is sensitive and* $|\phi_{max}|$ *is the largest depth we can detect.* $\delta\phi'$ *is the RMTF FWHM due to the non-continuous* λ^2 *coverage while* $\delta\phi$ *is the same for the continuous case.*

f_c	Target	$\delta\lambda^2$ [m^2]	λ^2_{min} [m^2]	λ^2_{max} [m^2]	$\phi_{\text{max-scale}}$ [rad m^{-2}]	$\delta\phi$ [rad m^{-2}]	$\delta\phi'$ [rad m^{-2}]	$\lvert\phi_{max}\rvert$ [rad m^{-2}]
1.306 - 1.962 GHz	NGC1097	0.0002	0.023	0.053	135	102	101.0 ± 17.6	10021->134.6
1.312 - 1.970 GHz	NGC1808	0.0002	0.023	0.052	135	121	98.0 ± 17.1	10174->135.6

2.6.2 RM Synthesis and RM Clean

Table 2.5 summarizes the ϕ-components we found at the $\sigma_{off,99.9}$ level for each source. The more *prominent* components show some width manifesting as a number of *minor* components around the main component, and the full-width-half-max (ϕ_{FWHM}) of these is given in the table. A Faraday emission component, with $\phi = \phi_i$, is called *most prominent* or *strongest* or *main* or *major* or *peak* if $|F(\phi_i)| = \text{maximum}(|F(\phi)|)$, and *minor* or *less prominent* otherwise. We could not reliably resolve some of the less prominent components. We sub-classify as Faraday thick (denoted by C in Table 2.5) those components that have minor components around the main peak component – $\phi_{FWHM} > 0$ rad m^{-2}, and sub-classify components as Faraday thin (denoted as S – $\phi_{FWHM} = 0$ rad m^{-2} denoted as a dash in Table 2.5) otherwise. This helps distinguish the two types of components we found in the data for each source.

J0240-231: This is a strong source with a number of prominent components that are above the RM clean threshold. The most prominent being that located at $\phi = 8.1$ rad/m^2 with a peak flux $|F| = 1.62\%$ and $\phi_{FWHM} = 17.0$ rad/m^2. Figure 2.13 shows that the source has a number of other relatively strong ϕ-components near $\phi = 33.6,\ -39.6,\ -116.0$ rad/m^2 and also other Faraday thin components in the range $\phi \sim 234.9 - 341.1$ rad m^{-2}. This suggests significant complexity in the Faraday depth profile of this source.

J0538-440: This source shows a relatively strong main component centered at $\phi = 103.7$ rad/m^2 with a peak flux $|F| = 0.52\%$. The component is also the broadest with $\phi_{FWHM} = 68.0$ rad/m^2. Another prominent component occurs at $\phi = 10.9$ rad/m^2 with a peak flux $|F| = 0.21\%$ and $\phi_{FWHM} = 40.1$ rad/m^2. Both these components are shrouded by a number of minor components (illustrated in Figure 2.14), that are above the RM clean threshold, suggesting that this source has a complex Faraday depth structure – especially in the regions of the source that produced Faraday rotation in the linear polarization intensities.

NGC1097: Displays a simpler Faraday depth profile than the two sources above – Figure 2.15, but with two more minor but more polarized components along with a prominent ϕ-component at $\phi = -13.1$ rad/m^2 with a peak flux $|F| = 1.13\%$ and $\phi_{FWHM} = 17.0$ rad/m^2.

NGC1808: Displays a Faraday spectrum similar to NGC1097 – Figure 2.16, in that most of the components we found have $F(\phi)$ less than the RM synthesis cut-off. We find a single prominent ϕ-component at $\phi = -0.2$ rad/m^2 with a peak flux $|F| = 0.51\%$ and $\phi_{FWHM} = 36.1$ rad/m^2. The emission compoent detected just below the threshold at $\phi = 144.3$ rad/m^2 is most likely due to the RMTF sidelobe located at $\phi = +140.5$ rad/m^2.

PKS1934-638: This source has only a single component above the threshold at $\phi = 50.6$ rad/m^2 with a peak flux $|F| = 0.06\%$. Figure 2.17 displays the Faraday spectrum.

PKSB0407-65: This source displays a single prominent peak (Figure 2.18) near zero at $\phi = 7.9$ rad m^2 with a peak flux $|F| = 0.16\%$ with a second component at $\phi = -119.2$ rad m^2 with a peak flux $|F| = 0.06\%$. Sidelobes in this source (at $\phi = \pm140.5$ rad/m^2) are likely significant contributors to the two emission compo-

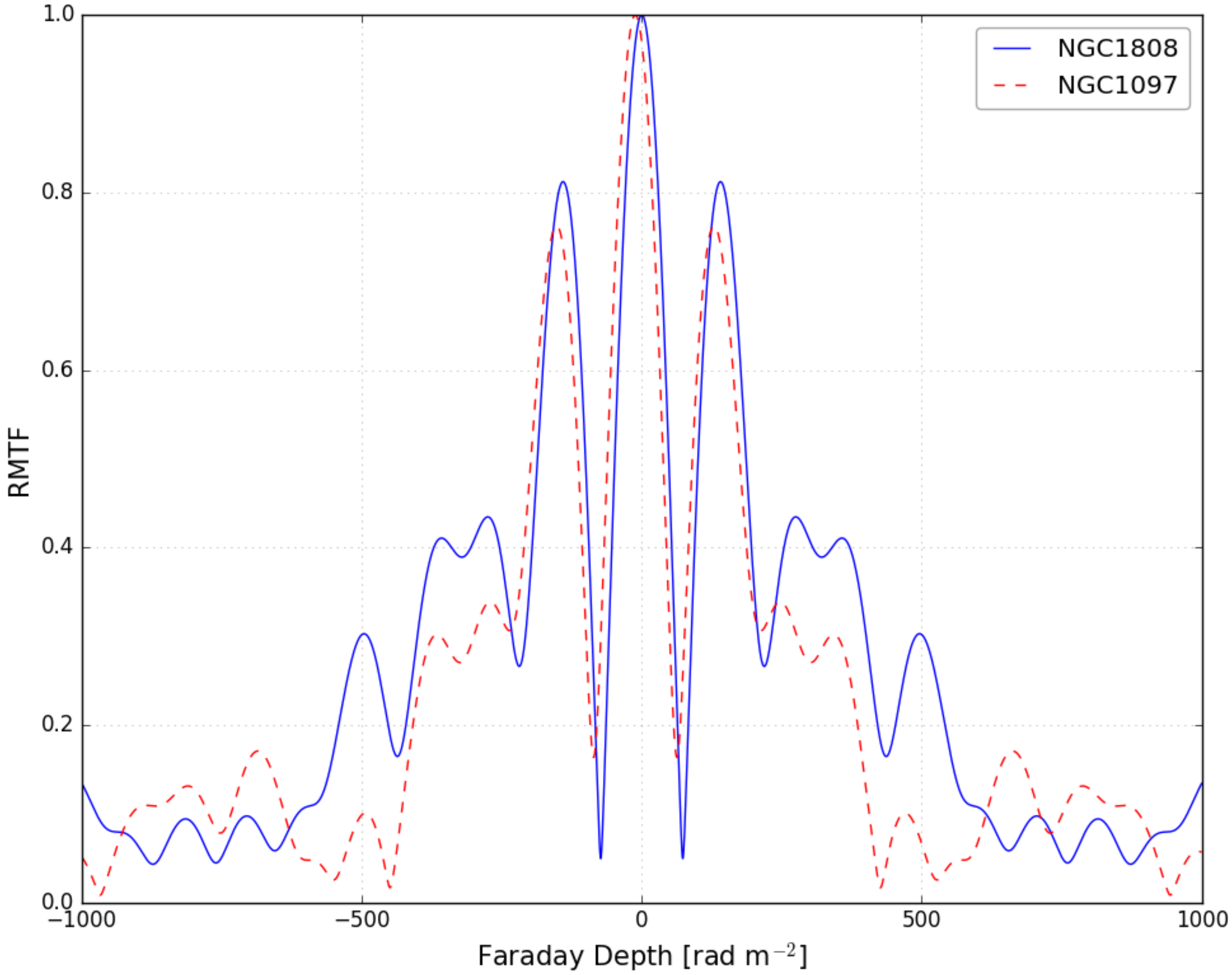

Figure 2.12: The RMTF (RMSF) of the KAT 7 observations. The RMTF was derived by combining the low and high bands from the NGC1808 and NGC1097 observations. The width of the main peak ($\delta\phi'$) in the NGC1808 case is 98.0 ± 17.1 *rad/m^2 with the first side lobes located at $\phi = \pm 140.5$ rad/m^2 and peaks with $RMTF = 0.81$. The case of NGC1097 has $RMTF$ main peak width 101.0 ± 17.6 rad/m^2 and sidelobes located at $\phi = \pm 129.0$ rad/m^2 with $RMTF = 0.76$. The RMSF was calculated from the combined low and high band, divided into 40 and 60 frequency channels in the NGC1808 and NGC1097 observations, respectively.*

Table 2.5: RM clean components for each of our sources. $|F|_{comp}$ is the peak of the Faraday spectrum derived during the RM clean algorithm, ϕ_{comp} is the ϕ at which $|F|_{comp}$ is found, ϕ_{FWHM} is the full-width-half-max of the ϕ-component, and $\sigma_{off,99.9}$ is the RM clean threshold. The last column shows our visual sub-classification of each component as Faraday thick (C – with more than one Faraday component) or Faraday thin (S – just one Faraday thin component).

Source	$\|F\|_{comp}$ [%]	ϕ_{comp} [rad m^2]	ϕ_{FWHM} [rad/m^2]	$\sigma_{off,99.9}$ [%]	Complexity
J0240-231	1.62	8.1	17.0	0.004	C
	0.42	-116.0	13.6	–	C
	0.63	-39.6	19.1	–	C
	0.61	33.6	10.2	–	C
	0.42	-109.3	–	–	–
	0.11	234.9	–	–	S
	0.09	341.1	–	–	S
J0538-440	0.52	103.7	68.0	0.009	C
	0.26	-7.3	–	–	–
	0.21	10.9	40.8	–	C
NGC1097	1.13	-13.1	17.0	0.028	S
	0.54	150.9	40.8	–	C
NGC1808	0.51	-0.2	36.1	0.027	S
PKS1934-638	0.06	51.8	16.3	0.006	C
PKSB0407-65	0.16	7.9	16.7	0.006	C
	0.06	-119.2	–	–	S

nents located near $\phi = \pm 120.0$ rad/m^2.

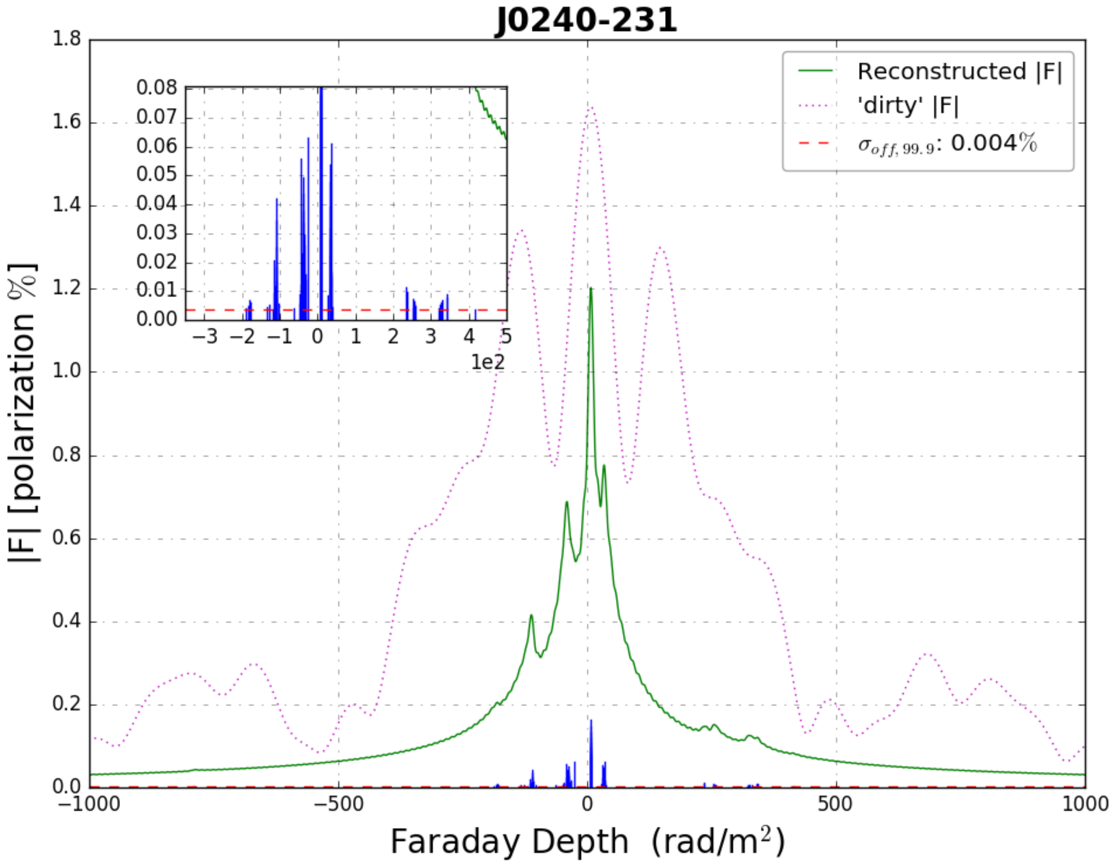

Figure 2.13: The clean Faraday spectrum, $|F(\phi)|$, of J0240-231 resulting from our RM clean algorithm. Top left: Zoom-in of the most prominent Faraday emission components. Blue vertical lines show the peak $\gamma|F(\phi_i)|$ at the corresponding ϕ_i of each emission component – γ is the loopgain parameter (Section 1.3.4). The red dotted line is the RM clean threshold ($1 \times \sigma_{off,99.9}$) as quoted in the legend. The dotted curve is the "dirty" Faraday spectrum.

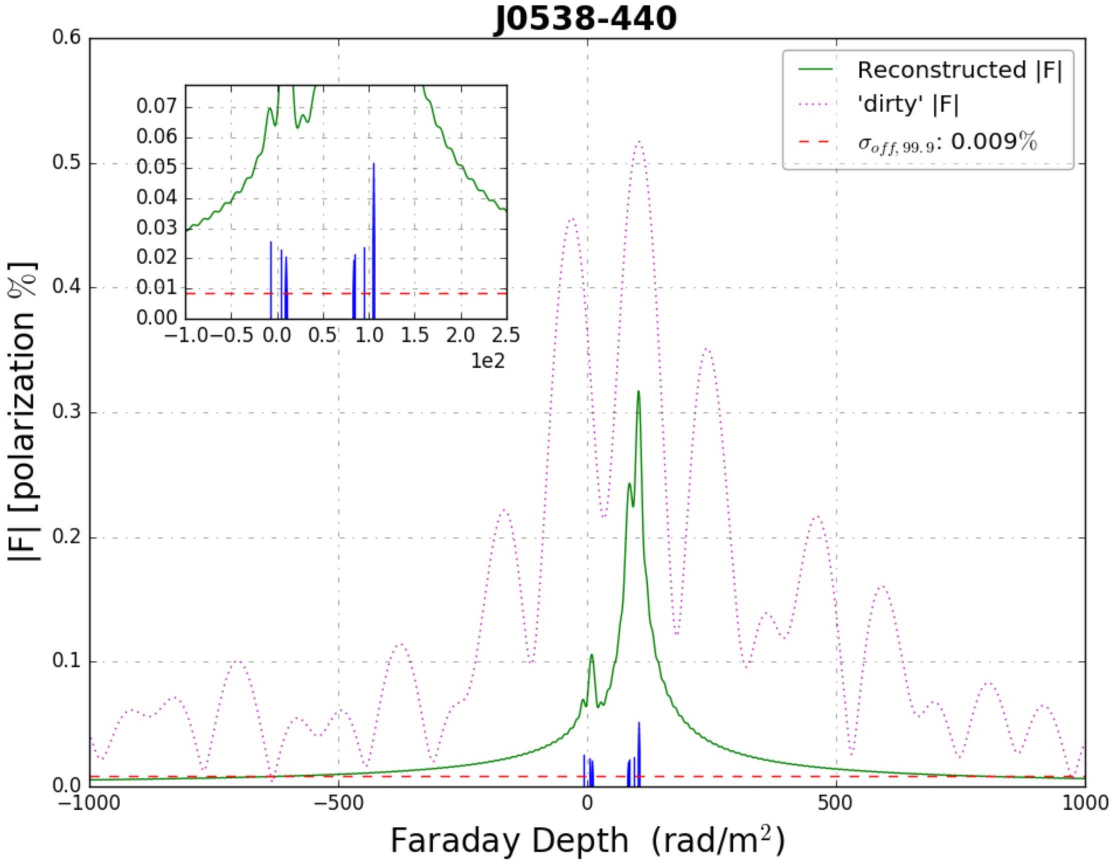

Figure 2.14: As described in Figure 2.13: The clean Faraday spectrum, $|F(\phi)|$, of J0538-440 resulting from our RM clean algorithm.

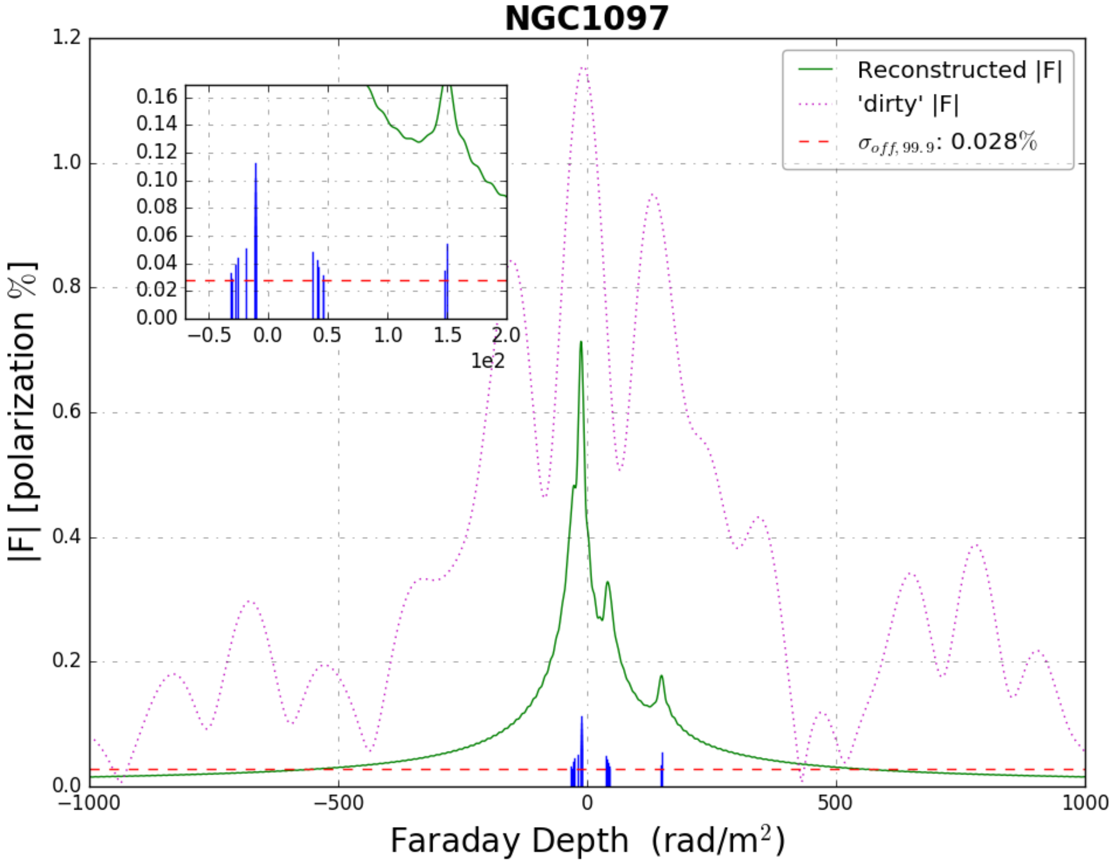

Figure 2.15: As described in Figure 2.13: The clean Faraday spectrum, $|F(\phi)|$ (green), of NGC1097 resulting from our RM clean algorithm.

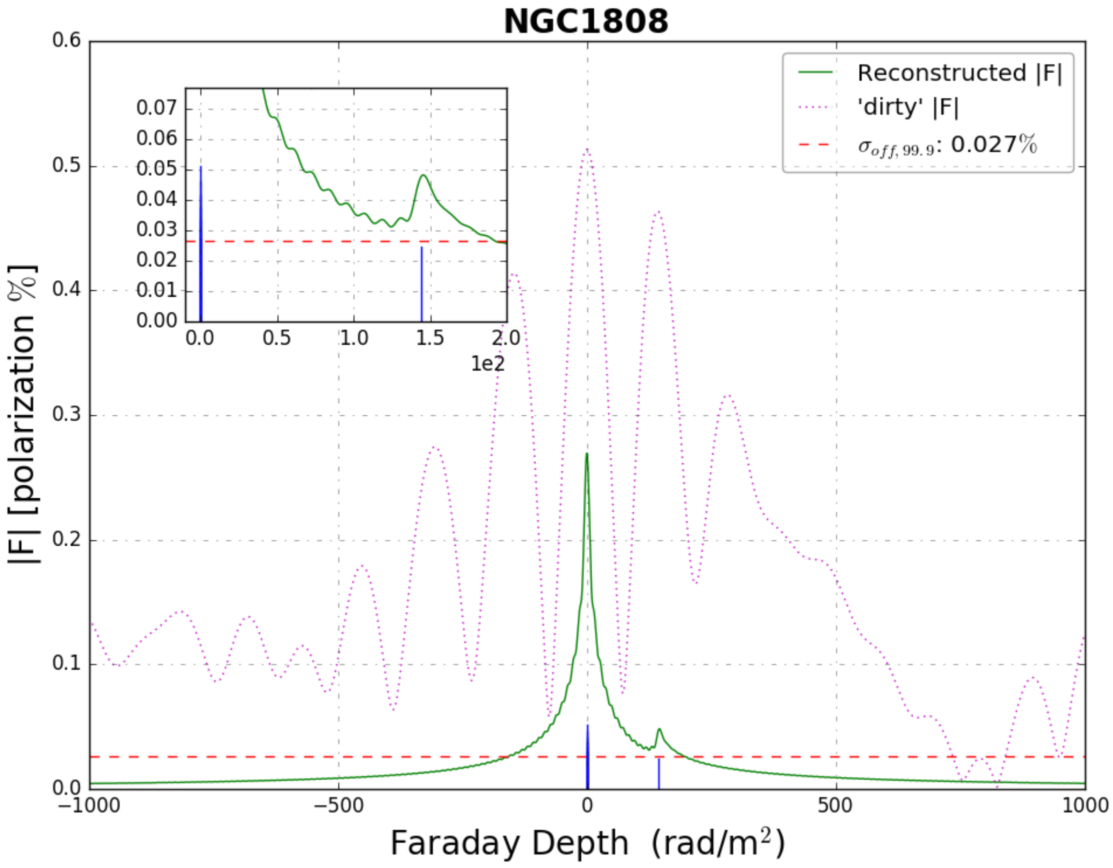

Figure 2.16: As described in Figure 2.13: The clean Faraday spectrum, $|F(\phi)|$, of NGC1808 resulting from our RM clean algorithm.

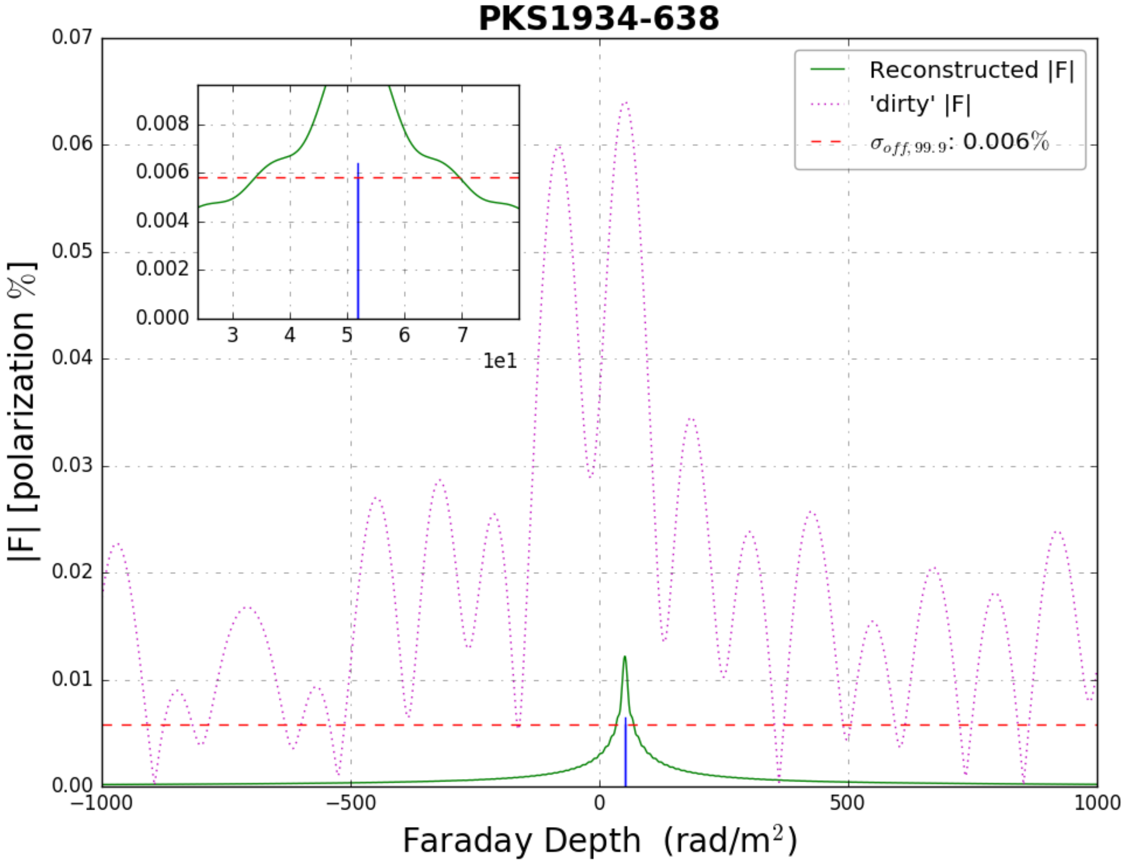

Figure 2.17: As described in Figure 2.13: The clean Faraday spectrum, $|F(\phi)|$, of PKS1934-638 resulting from our RM clean algorithm.

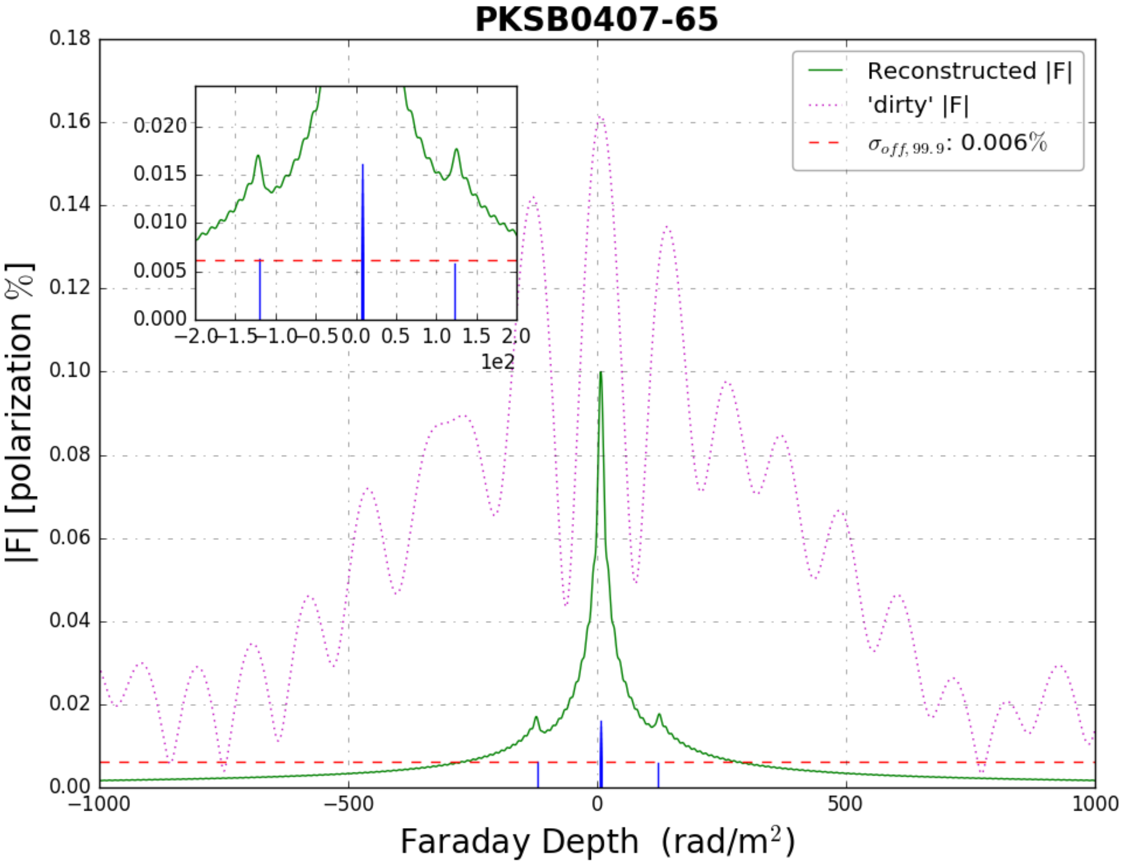

Figure 2.18: As described in Figure 2.13: The clean Faraday spectrum, $|F(\phi)|$, of PKSB0407-658 resulting from our RM clean algorithm.

2.7 Summary of Results

We have observed six radio sources, two disk galaxies and four AGN dominated sources, in full linear polarisation mode with KAT 7. The observations covered the entire KAT 7 RF band spanning 1200 - 1950 MHz. The mid-band, however, was contaminated with RFI and had no data that we could use further in our analysis. We thus, excluded the mid-band in analyses that followed. The data reduction and imaging was done using the CASA software suite.

We find that the total integrated fluxes of our sources do have values that are consistent with previous studies save for one of our AGN sources J0538-440, and to a lesser extent, the disk galaxy, NGC1097. In the NGC1097 case, we find consistency in spectral steepness with previous studies but the spectrum is poorly defined by previous works. The case of J0538-440 showed no consistency with literature results with the spectral shape suggesting variability with the presence of a GPS component below 1 GHz but with a rising spectrum towards higher frequencies.

In linear polarisation, we find good agreement between our work and the literature for those sources with reported values in the literature. The sources that we did find literature values for, were largely reported on a few decades ago (Eichendorf and Reinhardt, 1979) with the exception of the disk Galaxy NGC1097 which had data from Beck et al. (2002). The consistency with the available data is however, encouraging with regard to the validity of our results.

Rotation measure synthesis on our observations showed complexities in the two most polarised sources but also in the disk galaxy NGC1097. This agrees with the notion that the most polarised sources do tend to also have several Faraday components contributing to the polarisation measured and thus have some level of Faraday complexity in their Faraday spectra (Anderson et al., 2015, 2016). The most complex of these sources, J0240-231, shows significant depolarisation which is consistent with a Faraday thick/complex source (Brentjens and de Bruyn, 2005).

Chapter 3

Deep Broadband Polarimetry with MeerKAT (16)

3.1 MeerKAT (16)

The KAT 7 array was built as an engineering test bed for the 64-dish SKA precursor, MeerKAT. The name "MeerKAT" originates from the combination of the Afrikaans word "meer", meaning "more", and "KAT" from the "KAT 7" moniker. The meerkat animal belonging to the mongoose family is also indigenous to the region where MeerKAT is located and also serves as a mascot for the MeerKAT radio telescope. The telescope is located in the Karoo semi-desert of South Africa, in the Northern Cape Province of the country. It is located near the core location of the South African SKA site (Foley et al., 2016) and will later form part of the SKA when it is integrated into SKA phase 1 as the mid-frequency component.

The antennas have a Gregorian configuration where incident cosmic radio signals are not obstructed by any physical structures of the antenna. The primary/main reflector is of a diameter of 13.5 m, with the secondary/sub-reflector being 3.8 m in diameter. Each antenna's receptor can have up to four receivers attached. The array is in it's commissioning phase with L-band receivers currently installed. The array configuration, displayed in Figure 3.2, has 48 antennas in the core which spans $\sim$ 1 km, with the largest baseline, during the commissioning phase, being 8 km[1].

The observations we use utilise only 16 antennas which were fully operational at the time of this work. The current version of the correlator, the Reconfigurable Open Architecture Computing Hardware (ROACH2), constrains the number of usable antennas during this commissioning phase of MeerKAT to 16 with development under way to include all antennas. The rest of the array was still under construction with a large part of the physical structures for the 64 antennas already installed. Figure 3.3 displays the locations of the 16 antennas used to make the observations used in this work. The commissioning observations were made utilising both the shortest and longest baselines allowing for both high resolution of localised emission and detection of extended sources.

3.2 DEEP field Observations

We analyse full polarisation observations of the DEEP field, a region of sky centered on RA: 04:07:00 and Dec: -80:30:00. This portion of sky was chosen for commissioning both KAT 7 and MeerKAT. It was chosen from the SUMMS (Sydney University Molonglo Sky Survey) survey data (Bock et al., 1999; Mauch et al., 2003), based on it being relatively radio quiet with the brightest radio source having 843 MHz flux density of 238.8 mJy

---

[1] `http://public.ska.ac.za/meerkat`

Figure 3.1: The MeerKAT, as of late 2017, array in the Karoo semi-dessert of South Africa. Images publicly available on http://www.ska.ac.za

with the next brightest sources having flux densities in the range 50 to 60 mJy. SUMMS is a radio imaging survey performed with the Molonglo Observatory Synthesis Telescope (MOST) which observes at 843 MHz (Mills, 1981; Robertson, 1991; Bock et al., 1999). The telescope is located at the Molonglo Observatory in Hoskinstown, New South Wales, Australia. The survey was aimed at imaging the southern sky at declinations south of -30 degrees.

The choice for a radio quiet region of the sky was to avoid bright sources which make it difficult to produce images with noise levels as low as possible, generally as close to the theoretical value as can be achieved. The MeerKAT commissioning team observed the 4×4 square degree DEEP field in 9 partially overlapping pointings, named: DEEP1, DEEP2, DEEP2off (a pointing off-set from the DEEP2 pointing and centered on an FR II radio source that appears at the periphery of the DEEP2 pointing), DEEP3, DEEP4, DEEP5, DEEP6, DEEP7, and DEEP8. Positions of the field pointings are given in Table 3.1 and schematically represented in Figure 3.4. The duration of each observation was at least 12 hours for good parallactic angle coverage, with DEEP3 and DEEP7 observations exceeding 12 hours as they were observed for 15 and 13 hours, respectively. The pointings are separated by 30'.

PKS1934-638 and PKS0408-65 were chosen to be bandpass and primary flux calibrators, while J0252-712 (RA: 02:52:46.5 and Dec: -71:04:35.26) was the chosen polarisation and time-dependent gain calibrator (Mauch, 2016). Fifteen minute chunks were spent on target pointings with the gain calibrator observations of 2 minutes interlaced. The bandpass calibrators were observed every 6 hours for a 15 minute period.

3.3 Calibration and Imaging

Following on the work with KAT 7 data we perform calibrations and imaging using the CASA suite, but this time, the data reduction and analysis are done on high performance computing (HPC) facilities on the IDIA[2]

---

[2] http://idia.ac.za/

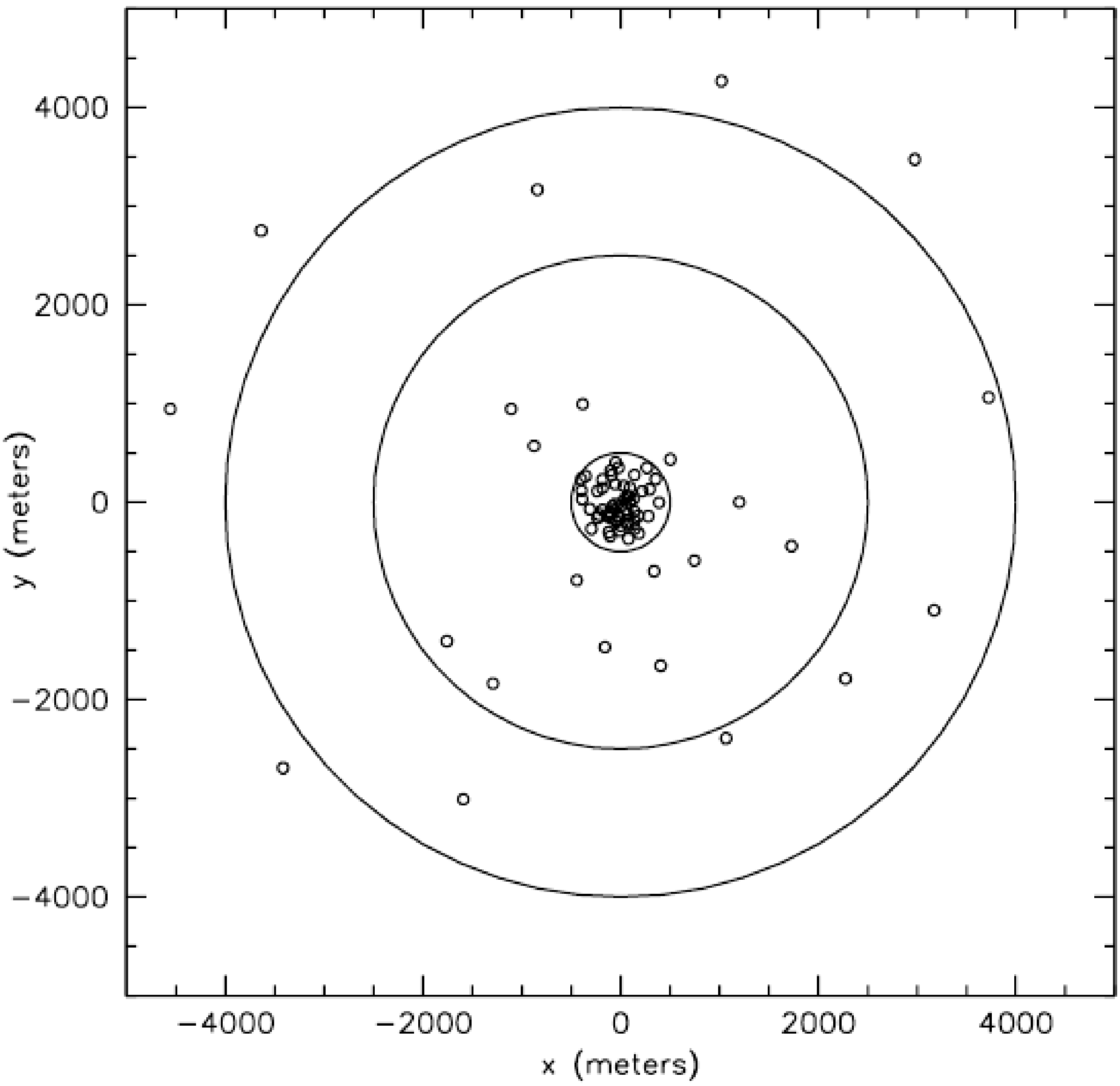

Figure 3.2: MeerKAT array configuration. Tiny circles are individual antennas, larger circles indicate radii of 1 km, 5km, and 8 km.

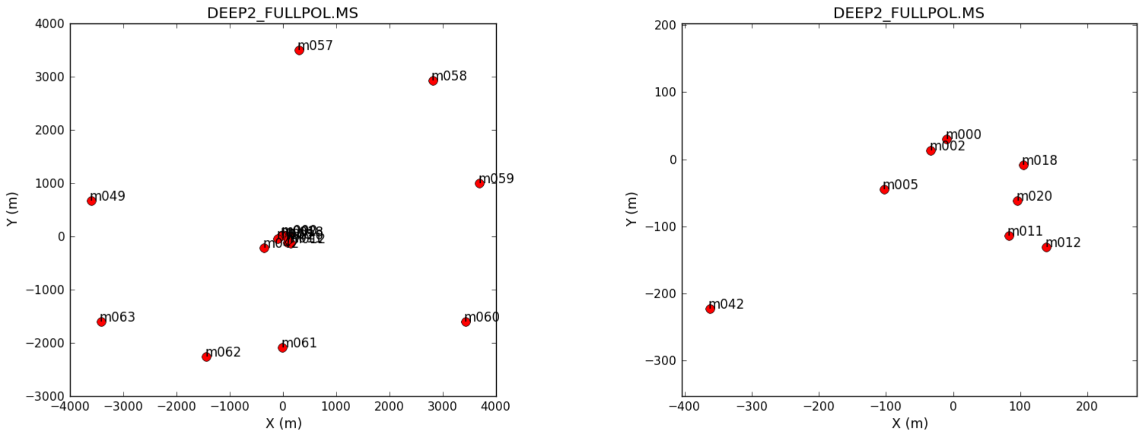

Figure 3.3: The antenna positions of MeerKAT 16 during observations for this work – the (X,Y) coordinate system is defined to have (0 m, 0 m) at the center of the array. Left: The full 16 dish commissioning array. Right: The central cluster of antennas.

Table 3.1: The DEEP field pointings, their sky positions and the dates of each observation. The starred pointings are those not used in this work.

Pointing name	RA (J2000)	Dec (J2000)	Observation date	Duration [Hours]	Number of antennas
DEEP1	04:16:16.27	-80:30:00.00	2017/06/15	12	16
DEEP2	04:13:26.40	-80:00:00.00	2017/04/04	12	16
DEEP2off	03:59:46.20	-80:36:20.60	2017/04/07	12	16
DEEP3	04:24:57.60	-80:00:00.00	2017/06/04	15	16
DEEP4*	04:28:28.47	-80:30:00.00	2017/07/13	13	11
DEEP5	04:17:08.57	-81:00:00.00	2017/06/10	12	12
DEEP6	04:04:17.14	-81:00:00.00	2017/07/15	13	11
DEEP7	04:04:17.14	-81:30:00.00	2017/06/18	13	15
DEEP8*	03:51:25.71	-81:30:00.00	2017/06/19	12	14

* Fields not included in this work

Data Intensive Astronomy Cloud using the Python Jupyterhub interface [3].

3.3.1 Calibration

The standard calibration steps followed for KAT 7 observations and discussed in Section 2.2 are also followed in the case of the MeerKAT observations. Automated flagging is done in this case, however, due to the much larger data sizes involved. We also aim to develop a reduction, calibration, and imaging pipeline for future observations and so automation forms a large part of the back-end of the pipeline. Flagging is done by utilising the “tfcrop”[4] and the “rflag” modes of the CASA flagging task “flagdata”[5]. The “tfcrop” mode automatically identifies outliers in the observations along both the time and frequency axes in an iterative fashion. It performs a polynomial fit to time-averaged amplitudes along the frequency axis and searches for outliers in the resulting band shape model. It is most effective at removing narrow-band RFI signals while it can often mistake wide band RFI as being part of the band shape of the radio source. Artefacts that may remain can be edited out of the data at a later stage, as done in this work. The RFlag[6] algorithm used in mode “rflag” was first developed by Eric Greisen for the Astronomical Image Processing System (AIPS). This algorithm is based on a sliding window statistical filter where the time axis is divided into chunks in which local statistics (along both the time and spectral axes) are determined. The operation is performed iteratively with each iteration removing outliers.

The parallactic angle coverage provided by the more than 12 hour long observations allowed the use of J0252-712 for determining source polarisation and also instrumental on-axis leakage solutions. We do not have observations of a calibrator with known polarisation and known position angle and as such, only the amplitudes, $p = \sqrt{q^2 + u^2}$, of the polarisation fluxes are calibrated but have an associated and unknown polarisation position angle. This constraint means that the ϕ-components of the same source from different fields will have the same ϕ and $|F(\phi)|$ values but the relative reconstructed $q(\lambda^2)$ and $u(\lambda^2)$ may be shifted due to the arbitrary unknown polarisation position angle. We note strange behaviour in the XY-phase angle (Figure 3.5), where the phase angle fluctuates by $\sim 90°$. This effect is calibrated out but is notably strange and may be associated with the correlator. The mean bootstrap flux density of J0252-712 is derived as 6.44 ± 0.03 Jy over seven of the DEEP field observations. The error is the standard deviation of the values from the seven calibrations. This is sufficiently strong to give a good polarization solution. The source is consistently found to have very low polarization. The mean and standard deviation of the percent polarization is 0.004 ± 0.003.

Antenna based delay calibrations find sub nanosecond delays between antennas, refer to Figures 3.6 and 3.7. We derive good bandpass solutions for channels that do not have RFI while the quality of solutions diminishes for RFI populated channels as displayed in Figures 3.8 and 3.9. We exclude the RFI populated channels (“bad”

---

[3] `http://jupyter.org/`

[4] See e.g. `http://www.aoc.nrao.edu/~rurvashi/TFCrop/TFCropV1/node2.html`

[5] `https://casa.nrao.edu/casadocs/casa-5.1.1/global-task-list/task_flagdata/about`

[6] See e.g. `https://casa.nrao.edu/Release4.2.1/docs/userman/UserMansu167.html`

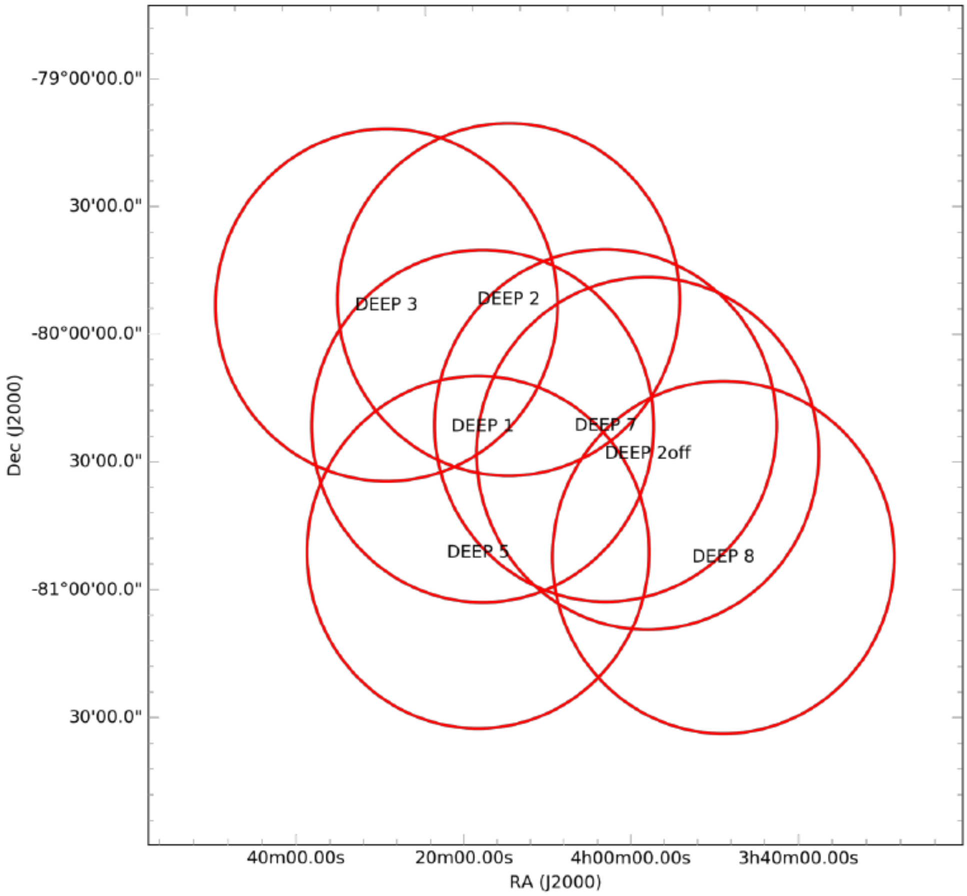

Figure 3.4: The areas covered by each of the DEEP field pointings detailed in Table 3.1. Adapted from (Mauch, 2017).

channels) when imaging these observations. The level of RFI contamination varies from antenna to antenna, as can be seen in the bandpass solutions but we exclude affected channels across all antennas in the imaging stage (Section 3.3.2). Our initial time-dependent gain solutions showed some discrepancies most likely due to RFI at certain times, especially near 16:48:00 (see Figures 3.10 - 3.11). These solutions were then later improved upon through self-calibration (see Figures 3.12 - 3.13). Four cycles of deconvolution, phase, and phase-amplitude calibration were carried out during self-calibration, two with phase only calibration, two with phase and amplitude calibration and deconvolution after each cycle of calibration. The clean depth was increased and the gain solution interval decreased after each cycle, so that the deconvolution model for self-calibration was deeper. The time scale for gain corrections was also decreased as self-calibration iteratively improves the gain solutions and the time resolution of the derived solutions also improves. Further automated flagging is done after each self-calibration cycle based on residual visibilities (difference between self-calibrated visibilities and model visibilities). We do not, however, understand the drops in the initial gain solution. Figures 3.12 - 3.13 display the best solutions achieved after the four cycles. The self-calibration analysis produces broad-band, multi frequency synthesis (MFS) images for each target field that have average rms noise of 7.4 ± 0.1 μJy/beam. These are the images used to search for sources in the source finding analysis described in Section 3.4.

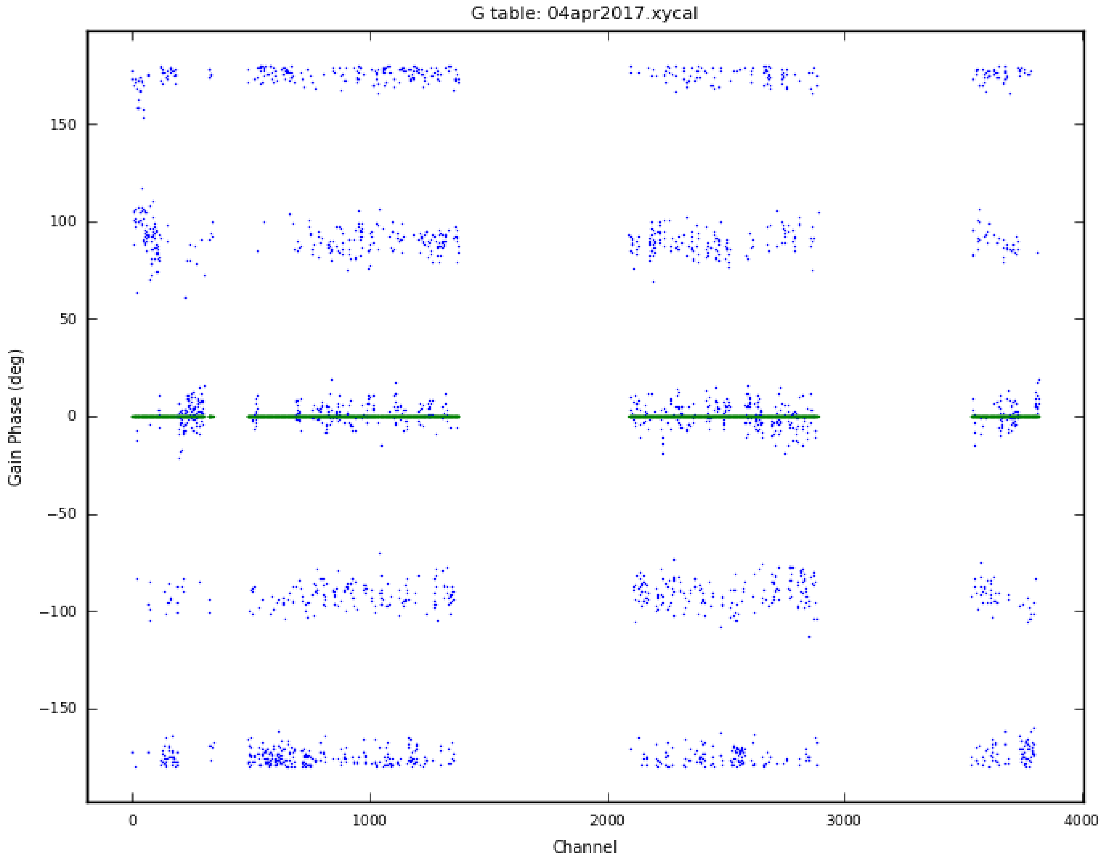

Figure 3.5: The per channel XY-phase solutions in the DEEP2 field

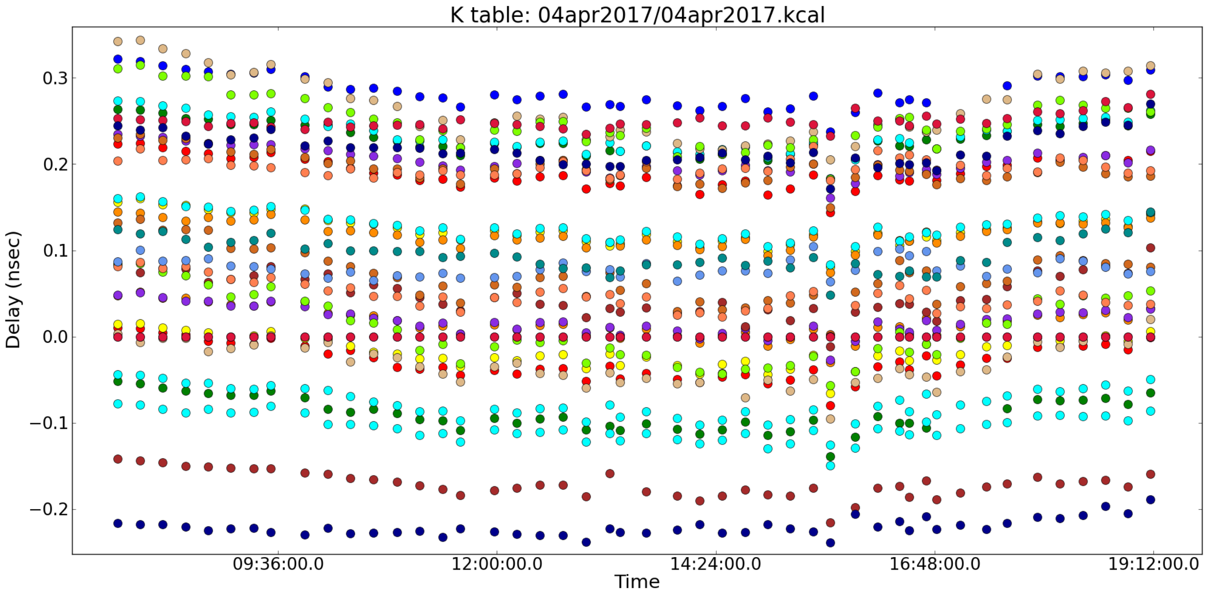

Figure 3.6: The antenna-based delay solutions for the X linear polarisation channel for the DEEP 2 field. The different colours indicate the different antennas.

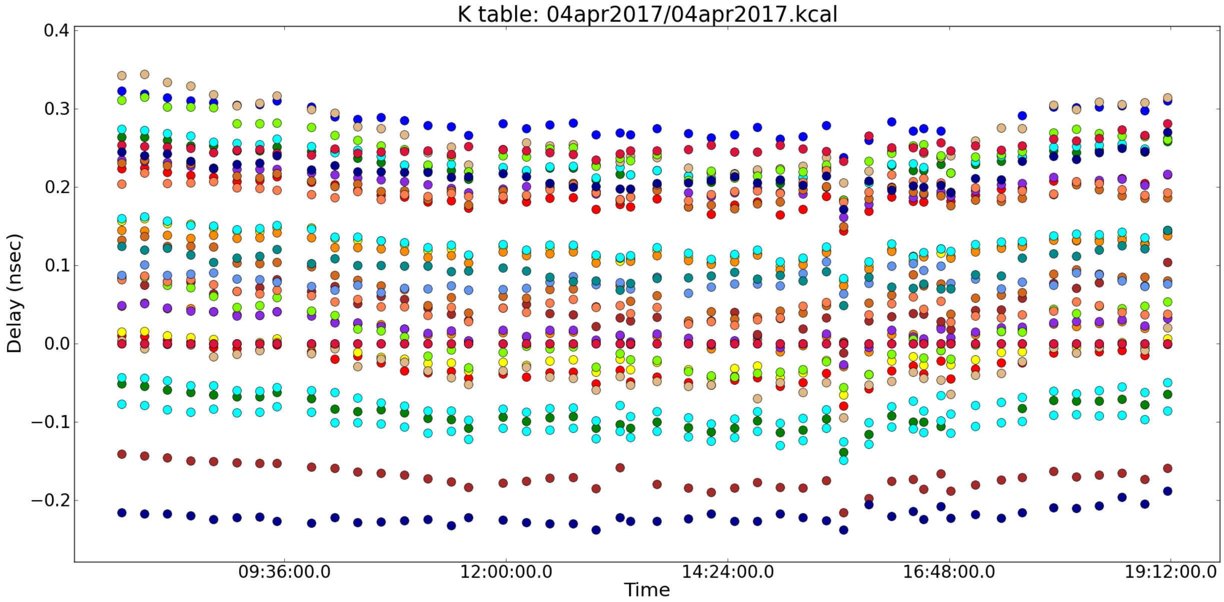

Figure 3.7: The antenna-based delay solutions for the Y linear polarisation channel for the DEEP 2 field. The different colours indicate the different antennas.

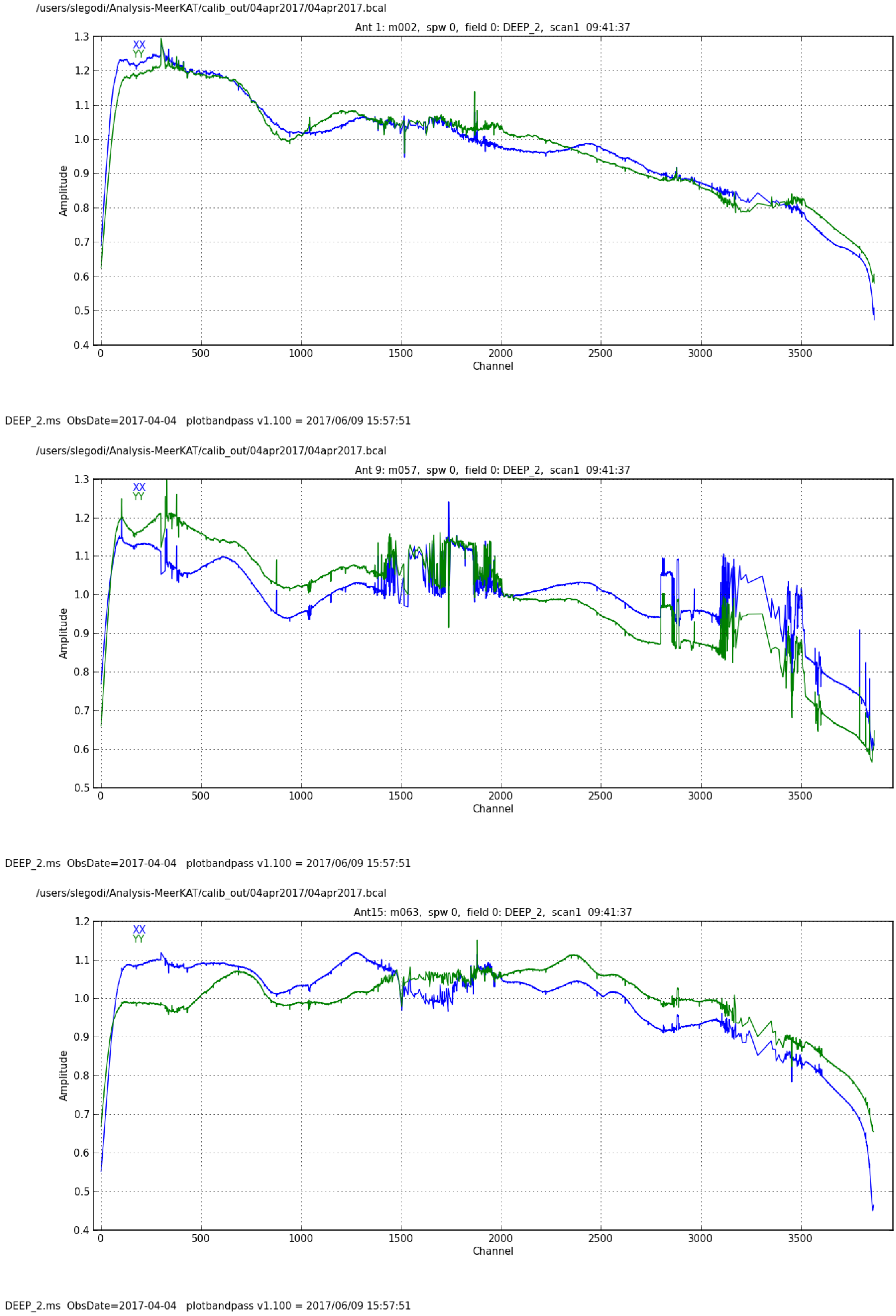

Figure 3.8: The bandpass amplitude solutions for three antennas for the DEEP 2 field.

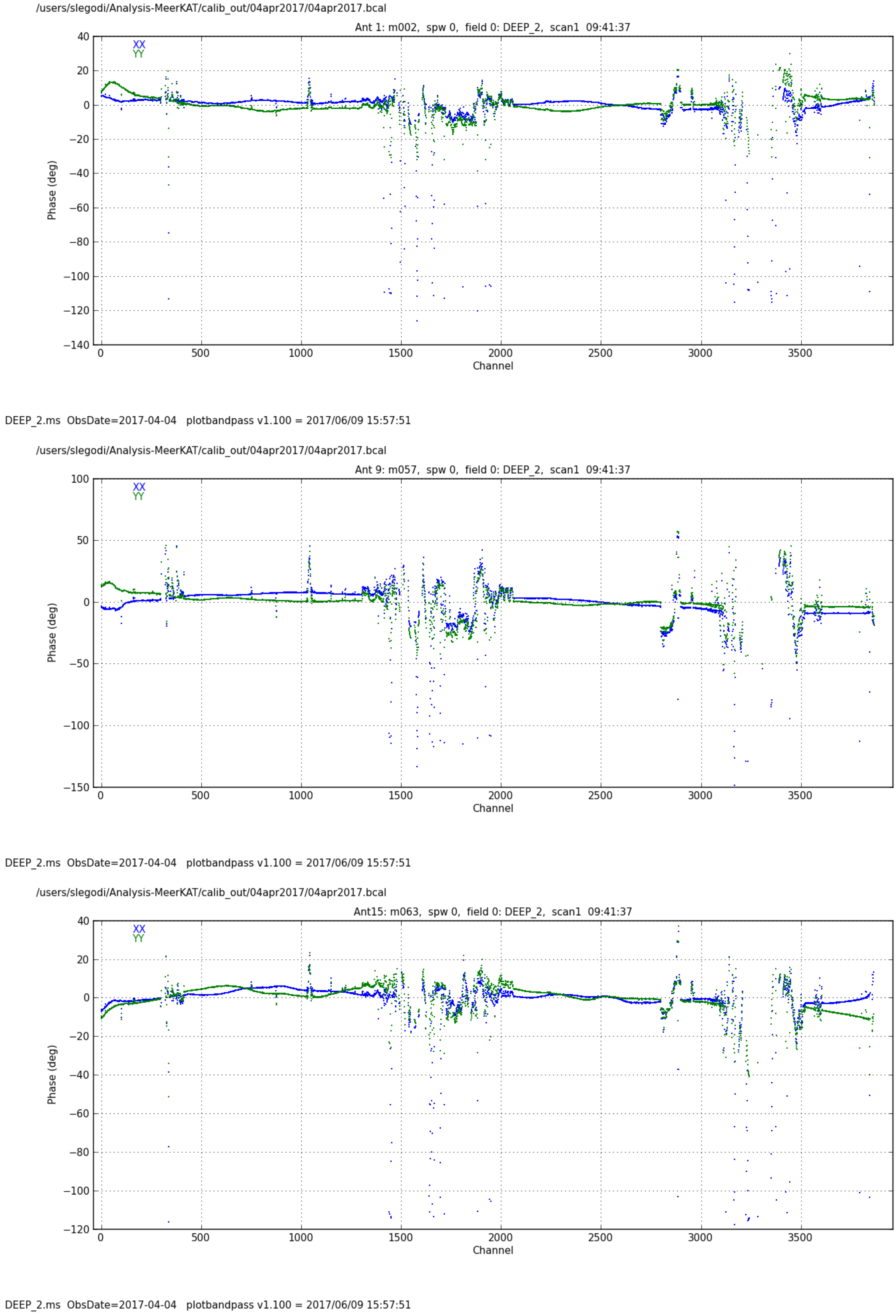

Figure 3.9: The bandpass phase solutions for three antennas for the DEEP 2 field.

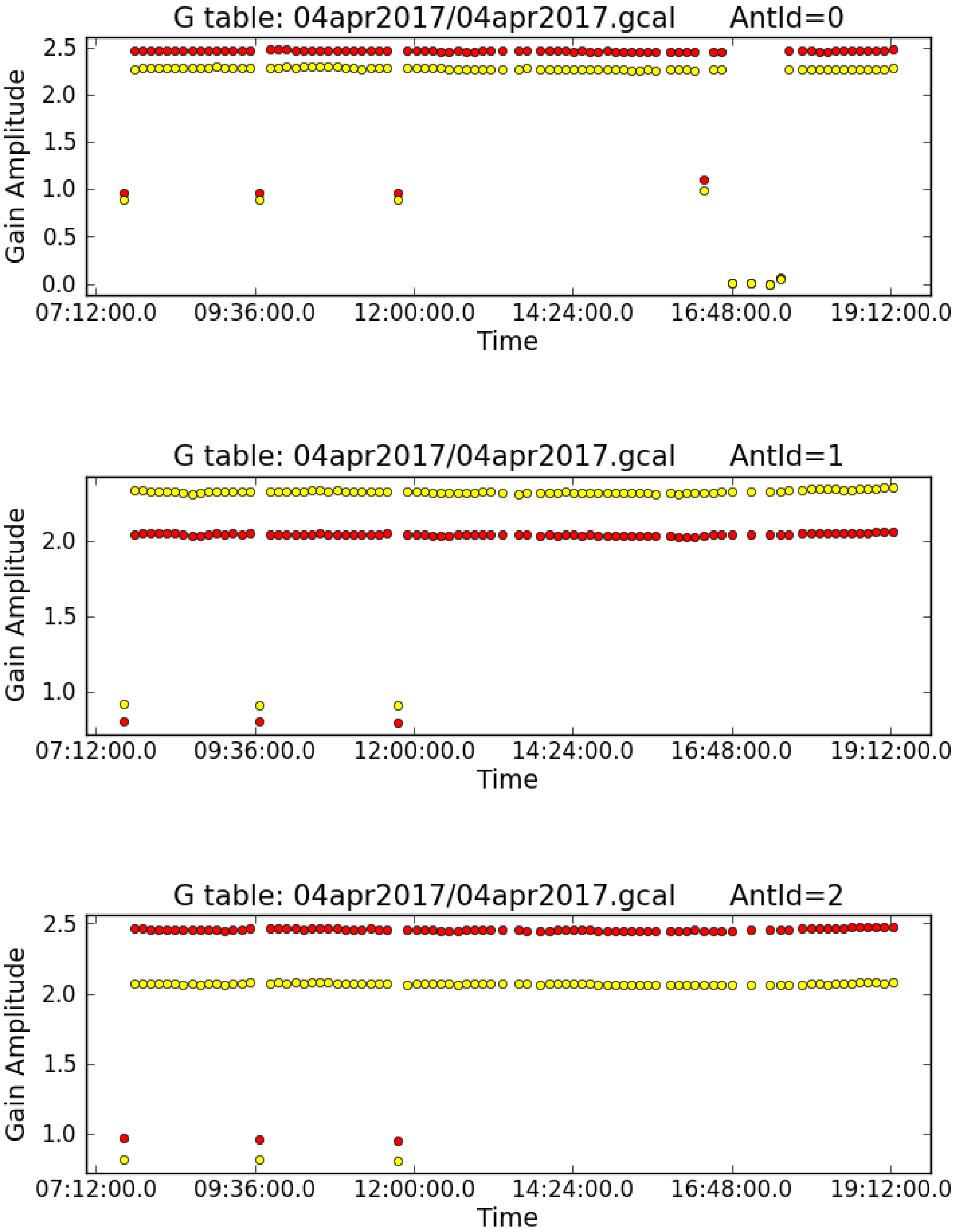

Figure 3.10: The initial gain amplitude solutions for the DEEP 2 field. Shown are the first three antennas.

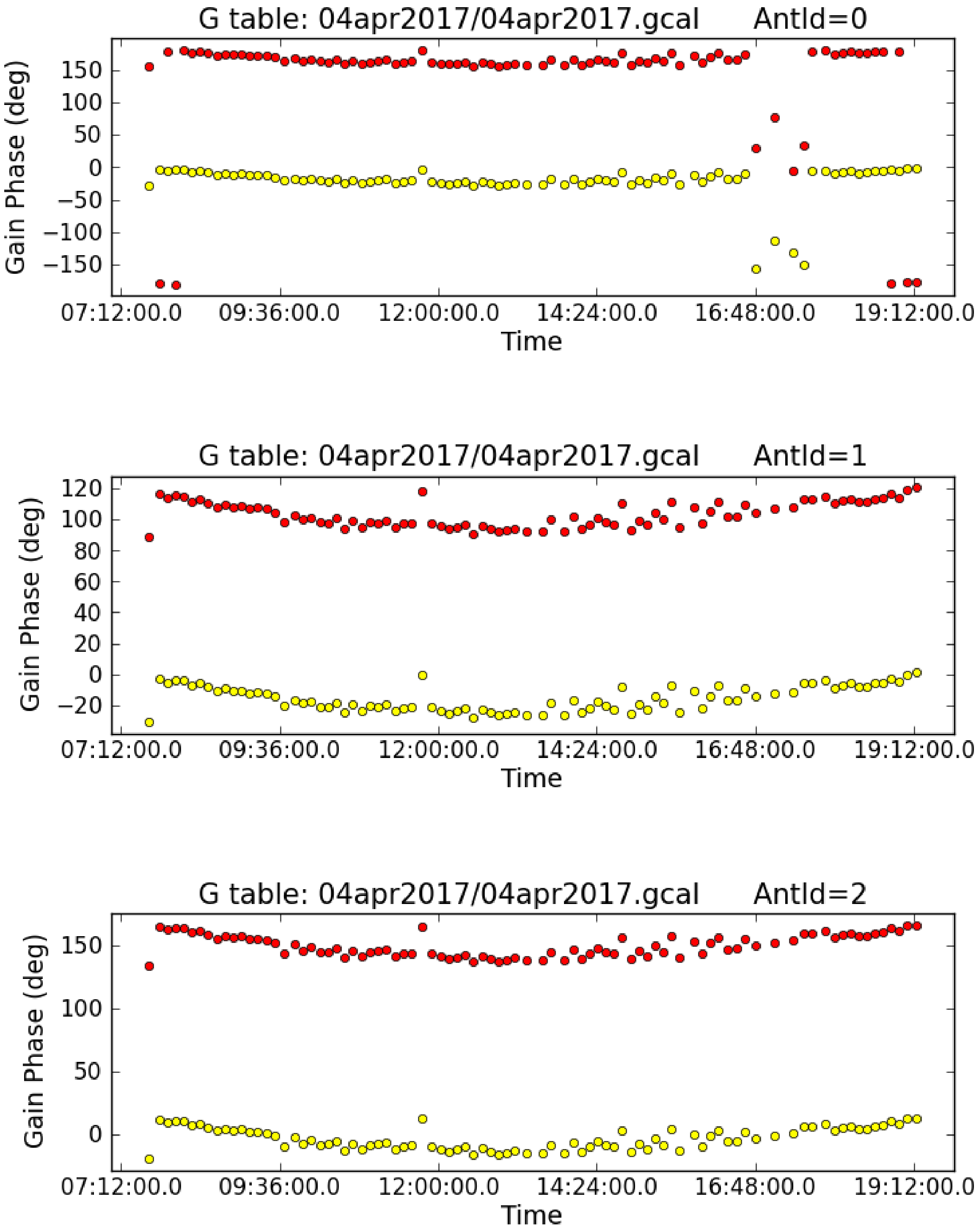

Figure 3.11: The initial gain phase solutions for the DEEP 2 field. Shown are the first three antennas.

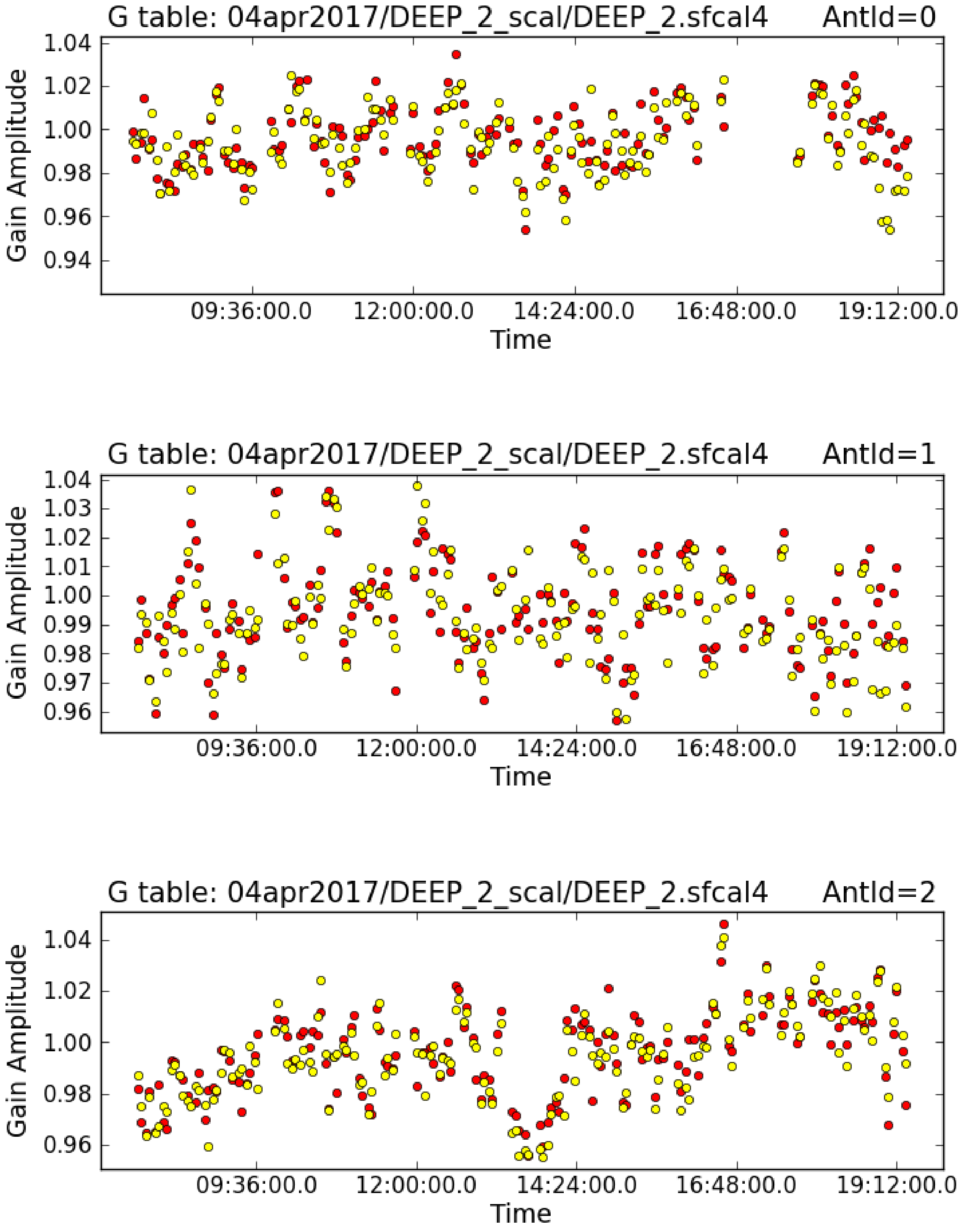

Figure 3.12: The self-calibrated gain amplitude solutions for the DEEP 2 field. Shown are the first three antennas as in the initial solutions.

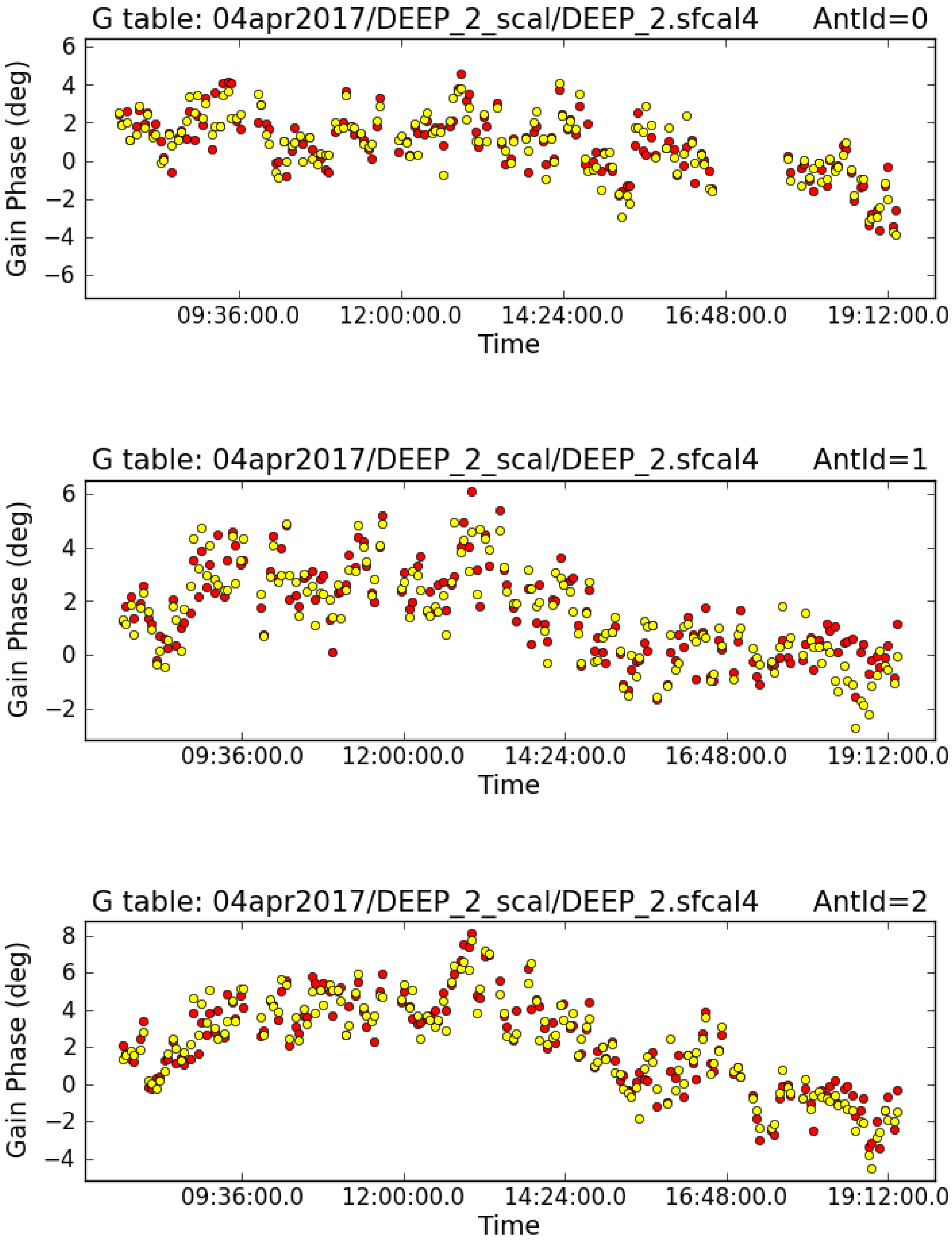

Figure 3.13: The self-calibrated gain phase solutions for the DEEP 2 field. Shown are the first three antennas as in the initial solutions.

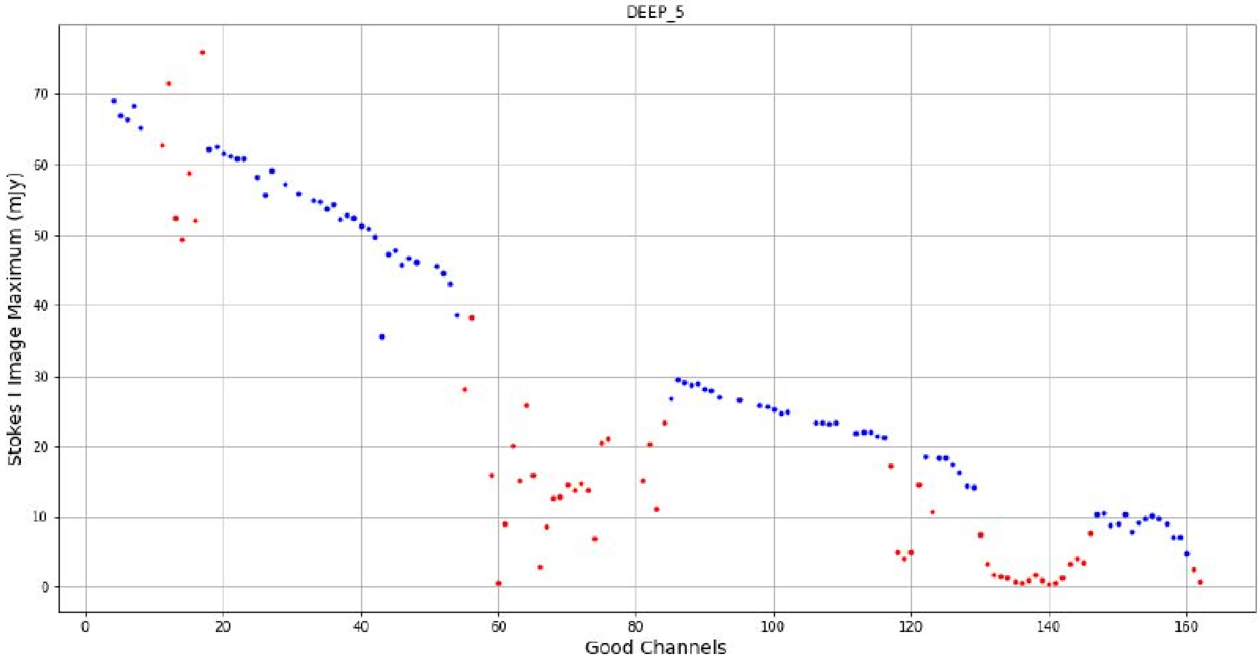

Figure 3.14: The amplitude of the map maximum as a function of channel. Each channel is 5.02 MHz and the spectrum spans 890 to 1700 MHz. Channels indicated in red have poor amplitude solution and have been removed from the spectro-polarimetric cubes.

3.3.2 Imaging

Multi-frequency images were created with the TCLEAN task in CASA 5.1.1. We use Briggs[7] weighting of the visibilities with robustness parameter set to -0.5 (Briggs, 1995). The frequency dependence of the clean model was fit by setting the mtmfs[8] Taylor series expansion to “nterms = 2” for our mosaic continuum case. The w-term wide-field phase error was corrected using “w-project” with the number of terms calculated automatically by TCLEAN (“wprojplanes = -1”). An automated clean mask was generated after each major cycle using “usemask = auto-multithresh”. Due to the large datasets involved, the SLURM[9] HPC cluster management and job scheduler was utilised to distribute tasks among a set of worker nodes, on the IDIA HPC servers, for parallel processing to a) split the self-calibrated visibility data into numerous small measurement sets based on the channelization for the polarization image cubes, and, b) image each channel measurements set into I, Q and U images and smooth the resulting images to a common resolution of 14″ – so that we have the same beam in each channel. Our flux measurements are in units of Jy/beam so the intensity measured will change if the beam changes. With all channels having the same resolution (beam) we have a uniform measure of intensity over the band. The value of 14″ corresponds to the angular resolution at the low end of the band. Since we are smoothing the only way to get a uniform beam is to smooth to the value of the worst resolution. Resulting I,Q,U images were then used to build spectropolarimetric image cubes for each field.

Statistics of the cube images show that channels contaminated by RFI do not have good calibration outcomes. Figure 3.14 shows an example, for the case of DEEP5. The plot shows the maximum flux density in the Stokes I image as a function of channel. This charts the flux of the strongest source in the image as a function of channel. There are 162 channels each of width 5.02 MHz. The spectrum spans the frequency range 890 MHz to 1702 MHz. For frequency channels that suffer significantly from RFI the amplitude of the image maximum is much reduced. The same effect is seen on all of the DEEP observations. The broad-band, MFS images do not show this effect directly as they are averaged across all channels. The dynamic range and flux densities of

---

[7] http://www.aoc.nrao.edu/dissertations/dbriggs/

[8] Multi-term multi frequency synthesis – an improved version of the standard MFS algorithm that accounts for changes in spectral index as a function of sky position.

[9] https://slurm.schedmd.com/

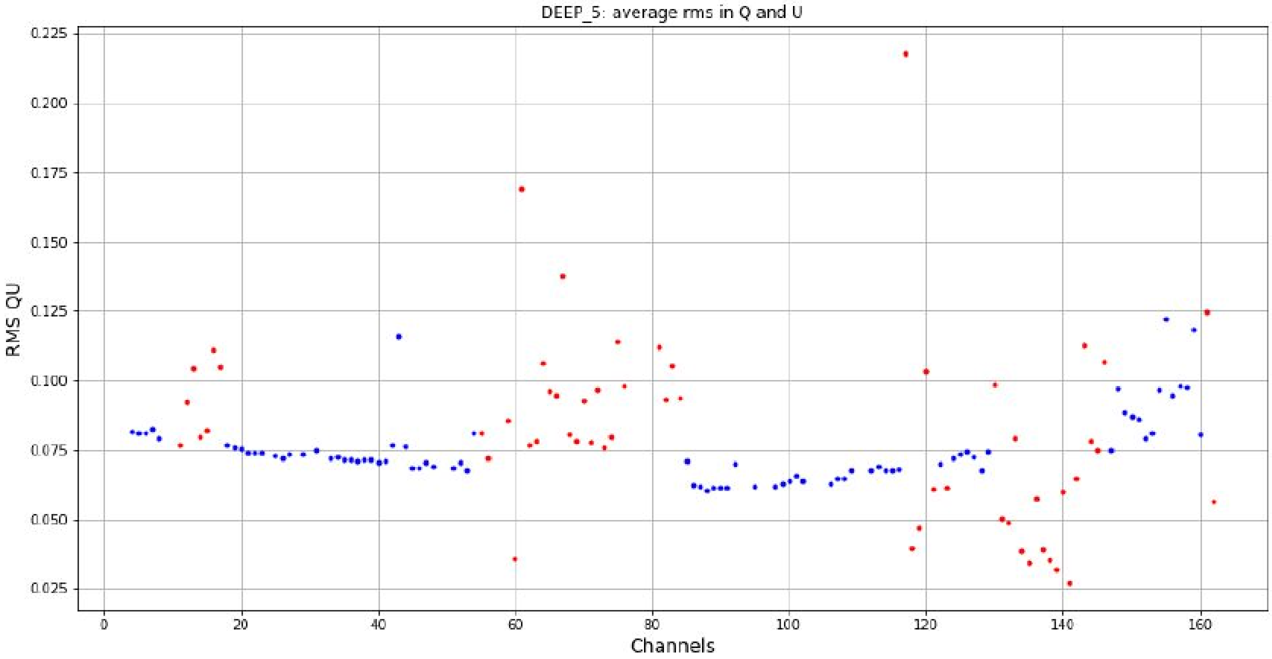

Figure 3.15: The average image rms in Q and U in the DEEP5 cubes as a function of channel. As for Figure 3.14, the good channels are indicated in blue. The average channel rms of the good channels is 72.0 μJy, and the minimum is 60.3 μJy.

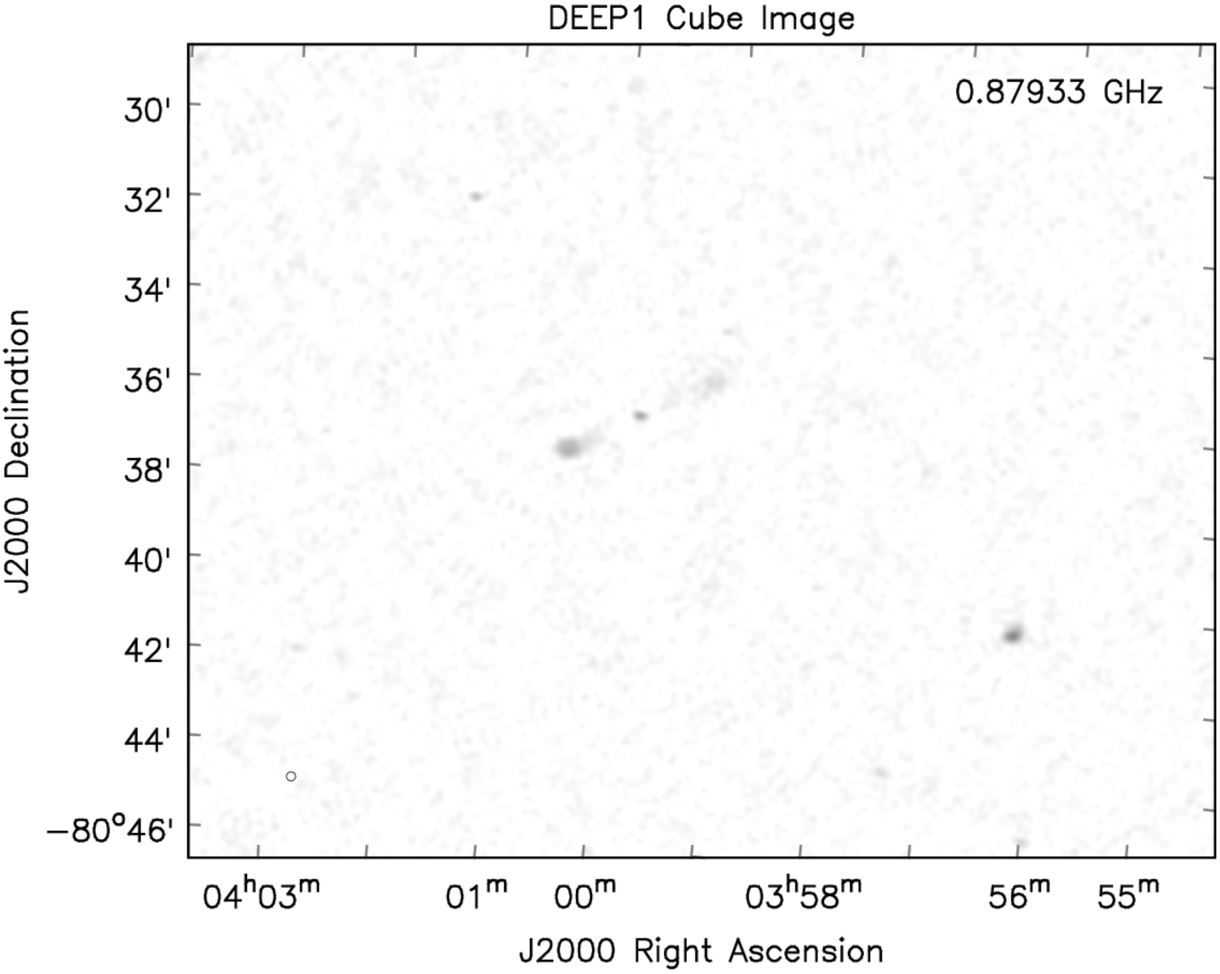

Figure 3.16: A zoomed in view in Stokes I of an FR II radio galaxy (RA: 03h59m45.9s Dec: -80d36m20.0s) in the DEEP1 cube image. This is an image of the brightest channel.

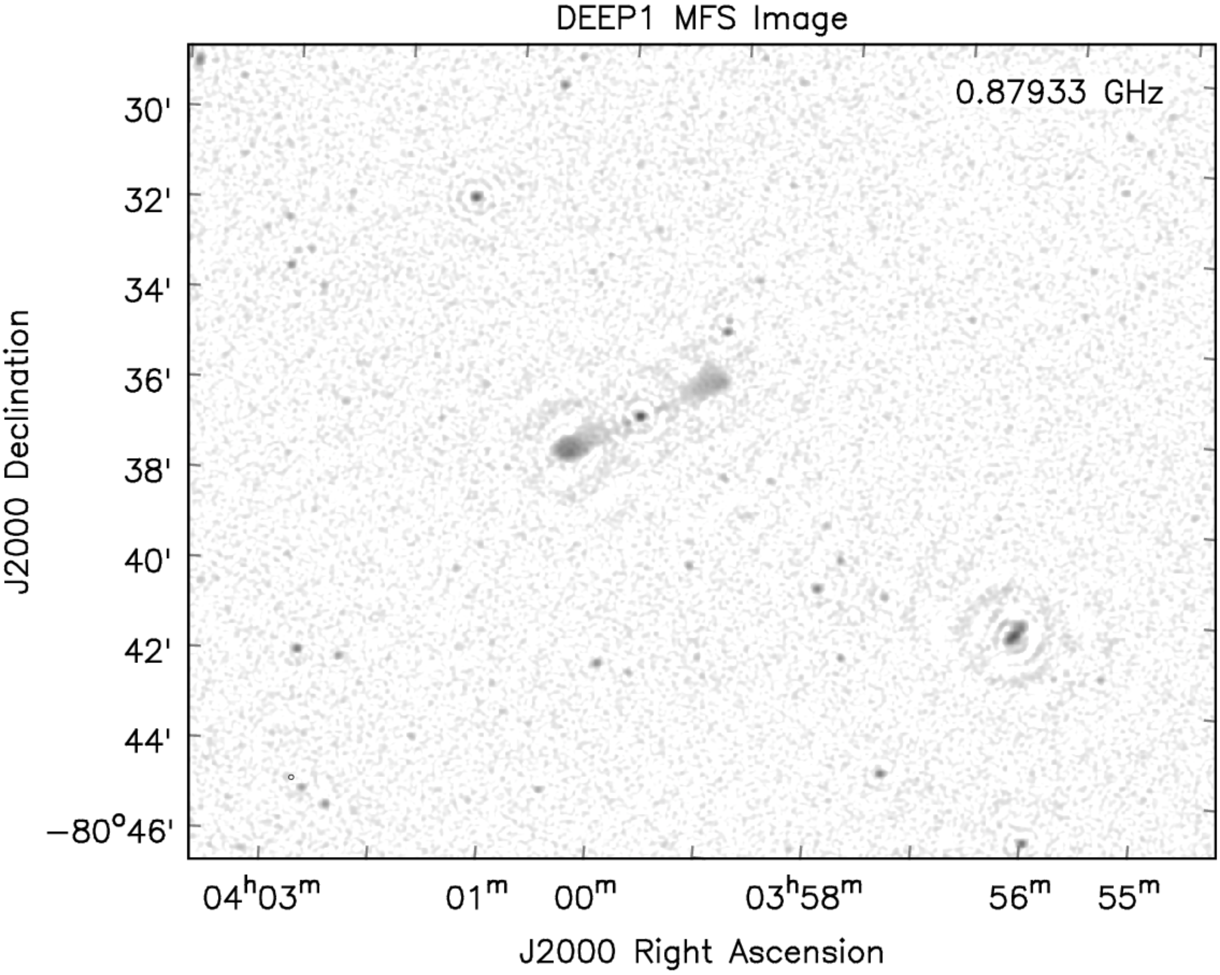

Figure 3.17: The same region as in Figure 3.16 but this time in the much more sensitive MFS image of the DEEP1 field.

sources in the MFS images would be affected, but the image itself would not show significant visual artefacts. Care should always be taken in interpretation of broad-band MFS images. The effects of issues in the frequency domain may not be directly apparent. Figure 3.15 shows the noise spectrum measured as the average Q and U image rms versus channel. For good channels the noise varies smoothly over the band, with a minimum rms of 60.3 μJy/beam near the band centre and a median value over the band is 72 μJy/beam. To build the spectral-polarimetric cubes the channels shown in red have been flagged and replaced with NANs. The spectro-polarimetric analysis thus uses data only from the well behaved channels (blue). A region of the DEEP1 field is shown in Figures 3.16 and 3.17, showing the visual differences between a cube and it's corresponding MFS image, respectively. The cube shows the brightest components while the MFS image reveals the main radio components of the FR II source, viz. the bright central point source, a bright extended foreground radio lobe, and a more diffuse background radio lobe.

3.4 Source Finding

We identified sources in the higher resolution and more sensitive MFS images using two source finders, viz. PYBDSF and AEGEAN. The outline and results for each analysis are given and compared below.

3.4.1 PYBDSF

We first perform source finding in the DEEP fields using PyBDSF (the Python Blob Detector and Source Finder, formerly PyBDSM[10]) (Mohan and Rafferty, 2015). PyBDSF is a source finding software that was originally written for the Low Frequency Array (LOFAR) observations as at the time it was developed, no other available software was best suited to the optimal analysis of LOFAR observations. The majority of the source finding software packages perform source finding by fitting Gaussians to image pixels, a logical approach as radio images are convolved with a Gaussian fitted to the dirty beam. This approach performs well for point sources, however, it fails in the case of extended sources. LOWFAR, and SKA path finder instruments such as MeerKAT and ASKAP, produce images of multiscale sources that is point-like and very extended sources. This is due to the their well sampled *uv*-coverage. PyBDSF was created with these kinds of observations in mind. Along with the traditional Gaussian fitting routine, it includes shapelet and wavelet fitting to extract extended sources.

Refregier (2003) developed the shapelet method in image analysis. This method is derived from a linear composition of each object in an image into a series of localized basis functions of various shapes. Refregier (2003) chose Gaussian-weighted hermite polynomials as their basis set of functions as these correspond to perturbed Gaussian functions, a familiar departure from the basis functions used in the point source centric image analysis methods preceding the shapelet method. Wavelets are localized functions of mean zero, wave-like, and are defined on a finite domain (Starck et al., 1998). This method involves the successive smoothing and downsampling of an image in an effort to analyse multi-scale properties of objects in the image. This method provides an efficient multi-scale image analysis due, in part, to it's finite nature. The wavelet transform was developed in different fields concurrently and is applied in various fields to construct and represent other and more complicated functions (see, for example, Ganesh (2003)). PyBDSF utilises the abilities to describe multi-scale image structures of shapelet and wavelet analysis methods.

PyBDSF takes 2-D and upto 4-D input images of FITS or CASA formats. It collapses any input cubes to a 2-D Stokes I image on which it performs the source extraction analysis. We use the sensitive and high resolution MFS image as the source finding image for each field. The self-calibrated image allows deeper and fainter detections than the averaged image cube and thus we search for sources in the more sensitive image and then extract the Stokes I, Q, and U fluxes from the full Stokes cube.

---

[10] `http://www.astron.nl/citt/pybdsm`

The thresholds we imposed are: 5σ detection i.e. signal-to-noise no less than 5, source flux no less than 10 μJy/beam (just above the rms noise in of $\sim$ 7 μJy/beam in the MFS image), and we restrict the source catalogue to regions of the map with a primary beam attenuation greater than 5%. We also used the shapelet method of source finding as this option in PYBDSF gave the best results over the Gaussian source model approach. Another option used was that of enabling PSF correction within PYBDSF. In this case the spatial variations in the PSF are estimated and their effects corrected for. PYBDSF does this by making a list of the most likely point source and unresolved sources and then derives the PSF from these. This derived PSF is then applied to all sources found. Fugure 3.18 displays a region in the DEEP3 field that is centred on an FR II radio galaxy near RA: 4h22m07s DEC: -80d03m42s. The magenta ellipses are the source models fitted.

3.4.2 AEGEAN

We identify sources in the second instance by making use of the source finding program AEGEAN (Hancock et al., 2012; Hopkins et al., 2015; Hancock et al., 2018). The program finds islands of image pixels that satisfy a given SNR threshold. Significant pixel islands are identified, and in the cases of extended sources they can be expanded to larger regions that include neighbouring pixels that have a lower but still significant measured SNR. The program identifies sources by fitting Gaussian models to significant pixel islands. Complex extended sources are fitted with a number of single Gaussians each of which represents a component of the larger source. The multiple Gaussians are fitted to local flux maxima in each island with position, flux, and shape constraints applied in order to different neighbouring components from overlapping. The program has been upgrade since the initial work of Hancock et al. (2012) and following new contributions to the literature (e.g. Huynh et al., 2012; Hopkins et al., 2015). It now includes functionality that enables better performance in SKA era telescopes as in the case of MeerKAT and the other SKA path finders. Such functionality includes the accurate modelling of spatially correlated data, optimisations for large fields of view, optimisations on the use of computing hardware, and ease of integration into larger processing pipelines.

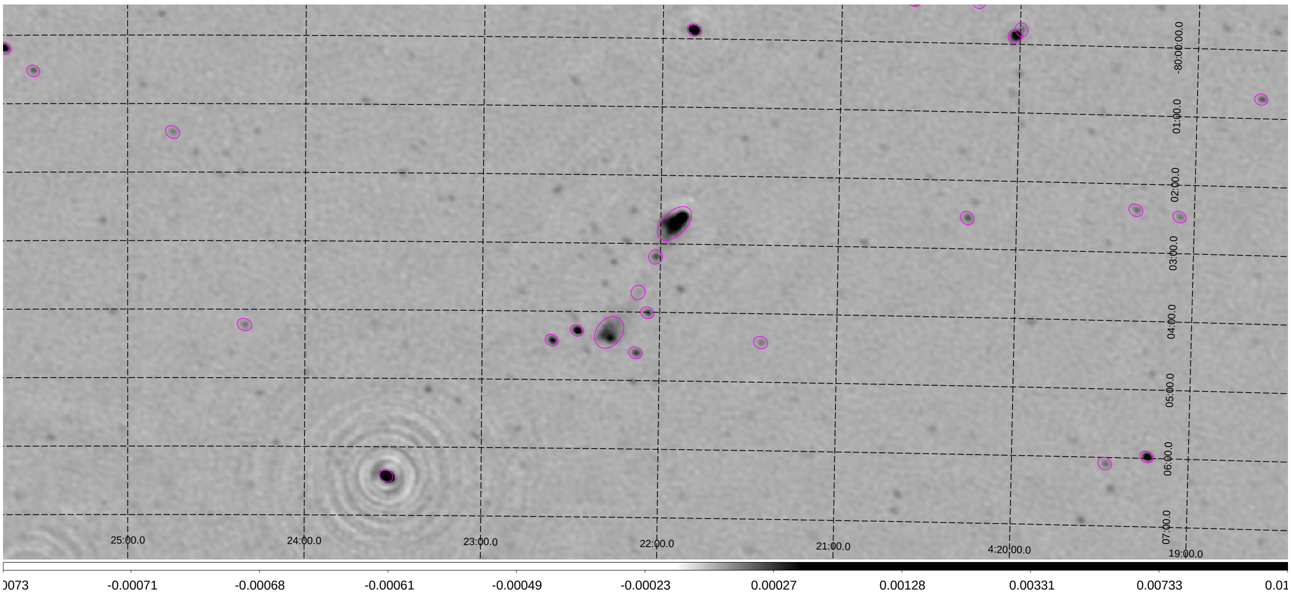

Figure 3.18: A region centred on an FR II galaxy in the DEEP3 field. Magenta ellipses indicate the fitted source finding models obtained with PYBDSF. The colour bar indicates the integrated flux in Jy/beam on an inverted logarithmic grey scale.

Table 3.2: The mean RA, DEC off-sets between sources observed in this work and those from SUMMS v2.1 catalog.

Field	RA off-set [″]	DEC Off-set [″]
DEEP1	-2.01 ± 2.46	-0.12 ± 0.33
DEEP2	-0.95 ± 1.92	-0.50 ± 0.35
DEEP2off	-10.21 ± 2.97	1.61 ± 0.48
DEEP3	0.18 ± 2.05	-0.51 ± 0.28
DEEP4	2.16 ± 2.12	-0.06 ± 0.33
DEEP5	-4.41 ± 2.52	-0.64 ± 0.33
DEEP7	-5.60 ± 2.58	-0.29 ± 0.43

3.4.3 Summary of Results

Many types of sources are detected in the DEEP fields. The brightest lobe in the FR II galaxy shown in Fugure 3.18 peaks at 1.3 mJy/beam with the central source emitting at 46 μJy/beam as identified with PYBDSF. The sources imaged are largely unresolved save for large scale structures such as radio lobes and radio jets that extend beyond the parent galaxy. It should be noted that there still remains artefacts in images, especially around bright sources (ringed emission), that are due to insufficient deconvolution depth and direction-dependent effects which are beyond the scope of this work and are therefore not deconvolved. We do not deconvolve deeply in the channel maps since we only collect data at the positions of peak total intensity, so residual side-lobe emission is negligible for our analysis.

A cross-match of the PYBDSF sources we have found with the SUMMS v2.1 catalog (Mauch et al., 2003) shows that a large fraction of the sources detected are new and never observed (see Figure 3.19). The cross-match is constrained by the 14″ smoothed resolution of the cube images and the best matching sources (one from each catalog) are chosen as those that have the smallest separation on the great circle passing through them. Slightly more than 10% of our sources have SUMMS counterparts in the case of the DEEP fields DEEP1 (13.9%), DEEP2 (11.5%), and DEEP3 (12.1%). The other four fields have fractions below 10% with DEEP2off at 6.1%, DEEP4 at 8.3%, DEEP5 at 4.6%, and DEEP7 at 3.6%. We also calculate the separations in both RA and Dec (ΔRA and ΔDec). These values, displayed in Figure 3.20, show that the mean separations between our sources and their counterparts are centred near zero arcseconds with a few outlying values.

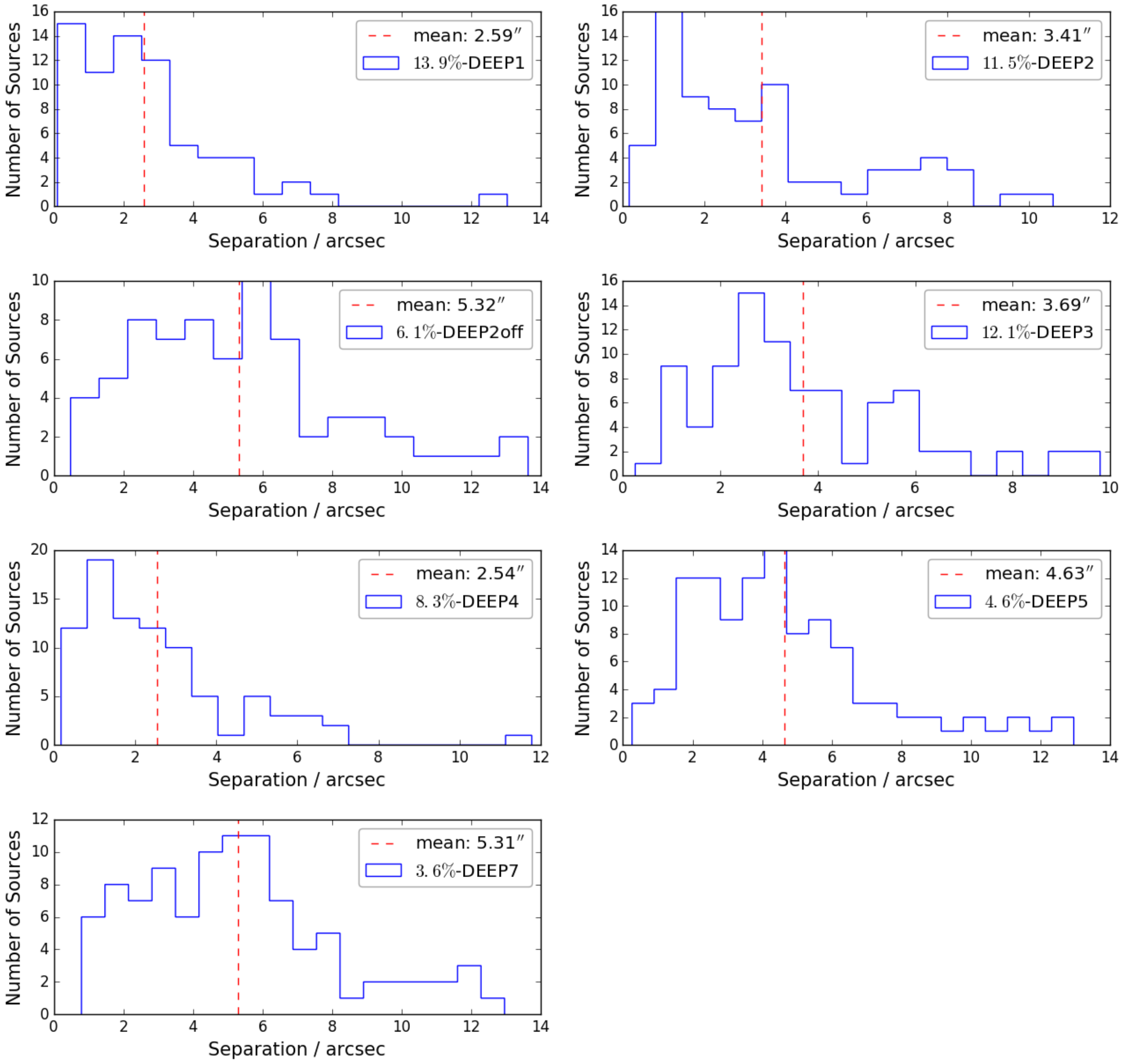

Figure 3.19: The great circle separation between sources we have detected in the DEEP fields and their closest matches in the SUMMS v2.1 catalog. A very small fraction of our sources have counterparts detected in the earlier SUMMS catalog. The vertical red dashed line indicates the mean separation.

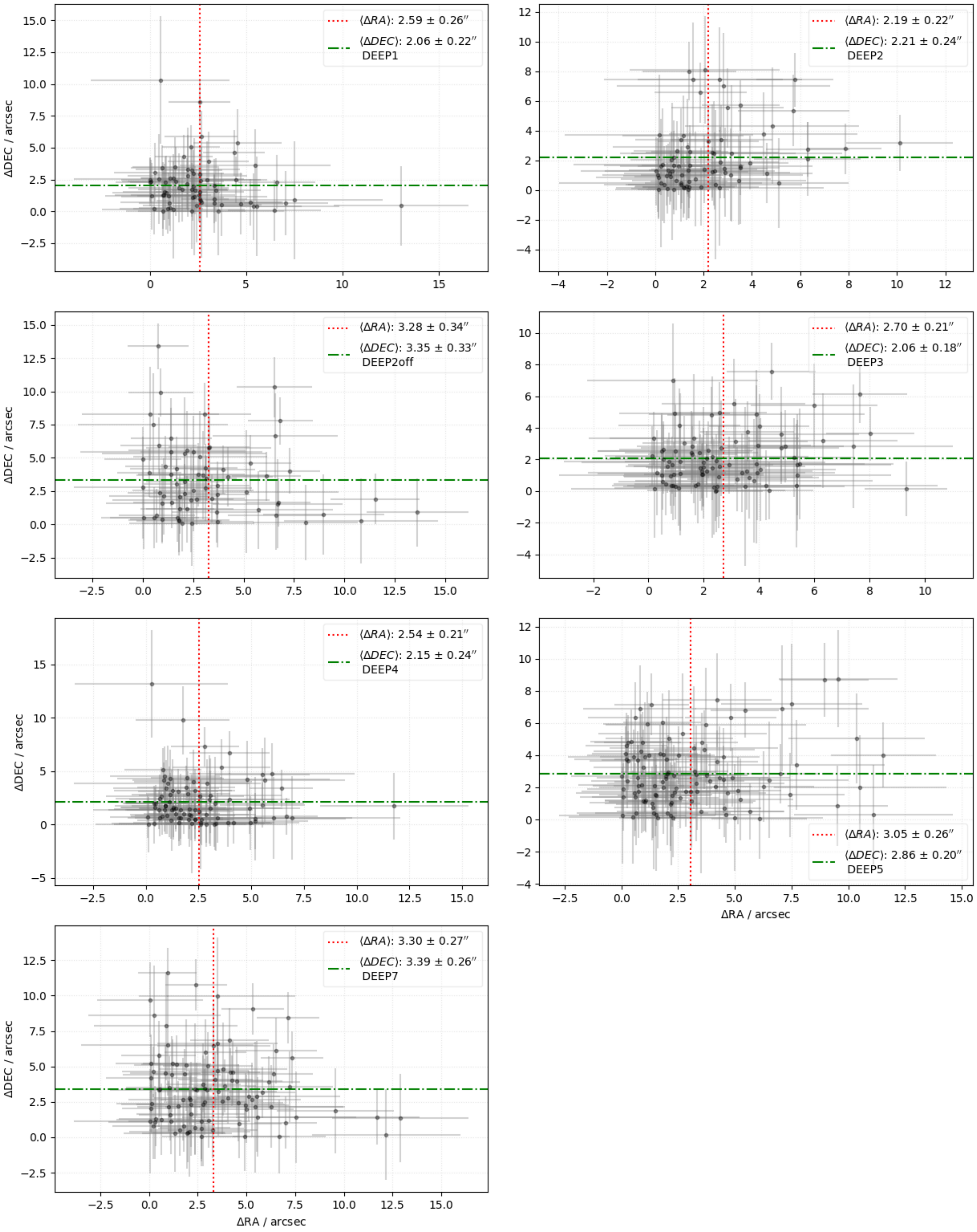

Figure 3.20: Distribution of differences in RA and difference in DEC for sources in DEEP fields found to have counterparts within 14″ from the SUMMS v2.1 catalog. The errors on the mean values are the standard errors associated with the mean, while those on the data points are the combined errors from our astrometry and those recorded in the SUMMS catalog.

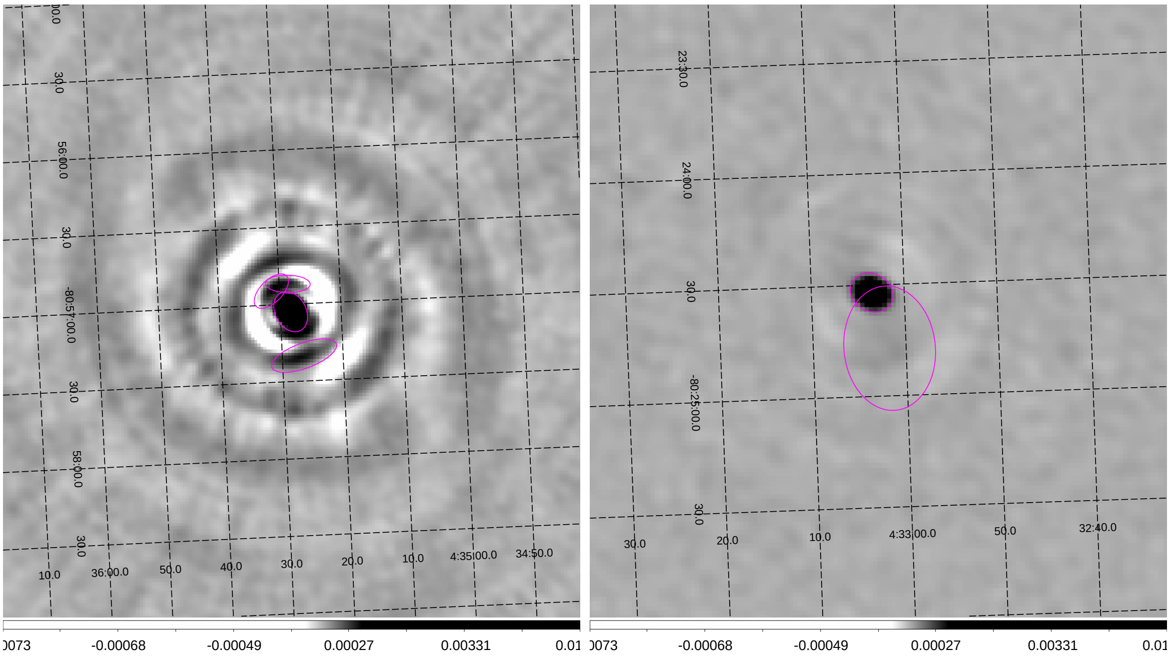

Figure 3.21: Two types of source finding artefacts near bright sources in the DEEP3 field. The colour scheme follows that in Figure 3.18.

Artefacts were encountered during both the PYBDSF and AEGEAN source finding analyses. the most prevalent of these were encountered with PYBDSF due to ripples in flux around very bright sources as shown in Figure 3.21. Other artefacts are extended diffuse regions of very low peak flux density $\sim 10\ \mu$Jy/beam as displayed by the right-hand panel in Figure 3.21. Sources with a complex extended structure were also sometimes fitted with multiple ellipses such as in the case of bent tail radio galaxies with an example displayed in the left-hand bottom panel of Figure 3.22. Other sources of this kind are fitted with a single ellipse that covers the entire extended structure of the source or only a portion of the source as in the right-hand panels of Figure 3.22. Some sufficiently bright sources are sometimes not fitted and so not identified as sources by PYBDSF. An example of one of the cases is shown in the top left-hand panel of Figure 3.22.

AEGEAN gave the most consistent source classification, visually. This was so especially in cases of complex sources where the fitted ellipses better approximated the extended structure of spatially complex sources. AEGEAN was also more consistent in finding compact isolated sources that were sometimes missed during the initial PYBDSF analysis. Some obvious artefacts such as the spurious ringed-shaped emission around bright sources, are visually identified and excluded from further analysis. AEGEAN was thus preferred for the creation of a source catalog that is used in later sections of this work. Further analysis (e.g. Hopkins et al., 2015) of source finding and characterisation is beyond the scope of this current work.

3.5 MeerKAT Spectropolarimetric Analysis

In this section we describe our spectropolrimetric methods for analysing the MeerKAT DEEP field observations and also present our findings. We follow a method similar to that described in section 2.3.2 where we analysed KAT 7 observations. The key difference being that we now extract Stokes I, Q, and U fluxes along lines of sight that are defined by the positions of the fitted ellipses (fitted to unknown sources observed in the MFS images) identified according to our source finding analysis which is described in Section 3.4. We then extract Stokes I, Q, and U spectra from the image cubes described in Section 3.3.2.

The flux extraction algorithm is divided into two main branches: one written for off-source positions scattered all over the cube map, and the other branch written for source positions. The reason for this branching

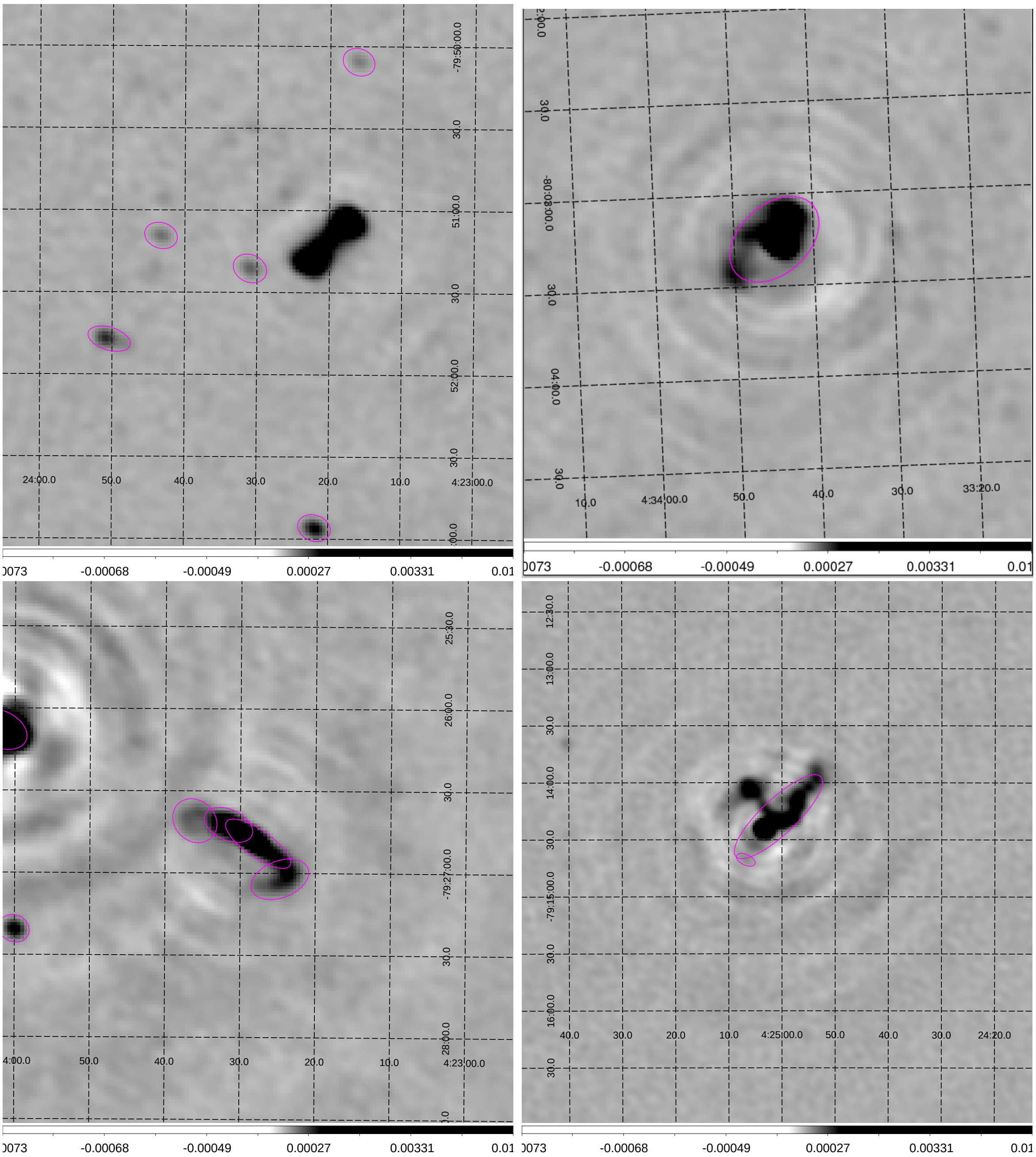

Figure 3.22: Different types of source finding artefacts near complex structured sources in the DEEP3 field. The colour scheme follows that in Figure 3.18.

and sampling of off-source positions is the same as in the KAT 7 analysis where we want to quantify effects of the noise in each field. In the case of the off-source positions' branch, the map was inspected by eye to find an approximate pixel area away from a true source from which to extract Stokes I, Q, and U fluxes. This area was chosen to be bounded by an annulus whose inner and outer boundaries have 20 and 40 pixel radii, respectively. The algorithm then selects a coordinate (x,y) within the annulus where the total flux is positive but below a flux limit similar to the lower threshold flux used in the source finding routine. The flux limit was set to 10 μJy/beam in the source finding image. Stokes I, Q and U are then extracted at these coordinates for all channels. We perform 1000 extractions of these off-source fluxes which results in 1000 files, each containing the off-source I, Q, and U fluxes at all frequency channels.

The on-source branch extracts I, Q, and U at the pixel coordinates of an identified source, under the condition that the source be bright enough – that the MFS total intensity is ≥ 1 mJy/beam. This way of extracting fluxes avoids contamination of extracted fluxes by PSF[11] artefacts such as the ring-like emission seen around bright sources. The cube map peak I for each source will also be ≥ 1 mJy/beam. The rms noise associated with each source I, Q, and U flux is then taken as the rms of 10 off-source fluxes (for each of the I, Q, and U) at locations around the source. The off-source fluxes are extracted in the same manner as those for sources and the locations contain no prevalent sources. The rms noise is then combined with the bootstrap flux density error, obtained for the secondary calibrator during calibration (Section 3.3.1). This approximates the error on the flux extracted, viz.

$$\sigma_{Q_i} = \sqrt{\sigma^2_{Q_i,rms} + \left(Q_i \frac{\sigma_{I_b}}{I_b}\right)^2}, \tag{3.1}$$

for the $i-$th channel Stokes parameter Q_i, as an example. Here $\sigma_{Q_i,rms}$ is the Stokes Q rms noise extracted from the map. σ_{I_b} and I_b are, respectively, the bootstrap error and flux derived for the secondary calibrator during the calibration process.

3.5.1 Instrumental Polarisation

Our KAT 7 study of direct pointing of radio sources was vulnerable to polarisation leakage (instrumental polarisation) from the pointing direction of the antennas – on-axis leakage. This kind of leakage is corrected for during polarisation calibration when D-terms are determined. Another contributor to polarisation measurement uncertainties is off-axis leakage which arises from the geometry of the antenna dishes. This form of leakage converts a fraction of the Stokes I signal into Stokes Q and U due to reflection off the dish surface. Off-axis leakage becomes significant when measuring polarisation for sources that are located away from the centre of the field – hence the term "off-axis". This is exactly the case in our study of the wider area commissioning phase data from MeerKAT. Below we present our analysis for estimating the off-axis leakage upper limit.

3.5.1.1 Polarisation detection and off-axis polarisation leakage

The probability of false detection as a function of threshold in units of the noise in q and u for broad-band RM synthesis was analysed (George et al., 2012). The false detection rate was measured as a function of signal-to-noise ratio, T

$$T = \frac{|F(\phi)|}{\sigma_{qu}}. \tag{3.2}$$

For an RM component with restored amplitude in fractional polarization $|F(\phi)|$. σ_{qu} is the noise in q, u for the band averaged signal, i.e. the noise on the average band values of q and u. From the MeerKAT observations we have a measure of σ^i_{qu}, σ_{qu} per channel i. For N channels, an estimate of the band averaged noise is

---

[11] Point Spread Function – for example, see `https://www.gnu.org/software/gnuastro/manual/html_node/PSF.html`.

$$\sigma_{qu} = \frac{1}{N}\sum_{i}^{N}\sigma_{qu}^{i}. \tag{3.3}$$

For the case of spatially unresolved sources with a single Faraday emission component, George et al. (2012) have shown that $T = 8.0$ has a false detection probability of $< 10^{-4}$. The probability increases quickly as T is reduced. At $T = 6.0$ the false detection probability is 0.43%, at $T = 5.0$ the probability rises to 3.6%, while at $T = 3.0$ the false detection rate reaches a highly significant rate of 43.9%.

For direct polarisation detections, we define the band averaged polarisation fraction

$$\langle p_0 \rangle = \frac{1}{N}\sum_{i}^{N} p_0^{i}, \tag{3.4}$$

where p_0^i is the bias corrected fractional polarization in an individual channel. Because the statistics of p_0^i are not Gaussian (they are a Rayleigh distribution for $p_0 = 0$ and Ricean for $p_0 > 0$ (Rice, 1945)), we cannot use simple Gaussian statistics to set thresholds. We approximate the significance of a signal in $\langle p \rangle$ by comparison to the rms scatter of p_0^i about the mean value of all p_0^i. We can also define a detection criteria for observations limited to any portion of the observed band, by signifying this *sub-band* by X, we define the sub-band averaged noise as

$$\sigma_{p_0,X} = \frac{1}{N}\sqrt{\sum_{i}^{N}(\langle p_{0,X}\rangle - p_0^i)^2}, \tag{3.5}$$

then thresholding for detection in the sub-band would be defined according to

$$\tilde{T}_X = \frac{\langle p_{0,X}\rangle}{\sigma_{p_0,X}}. \tag{3.6}$$

Polarimetry in different portions of the observed band can allow us to quantify broadband phenomena such as depolarisation where higher frequency measurements would be enhanced as compared to the lower frequencies. Direct polarisation detections made using the full band averaged polarisation fraction is then

$$\tilde{T} = \frac{\langle p_0 \rangle}{\sigma_{p_0}}, \tag{3.7}$$

with

$$\sigma_{p_0} = \frac{1}{N}\sqrt{\sum_{i}^{N}(\langle p_0\rangle - p_0^i)^2}. \tag{3.8}$$

Using the off-source pixels as the benchmark for non-detection and the direct polarisation detection threshold as the 99.9^{th} percentile of the distribution of off-source $\tilde{T}$, we calculate the threshold to be $\tilde{T} = 9.1 \pm 0.2$. We also divide the observed band according to the three sub-bands resulting from the removal of bad channels (see Figures 3.14 and 3.15) to assess the prevalence of detections in each sub-band and also to analyse the depolarisation state of each source. For convenience sake, the sub-bands are named *low-band* (for $\nu_1 \subset (0.810,\ 1.165)$ GHz, indicated by subscript 1), *mid-band* ($\nu_2 \subset (1.165,\ 1.522)$ GHz, indicated by subscript 2), and *high-band* ($\nu_3 \subset (1.522,\ 1.700)$ GHz, indicated by subscript 3)

To estimate the off-axis polarisation leakage we analyse the fractional polarisation levels measured for sources that are bright in Stokes I ($I_{peak} \geq 10$ mJy/beam) and also fall below our detection threshold for direct polarisation. Bright unpolarised sources are ideal for estimating off-axis leakage. This value is based on the lower envelope of the distribution of fractional polarizations for bright non-detections. If we measure polarization fraction of f_k for an unpolarised source k, then the instrumental polarization is f_k. If we do not know the polarization of the source, then some of f_k could come from true polarized signal of the source, so we can only report that the instrumental polarization is less than f_k, i.e. f_k is an upper limit on the off-axis instrumental polarization. We approximate the off-axis polarisation leakage by the median of $\langle p_0 \rangle$ for the bright unpolarised sources with low polarised signal to noise, as described above, and find the upper limit to be 0.7%. This value is consistent with the initial analysis of early MeerKAT holography simulations where cross polarisation leakages near one degree off-axis are of the order of 1%. This is work is still in the very early stages (private communication, de Villiers, 2019).

3.5.2 Total and polarised flux properties

There are some notable sources among the sources identified in the seven fields observed with MeerKAT (16). These include bright compact sources and extended structures such as radio lobes in radio galaxies. Of these 993, among all the fields combined, have peak fluxes of at least 1 mJy/beam, this is our milli-Jy sample. We present fluxes extracted for some of these sources in this section. Most of the sources have not been detected previously and thus do not have known counterparts, as we have shown in Section 3.4.3 and so we adopt a uniform naming scheme based on the J2000 RA and Dec coordinates of each source. We follow the standard naming scheme for J2000 source coordinates, that is, for a source located at RA: HHMMSS and DEC: DDMMSS, the name "JHHMMDDMM" is adopted to refer to said source. For example the bright object at RA: 03h52m37.2s and DEC: -05d21m29.4s is named "J0352-0521" according to this scheme. The RA and Dec of each source is also included in our catalogs (for example Tables 3.3 and A.1).

3.5.2.1 Total and polarised spectra

We made power law fits to the total flux according to $I(\nu) \sim \nu^{-\tilde{\alpha}}$. This fit to the total intensity limits the affects of noise fluctuations when deriving fractional polarisation as these values were calculated using the fitted total intensity instead of the noisier per channel measured total intensity. At the time of writing there was no available primary beam correction for the commissioning data and so the spectral indices, $\tilde{\alpha}$, derived this way will still contain the frequency and position (relative to the pointing center) dependence of the primary beam. Sources located farther from the pointing centre will tend to have steeper indices in this dataset. However, $\tilde{\alpha}$ may still suggest physically relevant correlations that may be independent of beam effects. Cases of significant spectral curvature were observed which motivated the use of more complex power law fits to the total intensity spectra. We thus made a second, curved power law fit to the observed spectrum defined by

$$I_c(\nu) \sim \nu^{\tilde{\alpha}_{c1} + \tilde{\alpha}_{c2}\log(\nu)}. \tag{3.9}$$

Figure 3.26 displays log scaled distributions of the peak cube total intensity, I_{peak}. The curves are normalised fixed-width smoothed Kernel density estimates (KDE) of cube I_{peak} distributions. Our milli-Jy samples display two major flux populations – one lower flux sub-sample and a brighter lower population sub-sample where $I_{peak} \gtrapprox 10$ mJy/beam. We divide our source population into two sub-samples in order to analyse spectropolarimetric properties with respect to peak total flux density. One that is referred to as "bright" where the peak total intensity, I_{peak}, is equal to or larger than 10 mJy/beam and the second sub-sample, referred to simply as the "low flux" sub-sample, contains only sources with 1 mJy/beam $< I_{peak} <$10 mJy/beam. Polarisation degrees of order $\lesssim$ 1% in our milli-Jy sample should be detectable as they would be above the q, u rms noise which is approximately ~ 70 μJy/beam.

With the aim of analysing the broad band polarisation properties of our sample, we perform a simple power law fit to the $p_0(\lambda)$ distribution – $p_0(\lambda) \sim \lambda^{\beta}$ (e.g. Eichendorf and Reinhardt, 1979; Battye et al., 2011; O'Sullivan et al., 2013; Farnes, 2014). The polarisation spectral index, β, is independent of primary beam effects due to the division of polarised intensity by total intensity. β can broadly characterise the broad band behaviour of $p_0(\lambda)$. $\beta < 0$ signifies depolarisation (polarisation degree decreasing with wavelength), $\beta > 0$ indicates a repolarised

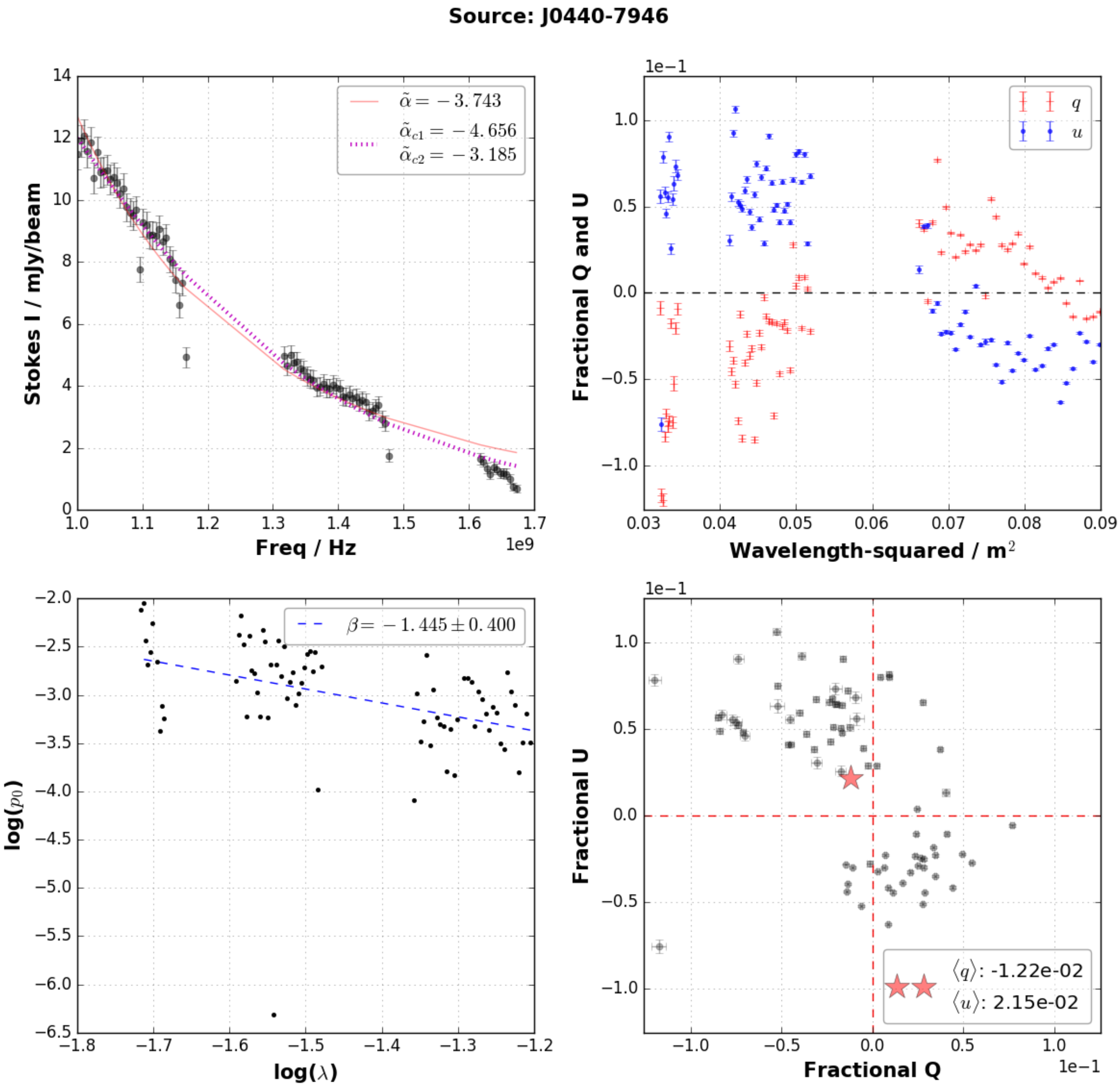

Figure 3.23: Spectra extracted for one of the bright sub-sample objects from the DEEP3 field. The object has RA: 04h40m15.4s and Dec: -79d46m40.8s and thus dubbed "J0440-7946". Top left: The total flux along with a power law fit, viz. $I(\nu) \propto \nu^{\tilde{\alpha}}$ *(red curve) and curved power law (magenta dotted curve with spectral indices* $\tilde{\alpha}_{c1}, \tilde{\alpha}_{c2}$*). Top right: Fractional Stokes Q (q) and U (u) as functions of wavelength-squared. Bottom left: Fractional linear polarisation (bias corrected) as a function of wavelength, along with the fitted power law (dashed line). Bottom-right: q v.s u along with the mean values indicated by the red star.*

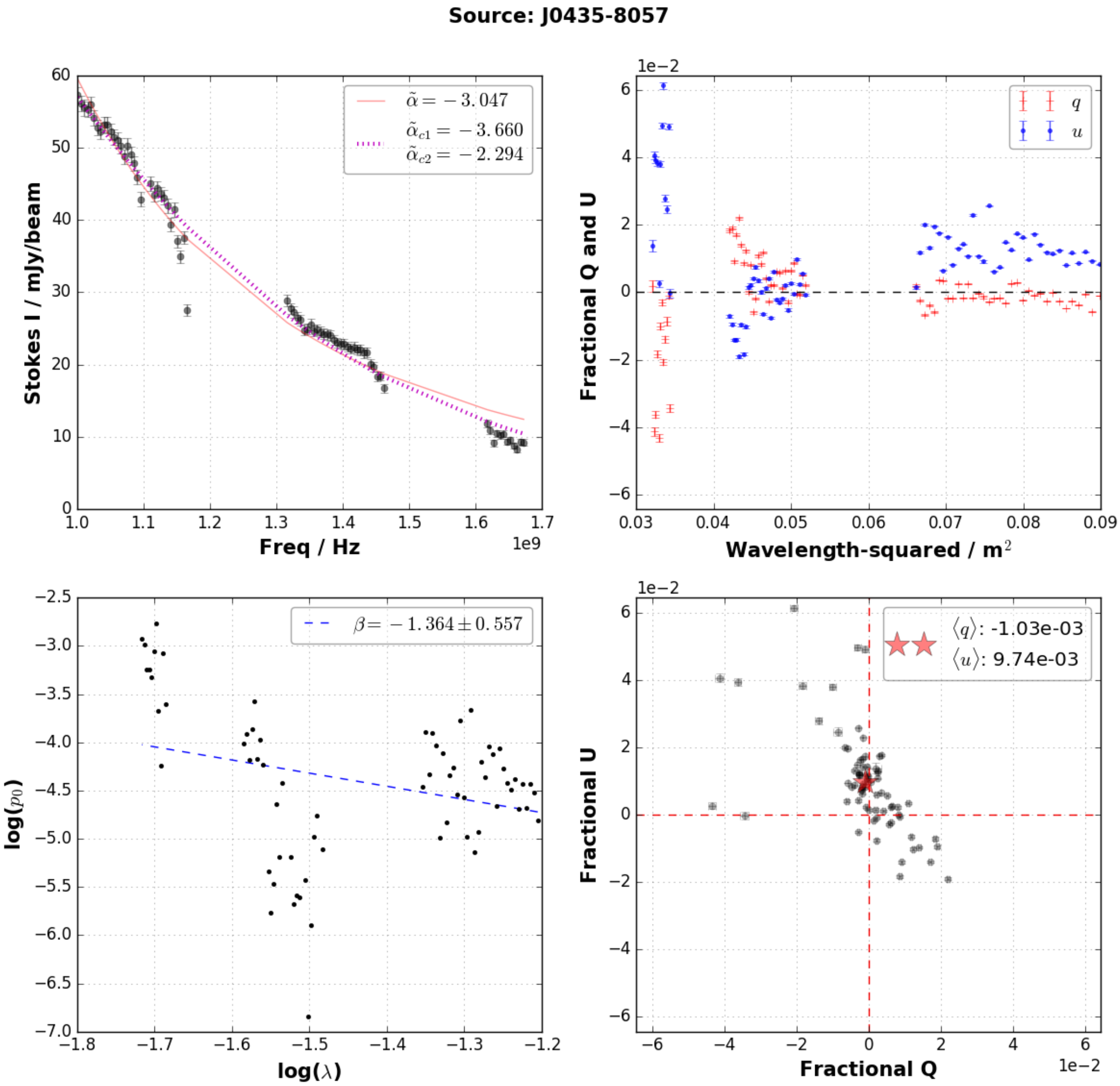

Figure 3.24: Total flux spectra extracted for one of the bright sub-sample objects, J0435-8057, from the DEEP5 field. The plots are arranged as in Figure 3.23.

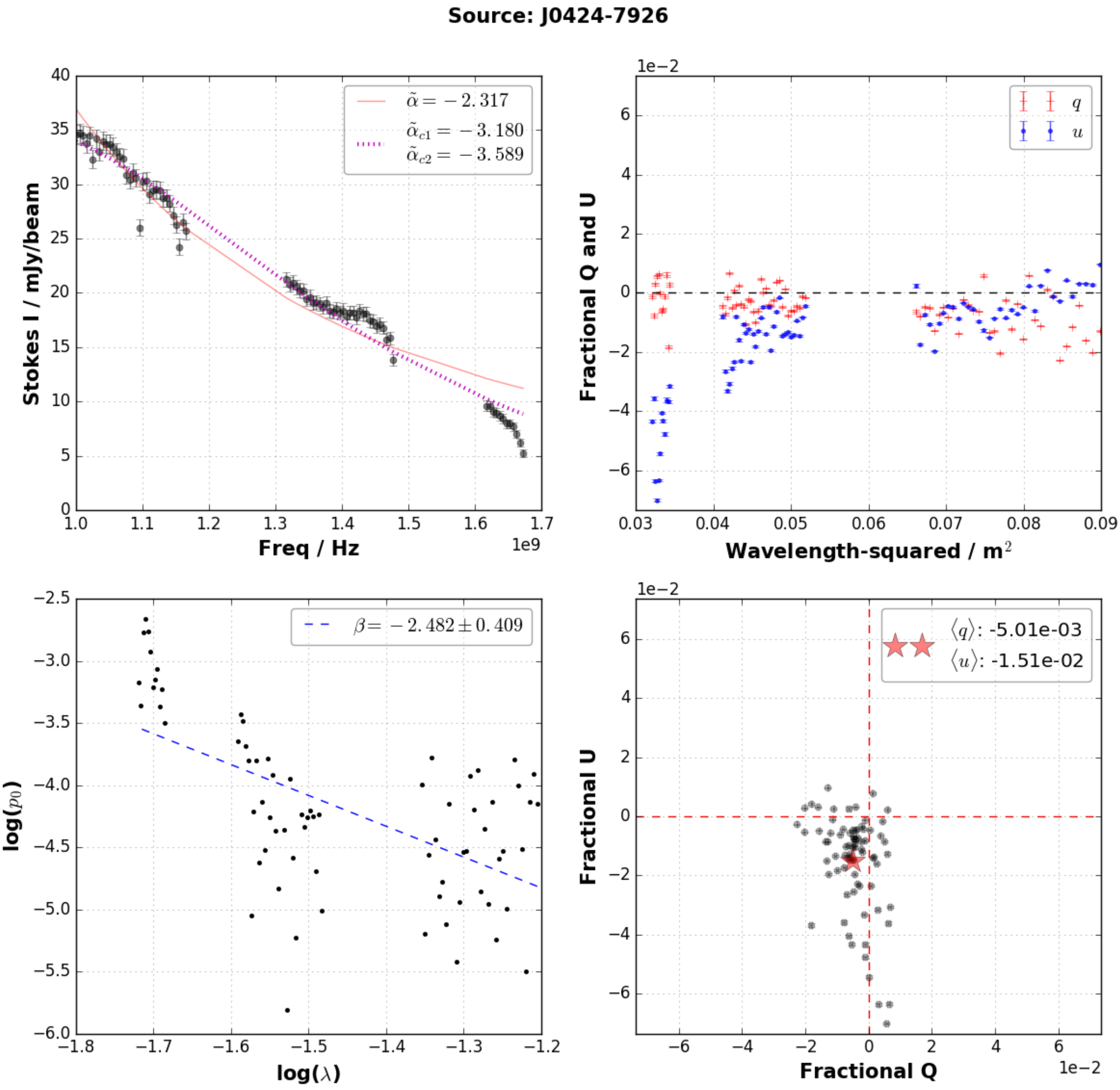

Figure 3.25: Total flux spectra extracted for one of the bright sub-sample objects, J0424-7926, from the DEEP3 field. The plots are arranged as in Figure 3.23. This is a bright unresolved source located at RA: 4h24m02.00 and Dec: -79d26m07.80s

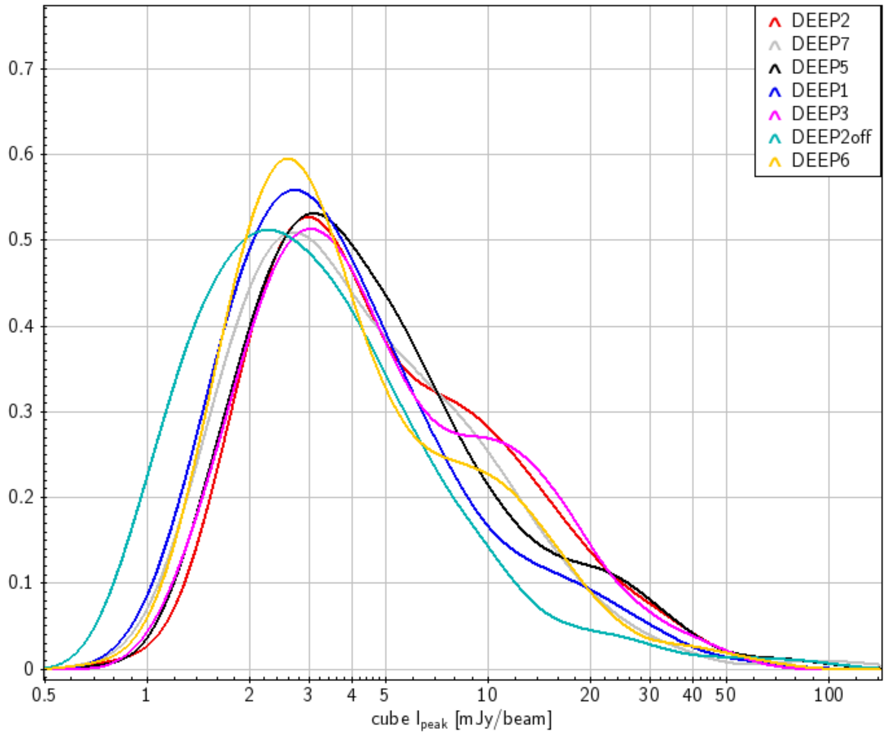

Figure 3.26: Fixed-width smoothed Kernel density estimates of cube I_{peak} distributions in each field.

spectrum while $\beta \approx 0$ indicates constant polarisation.

Distributions of spectral indices are displayed in Figure 3.27 where the left hand panel displays $\tilde{\alpha}$ for both direct polarised detections and unpolarised sources while the right hand panel displays β relative to $\tilde{\alpha}$. The majority of sources display steep spectra as noted visually and perhaps suggested by $\tilde{\alpha} \lesssim -1$ (see Figure 1.1) with a smaller population to the contrary – with $\tilde{\alpha} \sim 0$ and $\tilde{\alpha} > 0$. Population characteristics as suggested by $\tilde{\alpha}$ distributions cannot, however, be reliably inferred due to uncorrected primary beam effects. We observe sources that display spectral features akin to giga-hertz peaked sources with pronounced convex curvature near $\nu \sim 1$ GHz and still others with the opposite curvature in their spectra. The curved power law does better in approximating the spectral behaviour, especially in cases of significant curvature. Complex spectral energy distribution fitting (e.g. Lacki, 2013; Chen, 2014; Farnes, 2014) is most likely warranted in these cases but is beyond the scope of this work, but our curved power law fit provides a sufficient approximation for the purpose of fractional polarisation calculation in this work. The distribution of β shows that a highly significant fraction, $\sim 95\%$, of our sources display depolarisation behaviour in agreement with the notion that steep spectrum sources tend to be depolarised (e.g. Farnes, 2014) and thus supporting the spectral steepness of sources observed in this work, however, primary beam effects need to be mitigated to extract a more reliable correlation.

3.5.2.2 Polarisation detections

We detect a significant fraction of polarised sources in the radio quiet DEEP field. Our full milli-Jy sample consists of $24 \pm 8\%$ polarised $\gtrsim 8\sigma_{p0}$ detections (Section 3.5.1.1). We list all polarisation detections in Table 3.3 while unpolarised sources are listed in Table A.1. Figure 3.28 displays the band averaged polarised intensity, $\langle P_0 \rangle$, as a function of the mean total intensity, $\langle I \rangle$, for all milli-Jy sources. The undetected sources display $\langle P_0 \rangle$ that are consistent with negligible polarisation as they fall within the noise range defined by the off-source flux $\langle P_0 \rangle$ distribution. Detected sources are found to have $\langle I \rangle \gtrsim 1$ mJy/beam suggesting a selection bias for sources fainter than this. This selection bias is further suggested by the strong dependence of $\langle P_0 \rangle$ on $\langle I \rangle$ where polarisation detections tend to be bright in total intensity. We measure polarisation degrees in the range $\sim 1-10\%$,

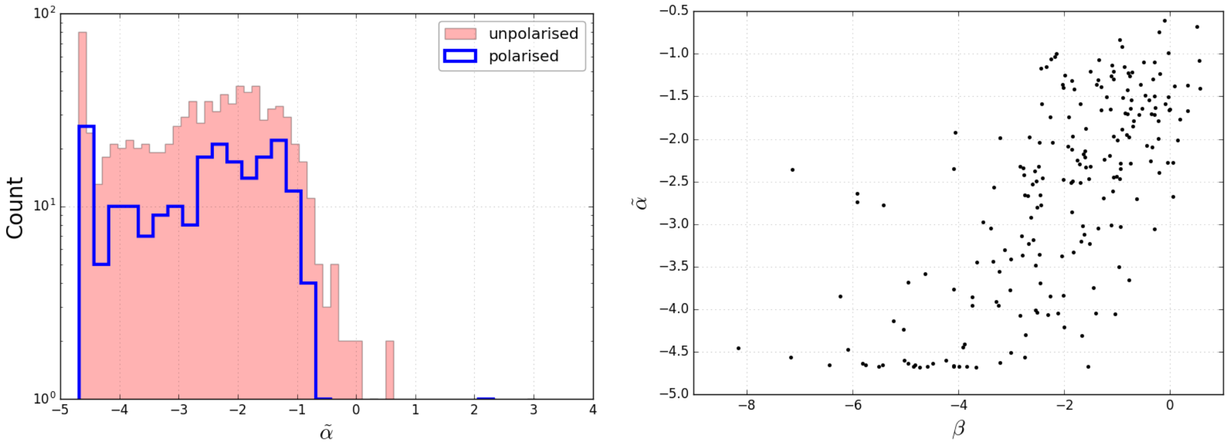

Figure 3.27: Distributions of simple power law spectral indices $\tilde{\alpha}$ (left panel) and also $\tilde{\alpha}$ as a function of β (right panel) of our milli-Jy sample. Polarised (open histogram) and unpolarised (filled) source $\tilde{\alpha}$ distributions are shown while the right hand panel only displays indices for polarised sources.

largely in agreement with previous spectropolarimetric surveys at similar wavelengths (e.g. O'Sullivan et al., 2015; Anderson et al., 2016). It should be noted that there seems to be "overpolarisation" measured for sources in DEEP2off suggesting contamination that is not seen in the other fields and thus uncorrected for in DEEP2off. The overpolarisation manifests as sources that are significantly more polarised than the 0.7% level of off-axis leakage (the upper limit on this level determined in DEEP2off is 5%). Overpolarisation can be seen in the DEEP2off panel of Figure 3.28. Excluding DEEP2off sources we find that the total polarisation detection rate does not alter save for a larger error of 9%. We thus exclude DEEP2off sources from further statistical analysis of the polarised and unpolarised ensemble. We do, however, report on some individual DEEP2off sources. DEEP6 may also display similar variation but we retain these sources as the variation does not seem as severe as in the DEEP2off case.

The power law fit approximates the total intensity well at low frequencies, especially in cases of bright polarised sources such as J0440-7946 (see Figure 3.23). The fit tends to be noisiest at higher frequencies as displayed in Figure 3.23 for spectra that have significant curvature. Depolarisation behaviour is observed in the q, u, and p spectra of sources such as J0440-7946, where it is evident that the polarisation degree decreases with λ^2 – along a very steep $\tilde{\alpha} \lesssim -3$ to ~ 5. J0440-7946 presents radio morphology akin to a resolved radio galaxy with discernible radio lobes, jets, and hot spots (see Figure 3.29). When looking at polarisation in this source, we find that $\langle p_0 \rangle = 2.1\%$ and $\langle p_0 \rangle = 5.4\%$ for two polarised components detected in DEEP3 – labelled as J0440-7947 and J0440-7946 in Table 3.3, respectively. The simple power law approximates the observed spectrum better in cases of negligible curvature where both the curved power law and simple power law are also most consistent. However, in cases faint total intensity ($\langle I \rangle \sim 1$ mJy) with negligible spectral curvature, the simple power law tends to deviate considerably from the more linear curved power law approximation and observed spectrum (Figure 3.32).

A small sub-sample of strong polarised sources is also detected in direct polarisation. These detections are J0352-8022 (where $\langle p_0 \rangle = 25.2\%$, $\tilde{T} = 10.2$, $T = 14.4$, and $I_{peak} = 9.2$ mJy/beam in DEEP2off), J0435-8057 (where $\langle p_0 \rangle = 28.0\%$, $\tilde{T} = 8.5$, $T = 3.2$, and $I_{peak} = 2.8$ mJy/beam in DEEP3), J0416-8115 (where $\langle p_0 \rangle = 50.7\%$, $\tilde{T} = 8.0$, $T = 5.4$, and $I_{peak} = 1.9$ mJy/beam in DEEP6), and J0345-8112 (where $\langle p_0 \rangle = 39.2\%$, $\tilde{T} = 7.7$, $T = 10.8$, and $I_{peak} = 2.5$ mJy/beam in DEEP6). These detections are dubious in some fields (especially DEEP2off with the noted overpolarisation), with the cases of J0435-8057 and J0416-8115 not even detected in RM synthesis in any of the fields. Half of these direct detections are located more than a degree from the field centre and follow an observed trend where the detection significance and also consistencies of fluxes in different fields decreases with increasing Δr. Another effect that produces inconsistencies between overlapping

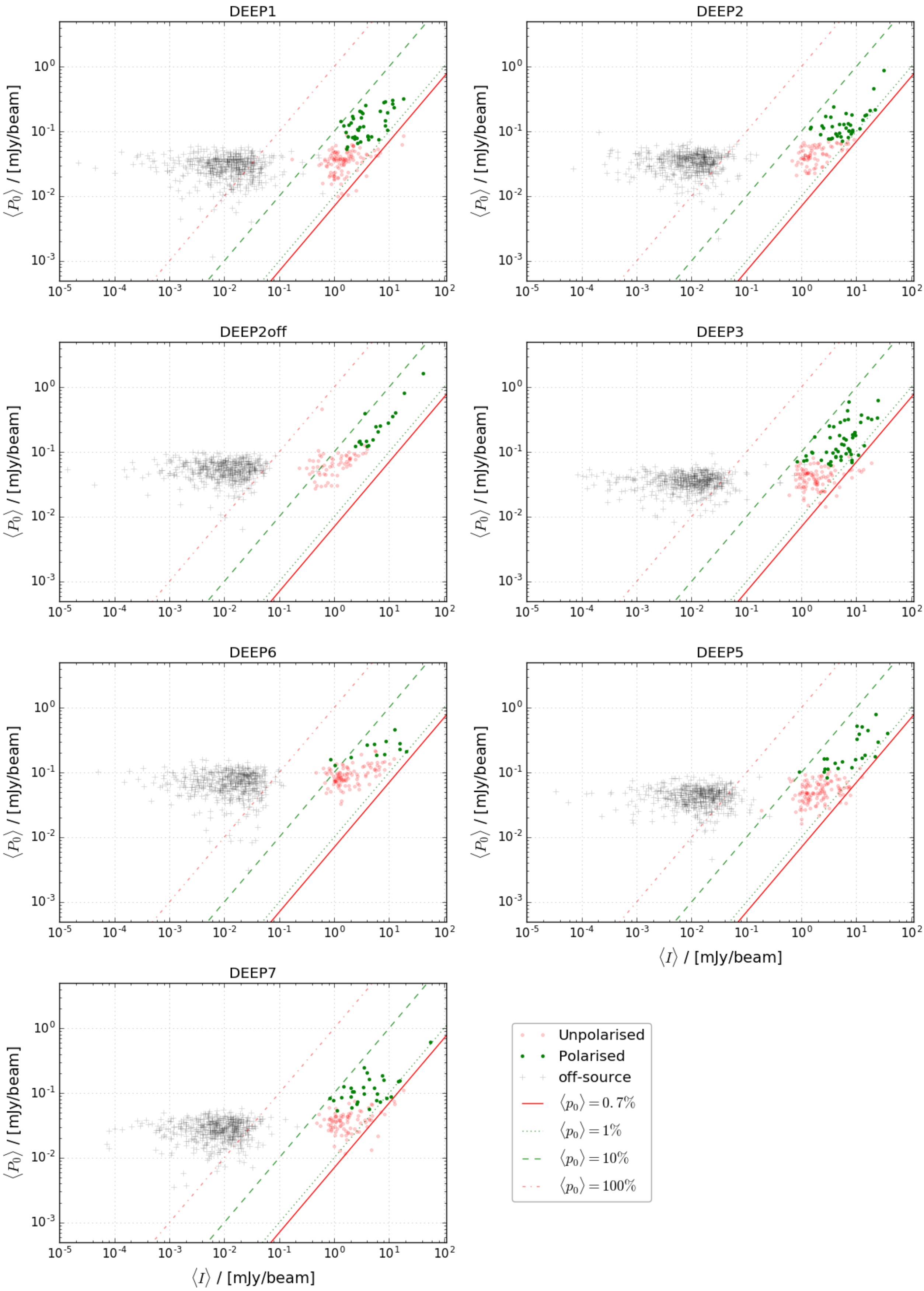

Figure 3.28: The distributions of band averaged polarisation intensity versus band averaged total intensity for unpolarised sources (red dots), off-source positions (grey pluses), and polarised sources (green dots). Diagonal lines show lower boundaries of 100% *(red dot-dashed),* 10% *(green dotted),* 1% *(green dotted), constant polarisation degrees. The* 0.7% *polarisation leakage upper limit is shown by the solid red line. DEEP2off sources display a level of "overpolarisation" that is not seen in the other fields – see main text.*

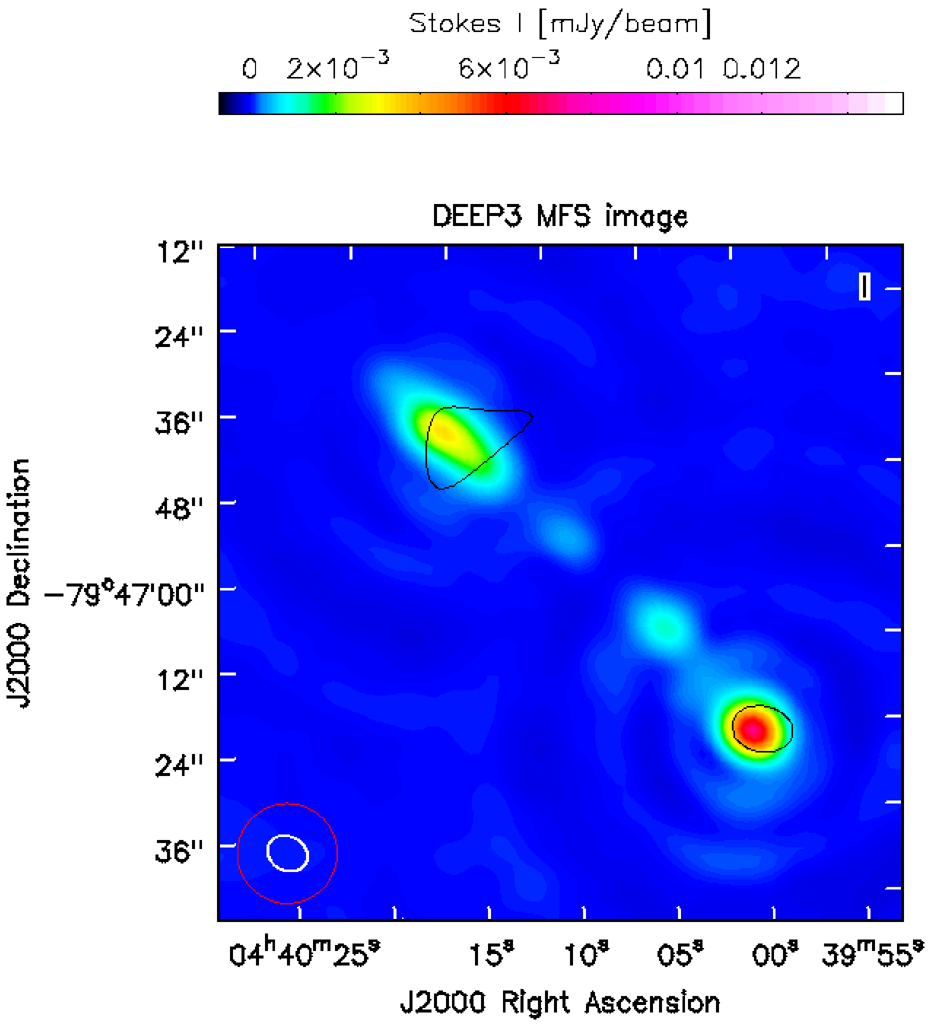

Figure 3.29: J0440-7946 in the DEEP3 source finding image. The colour map shows Stokes I intensity while the ellipses show the $14''$ *cube map beam (red) and the source finding image beam (white). The black contours show the band averaged polarisation intensity – the lowest contour is set at 10 micro-Jy/beam, with relative contour levels set at 0.2, 0.4, 0.6, 0.8.*

fields is primary beam asymmetry. The most dubious polarisation fractions derived for these sources are those corresponding to sub-mJy/beam Stokes I – owing to low signal to noise. This further displays primary beam effects where objects located farther from the pointing centre tend to have higher uncertainties owing to more pronounced primary beam effects at large Δr.

Figures 3.33 - 3.34 display distributions of $\langle p_0 \rangle$ for the low flux and the bright sub-samples. The mean $\langle p_0 \rangle$ in the bright sub-sample distribution is an order of magnitude lower than in the low flux sub-sample. The population of unpolarised sources (Table A.1) displays a sub-population with the highest polarisation degrees with accompanying large errors which make these measurements highly uncertain. The discrepancies observed between the two sub-samples may arise due to affects of the lower sample sizes in the bright sub-sample, which may have introduced some small number statistics bias, or perhaps due to a selection bias (Hales et al., 2013) or population differences of radio sources in different flux density bins (Tucci et al., 2002; Mesa et al., 2002; Taylor et al., 2007). The bright sub-sample may be composed of strongly bandwidth depolarised sources as compared to the low flux sub-sample or displaying the anti-correlation between luminosity and polarisation degree that has been observed in radio sources (e.g. Subrahmanyan et al., 2010; Banfield et al., 2011).

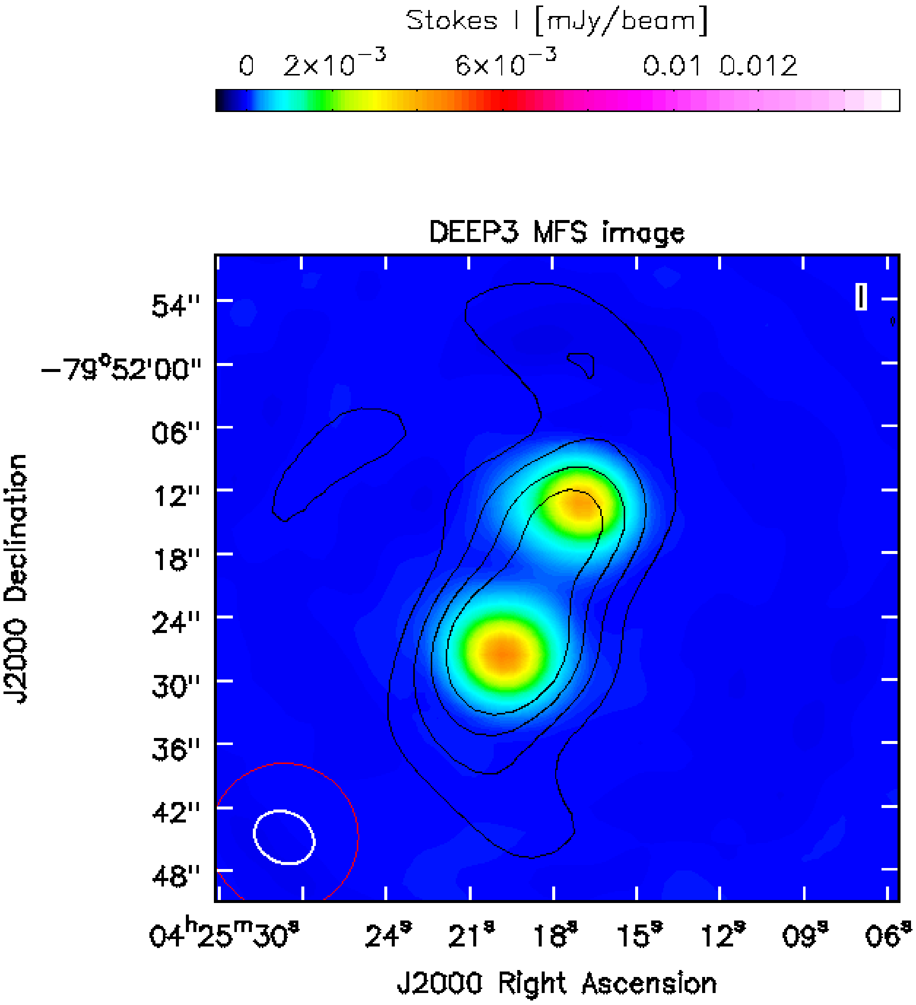

Figure 3.30: J0425-7952 in the DEEP3 source finding image. The plot arrangement is as in Figure 3.29.

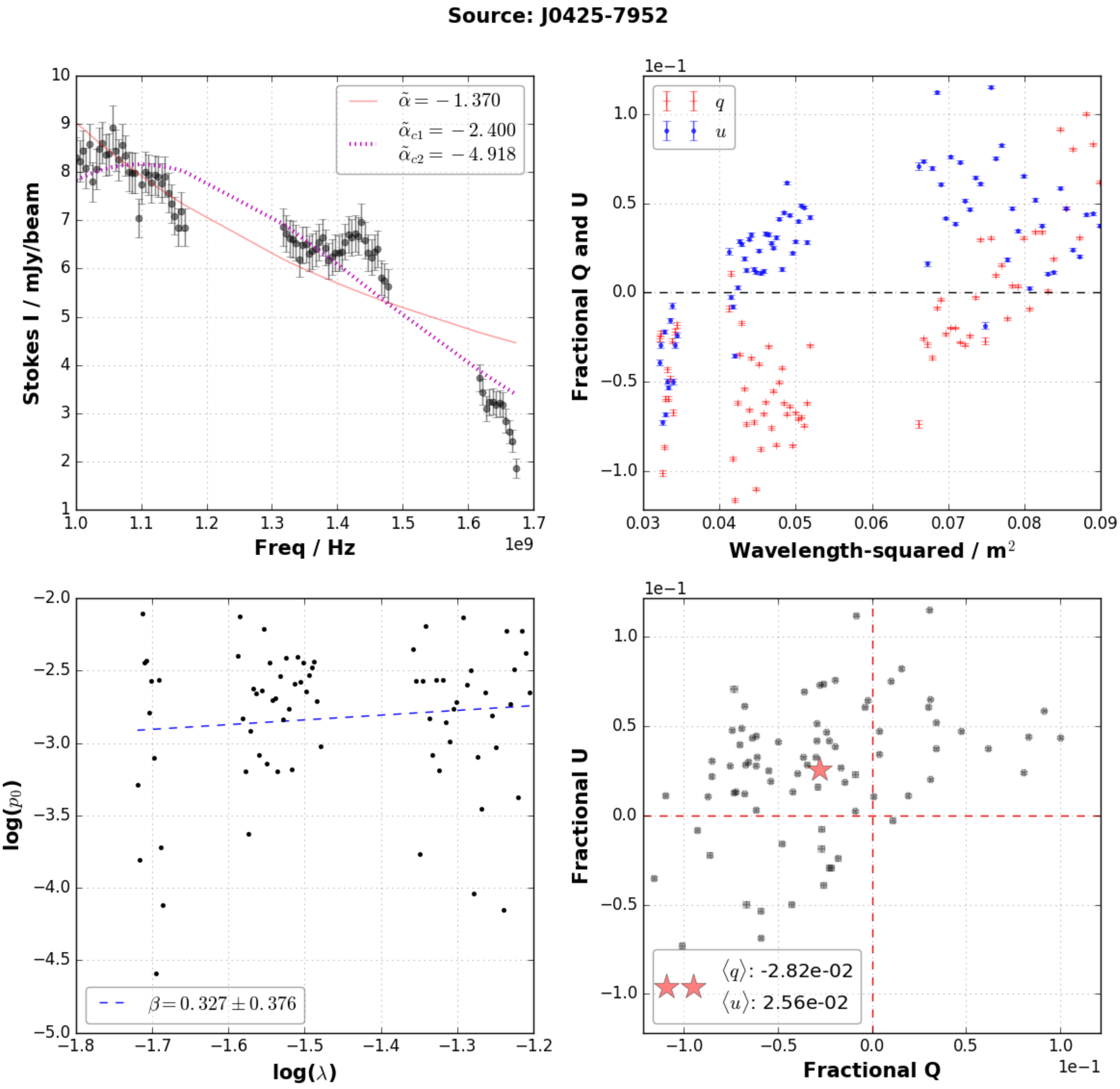

Figure 3.31: Spectra extracted for J0425-7952 from the DEEP3 field. The plots are arranged as in Figure 3.23. This source displays significant polarisation and repolarisation.

Figure 3.4 presents the locations of each field on the sky. We cross-match sources among all fields and display the spectral indices of cross-matches in Figure 3.35. This figure displays the indices $\tilde{\alpha}$ and β, and also fitted source finding ellipse areas, A_{fe}, for sources that are found in at least two fields – one of which being DEEP7 as it displays the largest sample of overlapping sources. These values are obtained by cross-matching all our sources in each field with those of each of the other fields. We declare a match for sources that are separated by no more than an arcsecond. The distributions show approximately consistent spectral steepness, especially when Δr_1 and Δr_2 are similar (top right panel), and similarly sized ellipses fitted to each source during source finding which indicates comparable source shapes. These properties are shown by points near the $y = x$ line in the panels that display this line. Primary beam effects are displayed again as variations in $\tilde{\alpha}$ are largest at large Δr between cross matched sources.

3.5.2.3 Bright unpolarised sources

We compare the 80th percentile of the unpolarised source distribution of signal-to-noise ratio, $\langle I \rangle / \langle \sigma_I \rangle$, to the polarised source population. We refer to this percentile of unpolarised sources as the *bright unpolarised* sub-sample. Figure 3.36 displays Distributions of $\tilde{\alpha}$ and fitted source ellipse area A_{fe} for both source types – *bright unpolarised* and polarised sources. The two sub-populations are consistent with with respect to $\tilde{\alpha}$. Bright unpolarised sources are also found to be largely unresolved and appear to span smaller on-sky areas than the polarised sources. Polarised sources tend to be largely unresolved but spanning a larger range of on sky sizes and also include a small sub-population of poorly resolved sources. The bright unpolarised sub-sample may be core dominated emission from unresolved radio sources.

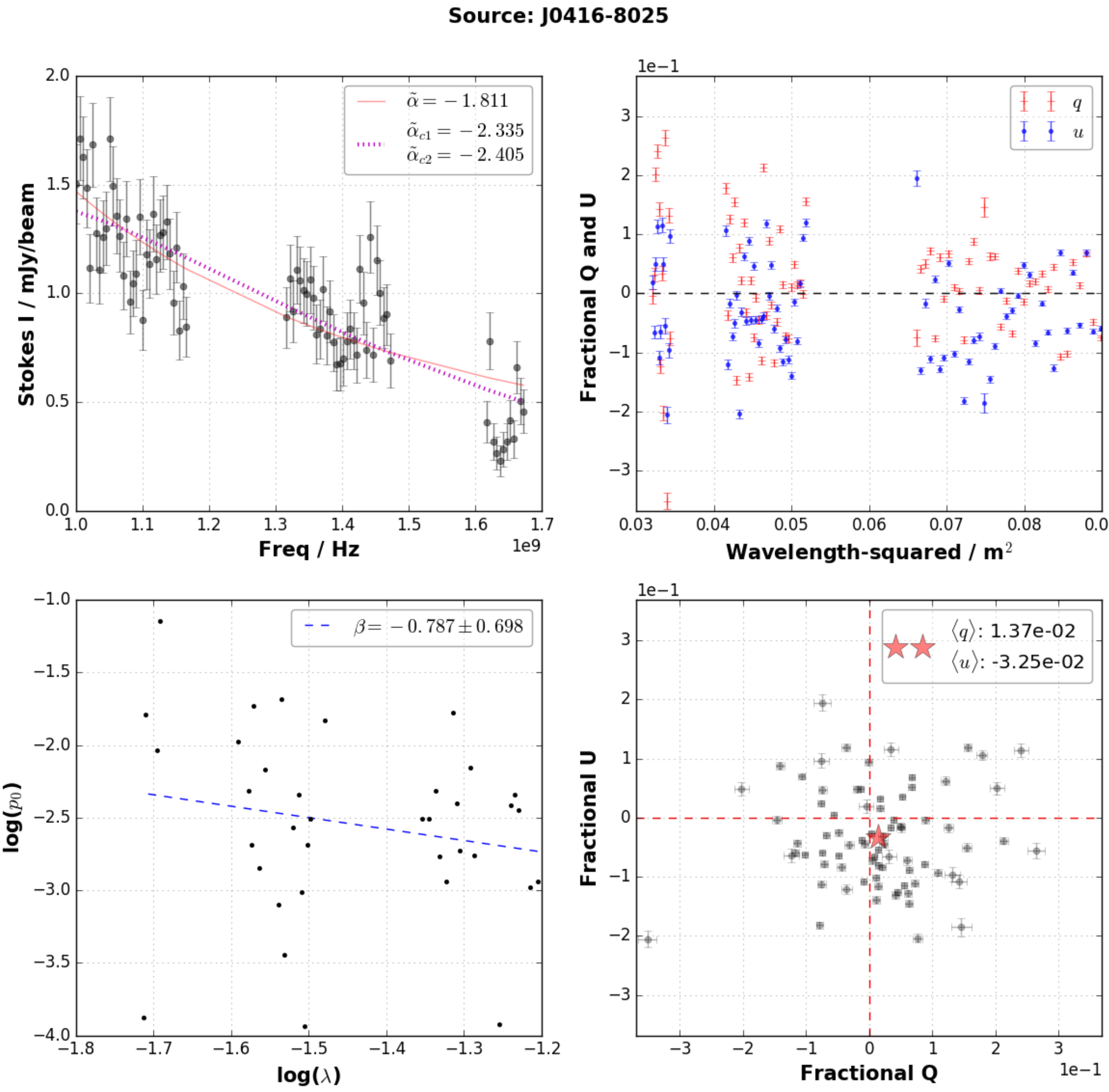

Figure 3.32: Spectra extracted for one of the lower flux (I_{max} < 10 mJy/beam) sub-sample objects, J0416-8025, from the DEEP2 field. The plots are arranged as in Figure 3.23. This source displays significant polarisation along with large scatter in q, u, and p.

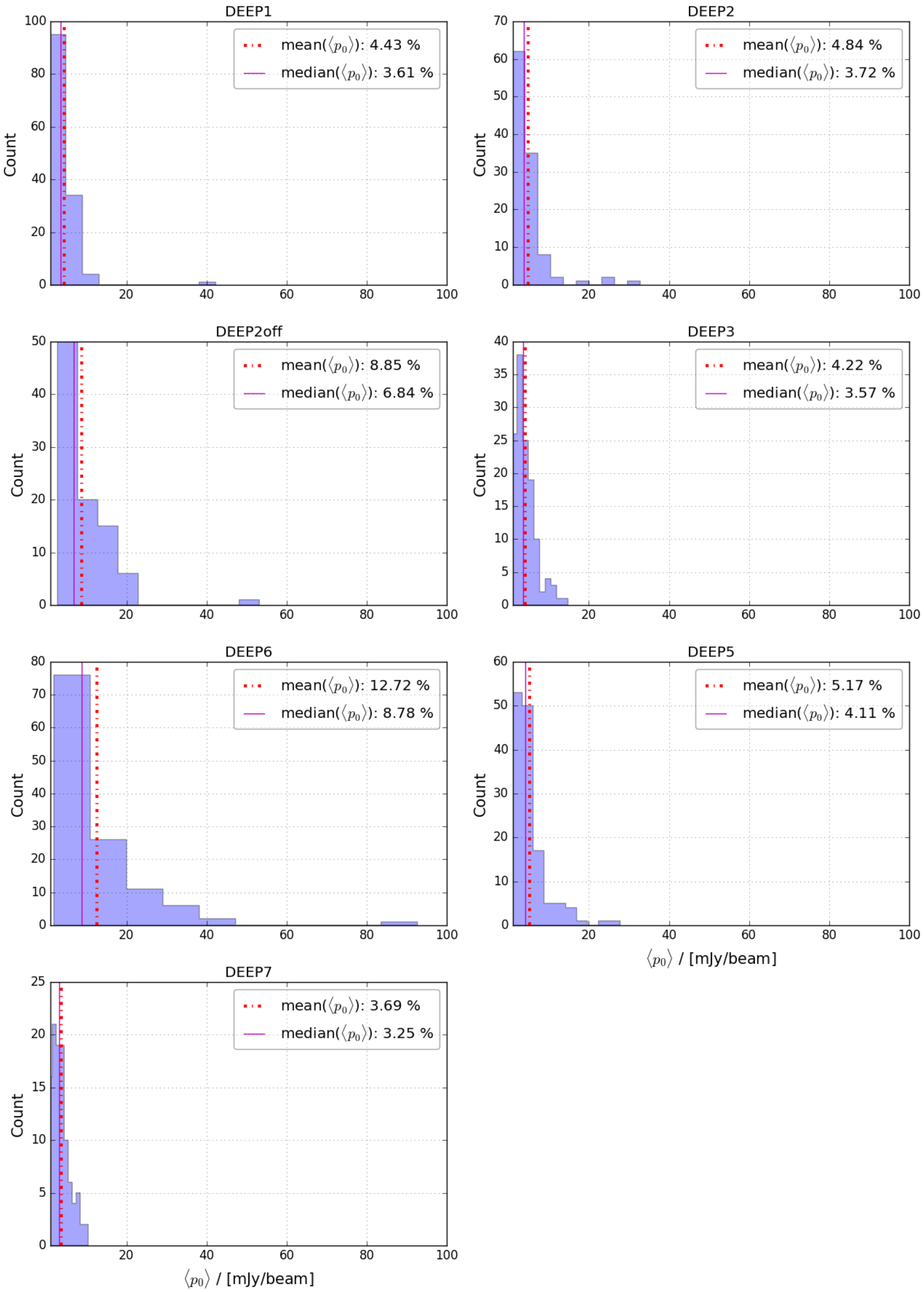

Figure 3.33: The distributions of band averaged polarisation degree ⟨p⟩ for the low flux sub-sample sources in all fields. The dot-dashed red and solid magenta lines indicate the mean and median values, respectively.

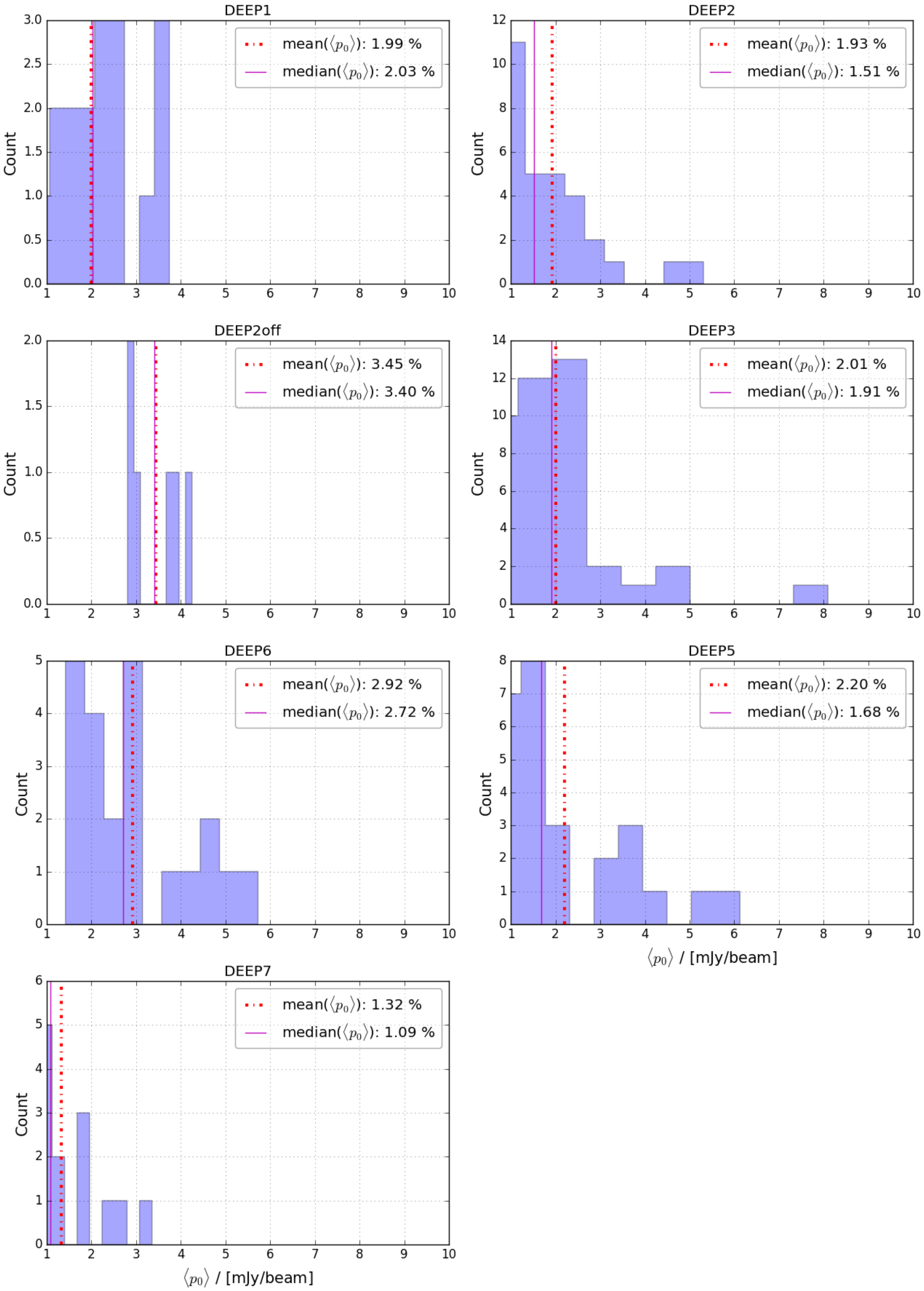

Figure 3.34: The distributions of $\langle p \rangle$, as in Figure 3.33, for the bright sub-sample.

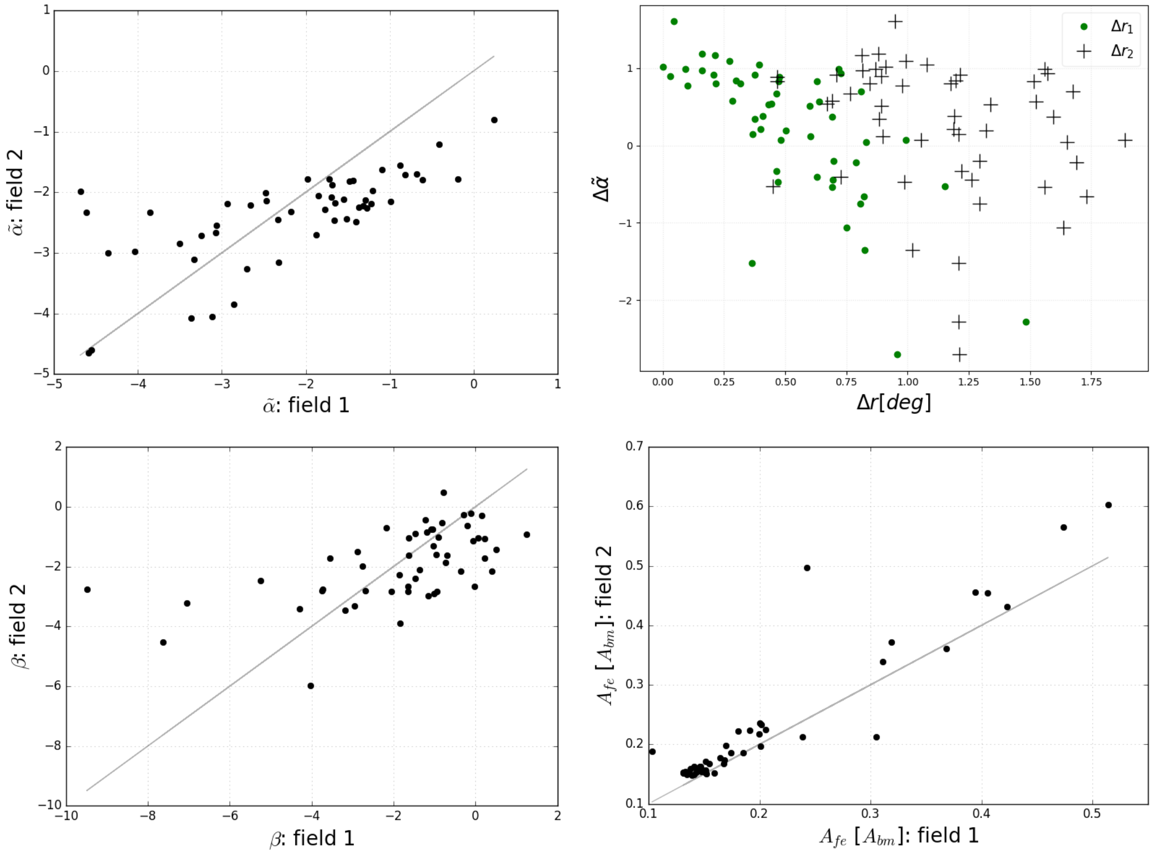

Figure 3.35: Top panels: $\tilde{\alpha}$ (top left) and (top right) the differences in $\tilde{\alpha}$ between cross matched sources, $\Delta\tilde{\alpha} = \tilde{\alpha}_1 - \tilde{\alpha}_2$, as a function of Δr for overlapping sources detected in DEEP7 and other fields. Bottom panel: β distributions (bottom left) and (bottom right) fitted source finding ellipse areas, A_{fe}, for the same sources as in the the top panels. The grey line indicates $y = x$.

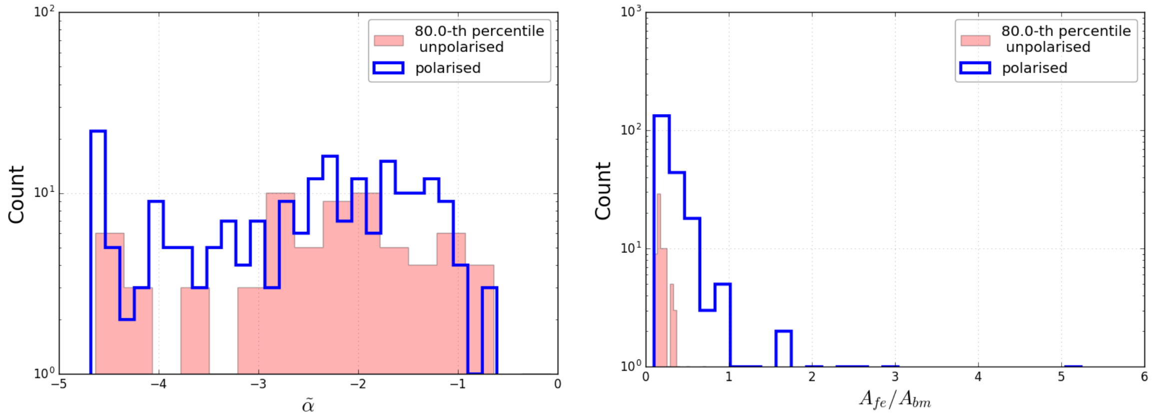

Figure 3.36: Distributions of $\tilde{\alpha}$ (left hand) and fitted source ellipse area A_{fe} (right hand). The filled histograms show the 80th percentile of the Stokes I SNR distribution of unpolarised sources while open histograms show distributions for polarised sources.

3.5.3 Summary of results

Following calibration and imaging of the observations, we perform source finding using the AEGEAN program which results in coordinates for lines of sight through the imaged radio sources. We extract Stokes Q, U, and I fluxes along the lines of sight identified. We have presented the total intensity and polarised broadband properties of our MeerKAT(16) milli-Jansky sample of radio sources. On-axis polarisation leakage is optimally minimised through calibration and an upper limit on the off-axis polarisation leakage was approximated. The off-axis polarisation leakage upper limits were determined with the use of observations of the unpolarised sources in the sample. The upper limit off-axis polarisation leakage was determined to be 0.7%, thereby placing great uncertainty in any polarisation measurement below this limit. Observations of the unpolarised primary and secondary calibrators (PKS1934-638 and J0252-704, respectively) proved useful in constraining relative on-axis leakages but due to their lack of polarisation signals, were not useful in providing polarisation angle solutions. The polarisation angle is therefore not calibrated as a polarised calibrator is required. Thus, the relative on-axis polarisation leakage was calibrated for during polarisation calibration.

Approximations of spectral steepness were attempted for each source using a simple power law fit to the measured total intensity spectrum. No primary beam corrections were applied and as such, approximations of spectral indices are convoluted with primary beam effects and thus we use the symbol $\tilde{\alpha}$ instead of the more conventional α. With that said, we did observe visual similarities between the observed intensities and the fitted power law as the power law was able to fit the measured spectra in most cases. $\tilde{\alpha}$ indicated a spectral shape that is consistent with synchrotron emission at $\nu \sim 1$ GHz. A small population of sources was found to have significant spectral curvature which was not well approximated by our simple power law fit. A curved power law was fitted which did offer an improved spectral fit. Sources such as these would most likely be modelled appropriately by a more complex curved or broken power law (e.g. Lacki, 2013; Chen, 2014; Farnes, 2014). These analyses are beyond the scope of this work.

We also performed a power law fit to the linear polarisation spectrum, $p(\lambda) \propto \lambda^{\beta}$. The polarised spectral index β is independent of primary beam effects and can thus indicate more conclusive spectral properties. We find that the large majority of sources display depolarisation behaviour ($\beta < 0$) with a small sub-population displaying repolarisation. The distributions of spectral indices suggest that the depolarisation is correlated with a steep total intensity spectrum. Which suggest that increased turbulence with age results in less ordered magnetic fields and thus diminished large scale fields.

We observed that 24±8% of our full sample from the radio quite DEEP field is detected in direct polarisation at $\sim 8\sigma_{p0}$. Unpolarised sources were observed to be a sub-population of brighter radio sources with peak total intensities displaying an order of magnitude difference between the brightest unpolarised sources and brightest polarised sources. The brightest unpolarised sources, however, do not differ in $\tilde{\alpha}$ significantly from polarised sources in this work which may suggest that these are similar sources which are below detection, and that bright unpolarised sources could also be a source population whose complex polarimetry is beyond detection given the constraints in this work. We have also found that sources found in multiple fields display consistent broadband spectral behaviour, with some scatter which we attribute to different lines of sight being sampled in each field as positions reported by our source finder for the same source in each field differed. This is a known issue with early MeerKAT observations where there is a rotational off-set due to incorrect timestamps. This produces differing source positions from observation to observation[12]. The lines of sight probed then, possibly sample slightly different portions of the same source especially in the case of spatially complex/resolved or partially resolved sources.

---

[12] MeerKAT technical background information available at `http://www.ska.ac.za/science-engineering/meerkat/observers/observing-programme/open-time/`

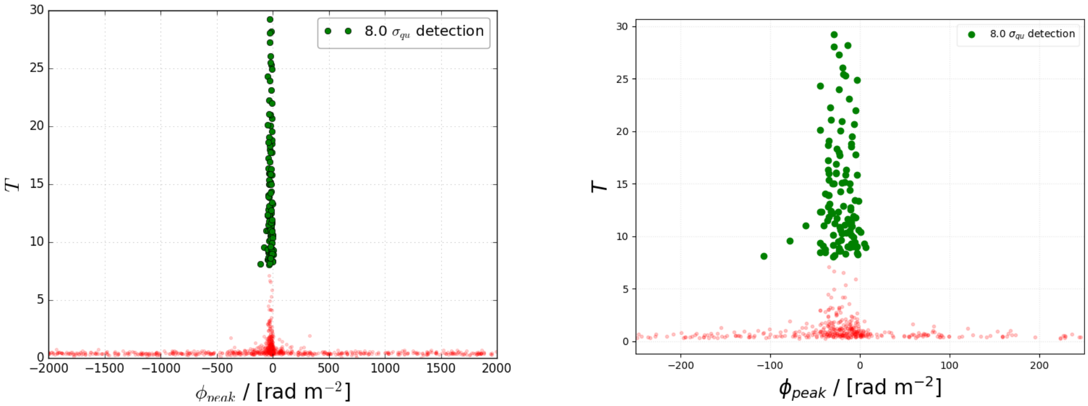

Figure 3.37: The distribution of direct detection signal to noise $\tilde{T} = \langle p_0 \rangle / \langle \sigma_{p_0} \rangle$*. The left panel shows the full range of* ϕ_{peak} *while right-hand panel zooms into the central range.*

3.6 Faraday spectral analysis

We present the results of Faraday synthesis on the DEEP fields in this section. We perform RM clean in the same manner as in Section 2.4 save for the way in which we determine the RM clean threshold. We set the threshold for significant Faraday components according to the SNR of Faraday spectrum peaks as defined in equation 3.2, with the threshold set to $T > T_o = 8$ at which the false detection probability falls to $< 10^{-4}$ (George et al., 2012). Figure 3.37 displays T as a function of ϕ_{peak} and it is evident that $T \gtrsim 4$ selects lines of sight with ϕ_{peak} values showing little scatter and well above the random distribution of ϕ_{peak} at lower significance. There may still be real emission components at lower significance but the false detection probability is also increased (e.g. Anderson et al., 2015). It is with Faraday components detected above T_o that we reconstruct the Faraday spectrum, $|F(\phi)|$, and determine the Faraday complexity of each source that is directly detected in polarisation. The Faraday peak $|F_p|$, ϕ_{peak} (Faraday depth at which $|F(\phi)| = |F_p|$), and the assigned Faraday complexity are tabulated in Table 3.3.

We determine Faraday complexity according to the second moment, σ_ϕ, of the RM clean model spectrum (Brown, 2011; Anderson et al., 2015)

$$\sigma_\phi = \frac{\sum_i (\phi_i - \mu_\phi)^2 |F(\phi_i)|}{\sum_i |F(\phi_i)|}, \tag{3.10}$$

with

$$\mu_\phi = \frac{\sum_i \phi_i |F(\phi_i)|}{\sum_i |F(\phi_i)|}, \tag{3.11}$$

The theoretical maximum scale/extent of a Faraday component in ϕ-space ($\phi_{\text{max-scale}}$, equation 1.24), largest detectable value of ϕ ($||\phi_{\text{max}}||$, equation 1.25), and resolution in ϕ-space ($\delta\phi$, equation 1.23) are approximately 101, 9430, and 12 rad m^{-2}, respectively. These values change negligibly from field to field due to slightly different λ-range sampling from field to field. These quantities were determined from the entire observed RF band, $\Delta\nu \approx 800$ MHz and channel width $\delta\nu = 5.02$ MHz. The channel width in λ^2-space, $\delta\lambda^2$ – equation 1.26, is calculated at the highest frequency of 1680 MHz and the band width, $\Delta\lambda^2$ – equation 1.27, is calculated at the lowest frequency of 880 MHz – where $\Delta\lambda^2$ is maximum. $\delta\lambda^2$, $\Delta\lambda^2$, and λ^2_{min} are $\approx 1.83 \times 10^{-4}$, 0.30, and 0.03 m^2, respectively. $\delta\phi$ is also the $FWHM$ of the RMTF (Figure 3.38) and we find that the average derived value from observations of all fields, $\delta\phi_{RMTF} = 51 \pm 10$ rad m^{-2}, is of order 4× the theoretical value. The discrepancy is due to the discontinuous sampling of wavelengths in the observed band, most severely due to the larger gaps in the λ^2 coverage owing to the removal of bad data during the calibration process.

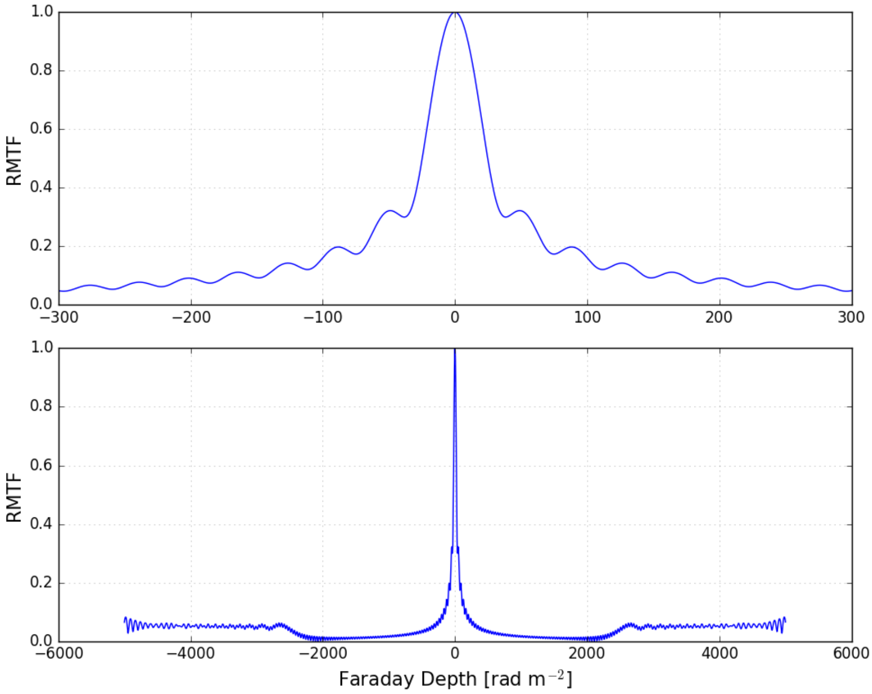

Figure 3.38: The RMTF (RMSF) of the DEEP field observations with MeerKAT(16) – zoomed into $\phi = \pm 300$ *rad m*$^{-2}$ *around the main peak (top) and also for the larger range of* $\phi = \pm 5000$ *rad m*$^{-2}$*. The average width of the peak is* 51 ± 10 *rad m*$^{-2}$ *with the first side lobes at* $\phi = \pm 49$ *rad m*$^{-2}$ *and peaks with* $RMTF = 0.3$*. The RMSF was calculated using the entire RF band, from 880 MHz to 1680 MHz, divided into 162 frequency channels.*

Our source catalogs of direct polarised detections (Table 3.3) and unpolarised sources (Table A.1) contain, for each source, the source name, RA (J2000), Dec (J2000), distance from field center (Δr), fitted source ellipse area (A_{fe}) in units of the 14″ smoothed common angular resolution area (A_{bm}), $\tilde{\alpha}$, curved power law spectral indices $\tilde{\alpha}_{c1}$ and $\tilde{\alpha}_{c2}$, the peak total intensity (I_{peak} in mJy/beam), band averaged σ_{qu} ($\langle\sigma_{qu}\rangle$), simple power law polarisation spectral index (β), band averaged polarisation degree $\langle p_0 \rangle$, DEEP field name in which the source is detected (DF), the peak of the reconstructed Faraday spectrum ($|F|_p \equiv |F(\phi_{peak})|$ for spectra made of Faraday emission components detected at $T > T_o$), the Faraday depth (ϕ_{peak} in rad m^{-2}) corresponding to $|F|_p$, the second moment of the RM clean model spectrum that is used for Faraday complexity classification (σ_ϕ also in rad m^{-2}) (Brown, 2011; Anderson et al., 2015)), signal-to-noise ratios T and $\tilde{T}$ used for indirect and direct polarisation detection, respectively. The last column contains the Faraday complexity classification (Fid – “c” for complex and “s” for simple. A dash is used for those cases where σ_ϕ was NaN or in the case of an undetected source where the Faraday spectrum was noise dominated). In the case of direct detections with no accompanying RM synthesis detections, we quote the ϕ_{peak} value of the Faraday spectrum reconstructed from emission components that are detected at a threshold of $T = 3$. Faraday properties are those of spectra reconstructed from $T > T_o$ ϕ-component detections. We define as “resolved” any source whose fitted ellipse is larger than the 14″ beam area and “unresolved” otherwise – thus sources with $A_{fe}/A_{bm} > 1$ ($A_{fe}/A_{bm} < 1$) are “resolved” (“unresolved”).

3.6.1 Faraday classification

Figure 3.40 displays σ_ϕ as a function of T for all direct polarisation detections. $\sigma_\phi \gg 1$ for complex Faraday spectra where $(\phi_i - \mu_\phi)^2$ is large, and σ_ϕ is small for simple spectra. We thus use unity as the division between the two types of Faraday spectra. The distribution of σ_ϕ supports this classification with three distinct populations of sources where $\sigma_\phi \lesssim 10^{-10}, \sim 0.01 - 0.1$, and $\gtrsim 100$ rad m^{-2}. Faraday complex sources make up the largest sub-population of polarised sources ($\sim 49\%$). We have observed that the probability of false detection increases as the RM clean threshold decreases and also do the false Faraday complex classifications (e.g George et al., 2012; Anderson et al., 2015). However, the Faraday complex sources we identify display the largest significance, T values, above the RM clean threshold where the probability of false detections is negligible and thus are most likely due to real complex Faraday structure. Faraday simple sources make up another significant sub-population of $\sim 39\%$ while polarised sources that are undetected in RM synthesis at T_o make up $\sim 12\%$. Figure 3.39 displays the fitted source finding ellipse distributions of the simple and complex classifications in units of A_{bm}. We observe that the two classifications are largely consistent with regard to source spatial resolution. The Faraday simple classifications with $\sigma_\phi \lesssim 10^{-10}$ rad m^{-2} tend to have several emission components at close proximity in Faraday depth with those that have only a single component found to have $\sigma_\phi = 0.0$ rad m^{-2}. The population of sources displaying $\sigma_\phi \sim 0.01 - 0.1$ rad m^{-2} are most likely complex sources whose complexity is beyond the capabilities of this dataset and thus classified as Faraday simple due to sensitivity bias (e.g Stil et al., 2014).

Our direct polarisation threshold excludes sources with ϕ_{peak} located at values of ϕ that do not represent real emission components (that is, emission significantly above the noise) along the line of sight – see Figure 3.37 where excluded ϕ are randomly distributed across the range of Faraday depths investigated. Detections become less reliable at lower significance levels where there are randomly distributed Faraday components as these are most likely due to noise peaks that are detected above the RM clean threshold (e.g. Anderson et al., 2015). The threshold also limits the detection of low signal to noise Faraday emission components located at very large ϕ_{peak}. We find that Faraday simple classifications are associated with $\phi_{peak} \pm 100$ rad m^{-2} with a lower variance and also less severe depolarisation as compared to complex classifications – Figure 3.41.

We find two main categories of Faraday spectra. One where the cleaned spectrum smoothly follows the trend in the data (see, for example, Figure 3.42) and another type where the cleaned spectrum displays complex broadband behaviour that manifests as “wiggles” superimposed on a larger scale trend that follows the measured data (example, Figure 3.43). The “wiggle” structure arises due to small amplitude ϕ-components and these are typical of complex spectra from bright polarised sources. Similar complex structure is also evident in Faraday thick components where ϕ_{peak} represents a significantly broad component, that is not consistent with a δ-function in Faraday depth space, with many smaller amplitude components. This can also be confirmed by inserting a small amplitude component into spectra that is devoid of such components and one can observe the wiggle structures emerge.

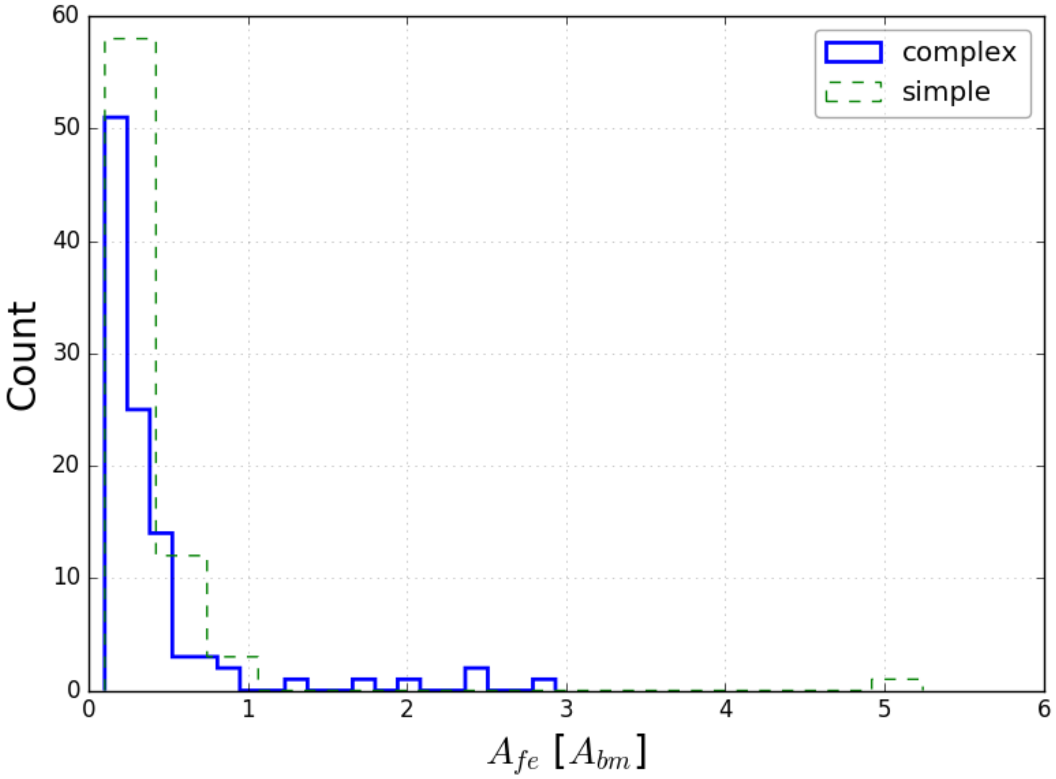

Figure 3.39: Fitted source finding ellipse distributions of the Faraday simple (dashed) and complex (solid) classifications.

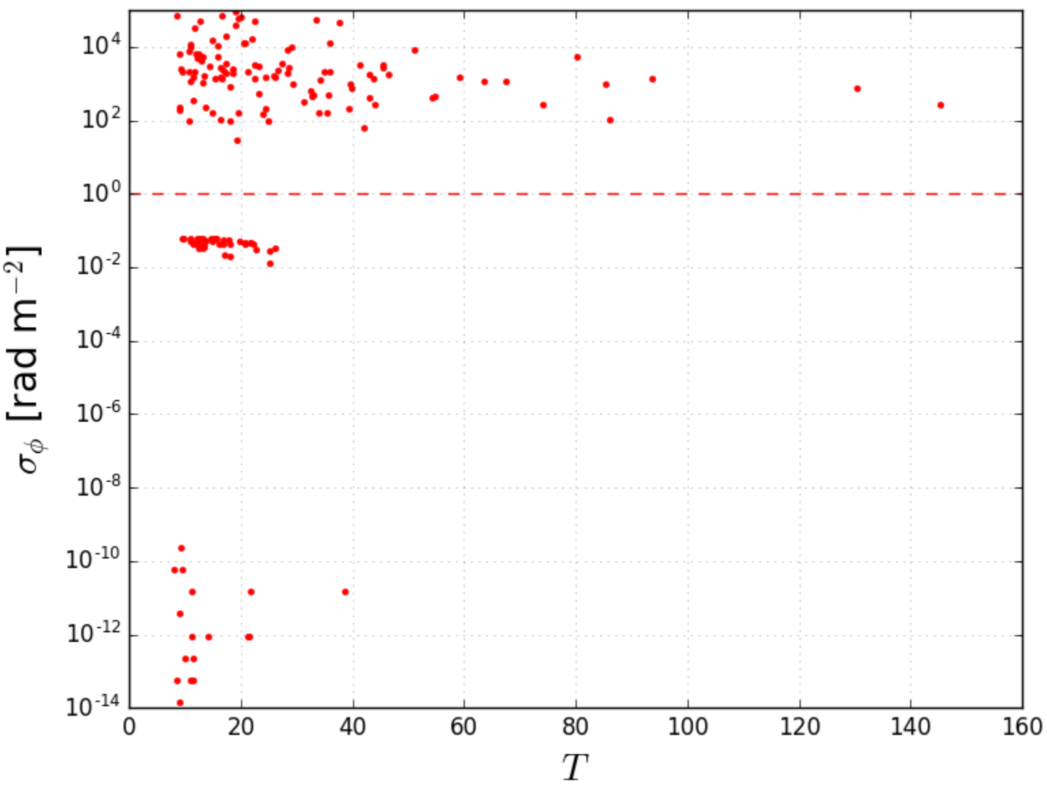

Figure 3.40: σ_ϕ as a function of T for all direct polarisation detections. The dashed line indicates $\sigma_\phi = 1$, separating Faraday simple from complex classifications at $\sigma_\phi \gg 1$.

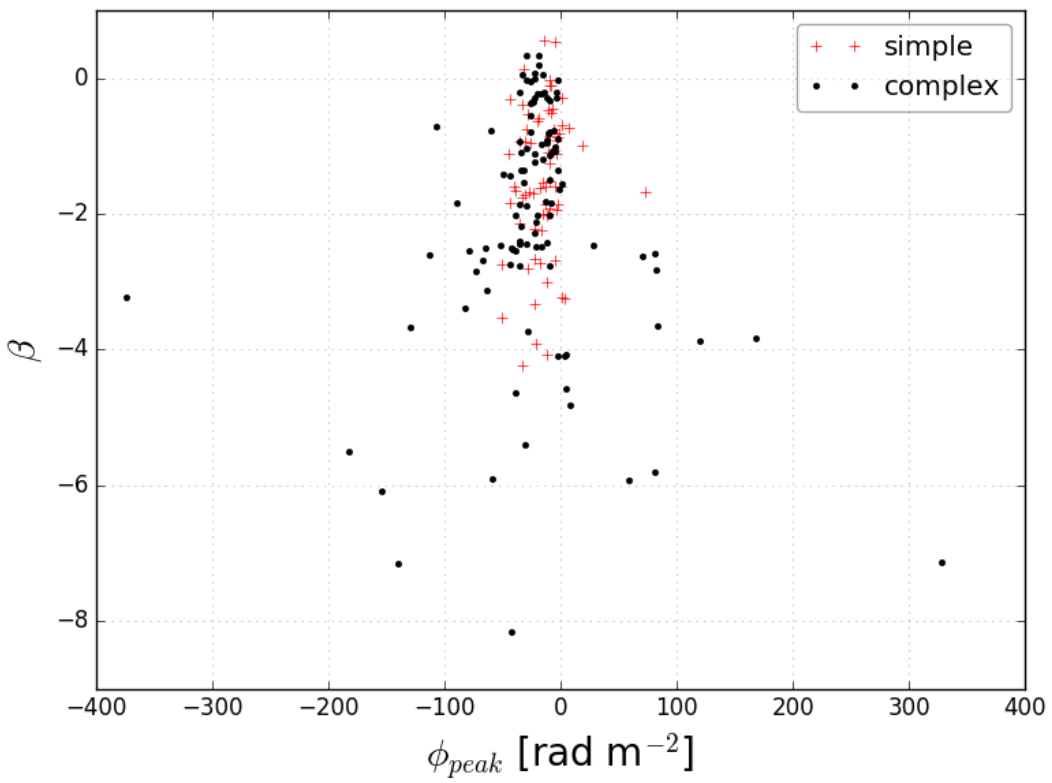

Figure 3.41: Polarisation spectral index β as a function of ϕpeak for all RM clean detections. Faraday complex (dots) and simple (crosses) classifications are indicated in the legend.

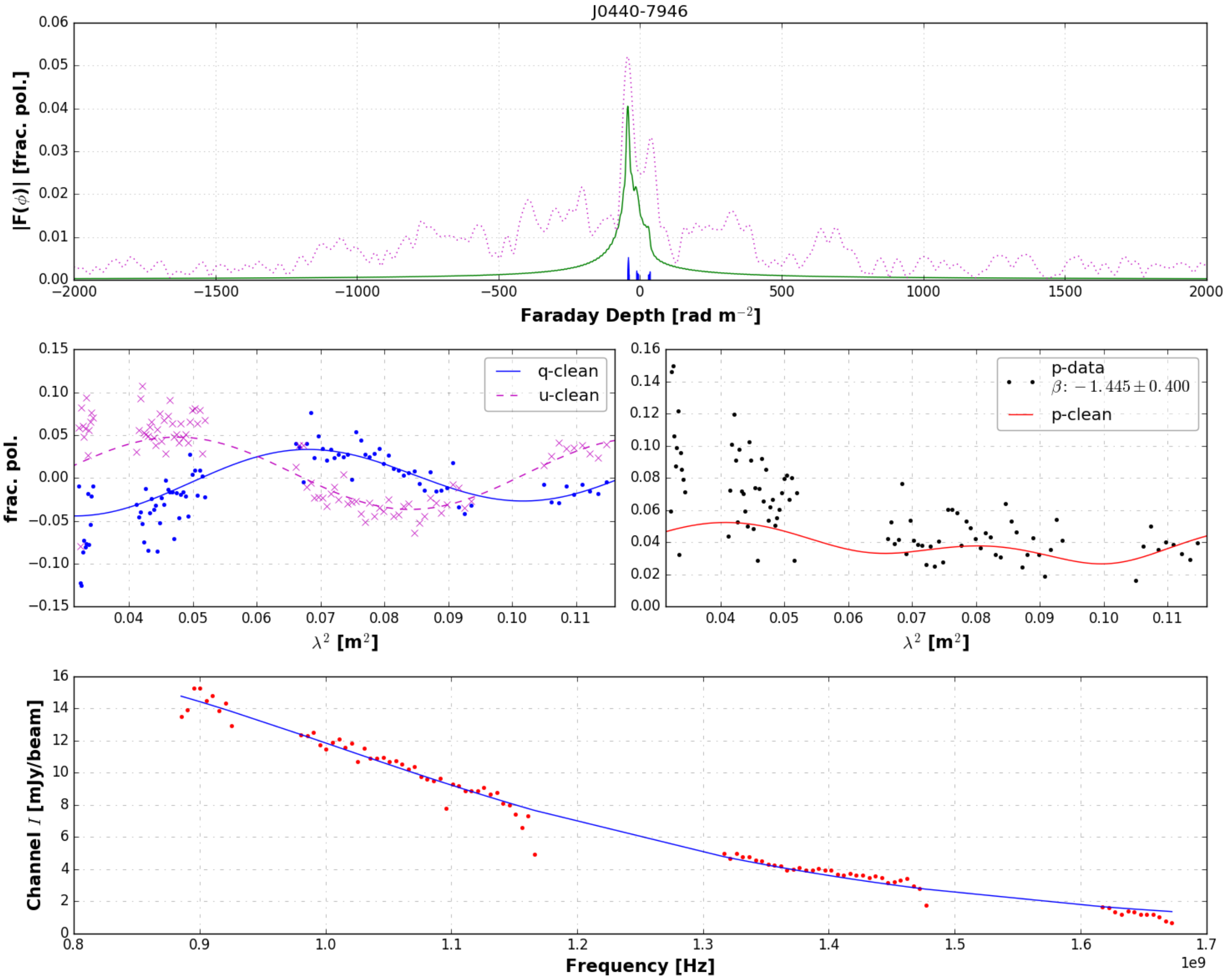

Figure 3.42: Polarisation spectra along with profiles resulting from our RM clean analysis of a relatively bright DEEP3 source, J0440-7946. This is an example of a Faraday complex classification. This source is a radio lobe, of a bright double lobed radio galaxy located at RA: 4h40m07.51s and Dec: -79d47m01.97s. Top panel: Faraday spectrum amplitude $|F(\phi)|$ *as a function of Faraday depth,* ϕ *both before RM clean (dotted curve) and after (solid curve) – the blue vertical lines indicate the* ϕ*-values of individual cleaned Faraday components (the height equals* $0.1 \times |F|_p$ *– 0.1 is the loop gain (Section 1.3.4)). Middle left: Reconstructed Stokes q (solid line) and u (dashed line) along with q and u data (points and crosses, respectively). Middle right: Reconstructed p (solid line) along with* $\langle p_0 \rangle$ *as a function of* λ^2*. Bottom row: Total intensity spectrum (dots) along with the fitted curved power law (solid line).*

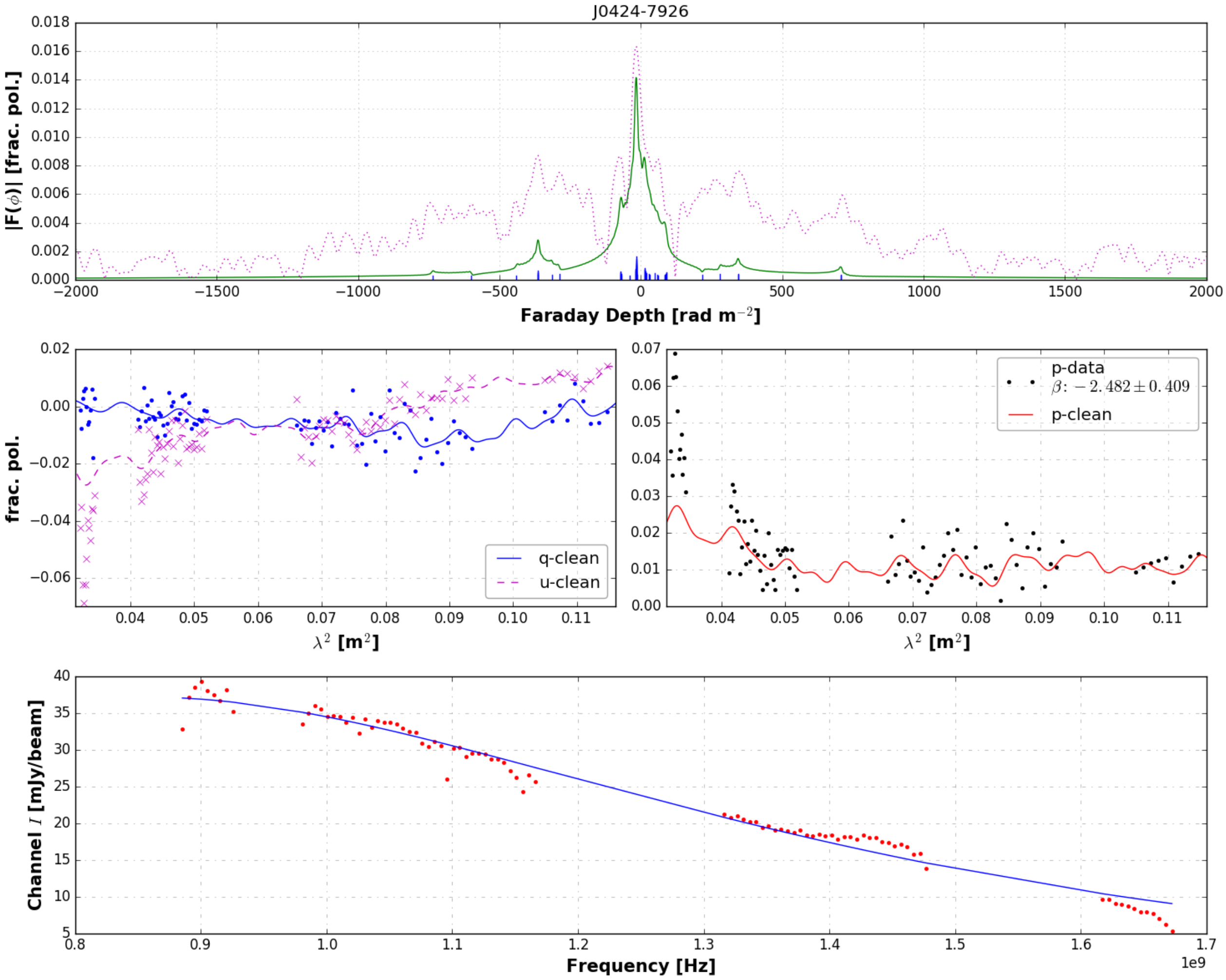

Figure 3.43: Polarisation and RM clean spectra for J0424-7926 as observed in the DEEP3 field. Plots are arranged as in Figure 3.42. This is classified as Faraday complex. This is an unresolved point-like.

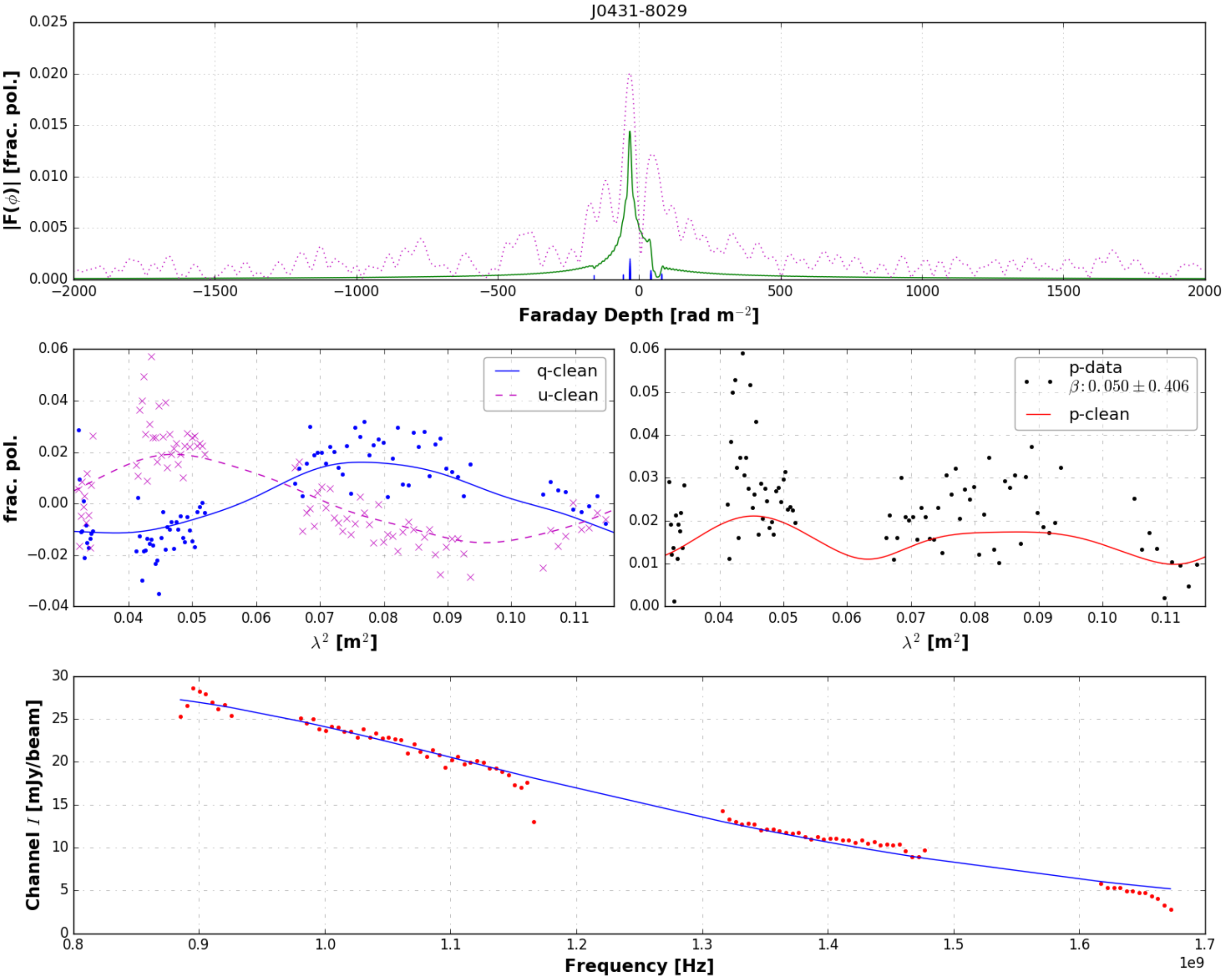

Figure 3.44: Polarisation and RM clean spectra for J0431-8029 as observed in the DEEP3 field. Plots are arranged as in Figure 3.42. This is classified as Faraday complex. This is an unresolved point-like.

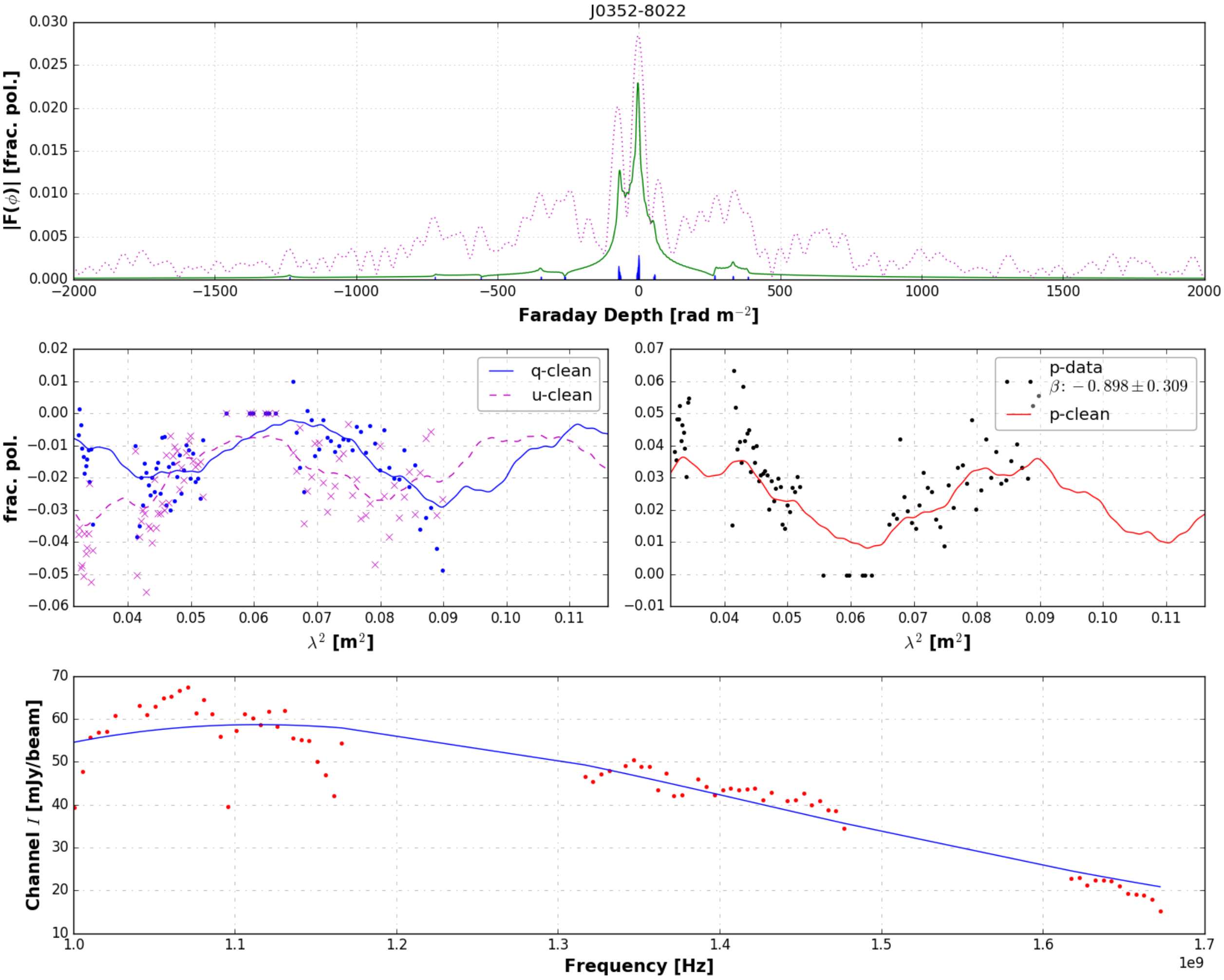

Figure 3.45: Polarisation and RM clean spectra for the compact unresolved component of J0352-8022 as observed in the DEEP2off field. Plots are arranged as in Figure 3.42. This is classified as Faraday complex.

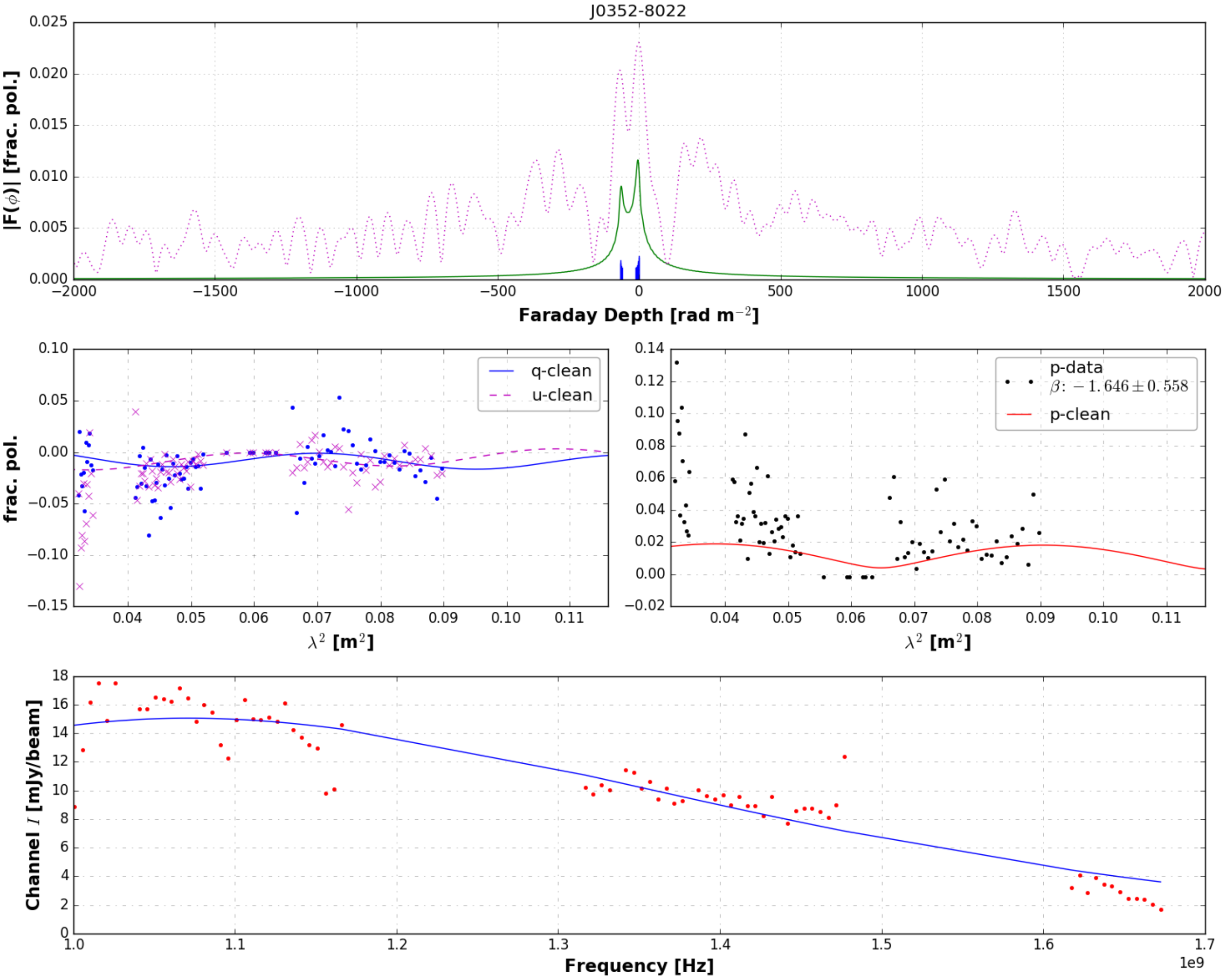

Figure 3.46: Polarisation and RM clean spectra for another component of J0352-8022 (the unresolved extended component in Figure 3.50 with RA = 58.197 and Dec = -80.378 degrees) as observed in the DEEP2off field. Plots are arranged as in Figure 3.42. This is classified as Faraday complex.

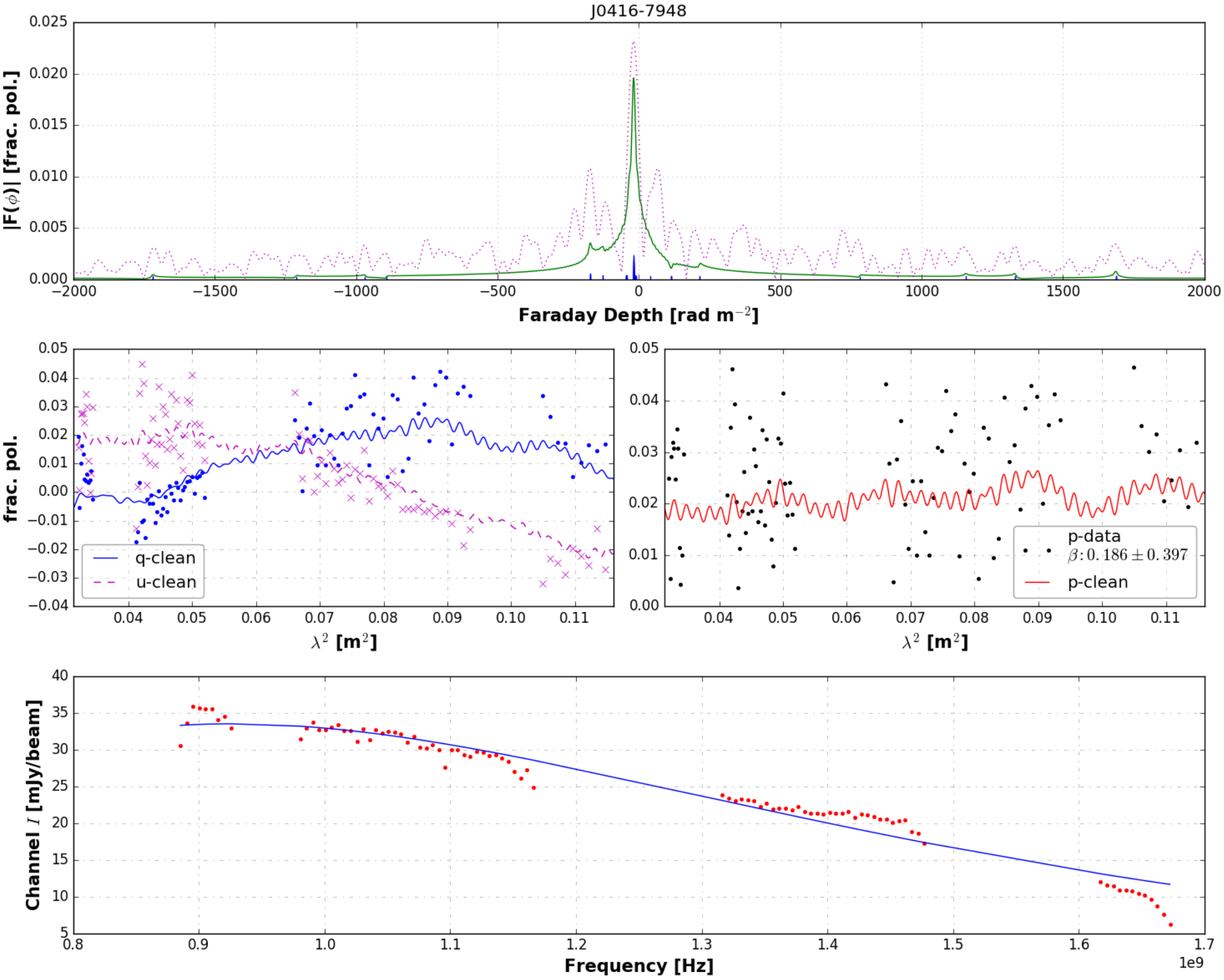

Figure 3.47: Polarisation and RM clean spectra of the Faraday complex source J0416-7948 as observed in the DEEP3 field. Plots are arranged as in Figure 3.42. This is an unresolved extended object with visual morphology suggestive of two radio lobes.

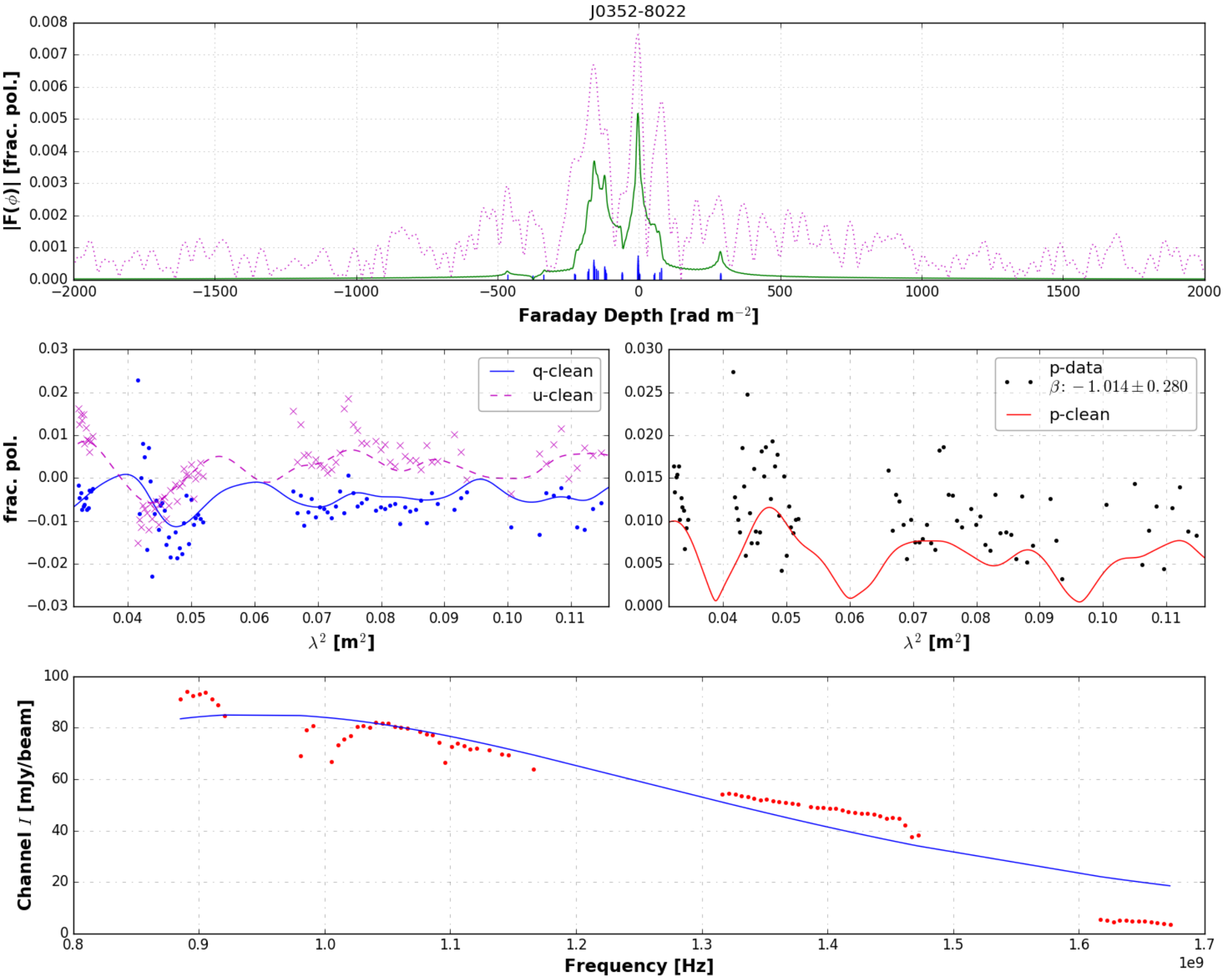

Figure 3.48: Polarisation and RM clean spectra for a Faraday complex component of J0352-8022 (the bright point-like component in Figure 3.50) as observed in the DEEP7 field. Plots are arranged as in Figure 3.42.

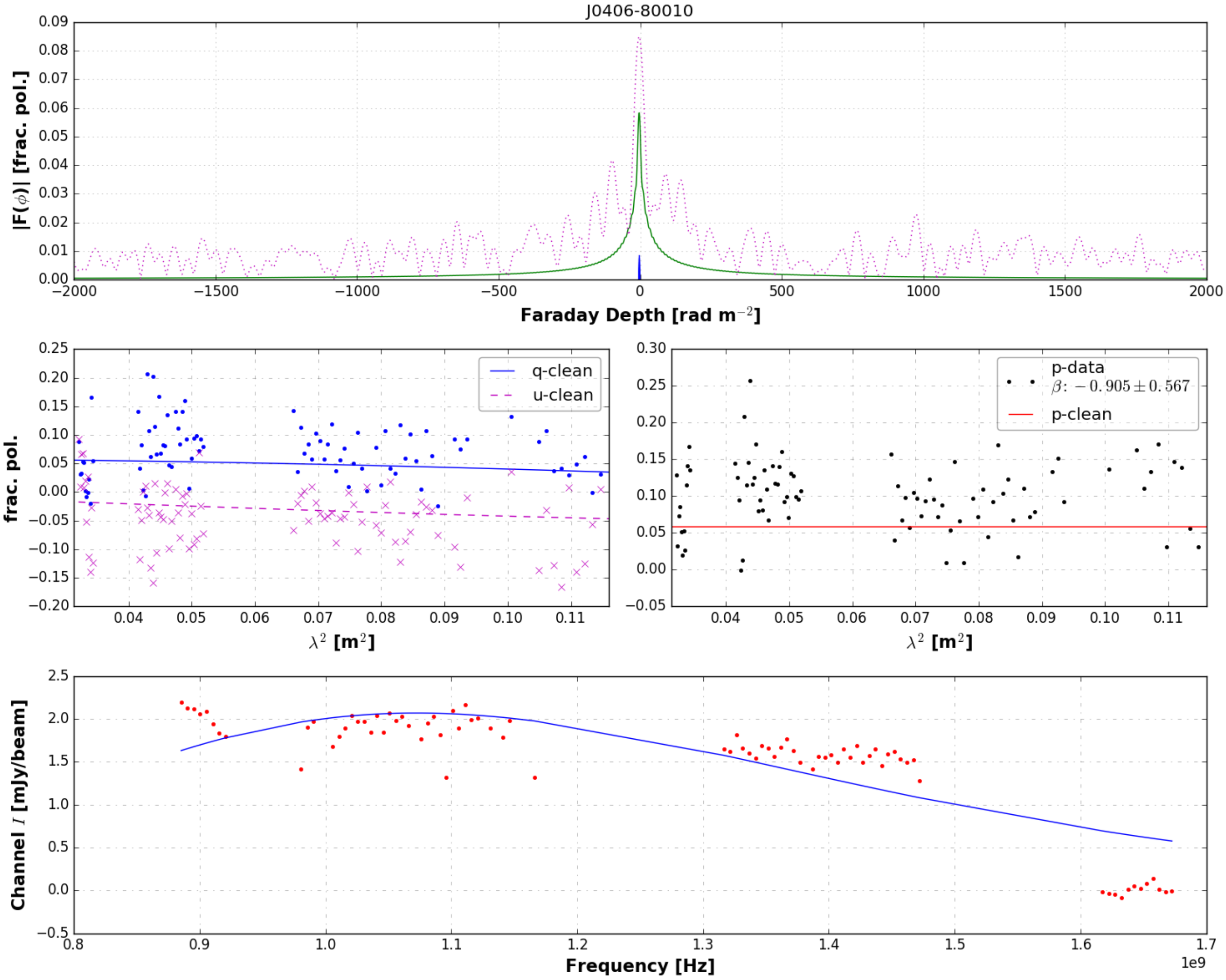

Figure 3.49: Polarisation and RM clean spectra for the Faraday simple source J0406-80010 as observed in the DEEP7 field. Plots are arranged as in Figure 3.42. This is point-like unresolved source.

Table 3.3: Catalog of polarised sources (direct detections – see main text). [**], [*], and [A_{bm}] indicate units of [mJy/beam], [rad m^{-2}], and 14″ beam area, respectively.

Source Name	RA [deg]	DEC [deg]	Δr [deg]	A_{fe} [A_{bm}]	$\tilde{\alpha}$	$\tilde{\alpha}_{c1}, \tilde{\alpha}_{c2}$	I_{peak} [**]	$\langle\sigma_{qu}\rangle$ [%]	β	$\langle p_0\rangle$ [%]	DF	$\|F\|_p$ [%]	ϕ_{peak} [*]	σ_ϕ [*]	T	$\tilde{T}$	Fid
J0400-79049	60.090	-79.817	0.963	0.30	-3.763	-3.565, -5.413	13.3	0.5	-4.10±0.48	2.3	1	–	-71.5±4.2	–	7.6	9.5	–
J0412-8110	63.046	-81.169	0.688	0.27	-2.614	-2.861, -6.982	15.1	0.2	-1.09±0.36	3.1	1	2.9	-34.5±1.2	1.3E+3	24.0	18.2	c
J0411-8028	62.776	-80.479	0.215	0.28	-1.219	-3.110, -4.454	3.5	0.4	-0.73±0.57	3.4	1	3.3	6.5±2.2	0.0	11.5	10.1	s
J0352-8022	58.189	-80.376	0.984	0.73	-4.063	-3.183, -7.419	10.6	0.5	-2.31±0.42	4.1	1	–	-139.0±2.6	–	6.8	11.2	–
J0437-8016	69.466	-80.274	0.929	0.54	-3.437	-3.145, -3.641	7.3	0.7	-3.34±0.50	4.1	1	–	1379.0±3.3	–	6.2	10.7	–
J0404-80048	61.181	-80.807	0.560	0.25	-2.017	-3.172, -6.484	7.8	0.2	-1.00±0.48	1.8	1	1.5	18.5±2.7	0.0	8.4	8.6	s
J0414-8041	63.611	-80.693	0.207	0.26	-1.210	-8.418, -8.252	4.3	0.3	-1.50±0.43	5.4	1	5.5	-9.5±1.1	1.6E+2	24.7	18.1	c
J0425-7952	66.335	-79.875	0.735	0.31	-2.468	-3.045, -1.648	4.5	0.7	-1.54±0.46	8.3	1	8.5	-32.5±1.7	1.3E+3	22.7	15.6	c
J0414-8041	63.618	-80.690	0.204	0.51	-1.260	-2.848, -4.763	4.8	0.3	-0.76±0.37	5.8	1	5.8	-6.5±1.0	4.1E+1	28.5	19.5	c
J0354-8023	58.517	-80.393	0.927	0.31	-3.773	-3.758, -6.130	12.2	0.4	-3.03±0.65	2.8	1	–	-1127.5±3.1	–	5.9	8.9	–
J0432-7944	68.027	-79.741	1.018	0.31	-4.233	-6.795, -7.035	8.5	0.9	-5.03±0.75	3.1	1	–	-1033.5±5.7	–	6.3	8.3	–
J0400-80037	60.093	-80.618	0.662	2.47	-1.972	-3.046, -5.598	3.1	0.6	-1.07±0.53	5.8	1	5.0	-7.0±2.3	5.5E-2	11.0	11.0	s
J0425-8015	66.261	-80.252	0.443	0.32	-1.708	-5.682, -6.539	6.1	0.4	-0.80±0.33	6.4	1	6.7	-26.5±1.3	3.8E+3	35.0	17.0	c
J0424-7939	66.006	-79.653	0.910	0.40	-3.684	-4.257, -5.205	8.8	0.5	-4.96±0.62	3.1	1	–	-860.5±3.4	–	6.3	8.9	–
J0435-8053	68.869	-80.888	0.868	0.28	-3.226	-7.530, -8.575	21.6	0.2	-2.68±0.60	1.5	1	1.0	-4.5±2.3	0.0	8.8	12.9	s
J0418-8032	64.722	-80.550	0.119	0.23	-1.101	-6.279, -6.488	3.9	0.3	-0.50±0.50	4.0	1	3.9	-8.5±1.7	4.9E-2	15.3	12.4	s
J0435-8057	68.872	-80.951	0.896	0.27	-3.504	-4.090, -4.678	50.1	0.1	-0.98±0.60	1.6	1	1.1	-16.5±1.7	2.0E+3	18.4	13.1	c
J0425-7952	66.324	-79.871	0.737	0.30	-2.294	-3.000, -5.989	4.0	0.6	-1.71±0.48	7.4	1	7.5	-30.5±1.7	6.2E-2	19.1	13.5	s
J0419-8030	64.794	-80.509	0.120	0.49	-0.831	-4.600, -5.285	2.0	0.7	-0.96±0.45	11.3	1	10.7	-11.5±1.4	5.7E+2	20.2	15.5	c
J0406-80018	61.643	-80.311	0.446	0.27	-1.849	-6.288, -6.370	11.5	0.1	-0.70±0.54	1.0	1	1.2	-107.0±2.8	2.1E+3	10.5	9.2	c
J0416-7948	64.199	-79.813	0.687	0.25	-2.279	-6.474, -5.573	22.7	0.1	-0.06±0.45	2.5	1	2.0	-26.5±1.1	1.3E+4	30.9	17.8	c
J0425-8013	66.265	-80.231	0.456	0.33	-1.703	-2.574, -6.242	13.1	0.2	-0.35±0.34	3.4	1	3.5	-23.5±1.2	3.4E+3	39.6	19.6	c
J0438-8016	69.699	-80.275	0.966	0.69	-3.692	-5.319, -5.773	6.3	0.9	-2.46±0.53	7.6	1	6.1	-52.5±2.4	3.2E+5	11.4	11.8	c
J0400-80037	60.098	-80.621	0.662	0.87	-2.197	-4.486, -5.466	2.9	0.7	-1.14±0.61	7.4	1	7.4	-10.0±2.0	2.0E+3	14.9	12.3	c
J0416-8025	64.069	-80.417	0.083	0.24	-1.151	-4.891, -5.819	2.5	0.4	-0.87±0.69	3.5	1	3.7	-3.0±2.6	5.7E-14	9.4	8.2	s
J04023-8107	65.797	-81.130	0.688	0.51	-2.493	-4.544, -4.896	6.2	0.4	-2.53±0.54	4.1	1	4.0	-41.5±2.2	6.7E+2	14.5	12.1	c
J0430-8036	67.741	-80.612	0.613	0.48	-2.245	-4.858, -5.098	18.5	0.1	-1.76±0.47	1.2	1	0.7	-33.0±1.7	0.0	9.2	13.2	s
J0431-8111	67.778	-81.189	0.907	0.43	-3.366	-5.165, -6.554	10.4	0.4	-2.79±0.57	2.5	1	–	65.5±3.0	–	6.5	9.0	–
J0412-8050	63.060	-80.846	0.382	0.25	-1.389	-4.571, -6.297	2.5	0.4	-1.30±0.67	3.6	1	–	1007.0±2.5	–	6.5	8.5	–
J04021-8002	65.484	-80.045	0.514	0.98	-1.717	-8.871, -8.472	3.4	0.6	-0.59±0.50	7.4	1	7.7	-18.5±1.6	6.0E-2	20.0	12.4	s
J0424-7938	66.028	-79.649	0.915	0.43	-3.551	-4.904, -6.285	5.7	0.7	-3.24±0.44	5.1	1	3.9	0.5±2.6	0.0	8.0	10.3	s
J0416-7948	64.205	-79.815	0.685	0.25	-2.397	-3.805, -5.351	19.2	0.1	-0.21±0.46	2.1	1	1.5	-35.5±1.2	7.1E+3	18.2	17.2	c
J0435-8045	68.951	-80.754	0.835	0.36	-2.975	-4.038, -3.866	6.4	0.6	-3.53±0.50	4.2	1	3.8	-51.0±2.8	6.2E-2	11.0	8.8	s
J04023-8108	65.810	-81.134	0.692	0.47	-2.457	-3.114, -6.839	17.6	0.2	-2.41±0.35	3.6	1	3.6	-35.5±1.2	3.2E+3	38.6	18.7	c

... Continued on next page

Table 3.3 – … *Continued from previous page*

Source Name	RA [deg]	DEC [deg]	Δr [deg]	A_{fe} [A_{bm}]	$\tilde{\alpha}$	$\tilde{\alpha}_{c1}, \tilde{\alpha}_{c2}$	I_{peak} [**]	$\langle\sigma_{qu}\rangle$ [%]	β	$\langle p_0\rangle$ [%]	DF	$\|F\|_p$ [%]	ϕ_{peak} [*]	σ_ϕ [*]	T	$\tilde{T}$	Fid
J0431-8029	67.939	-80.490	0.639	0.28	-2.349	-8.139, -7.744	25.4	0.1	-0.94±0.41	2.0	1	1.9	-35.5±1.1	4.6E+3	29.8	18.1	c
J0417-8012	64.260	-80.209	0.292	0.28	-1.129	-3.642, -5.311	3.3	0.4	-1.10±0.52	3.1	1	3.4	-11.0±2.5	9.1E-13	11.7	9.1	s
J0352-8022	58.210	-80.378	0.980	0.54	-3.908	-4.644, -5.207	5.6	1.0	-3.28±0.73	4.2	1	–	474.5±4.8	–	5.7	8.3	–
J04012-8109	63.048	-81.166	0.685	0.29	-2.511	-3.284, -5.989	17.7	0.2	-1.88±0.41	1.9	1	1.4	-30.0±1.6	1.9E+3	14.6	14.9	c
J0414-8041	63.602	-80.697	0.211	0.47	-1.294	-3.331, -5.673	4.6	0.4	-0.32±0.34	7.1	1	7.0	-9.0±1.0	7.2E+2	29.9	19.3	c
J0352-8022	58.154	-80.375	0.990	0.39	-4.034	-4.290, -5.357	34.8	0.2	-2.51±0.45	2.5	1	1.9	-64.5±2.0	1.9E+4	16.3	13.8	c
J0414-8041	63.608	-80.695	0.209	0.31	-1.227	-4.886, -4.813	4.4	0.4	-0.80±0.36	6.5	1	6.7	-9.5±1.1	1.1E+3	30.6	18.2	c
J0425-8013	66.263	-80.231	0.549	0.19	-2.480	-4.365, -3.515	11.2	0.2	-2.02±0.49	3.5	2	3.1	-20.0±1.2	2.7E+3	26.0	18.1	c
J0425-8015	66.259	-80.252	0.557	0.15	-2.465	-3.041, -3.049	4.2	0.4	-0.95±0.82	5.1	2	5.0	-25.5±1.7	5.7E-2	15.8	11.3	s
J0416-7948	64.202	-79.816	0.236	0.13	-1.507	-7.910, -6.035	27.9	0.1	-1.20±0.32	2.3	2	2.2	-16.0±0.8	1.7E+4	67.8	26.8	c
J0352-8022	58.152	-80.375	0.963	0.16	-4.679	-2.217, -5.223	36.6	0.4	-3.67±0.53	2.7	2	2.2	-129.0±2.9	1.4E+4	12.0	12.9	c
J0425-7952	66.332	-79.875	0.534	0.17	-2.259	-1.914, -3.608	6.5	0.4	-0.37±0.37	6.2	2	6.4	-26.5±1.2	5.9E+4	33.0	13.6	c
J04025-8008	66.391	-80.134	0.540	0.27	-2.317	-5.064, -3.434	9.4	0.2	-1.51±0.88	1.3	2	1.1	-9.0±2.5	0.0	8.4	9.7	s
J0421-7928	65.394	-79.483	0.632	0.31	-2.529	-1.635, -4.651	12.1	0.2	-2.61±0.62	1.5	2	1.3	-113.5±2.4	6.7E+3	12.5	10.4	c
J0406-80010	61.564	-80.182	0.359	0.11	-1.483	-2.737, -3.095	2.3	0.6	-0.47±0.64	7.8	2	7.5	-10.5±1.6	0.0	16.1	13.1	s
J0413-7925	63.428	-79.426	0.574	0.11	-2.136	-3.446, -3.010	13.1	0.1	-1.61±0.80	1.2	2	1.0	0.0±2.2	0.0	11.3	11.4	s
J0404-79056	61.052	-79.940	0.406	0.25	-2.036	-11.268, -11.567	7.8	0.2	-2.22±0.71	2.0	2	2.0	-23.0±2.3	3.6E-12	13.7	9.8	s
J0417-8012	64.258	-80.210	0.260	0.13	-0.990	55.465, 0.180	3.2	0.4	-0.03±0.69	4.2	2	4.6	-9.5±2.1	3.6E-12	15.2	10.1	s
J0414-8016	63.610	-80.268	0.272	0.10	-0.746	-12.670, 1.196	24.6	0.0	-0.21±0.34	1.0	2	1.0	-3.5±0.8	1.6E+2	33.9	25.0	c
J0359-7919	59.918	-79.320	0.918	0.13	-4.668	-3.341, -5.011	19.8	0.8	-4.58±0.53	3.8	2	3.1	4.0±4.1	6.9E+3	11.7	10.5	c
J0426-7949	66.693	-79.818	0.612	0.19	-2.653	-1.991, -3.553	7.2	0.3	-2.45±0.79	2.8	2	2.1	27.5±2.0	5.2E+2	11.2	10.1	c
J0408-79046	62.149	-79.780	0.306	0.11	-1.259	-1.785, -4.587	7.3	0.2	-1.12±0.56	1.6	2	1.5	-3.5±2.1	5.7E-14	12.1	9.8	s
J0431-8029	67.938	-80.490	0.917	0.16	-4.661	-8.407, -4.503	12.7	1.0	-4.09±0.72	4.3	2	3.8	-12.0±4.7	0.0	8.2	11.8	s
J0415-7959	63.784	-79.995	0.074	0.10	-1.952	-3.230, -3.520	17.9	0.1	-0.82±0.53	1.0	2	1.1	-1.5±1.7	0.0	17.7	12.8	s
J0424-7926	66.007	-79.436	0.736	0.28	-3.178	-2.705, -3.462	27.6	0.1	-2.59±0.35	1.3	2	0.8	81.5±1.6	1.2E+3	12.8	16.1	c
J0406-80018	61.594	-80.314	0.436	0.11	-2.089	-8.599, -5.319	5.9	0.2	-1.94±0.93	2.4	2	2.2	-4.0±2.1	0.0	11.0	10.9	s
J0418-7942	64.616	-79.712	0.363	0.17	-1.363	-2.145, -3.581	5.0	0.3	-1.39±0.78	2.3	2	–	-19.0±2.3	–	7.8	9.4	–
J0404-79027	61.130	-79.466	0.665	0.20	-3.230	-25.916, -26.598	5.3	0.6	-1.53±0.47	6.1	2	6.4	-15.0±2.1	0.0	19.4	11.0	s
J04021-8002	65.480	-80.045	0.370	0.45	-2.044	-3.375, -2.600	3.9	0.5	-2.48±0.53	5.7	2	4.9	-21.5±1.6	1.5E+3	15.9	13.4	c
J0359-8010	60.000	-80.173	0.604	0.10	-1.969	-2.169, -3.244	10.0	0.1	-1.85±0.61	1.4	2	1.2	-89.0±2.2	1.3E+3	11.4	9.6	c
J0404-79056	61.063	-79.939	0.405	0.11	-1.880	-2.586, -2.410	10.9	0.1	-1.60±0.60	1.6	2	1.6	-5.0±1.8	6.2E-2	16.9	12.4	s
J0416-7948	64.196	-79.813	0.237	0.12	-1.233	-7.963, -6.838	40.3	0.1	-0.20±0.36	2.8	2	2.8	-14.0±0.7	1.0E+5	129.4	23.4	c
J0402-7907	60.587	-79.119	1.014	0.13	-4.665	-2.975, -4.650	22.1	0.6	-1.56±0.64	3.4	2	2.9	1.5±3.8	4.4E+3	8.1	12.4	c
J0413-7946	63.414	-79.781	0.219	0.47	-1.423	-1.444, -6.106	2.5	0.7	-0.81±0.46	7.9	2	7.4	-11.0±1.8	2.7E+3	15.7	10.9	c
J0425-7952	66.321	-79.871	0.533	0.15	-2.091	-8.473, -5.767	5.6	0.4	-0.34±0.54	4.7	2	4.6	-24.5±1.6	1.4E+3	22.1	10.9	c
J0408-79046	62.158	-79.779	0.305	0.13	-1.299	-9.262, -6.404	6.2	0.2	-1.08±0.66	2.1	2	1.8	-5.5±1.9	0.0	11.8	11.1	s

… *Continued on next page*

Table 3.3 – … *Continued from previous page*

Source Name	RA [deg]	DEC [deg]	Δr [deg]	A_{fe} [A_{bm}]	$\tilde{\alpha}$	$\tilde{\alpha}_{c1}, \tilde{\alpha}_{c2}$	I_{peak} [**]	$\langle \sigma_{qu} \rangle$ [%]	β	$\langle p_0 \rangle$ [%]	DF	$\lvert F \rvert_p$ [%]	ϕ_{peak} [*]	σ_ϕ [*]	T	$\tilde{T}$	Fid
J0415-7912	63.867	-79.212	0.793	0.13	-4.211	-0.025, -4.094	13.4	0.3	-2.01±0.68	2.4	2	1.8	-15.0±2.2	0.0	9.1	12.3	s
J0421-7928	65.409	-79.483	0.633	0.17	-2.692	-3.236, -1.464	12.8	0.2	-1.26±0.49	2.0	2	1.9	-10.0±1.8	5.6E-2	17.0	14.3	s
J0359-7919	59.926	-79.321	0.917	0.16	-4.654	-4.504, -3.552	17.3	0.8	-4.82±0.56	3.4	2	3.2	8.5±5.0	4.4E+4	9.6	10.4	c
J0400-79049	60.087	-79.817	0.602	0.12	-2.373	-3.625, -3.288	28.2	0.1	-2.55±0.43	1.4	2	1.0	-78.5±1.5	3.0E+4	24.1	21.3	c
J0418-8019	64.510	-80.325	0.380	0.10	-1.077	-2.753, -3.195	16.4	0.1	0.55±0.55	1.1	2	1.1	-4.5±1.2	2.9E-2	22.7	17.6	s
J0423-7926	65.868	-79.447	0.711	0.16	-3.412	-30.171, -32.341	6.2	0.5	-3.02±0.67	4.1	2	3.8	-12.0±2.4	3.4E-2	12.9	9.6	s
J0352-8022	58.162	-80.376	0.962	0.93	-4.669	-13.766, -13.192	23.0	1.1	-5.51±0.76	3.6	2	4.0	-182.5±6.3	2.9E+2	9.3	10.2	c
J0421-7928	65.370	-79.482	0.629	0.17	-2.773	-5.351, -4.300	6.3	0.5	-2.44±0.60	4.4	2	4.0	-30.0±2.3	3.1E+4	18.2	11.7	c
J0424-7926	66.009	-79.438	0.735	5.24	-3.442	-3.351, -3.316	15.1	0.2	-3.66±0.55	1.5	2	1.3	83.0±3.2	7.1E+3	10.7	10.2	c
J0437-7925	69.426	-79.424	0.810	0.23	-4.047	-2.965, -3.727	10.9	0.4	-1.41±0.46	3.7	3	3.1	-49.5±2.1	2.0E+3	14.0	13.5	c
J0443-7950	70.846	-79.834	0.823	0.17	-4.634	-6.377, -5.328	5.7	1.3	-4.95±0.55	5.3	3	–	605.5±5.2	–	5.0	9.4	–
J0435-8057	68.864	-80.956	1.050	0.51	-4.651	-3.935, -3.749	2.8	5.8	-6.44±0.77	28.0	3	–	-38.5±4.2	–	3.2	8.5	–
J04033-8003	68.430	-80.052	0.383	0.45	-1.545	-3.538, -4.441	9.3	0.1	-0.40±0.52	1.5	3	1.7	-33.5±1.9	4.1E-2	16.7	10.9	s
J0435-8057	68.863	-80.953	1.047	0.43	-4.676	-3.843, -4.543	16.4	1.4	-4.73±0.59	4.6	3	–	-183.5±6.0	–	7.4	9.6	–
J0440-7947	70.002	-79.790	0.692	0.17	-3.652	-3.020, -5.337	20.1	0.1	-0.78±0.47	2.1	3	1.6	-60.5±1.5	5.4E+3	16.2	14.3	c
J0436-7918	69.028	-79.313	0.850	0.18	-4.563	-11.842, -12.011	12.6	0.4	-2.74±0.57	2.7	3	2.3	-50.5±3.3	1.5E-11	8.8	8.8	s
J0425-8013	66.262	-80.231	0.231	0.25	-1.665	-10.756, -10.030	17.4	0.1	0.33±0.38	3.1	3	3.0	-19.0±0.8	9.1E+3	53.0	26.4	c
J0432-7912	68.093	-79.209	0.859	0.20	-4.597	-5.518, -0.867	9.2	0.7	-4.23±0.48	4.4	3	4.9	-33.5±3.1	0.0	12.5	10.0	s
J0420-7927	65.196	-79.460	0.571	0.15	-1.737	-3.222, -3.753	11.1	0.1	-2.27±0.77	1.0	3	–	169.0±2.5	–	7.5	9.0	–
J0425-8014	66.258	-80.250	0.250	0.39	-1.499	-5.374, -4.748	5.7	0.3	-0.29±0.42	6.4	3	6.2	-22.0±1.0	1.8E+2	34.9	20.5	c
J0421-7928	65.372	-79.482	0.540	0.22	-2.513	-5.019, -4.767	7.1	0.2	-1.70±0.68	1.9	3	2.4	-24.0±2.7	0.0	13.1	9.5	s
J0426-7948	66.606	-79.813	0.198	0.26	-1.643	-2.501, -4.420	2.6	0.6	-0.74±0.61	6.5	3	6.4	-30.0±2.0	3.6E-12	14.5	10.5	s
J0421-7928	65.395	-79.482	0.539	0.37	-2.287	-3.169, -4.180	13.5	0.1	-0.94±0.51	1.9	3	2.0	-30.5±1.4	6.1E-2	22.5	15.5	s
J0430-8036	67.734	-80.613	0.662	0.18	-3.202	-2.818, -3.967	15.9	0.1	-1.69±0.51	1.3	3	0.9	73.0±2.4	0.0	8.6	10.8	s
J0434-7948	68.518	-79.804	0.445	0.29	-2.016	-10.277, -25.570	11.6	0.1	0.14±0.53	1.3	3	1.5	-32.0±1.9	0.0	15.6	12.0	s
J0413-7925	63.430	-79.426	0.763	0.16	-3.297	-4.263, -2.669	10.4	0.3	-3.13±0.57	2.1	3	1.5	-63.5±3.2	1.2E+3	8.9	8.9	c
J04033-8003	68.457	-80.056	0.388	1.69	-2.497	-2.956, -3.502	2.4	0.8	-1.85±0.79	6.7	3	6.6	-44.0±2.4	0.0	10.8	8.7	s
J0436-7940	69.052	-79.671	0.596	0.32	-3.026	-6.475, -5.099	3.2	0.7	-0.94±0.63	9.7	3	10.2	-35.0±1.6	5.6E-2	20.8	15.4	s
J0436-7940	69.102	-79.674	0.601	0.48	-3.006	-2.929, -0.622	2.9	0.7	-1.11±0.67	5.8	3	6.3	-44.5±2.4	1.5E-11	11.7	10.6	s
J0436-7959	69.240	-79.991	0.521	0.16	-2.332	-5.247, -6.220	5.0	0.4	-1.60±0.71	3.5	3	4.2	-40.0±2.2	1.5E-11	16.0	10.6	s
J0426-7949	66.694	-79.817	0.199	0.23	-1.363	-2.400, -4.918	12.1	0.1	-0.55±0.41	2.3	3	2.3	-26.0±1.1	5.7E+2	32.6	18.2	c
J0425-8015	66.258	-80.252	0.252	0.19	-1.652	-5.688, -4.632	7.4	0.2	-0.01±0.39	5.8	3	5.6	-23.0±0.7	7.1E+1	41.3	24.0	c
J0414-8041	63.614	-80.690	0.818	0.50	-4.508	-6.889, -2.714	3.0	1.8	-3.01±0.75	9.1	3	–	-13.5±4.1	–	5.0	8.4	–
J04021-8002	65.481	-80.045	0.139	0.85	-1.654	-2.632, -4.165	4.9	0.3	-1.12±0.53	5.0	3	4.9	-22.5±1.1	2.6E+2	23.7	19.2	c
J0424-7926	66.008	-79.436	0.566	0.34	-2.317	-28.312, -32.234	39.3	0.1	-2.48±0.41	1.7	3	1.6	-17.0±1.3	4.1E+4	53.4	25.0	c
J0429-7916	67.293	-79.281	0.744	0.26	-4.296	-2.805, -4.417	9.6	0.4	-2.73±0.67	3.0	3	2.8	-18.0±3.0	3.6E-12	9.8	9.6	s

… *Continued on next page*

Table 3.3 – ... *Continued from previous page*

Source Name	RA [deg]	DEC [deg]	Δr [deg]	A_{fe} [A_{bm}]	$\tilde{\alpha}$	$\tilde{\alpha}_{c1}, \tilde{\alpha}_{c2}$	I_{peak} [**]	$\langle \sigma_{qu} \rangle$ [%]	β	$\langle p_0 \rangle$ [%]	DF	$\lvert F \rvert_p$ [%]	ϕ_{peak} [*]	σ_ϕ [*]	T	$\tilde{T}$	Fid
J0431-8029	67.936	-80.490	0.568	0.18	-2.676	-2.277, -4.113	28.6	0.1	0.05±0.41	2.1	3	2.0	-33.0±0.9	1.9E+3	41.2	21.3	c
J0416-7948	64.196	-79.813	0.404	0.17	-1.772	-2.481, -4.159	35.9	0.1	0.19±0.40	2.5	3	2.3	-18.5±0.8	2.3E+5	83.4	21.3	c
J0424-7939	66.003	-79.653	0.350	0.25	-1.918	-2.693, -3.738	21.4	0.1	-4.07±0.55	1.3	3	1.2	5.0±2.1	2.1E+4	23.8	11.1	c
J0437-8016	69.468	-80.273	0.617	0.20	-2.799	-4.166, -4.355	11.3	0.2	-2.51±0.41	2.8	3	2.7	-43.0±1.6	2.6E+3	21.6	15.8	c
J0436-7940	69.063	-79.672	0.596	0.64	-3.020	-7.128, -6.591	2.3	0.9	-1.66±0.51	7.7	3	7.5	-39.0±2.3	1.5E-11	10.7	10.7	s
J0416-7916	64.232	-79.279	0.807	0.15	-3.956	-2.329, -4.539	6.7	0.5	-3.25±0.51	3.2	3	2.8	3.0±3.1	0.0	8.7	8.7	s
J04033-8003	68.434	-80.054	0.384	0.16	-1.639	-2.723, -4.258	11.5	0.1	-0.54±0.44	0.9	3	1.2	-28.0±2.4	0.0	14.8	8.7	s
J0421-7928	65.410	-79.482	0.538	0.21	-2.279	-2.691, -3.772	14.9	0.1	0.05±0.34	2.2	3	1.9	-15.0±1.1	1.6E+2	23.1	17.2	c
J0435-8057	68.868	-80.951	1.045	0.18	-4.666	-3.969, -3.540	35.3	0.9	-3.84±0.47	4.3	3	4.3	168.0±4.5	1.5E+4	12.5	13.3	c
J0438-8016	69.697	-80.275	0.653	0.49	-3.056	-2.941, -3.998	11.1	0.3	-0.30±0.45	5.3	3	5.2	-44.0±1.0	5.6E-2	37.1	17.8	s
J0437-7925	69.381	-79.420	0.807	0.26	-4.303	-2.946, -3.208	13.9	0.3	-1.67±0.63	3.1	3	2.0	-27.5±2.0	5.5E-2	10.2	13.0	s
J0443-7949	70.837	-79.833	0.822	0.16	-4.597	-4.240, -2.431	7.6	0.9	-5.02±0.54	4.2	3	–	-564.5±4.5	–	5.7	8.9	–
J0440-7946	70.064	-79.778	0.707	0.36	-3.743	-5.564, -4.119	15.3	0.2	-1.44±0.40	5.4	3	5.2	-44.0±0.8	6.7E+2	37.3	25.4	c
J0423-7926	65.868	-79.447	0.557	0.22	-2.242	-4.159, -4.243	7.2	0.2	-1.24±0.48	2.4	3	2.4	-22.5±1.9	1.5E+3	14.9	11.4	c
J0425-7952	66.332	-79.874	0.127	0.20	-1.508	-1.973, -6.487	10.3	0.3	-0.04±0.43	8.1	3	7.9	-29.0±0.7	1.8E+5	84.9	26.7	c
J0424-7938	66.025	-79.649	0.353	0.29	-1.699	-2.335, -6.977	15.8	0.1	-0.85±0.51	0.9	3	0.8	-10.0±2.0	0.0	13.0	9.9	s
J0415-7912	63.869	-79.212	0.897	0.17	-4.624	-2.410, -4.425	10.6	0.7	-3.21±0.68	2.8	3	–	-1105.5±5.3	–	5.8	9.7	–
J0425-7914	66.264	-79.240	0.760	0.16	-2.668	-2.496, -4.440	12.6	0.2	-2.69±0.60	1.8	3	1.3	-67.5±2.3	5.8E+4	12.3	11.3	c
J0425-7952	66.321	-79.870	0.130	0.19	-1.370	-2.861, -5.835	9.0	0.2	0.33±0.38	6.4	3	6.2	-29.0±0.7	1.4E+3	62.8	25.6	c
J0418-7942	64.616	-79.712	0.406	0.22	-1.660	-3.269, -2.794	4.8	0.2	-1.31±0.71	1.7	3	–	-16.0±2.7	–	7.1	8.4	–
J0435-8053	68.866	-80.888	0.989	0.18	-4.670	-2.578, -4.181	16.0	1.0	-4.85±0.66	4.1	3	–	70.5±4.8	–	6.0	11.9	–
J04021-8002	65.470	-80.043	0.140	0.14	-1.380	-5.747, -7.075	4.4	0.3	0.08±0.42	7.9	3	8.0	-23.0±0.9	7.6E+1	38.5	22.0	c
J04031-7903	67.781	-79.051	0.990	0.33	-4.667	-2.486, -4.433	23.5	0.9	-4.09±0.51	3.8	3	3.1	3.5±4.6	9.7E+4	10.4	12.2	c
J0437-8016	69.457	-80.274	0.615	0.21	-2.654	-2.686, -4.659	11.8	0.2	-2.75±0.55	2.1	3	2.2	-44.0±1.7	2.7E+3	19.8	14.4	c
J0416-7948	64.203	-79.815	0.402	0.17	-1.993	-9.181, -8.259	28.6	0.1	-0.23±0.39	1.7	3	1.6	-20.5±0.9	5.3E+4	42.0	20.2	c
J0414-8041	63.621	-80.690	0.602	0.45	-1.400	-2.370, -2.500	4.6	0.6	-2.02±0.62	5.8	5	6.6	-12.0±2.0	0.0	21.1	12.6	s
J04018-8108	64.733	-81.134	0.739	0.44	-0.994	-2.072, -3.198	7.5	0.3	-2.15±0.56	2.8	5	3.0	-36.0±2.0	4.9E-2	19.4	12.1	s
J0431-8029	67.943	-80.490	0.136	0.21	-3.582	-1.696, -2.519	17.9	0.4	-4.63±0.66	2.5	5	2.0	-39.5±3.4	7.7E+3	11.2	11.7	c
J0435-8057	68.875	-80.951	0.532	0.17	-3.047	-5.074, -3.958	70.5	0.1	-1.36±0.56	1.4	5	1.0	-3.0±1.7	4.0E+4	27.0	18.7	c
J04012-8109	63.051	-81.166	0.929	0.20	-1.167	-4.359, -3.898	29.7	0.1	-2.44±0.56	0.8	5	0.8	-35.0±1.7	1.0E+3	20.2	13.9	c
J0435-8126	68.823	-81.440	0.977	0.27	-3.833	-5.237, -5.456	22.9	0.4	-2.01±0.51	5.9	5	5.9	-38.5±1.4	6.3E+2	35.7	16.0	c
J0410-8153	62.645	-81.893	1.551	0.32	-4.468	-1.949, -2.811	27.8	0.9	-6.09±0.60	4.0	5	3.8	-154.5±4.3	2.8E+5	16.4	11.5	c
J0435-8126	68.796	-81.442	0.978	0.30	-4.010	-3.656, -2.295	24.1	0.4	-2.54±0.62	4.4	5	3.8	-39.0±2.1	1.2E+5	22.1	17.5	c
J0435-8053	68.872	-80.888	0.481	0.17	-3.043	-1.589, -6.842	26.4	0.2	-3.39±0.38	1.9	5	1.1	-83.0±2.1	1.0E+4	12.5	16.5	c
J0425-8013	66.269	-80.231	0.304	0.27	-4.135	-7.699, -6.299	6.2	1.8	-5.23±0.66	7.1	5	–	-1879.0±5.2	–	5.6	9.2	–
J0435-8045	68.955	-80.754	0.392	0.29	-3.486	-2.371, -4.542	6.4	0.9	-2.54±0.45	3.6	5	–	60.5±5.0	–	7.3	10.9	–

... *Continued on next page*

Table 3.3 – … *Continued from previous page*

Source Name	RA [deg]	DEC [deg]	Δr [deg]	A_{fe} [A_{bm}]	$\tilde{\alpha}$	$\tilde{\alpha}_{c1}, \tilde{\alpha}_{c2}$	I_{peak} [**]	$\langle\sigma_{qu}\rangle$ [%]	β	$\langle p_0\rangle$ [%]	DF	$\lvert F\rvert_p$ [%]	ϕ_{peak} [*]	σ_ϕ [*]	T	$\tilde{T}$	Fid
J0414-8041	63.606	-80.697	0.606	0.45	-1.254	-2.082, -3.864	3.8	0.5	-1.99±0.67	6.3	5	7.0	-10.5±1.8	5.2E-2	20.4	13.9	s
J0410-8153	62.660	-81.891	1.549	0.18	-4.403	-13.531, -15.080	53.9	0.4	-3.88±0.54	2.2	5	1.5	120.0±3.3	2.0E+4	15.4	17.2	c
J0407-81042	61.961	-81.712	1.449	0.17	-2.917	-1.447, -2.469	7.3	0.6	-2.63±0.44	4.9	5	2.8	71.0±2.5	1.1E+4	8.9	13.2	c
J0404-8101	61.233	-81.032	1.083	0.18	-1.979	-1.762, -3.422	7.3	0.4	-2.66±0.54	2.6	5	3.2	-23.0±2.9	3.6E-12	14.6	10.0	s
J0414-8041	63.613	-80.694	0.604	0.34	-1.058	-4.037, -3.371	4.0	0.4	-2.25±0.66	4.6	5	4.8	-17.0±1.9	5.4E-2	14.8	11.4	s
J04023-8108	65.813	-81.134	0.667	0.21	-1.072	-6.753, -5.094	28.7	0.2	-1.35±0.47	3.6	5	3.5	-34.5±1.0	1.2E+4	90.6	22.3	c
J04019-8107	64.761	-81.131	0.735	0.43	-1.149	-7.761, -8.848	4.1	0.4	-2.34±0.62	3.2	5	–	229.0±2.4	–	6.1	9.6	–
J0410-8153	62.675	-81.890	1.546	0.31	-4.629	-3.258, -4.932	26.6	0.5	-5.80±0.87	3.4	5	3.1	80.5±3.2	1.1E+5	11.0	12.0	c
J0427-8042	66.960	-80.712	0.214	0.50	-1.588	-0.514, 5.602	2.1	1.2	-1.69±0.71	12.3	5	–	-32.5±2.1	–	6.7	11.4	–
J0412-8110	63.049	-81.169	0.931	0.19	-1.305	-6.138, -2.958	22.7	0.1	-1.36±0.50	3.0	5	3.0	-32.0±1.0	2.4E+3	53.5	24.1	c
J04023-8107	65.804	-81.131	0.665	0.62	-1.033	-1.780, -3.250	13.4	0.2	-2.19±0.48	3.4	5	3.3	-34.5±1.3	8.8E+2	38.2	18.3	c
J04023-8108	65.820	-81.136	0.669	0.72	-1.314	-4.911, -6.995	17.5	0.2	-1.86±0.47	4.3	5	4.1	-35.5±1.0	5.8E+3	57.0	23.2	c
J04012-8109	63.052	-81.166	0.253	0.14	-2.739	-7.040, -9.160	25.2	0.5	-5.91±0.75	2.9	6	2.7	-59.5±3.3	1.6E+5	21.5	7.7	c
J0400-8107	60.087	-81.124	0.664	0.12	-2.351	-10.677, -18.852	13.4	0.5	-4.09±0.56	5.1	6	4.4	-2.5±2.2	6.8E+4	21.3	12.9	c
J0352-8022	58.157	-80.375	1.171	0.19	-4.558	-5.566, -9.644	47.6	0.4	-7.16±0.76	1.8	6	2.0	-140.5±4.3	3.0E+2	11.1	9.1	c
J0416-8115	64.205	-81.266	0.266	0.13	-3.841	-3.687, -3.934	1.9	8.9	-6.23±0.78	50.7	6	–	1536.5±3.6	–	5.4	8.0	–
J0410-8153	62.664	-81.892	0.924	0.14	-4.674	-5.186, -9.078	40.0	0.8	-3.99±0.73	1.5	6	–	-134.5±11.4	–	7.1	10.2	–
J03058-8103	59.636	-81.064	0.727	0.29	-2.357	-6.485, -10.344	9.1	1.3	-7.13±0.92	9.3	6	8.1	327.5±2.8	6.3E+4	25.1	8.1	c
J0404-8101	61.234	-81.032	0.478	0.11	-2.570	-4.956, -7.980	9.6	0.6	-3.33±0.73	3.9	6	2.7	-22.0±3.3	0.0	8.2	9.2	s
J0400-8107	60.091	-81.126	0.663	0.11	-2.418	-5.004, -9.929	13.0	0.4	-2.76±0.68	2.5	6	1.9	-9.0±3.2	3.2E+4	8.7	9.8	c
J0345-8112	56.472	-81.210	1.225	0.12	-4.448	-5.570, -10.981	2.5	7.5	-8.16±0.92	39.2	6	32.5	-43.0±3.9	6.4E+4	10.8	7.7	c
J0412-8110	63.051	-81.169	0.255	0.13	-2.773	-3.822, -6.048	20.7	0.8	-5.41±0.60	6.4	6	6.3	-30.5±2.5	8.6E+4	40.5	13.5	c
J03058-8103	59.616	-81.062	0.730	1.31	-2.636	-5.852, -7.822	7.0	1.4	-5.92±0.92	11.4	6	9.3	59.0±2.5	3.9E+4	20.8	9.0	c
J0400-80037	60.097	-80.621	0.769	0.35	-3.352	-6.431, -12.263	4.4	1.7	-2.47±0.86	9.5	6	–	-22.0±3.8	–	7.1	8.4	–
J0404-80048	61.181	-80.808	0.693	0.16	-2.120	-9.431, -11.817	10.6	0.1	-1.86±0.38	1.1	7	1.2	-2.0±2.1	0.0	15.1	9.4	s
J0351-7940	57.957	-79.671	1.898	0.23	-4.652	-10.456, -12.878	7.1	1.1	-5.43±0.72	6.0	7	–	-136.5±3.6	–	6.9	9.4	–
J0352-8022	58.210	-80.379	1.208	0.21	-2.335	-4.485, -10.781	12.5	0.2	-2.77±0.58	2.9	7	2.3	-35.5±1.2	2.0E+4	30.3	17.6	c
J0352-8022	58.154	-80.375	1.215	0.22	-2.436	-4.468, -13.338	93.9	0.1	-1.01±0.28	1.1	7	0.8	-4.5±0.6	1.6E+4	75.1	26.7	c
J0400-80037	60.114	-80.620	0.893	0.93	-1.745	-6.615, -10.504	4.1	0.3	-1.92±0.42	2.9	7	3.1	-9.0±2.1	9.1E-13	15.4	10.9	s
J0406-80010	61.567	-80.183	1.320	0.16	-1.882	-5.570, -10.998	2.2	0.5	-0.90±0.57	7.9	7	8.5	-3.5±1.4	6.2E-2	23.7	14.7	s
J0359-8035	59.783	-80.591	0.931	2.93	-1.363	-4.493, -9.887	1.9	0.6	-2.03±0.60	6.7	7	5.7	-9.0±1.9	2.5E+3	14.7	9.8	c
J0414-8041	63.610	-80.694	0.896	0.32	-2.213	-6.486, -9.407	3.4	0.5	-1.61±0.57	4.2	7	4.2	-13.5±2.3	0.0	15.3	9.5	s
J0400-80010	60.002	-80.173	1.338	0.15	-1.630	-8.826, -9.507	14.2	0.1	-0.28±0.62	0.8	7	0.5	-3.5±1.8	1.2E+4	10.9	10.8	c
J03048-8003	57.041	-80.065	1.573	0.23	-4.054	-4.617, -11.911	9.5	0.3	-1.04±0.43	4.9	7	4.6	-29.0±1.3	4.2E+3	23.7	13.8	c
J0356-8040	59.054	-80.676	0.881	0.36	-1.789	-5.247, -11.031	11.4	0.1	-0.23±0.34	1.9	7	1.8	-16.5±1.2	3.0E+3	27.2	15.1	c
J0400-80036	60.054	-80.616	0.898	1.95	-1.416	-5.224, -10.952	1.6	0.7	-1.82±0.47	8.8	7	8.5	-13.5±1.7	1.2E+2	15.3	11.4	c

… *Continued on next page*

Table 3.3 – … *Continued from previous page*

Source Name	RA [deg]	DEC [deg]	Δr [deg]	A_{fe} [A_{bm}]	$\tilde{\alpha}$	$\tilde{\alpha}_{c1}, \tilde{\alpha}_{c2}$	I_{peak} [**]	$\langle \sigma_{qu} \rangle$ [%]	β	$\langle p_0 \rangle$ [%]	DF	$\lvert F \rvert_p$ [%]	ϕ_{peak} [*]	σ_ϕ [*]	T	$\tilde{T}$	Fid
J0404-8101	61.230	-81.032	0.468	0.17	-2.706	-5.975, -8.202	6.3	0.3	-0.63±0.85	2.5	7	2.7	-20.5±2.2	4.9E-2	15.7	9.7	s
J0411-8028	62.776	-80.479	1.055	0.22	-1.788	-5.134, -12.176	3.2	0.3	-0.70±0.51	3.0	7	3.2	1.0±2.1	6.0E-2	12.4	9.5	s
J0404-80028	61.044	-80.481	1.019	0.38	-1.589	-4.264, -10.118	1.7	0.5	-0.10±0.60	5.0	7	4.7	-8.0±2.2	5.5E-2	10.0	8.9	s
J0400-8107	60.083	-81.125	0.403	0.47	-3.137	-6.281, -8.194	8.4	0.2	-2.80±0.61	1.5	7	1.5	-28.5±2.5	1.5E-11	9.9	8.6	s
J0416-7948	64.199	-79.814	1.760	0.18	-4.445	-5.690, -9.770	14.8	0.2	-3.91±0.65	2.0	7	2.0	-21.5±2.4	5.2E-2	13.8	11.7	s
J0414-8041	63.603	-80.697	0.893	0.43	-2.281	-3.849, -12.239	3.5	0.4	-0.75±0.55	5.3	7	5.3	-5.5±1.5	2.3E-13	19.2	15.1	s
J0414-8041	63.618	-80.691	0.900	0.45	-2.447	-9.688, -12.451	3.9	0.4	-1.07±0.59	4.4	7	4.4	-7.5±1.7	8.6E+2	16.5	13.5	c
J0351-7940	57.924	-79.677	1.894	0.26	-4.630	-5.249, -10.626	2.6	2.5	-4.49±0.69	14.9	7	–	-179.0±3.5	–	4.1	9.6	–
J0352-8022	58.197	-80.378	1.210	0.46	-2.321	-6.776, -9.707	24.0	0.1	-2.83±0.64	1.2	7	0.7	82.5±1.7	1.1E+5	17.9	11.7	c
J0352-8022	58.184	-80.376	1.212	0.19	-1.989	-5.547, -12.102	25.1	0.1	-3.22±0.62	1.2	7	0.8	-374.0±1.7	1.1E+5	22.0	11.0	c
J0400-80037	60.088	-80.618	0.895	1.73	-1.583	-5.206, -11.597	4.9	0.2	-2.43±0.42	3.7	7	3.7	-11.5±1.4	8.8E+1	24.1	14.9	c
J0400-80037	60.095	-80.621	0.892	0.60	-1.717	-2.667, -6.834	5.1	0.3	-0.30±0.40	6.8	7	6.8	-12.5±0.9	9.8E+2	44.9	21.6	c
J0406-80018	61.643	-80.312	1.192	0.19	-2.080	-4.184, -12.860	14.6	0.1	-0.44±0.79	0.8	7	0.8	-7.0±2.0	2.3E-13	13.3	10.3	s
J03048-8004	57.007	-80.083	1.559	0.22	-3.844	-8.535, -8.720	10.1	0.3	-2.27±0.66	3.5	7	4.0	-22.0±1.6	2.0E+2	23.8	12.0	c
J0350-7941	57.526	-79.696	1.894	1.04	-4.656	-7.549, -9.805	7.8	1.0	-5.75±0.74	5.9	7	–	-1280.0±3.4	–	7.5	10.1	–
J0348-7956	57.144	-79.947	1.676	0.16	-4.071	-3.534, -6.538	13.4	0.2	-2.84±0.60	1.5	7	1.3	-73.5±3.0	4.6E+2	10.1	9.6	c
J0412-8110	63.046	-81.169	0.445	0.18	-4.042	-14.051, -17.689	12.5	0.2	-2.11±0.56	2.6	7	2.3	-21.0±1.9	4.7E+3	15.8	11.9	c

3.6.2 Bright Faraday detections

We now present RM clean results for the 95th percentile $\tilde{T}$ distribution sources – that is the 5% highest SNR direct polarised detections. Table A.2 lists each of these sources and along with their detected Faraday components. This sub-population of polarised sources displays the following:

1. *Different emission properties for different lines of sight through the same sources detected in multiple fields*: Extended and unresolved sources, such as J0352-8022 (Figure 3.50), tend to be fitted with several ellipses during source finding which results in slightly different lines of sight passing through different parts of the source being analysed. Different lines of sight display different features in broad band spectra as they sample different spatial and potentially different emission components of the extended source. Coupled to this effect is also the early MeerKAT pointing offset noted earlier in this work[13].

2. *Significant instances of Faraday complexity*: Near ubiquitous Faraday complexity is observed in the Faraday spectra of these sources. The complexity is primarily observed in the form of Faraday thick ϕ-components presenting as several components in a localised region of Faraday depths (for example Figures 3.42 and 3.48). Faraday complex spectra do also show a combination of thin (single isolated peak/component that is consistent with a δ-function in Faraday depth space) and thick ϕ-components (for example Figure 3.43).

3. *Presence of both repolarisation and depolarisation*: Depolarisation is observed in the majority of bright Faraday detections with a smaller sub-population of sources that repolarise over the range of λ^2 observed. Repolarisation is observed in both highly complex spectra (Figure 3.45) and less complex spectra (Figure 3.52). Bright and highly polarised radio sources have been observed to be consistent with repolarising models (O'Sullivan et al., 2012).

4. *Presence of Faraday simple sources*: We find a small number of Faraday simple sources (6 sources) half of which repolarise while the other displays depolarisation. The ratio of depolarisation to repolarisation is significantly lower than in the sub-population of all complex classifications. Enhanced Faraday complexity has been observed in bright polarised sources (e.g. Anderson et al., 2016) and our results do suggest this given the low number of bright but Faraday simple classifications in our sample.

5. *Instances of complex "wiggle" structure in RM cleaned spectra*: The bright Faraday detections show the highest instances of "wiggle" sub-structure in their RM cleaned spectra (see e.g. Figure 3.43). This structure is due to minor (low signal to noise) ϕ-components that are detected at significant ϕ separations from the major components. As the ϕ separation increases, so does the oscillation frequency of this sub-structure in λ^2-space due to the Fourier relation between the observed polarisation $p(\lambda^2)$ and Faraday spectra, $F(\phi)$. This sub-structure is due to sampling of the λ^2 range being too sparse to resolve minor ϕ-components in ϕ-space. We thus are limited by the channel widths $\delta\lambda^2$ with regard to the level of complexity we can resolve in Faraday spectra, but given the level of significance at which the minor components are detected we can conclude that they are most likely real emission components somewhere along the line of sight.

---

[13] See MeerKAT technical background information available at `http://www.ska.ac.za/science-engineering/meerkat/observers/observing-programme/open-time/`

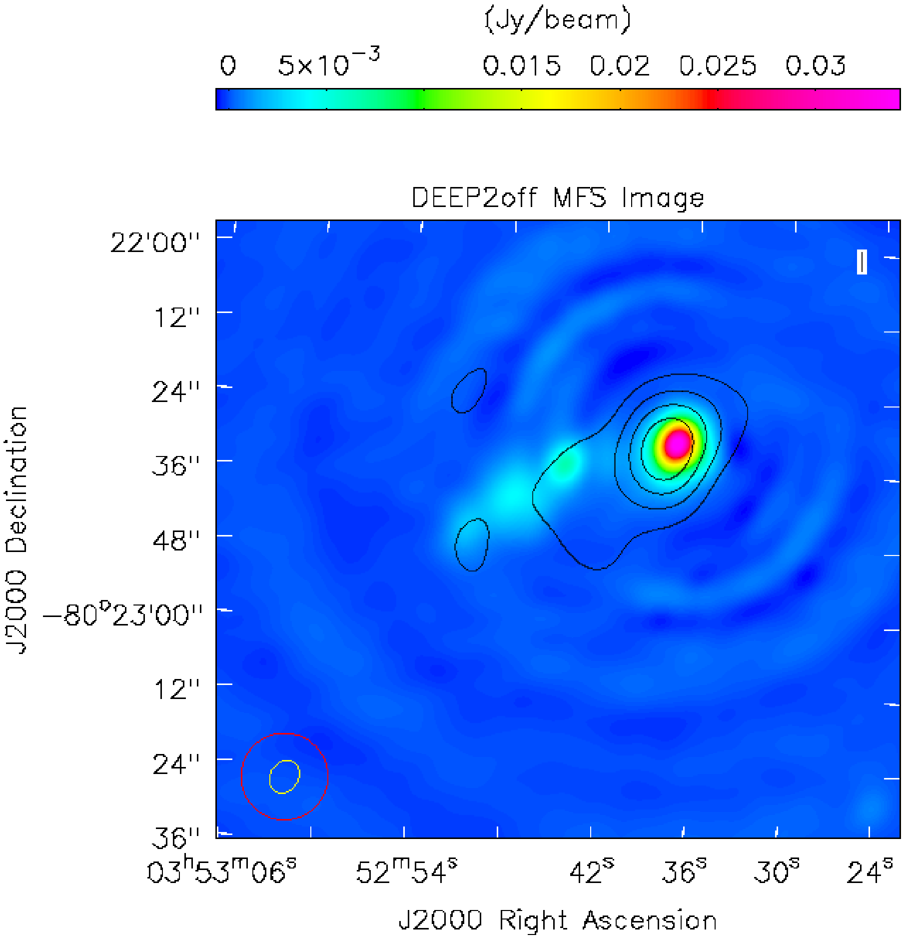

Figure 3.50: J0352-8022 in the DEEP2off source finding image. The plot arrangement is as in Figure 3.29.

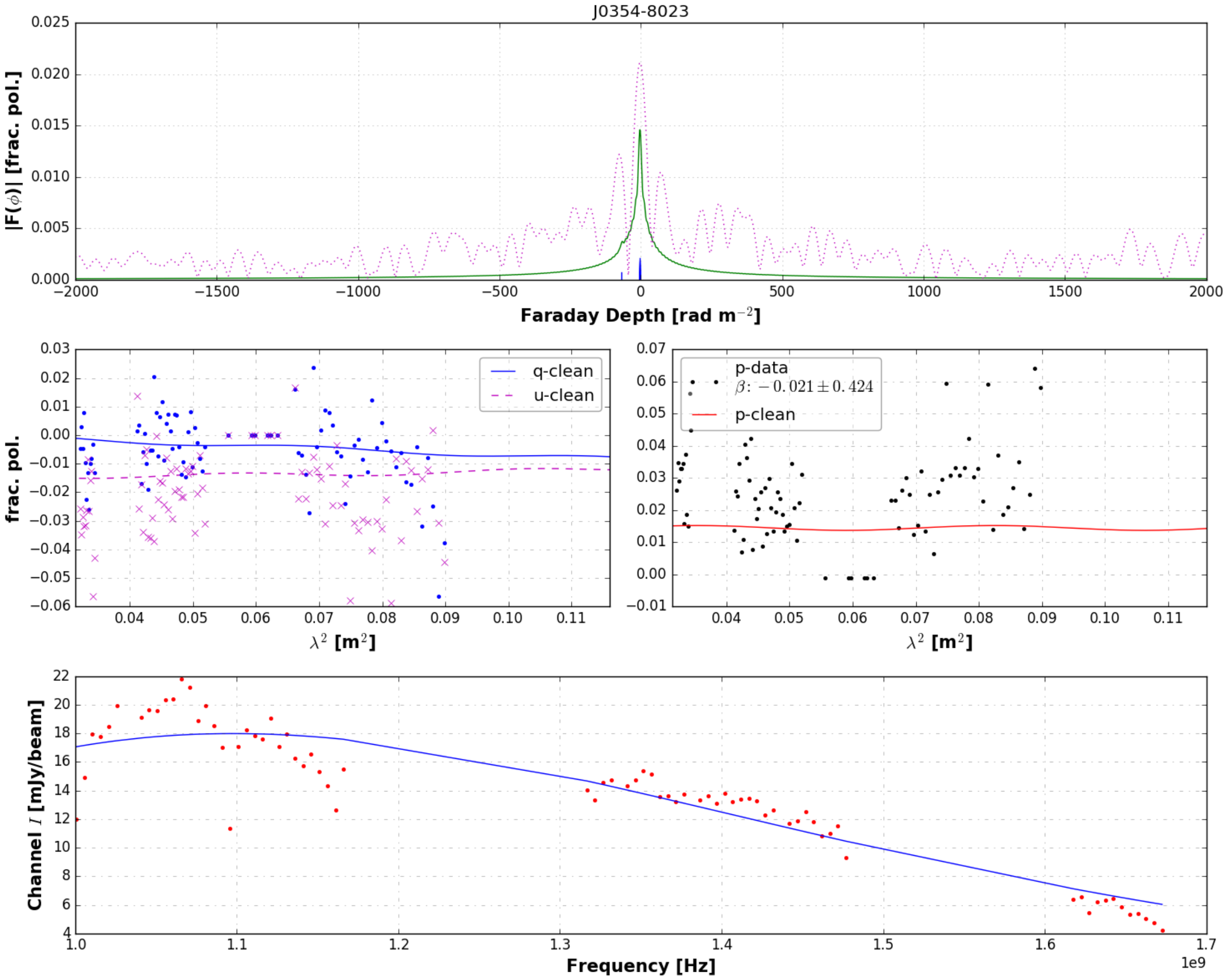

Figure 3.51: Polarisation and RM clean spectra for a bright Faraday complex component of J0354-8023 as observed in the DEEP2off field. Plots are arranged as in Figure 3.42. This is an unresolved point source.

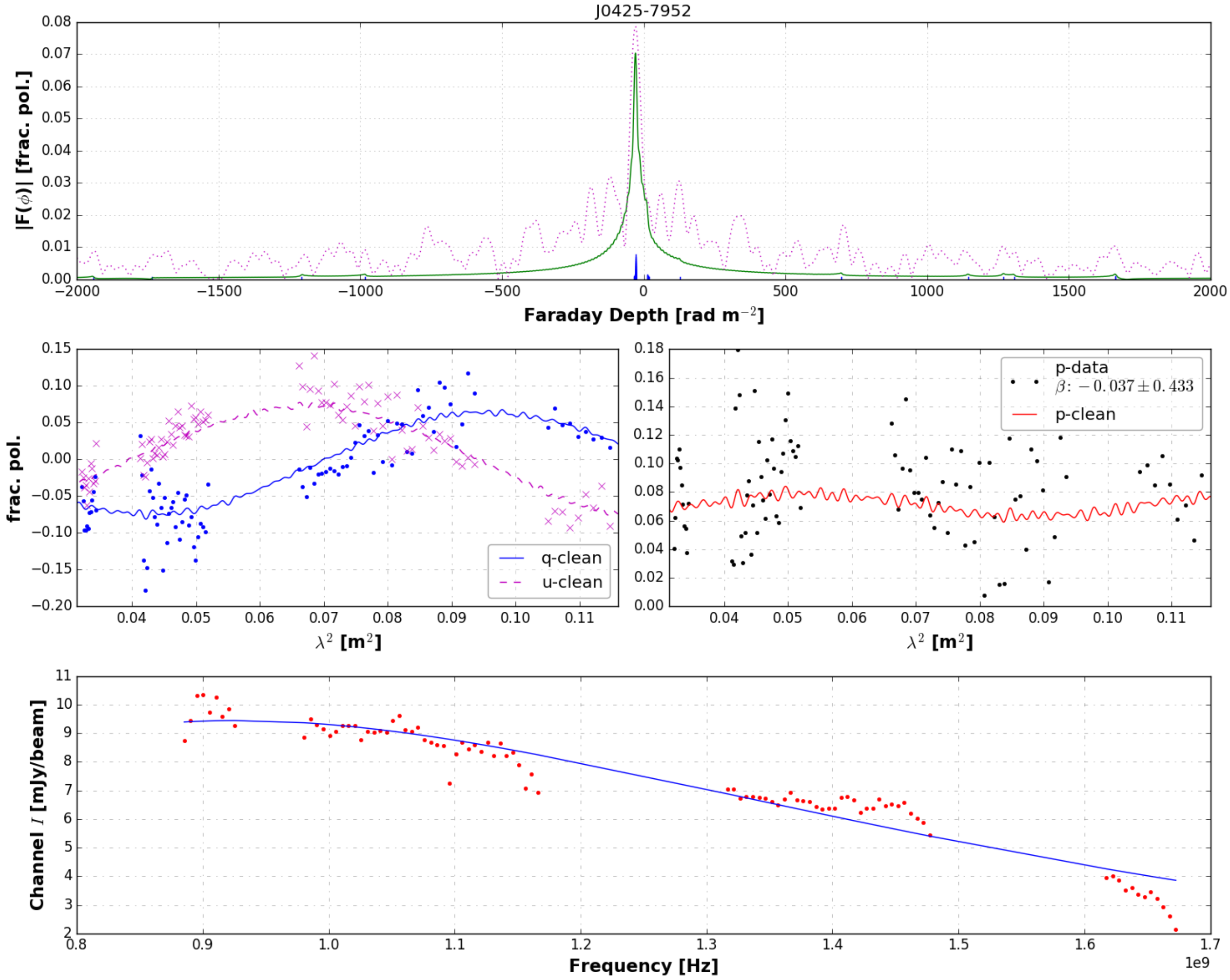

Figure 3.52: Polarisation and RM clean spectra for a bright Faraday complex component of J0425-7952 as observed in the DEEP3 field. Plots are arranged as in Figure 3.42. This is a lobe-like component in an unresolved double component source.

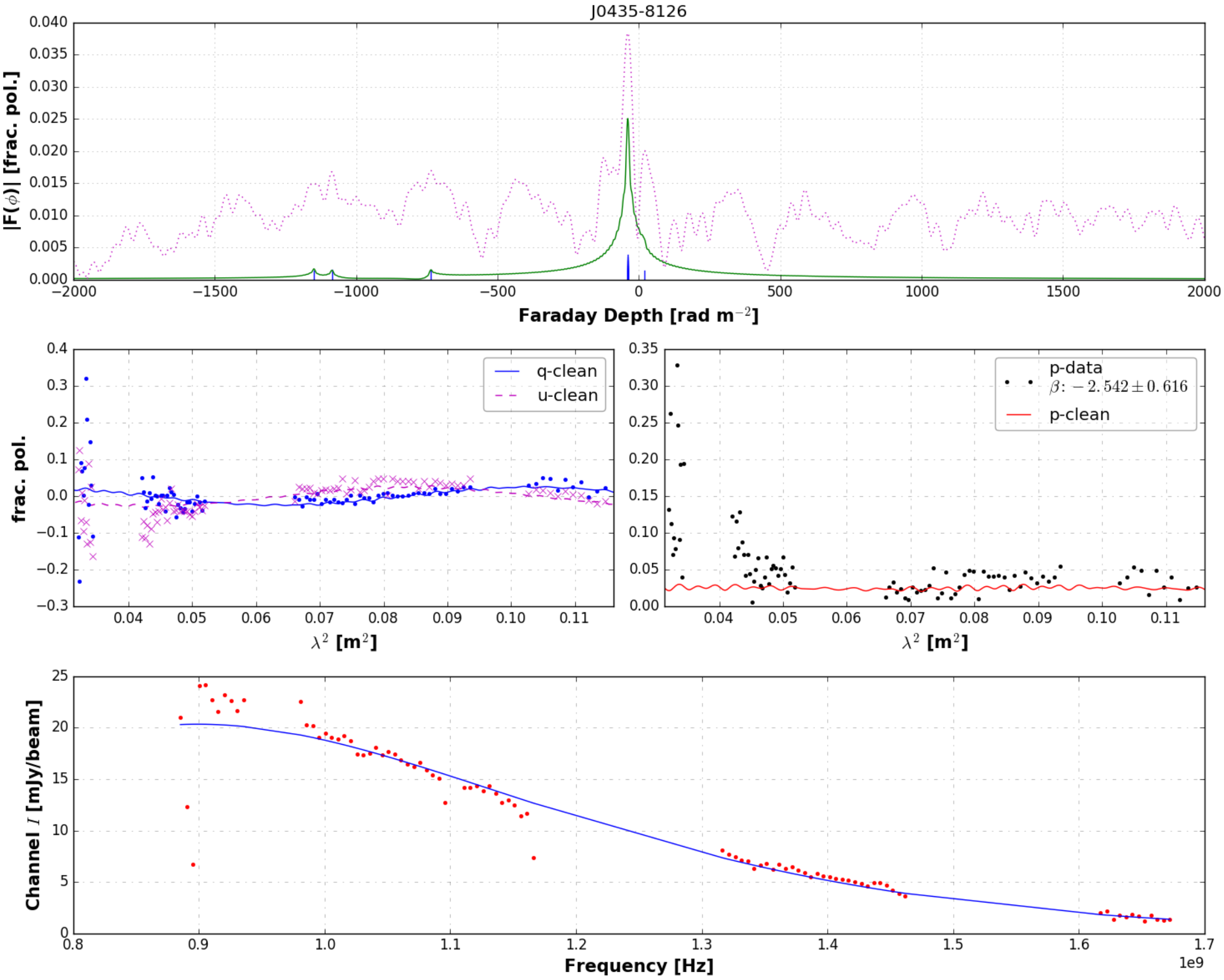

Figure 3.53: Polarisation and RM clean spectra for a bright Faraday complex component of the double lobed source J0435-8126 as observed in the DEEP5 field. Plots are arranged as in Figure 3.42.

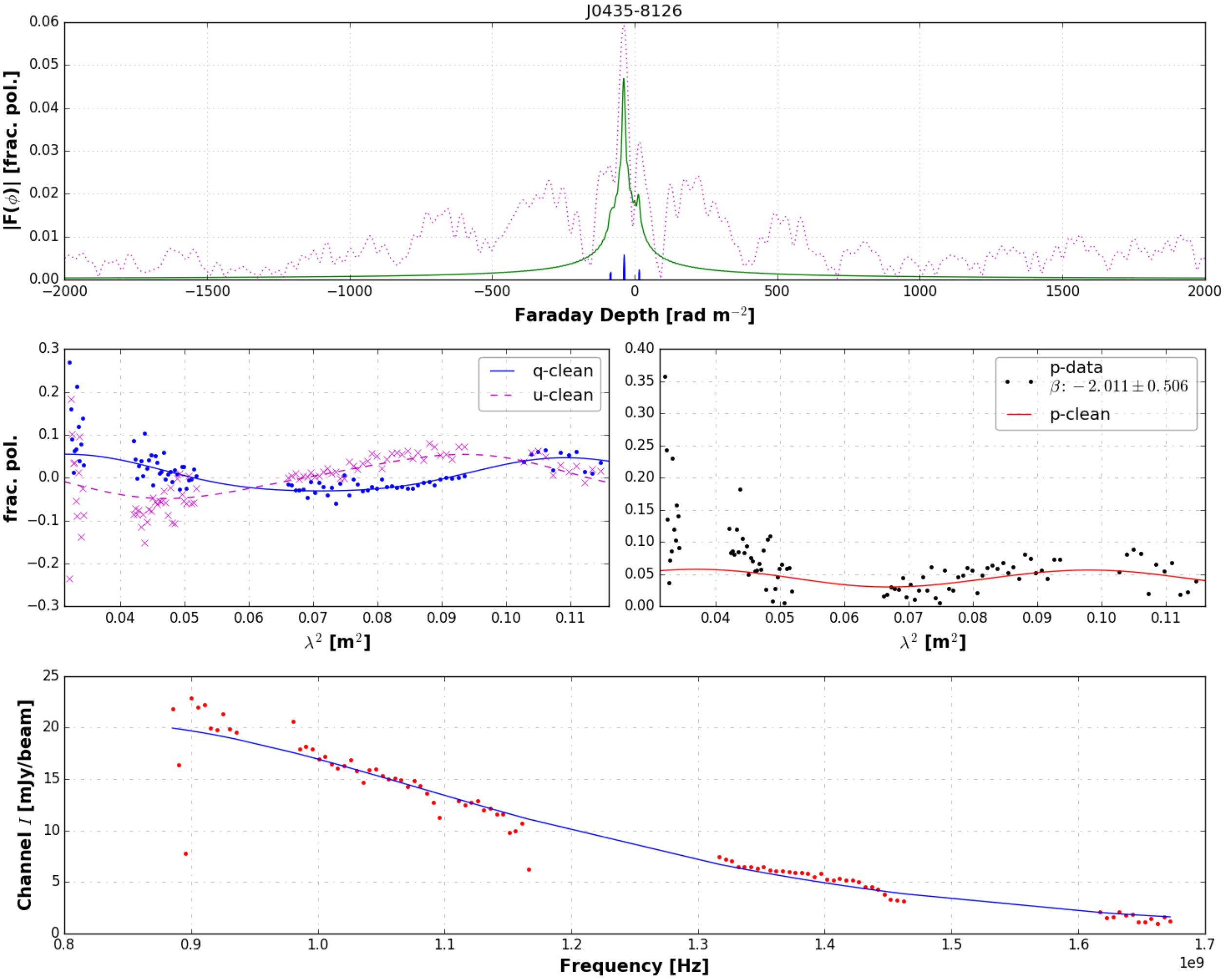

Figure 3.54: Polarisation and RM clean spectra for the second bright Faraday complex component of the double lobed source J0435-8126 as observed in the DEEP5 field. Plots are arranged as in Figure 3.42.

3.6.3 Faint Faraday detections

We select sources with $\tilde{T}_i$ below the 25th percentile of the $\tilde{T}$ distribution of Faraday detections and call this sub-sample the faint Faraday detections sub-sample. The sub-population is cataloged in Table A.3. We present the results of our RM synthesis analysis here. The sources in this sub-sample display the following characteristics:

1. *Evidence for locations of localised high polarisation and Faraday complexity*: A source, J0400-79049, not detected in RM synthesis in DEEP1 is part of this sub-sample (Figure 3.57) while different lines of sight through the same source (separated by $\sim 1''$) detected in DEEP2off and DEEP2 show significantly different polarisation behaviour. The component of J0400-79049 detected in DEEP2off (Figure 3.55) and classified as Faraday complex is also similarly classified in DEEP2 but it presents a significantly more complex emission structure suggesting a higher level of Faraday thick components (larger σ_ϕ along with a larger T – Figure 3.56). This suggests a region of localised high polarisation and a strong ordered magnetic field component along the line of sight. The major ϕ-component in the DEEP2off measurement occurs at $\phi_{peak} = -8.0 \pm 2.4$ rad m^{-2} while the DEEP2 measurement occurs at $\phi_{peak} = -78.5 \pm 1.5$ rad m^{-2}. Lines of sight measured in different fields through another FR II source J0425-8013 present another such scenario. Two spatially consistent (on sky separation $\sim 0.6''$) lines of sight through a detectable radio lobe of the source that are measured in two fields (DEEP2 and DEEP3) show consistency in their measured ϕ_{peak}, $\langle p_0 \rangle$, and Faraday classifications while lines of sight with larger separations ($\sim 4.3''$ – contrast the DEEP2, DEEP3, and DEEP5 detections) show more inconsistencies. The DEEP5 line of sight shows the most inconsistency with low significance detection $\phi_{peak} = -1879.0 \pm 5.2$ rad m^{-2} where $\tilde{T} = 9.2$, and $T = 5.6$. These observations, however, are still coupled to the pointing offsets of early MeerKAT observations as noted earlier. The synthesised beam of $14''$ is also much larger than the $1''$ cross-matching separation upper limit. This suggests that the independence of these lines of sight is dubious. The asymmetry of the beam from pointing to pointing and over time does also add to the uncertainty. Quantifying these technical issues should be the subject of future work.

2. *Higher occurrence of Faraday simple classifications*: The majority of sources in this sub-sample are classified as Faraday simple. Any significant Faraday complexity is most likely undetected due to signal to noise limitations along the particular line of sight as suggested by the above. Another bias is that of resolution limitations where Faraday complexity may be revealed given high enough resolution (e.g Dreher et al., 1987; Anderson et al., 2018).

3. *Lines of sight with high ϕ_{peak} not detected in RM synthesis but detected in direct polarisation*: These direct detections form part of a sub-sample that is not detected in RM synthesis – displayed as points below T_o but with similar variance as the higher T detections in Figure 3.37. This sub-sample also includes lower ϕ_{peak} lines of sight that are less distinguishable from noise due to low signal to noise. An example of an undetected high ϕ_{peak} ($T = 3$ detection) is J0416-8115 displayed in Figure 3.58.

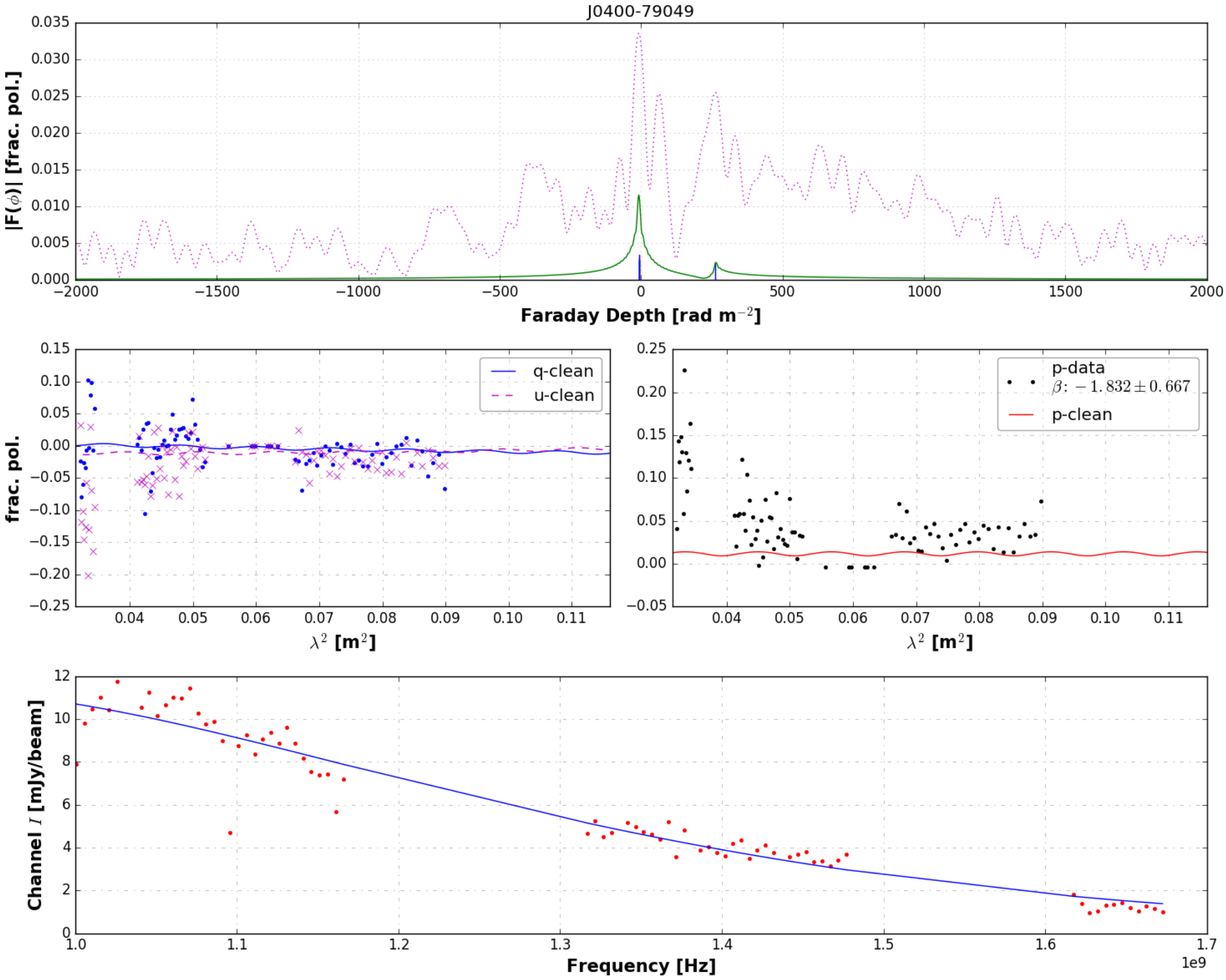

Figure 3.55: Polarisation and RM clean spectra for a faint Faraday simple component of J0400-79049 as observed in the DEEP2off field. Plots are arranged as in Figure 3.42. This an unresolved and extended source.

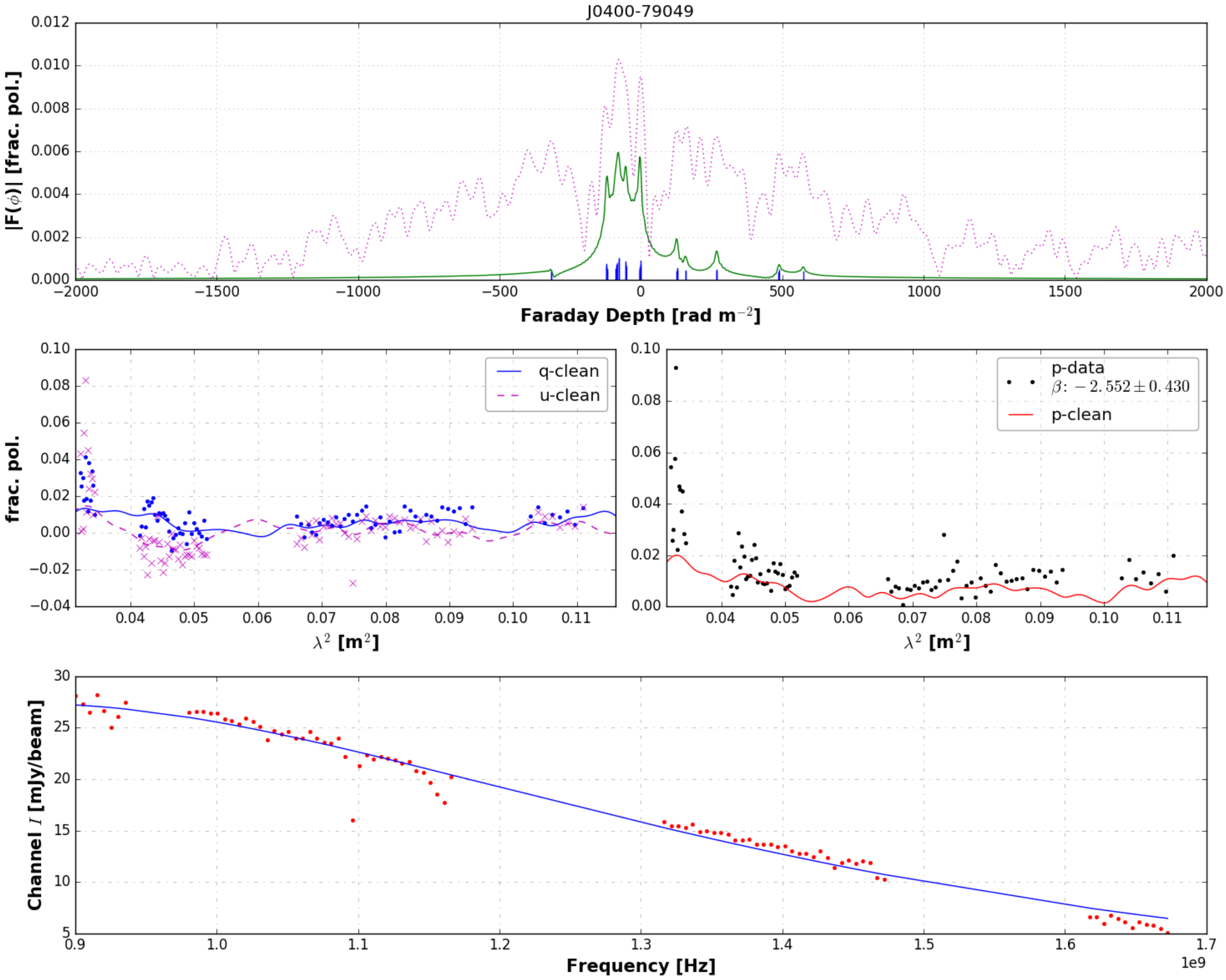

Figure 3.56: Polarisation and RM clean spectra for a faint Faraday simple component of J0400-79049 as observed in the DEEP2 field. Plots are arranged as in Figure 3.42.

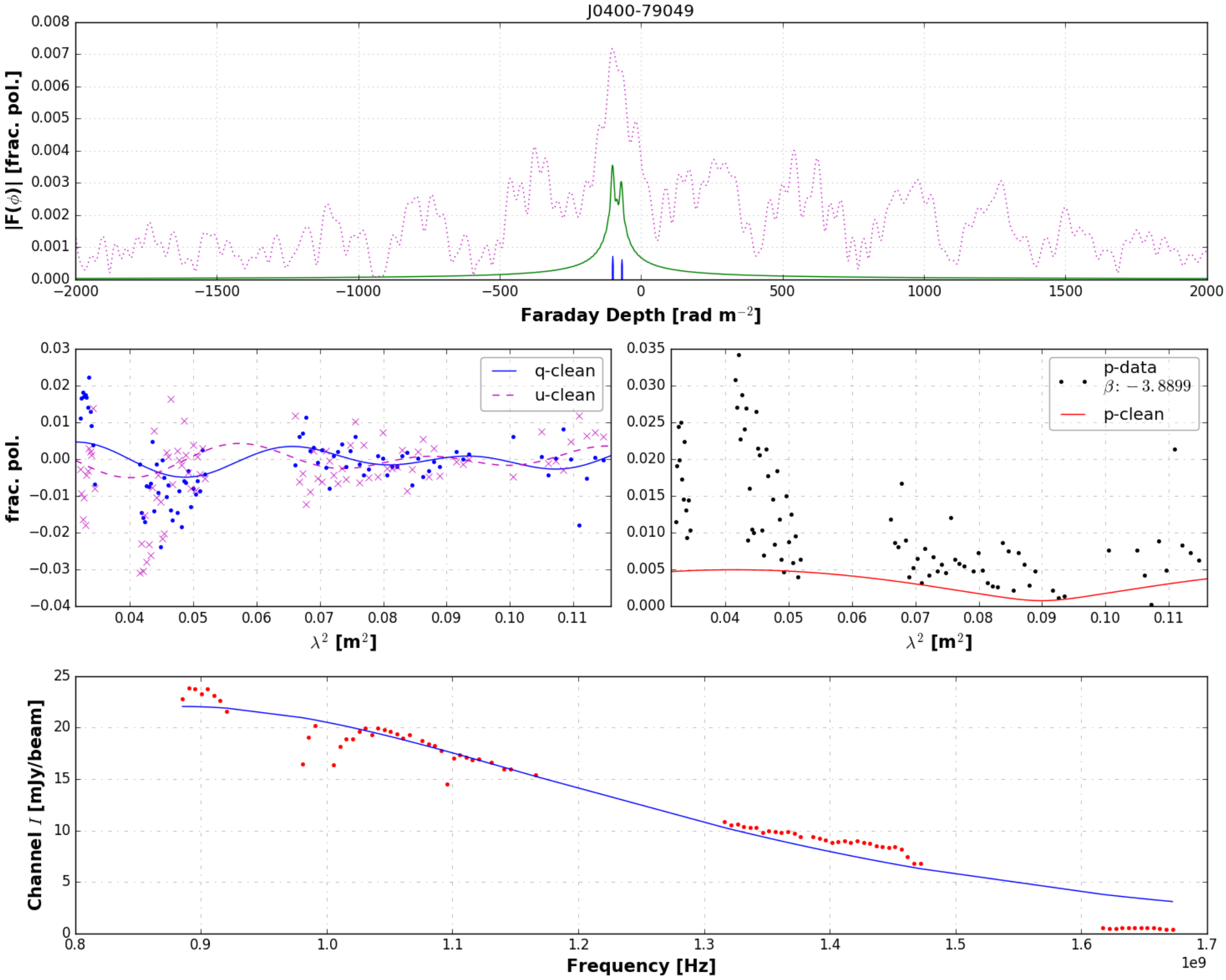

Figure 3.57: Polarisation and RM clean spectra for a faint Faraday complex component of J0400-79049 as observed in the DEEP7 field. Plots are arranged as in Figure 3.42. This is a bright point source.

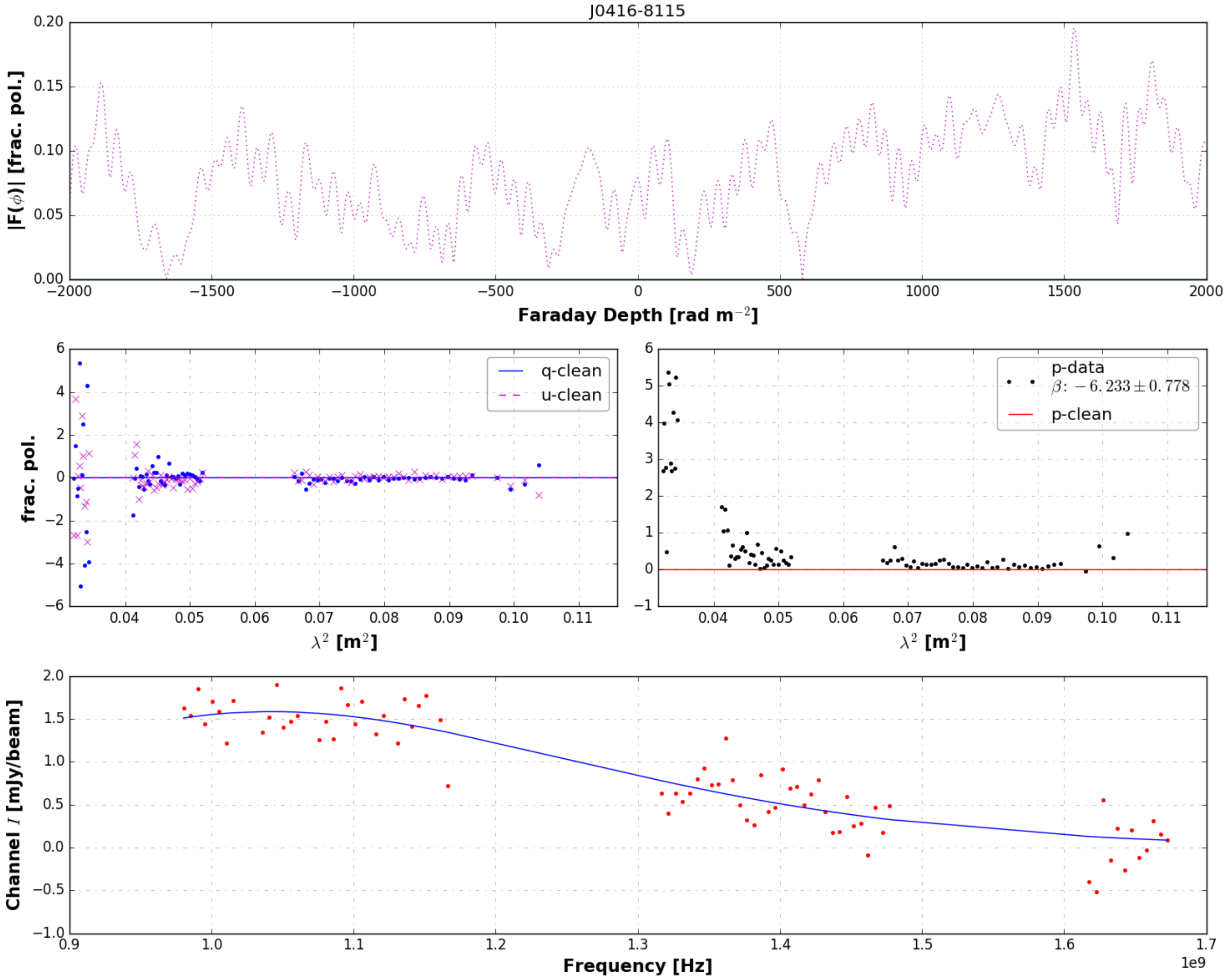

Figure 3.58: Polarisation and "dirty" RM clean spectra for a DEEP6 line of sight through one of the direct detections of the unresolved point-like source J0416-8115, that are undetected in RM synthesis. Plots are arranged as in Figure 3.42.

3.6.4 Summary of Results

We have performed RM synthesis analysis on our milli-Jy sample with direct polarisation detections. We perform RM synthesis deconvolution, known as RM clean, to reveal the Faraday emission components and the broadband spectral properties along lines of sight with full polarisation observations. RM clean is performed on the fractional $q(\lambda^2), u(\lambda^2)$ spectra to eliminate effects of the primary beam which are not constrained. We deconvolve Faraday spectra with the limiting constraint placed on the signal to noise of spectral peaks. This is set to $T = T_o = 8$ at which the probability of false detection is $< 10^{-4}$ (George et al., 2012). We classify as Faraday complex or simple according to their Faraday complexity of the RM "cleaned" Faraday spectra. Faraday complex classifications are found to make up $\sim$ 49% of the direct polarisation sample while Faraday simple classifications make up $\sim$ 39% and unclassified sources make up the remaining 12%. Unclassified lines of sight are undetected at the threshold T_o while detected in direct polarisation. The simple and complex categories display various complex spectropolarimetric behaviours.

We have found that the Faraday bright sub-population (80-th percentile signal to noise detections) display significant spectropolarimetric complexity that is detectable at high significance. This sub-population was found to display both depolarisation and repolarisation and was also found to have a small subset of Faraday simple classifications. The source finding analysis performed fits several ellipses to a spatially complex source and thus may provide several distinct lines of sight through different spatial components of the same source. This was found to manifest in the analysis of different parts making up a single radio source, such as in some cases of extended radio lobes. The observed spectropolarimetric behaviour, in these cases, was also found to be inconsistent amongst the various lines of sight which points to different emission components and perhaps also different magnetoionic environments and emission mechanisms in the different parts of such radio sources.

Faraday emission components that are significantly separated from the major components in ϕ-space were found to introduce complex oscillatory "wiggle" behaviour in the model Faraday spectra. The resolution of these components is beyond the limitations of this work as they are due to the relatively sparse sampling of the λ^2 range observed. This limits the range of detectable Faraday emission components. Denser sampling would minimise these effects.

Faint Faraday detections also displayed source complexity with regard to spatially complex sources, be it at lower signal to noise. This sub-population was found to have the highest subset of Faraday simple classifications which may suggest that the emission does indeed emanate from a single Faraday depth or that any level of complexity is undetectable. This sub-population was also found to have some high ϕ_{peak} classifications with low signal to noise suggesting that these may be highly depolarised real detections or a significant noise contribution or even artefacts of a limited λ^2 coverage (e.g. Taylor et al., 2009).

Chapter 4

Discussion

4.1 KAT 7 Spectropolarimetry

Our RM synthesis analysis shows Faraday complexity, of varying degrees, in four of the six sources in our KAT 7 sample. The most polarized source, 0240-231, displays the most complex Faraday spectrum with many emission components displaying Faraday depths, $\phi \sim 8 - 400$ rad m^{-2} (see Figure 2.13). The presence of Faraday thick components can be seen in the Faraday spectrum near the region of $\phi = 0.0$ rad m^{-2}. Our analysis clearly resolves this complex spectrum both near the main peak and the smaller peaks that extend towards $\phi \sim 400$ rad m^{-2}. This source also shows the most rapidly changing polarization intensity that depolarizes toward larger wavelengths (see the bottom panel of Figure 2.9). The behaviour of $q(\lambda^2)$ and $u(\lambda^2)$ is also far from the simple ideal sinusoidal behaviour, displayed by a single Faraday component, and this deviation is best illustrated in the plot of $u(\lambda^2)$ against $q(\lambda^2)$ in Figure 2.9. This plot resembles a circular geometry in the Faraday simple case, but we see quite a substantial deviation from this. Our RM clean model can however, reproduce the behaviour we see in the spectra. The $q(\lambda^2)$ and $u(\lambda^2)$ profiles have little scatter and are in good agreement with our RM clean model adding confidence to the derived ϕ-components. Anderson et al. (2016) show that Faraday-complexity is common in highly polarized sources and our observations in the case of 0240-231 agree with their conclusion. Faraday complex sources are also found to more likely have steep spectra (e.g. Anderson et al., 2015), and 0240-231 possesses this trait as well with $\langle\alpha\rangle_{1850}^{1350} = 0.562 \pm 0.006$ (see Table 2.3). These emission properties of 0240-231 agree with previous findings that the source is a bright compact radio source (Fanti et al. (1990); Fanti et al. (2000)). The double lobed structure reported by Dallacasa et al. (1998) may also be the cause of some of the observed Faraday complexity but we cannot confirm this.

The case of 0538-440 is another where we find evidence of Faraday complexity, although not to the level of 0240-231. This source is found to have two major components that are also likely Faraday thick (Figure 2.14). The Faraday components also span a smaller range $\phi \sim 0 - 100$ rad m^{-2}. The behaviour of $q(\lambda^2)$ and $u(\lambda^2)$ profiles for this source (bottom panels of Figure 2.10) resemble that of a simple one component Faraday spectrum source with somewhat larger scatter than in the 0240-231 case, indicating that perhaps higher sensitivity observations with a larger λ^2 coverage and thus Faraday depth resolution are needed to further explore the behaviour and further resolve the $\phi-$components. This source is highly polarized in the optical (Scarpa and Falomo, 1997). Our current resolution, however, is sufficient to tease out the complexity in the Faraday spectrum. Our RM clean implementation is also able to model the behaviour well at the $\sim 2.5\sigma$ level imposed. The 0538-440 total intensity spectrum is flatter than in the case of 0240-231 with $\langle\alpha\rangle_{1850}^{1350} = 0.098 \pm 0.003$ and a low degree of polarization of less than 1% in the two KAT 7 bands.

NGC1097 displays the most complex Faraday spectrum of our two disk galaxies. We classify the source as Faraday complex through our RM-clean implementation. The source shows two major components that are separated by a large ϕ range of ~ 160 rad m^{-2} (see Figure 2.15). NGC1808 is classified as Faraday simple with our RM clean treatment finding just a single Faraday component near $\phi = -0.2$ rad m^{-2} (see Figure 2.16). The $q(\lambda^2)$ and $u(\lambda^2)$ profiles for these two galaxies also differ, with NGC1097 displaying general depolarization while NGC1808 is flatter in $p(\lambda^2)$ with $q(\lambda^2)$ and $u(\lambda^2)$ profiles similar to those of NGC1097. Our RM-clean implementation does not find any structure in the profiles of the two galaxies. This is supported by the featureless $u(\lambda^2)$ v.s $q(\lambda^2)$ behaviour in the top right-most panels of Figures 2.9 and 2.10. The spectral indices we derive do agree with those expected for spiral galaxies ($\alpha = -0.8$ to -1.0, Beck (2015)) with $\langle\alpha\rangle^{1350}_{1850} = -0.815 \pm 0.011$ for NGC1808 and $\langle\alpha\rangle^{1350}_{1850} = -1.060 \pm 0.020$ for NGC1097. NGC1808 is weakly polarized, with $p \lesssim 1\%$ in accordance with previous findings (Stil et al., 2009; Sun and Reich, 2012). Sun and Reich (2012) modelled disk galaxies and found them to be polarized at sub-one percent levels near $\nu \sim 1.4$ GHz. NGC1808 also shows evidence of having its polarized emission originate from a single Faraday depth, while NGC1097 posses more Faraday structure. The depolarization behaviour in NGC1097 suggests that the galaxy disk is responsible for the depolarization of emission from the galaxy core region, similar to a Burn slab (Burn, 1966). The central region of NGC1097 may also have an effect on Faraday complexity as turbulent motions from the bar and circumnuclear ring may give rise to tangled fields which alter the polarized emission.

The case of PKS1934-638 is one of the simplest in our entire sample. This source shows polarization levels that are consistent with zero polarization across both KAT 7 bands and our RM-clean implementation is able to find one Faraday component (Figure 2.17). The $q(\lambda^2)$, $u(\lambda^2)$, and $p(\lambda^2)$ profiles (Figure 2.11) are featureless and we find band averaged polarization degrees of $0.1 \pm 0.03\%$ and $0.04 \pm 0.01\%$ at KAT 7 low and high band, respectively, further suggesting that this may be an un-polarized source. The older studies of Eichendorf and Reinhardt (1979) quote degrees that are of order double what we have found but the significance of the earlier results could not be obtained so we interpret their result as upper limits. The authors report a collection of polarimetric measurements done between 1965 and 1979, however, they do not quantify the statistical significance of these measurements. Our results are still comparable to theirs (Table 2.3) showing that PKS1934-638 is poorly polarised.

PKSB0407-65, however, is similar to the disk galaxy, NGC1808, with one prominent component where $\phi = 7.9$ rad m^{-2} (Figure 2.18). It has two minor components just at the RM-clean threshold with one of these detected just above the threshold at $\phi = -119.2$ rad m^{-2}. The $q(\lambda^2)$, $u(\lambda^2)$, and $p(\lambda^2)$ profiles of this source are not as featureless as in PKS1934-638 and may require a larger λ^2 coverage to further resolve the $q(\lambda^2)$, $u(\lambda^2)$, and $p(\lambda^2)$ behaviour as our model suggests that the source might be repolarised at larger λ^2. O'Sullivan et al. (2012) display that this is possible in some AGN powered sources.

There exists no relation between Faraday complexity and morphological complexity (e.g Anderson et al. (2015)) so even the most complex sources may be much simpler morphologically. More sensitive and higher resolution broad-band spectrophotometry studies are needed to further resolve Faraday components in Faraday depth, across wide bandwidths, and also spatially with high S/N.

Oppermann et al. (2012) have created a map of the smoothly varying Galactic Faraday component, ϕ_{gal}, by utilising all-sky Faraday rotation measures of compact sources from the literature. We list ϕ_{gal} at the locations of each our targets in Table 4.1. The Galactic component in regions near PKS1934-638 and J0240-231 are detected in RM clean as evident in the Faraday emission components listed in Table 2.5. The Galactic component near PKS1934-638 is indistinguishable from the component found at $\phi_{comp} = 51.1$ rad m^{-2} detected at a significant Faraday spectral peak signal to noise, ~ 22.5 – signal to noise of the peak calculated as $|F|_{comp}/\sigma_{off,99.9}$. In the case of J0240-231, the Galactic component is near the main peak located at $\phi_{comp} = 8.1$ rad m^{-2}. The Galactic component in each of these cases cannot be resolved from the nearest ϕ_{comp} as $|\phi_{comp} - \phi_{gal}|$ is significantly less than the widths of the RMTF in these observations. Given that the nearest ϕ_{comp} are detected at high signal to noise, we can conclude that Galactic components in these cases would require a larger observed λ^2 range. Brown et al. (2017) have shown that sufficiently bright (signal to noise > 5) Faraday components separated by $> 10\%$

Table 4.1: Estimates of the Galactic foreground Faraday depths at the locations of each our targets.

Source	l [deg]	b [deg]	ϕ_{gal} rad m^{-2}
NGC1097	41.579	-30.275	9.1
NGC1808	76.926	-37.513	35.3
J0538-440	84.491	-43.997	42.8
J0240-231	39.415	-23.224	9.1
PKS1934-638	65.146	-63.713	44.7
PKSB0407-65	62.085	-65.753	23.9

of $\delta\phi$ can be reliably identified, at a rate of 99%, using machine learning techniques based on convolutional neural networks. With $\nu_{\rm min} \approx 1.2$ GHz and $|\phi_{comp} - \phi_{gal}| \approx 1$ rad m^{-2}, we would require an observed frequency range $\Delta\nu \approx 3.3$ GHz to distinguish the extragalactic components from their Galactic counterparts.

4.2 Spectropolarimetry with early MeerKAT

The results of our broadband spectropolarimetric analysis on commissioning phase MeerKAT observations are presented in section 3.5. The key observations made and their implications on understanding broadband Faraday structures in extra-galactic radio sources, are discussed in the sections to follow. The strengths and shortfalls of the data used and the implications on interpretation of results, are also discussed.

4.2.1 Source finding and broadband properties

Our final source catalog results from the use of AEGEAN as the source finder. The program performs satisfactorily for the needs of source finding in this work. It is however, not optimised for diffuse and extended sources (Hancock et al., 2018) but tends to "overfit" these types of sources. The program has been shown to perform well at fitting so called "blended" sources (Hopkins et al., 2015) with a tendency to fit several ellipses to an extended source structure which supplies several lines of sight through such a source. We have found detectable polarisation and unique, and sometimes consistent, Faraday emission components along such lines of sight – such as in the case of the spatially complex source J0352-8022. This offered multiple spectropolarimetric probes of the different regions of spatially complex and also more generally unresolved sources.

Three total intensity spectral shapes are observed in our sample of milli-Jy sources: that approximated well by a simple power law, that which curves in a concave manner near $\nu \sim 1$ GHz, and finally, that which curves in a convex manner toward higher frequencies while being similar to the first case at lower frequencies. All cases are well approximated by the simple power law at frequencies near and just above 1 GHz but some spectra deviate significantly otherwise. A curved power law approximates all cases best, but is less physically meaningful and is thus used only to minimise scatter in fractional polarisation due to the variance in the measured total intensity spectra. Primary beam effects are most likely responsible for some of this observed curvature and will be investigated in future. The first case suggests sources with a flat spectrum as is the case with compact radio sources where $0 < |\alpha| \lesssim 0.5$. We find that polarised sources tend to be more extended as compared to unpolarised sources. Polarised detections also tend to be steeper than 0.5 with no detections showing flatter spectra. This suggests that the low polarisation levels of flat compact sources may not be detected in this work.

The $\langle p_0 \rangle$ distribution indicates that most lines of sight display a median $\lesssim 10\%$, save for a few outliers with $\langle p_0 \rangle > 10\%$ (right hand panel in Figure 4.1). The median detected polarisation degree is 3.6% with the outliers influencing the scatter of 5.2%. This supports conventional knowledge of flat spectrum sources typically display linear polarisation degrees of order $\sim 1\%$ (e.g. Pollack et al., 2003; Agudo et al., 2010). The lack of lines of sight with $|\tilde{\alpha}| \lesssim 0.5$ may be attributed to the yet unconstrained primary beam effects in our MeerKAT commissioning observations, but Figure 3.27 does show that our data suggests that flatter spectrum sources sources are less polarised as we observed no direct polarisation detections for $\tilde{\alpha} \gtrsim -0.5$. We expect that $\tilde{\alpha}$ should steepen, for intrinsically flat spectra, as a function of distance from the pointing centre. The distribution of $\tilde{\alpha}$ with respect to the angular distance from field centre supports this assertion, be it with some variance where steep spectra are also found for sources that are relatively near the pointing centre – Figure 4.1. The large negative values of $\tilde{\alpha}$ at large Δr indicate the spectral dependence of the primary beam. Tight constraints on primary beam parameters (e.g. Asad et al., 2016; Line et al., 2018) will greatly cement conclusions related to these matters but is beyond the scope of this work.

The second spectral shape suggests the detection of GPS radio sources where the spectrum peaks at $\nu \sim 1$ GHz. Visual inspection of these sources supports the suggestion of GPS classifications as these sources tend to be unresolved and point-like at the $\sim 14''$ resolution of this work. GPS sources are unresolved at these angular resolutions and tend to show spatial complexity at sub-arcsecond resolutions (e.g. O'Dea, 1998b; Lister et al., 2002). Visual inspection of the spectra of these sources suggests $\langle p_0 \rangle < 10\%$ with considerable scatter across the observed band. These values present significant overestimations as compared to linear polarisation in GPS sources at $\nu \sim 1$ GHz (e.g. Stanghellini et al., 1998; O'Dea, 1998b; Pasetto et al., 2016) and we suggest that the inconsistencies between the fitted power law estimation and the measured spectrum may have significantly contributed to this discrepancy. These inconsistencies carry over into the third type of spectrum. These sources are better approximated by the curved power law over the largest range of frequencies and indicate steep spectra with negative curvature suggestive of radio lobe or diffuse extended emission (e.g. Pasetto et al., 2016; de Gasperin et al., 2018). Visual inspection of these sources reveals that they are mostly likely unresolved radio lobes and extended components of radio sources.

The distribution of polarisation spectral index, β, suggests that the steepest total intensity spectra also display higher levels of depolarisation while flatter spectra tend to have $\beta \sim 0$, which is more reminiscent of lines of sight with constant polarisation across the range of observed wavelengths. A two population Kolmogorov-Smirnov test (KS test) between the β distribution and a normal distribution with the same mean and standard deviation suggests that the β distribution is not well characterised by the single population normal distribution – with p-value $= 0.045$ (Figure 4.2). The tail of the distribution suggests a sub-population of significantly depolarised steep spectrum emitters as is the case with diffuse and extended radio sources such as radio lobes and jets while the flatter portion of the distribution suggests another sub-population of compact flatter polarisation spectrum sources such as is case of compact radio cores of radio galaxies. Our results support previous observations (e.g. Farnes, 2014) and are also supported by visual inspection of our images where we observe that spatially compact/unresolved sources tend to have $\beta \sim 0$ while their more extended and diffuse counterparts show steeper β. Repolarisation, $\beta > 0$, has been observed at $\nu \sim 1 - 3$ GHz and found to be consistent with models where there at least two Faraday emission components that are intrinsic to the radio source (O'Sullivan et al., 2012; Anderson et al., 2015, 2016).

4.2.2 Polarisation detections and Faraday complexity

The results of our direct polarisation detections and their relations to the indirect Faraday synthesis detections are discussed in the sections to follow.

4.2.2.1 Polarisation detections

We present polarisation detections in Section 3.5.2.2 where detections are defined as those lines of sight that have mean polarisation degrees above $\tilde{T_o} \times \langle \sigma_{qu} \rangle$ – where $\tilde{T_o} = 8.2 \pm 0.5$. This results in an overall estimated mean detection rate of $24 \pm 9\%$ across all fields, except DEEP2off, that each span a ~ 1 square degree portion of the DEEP field. The error indicates the scatter in the detection rate among the different fields – with

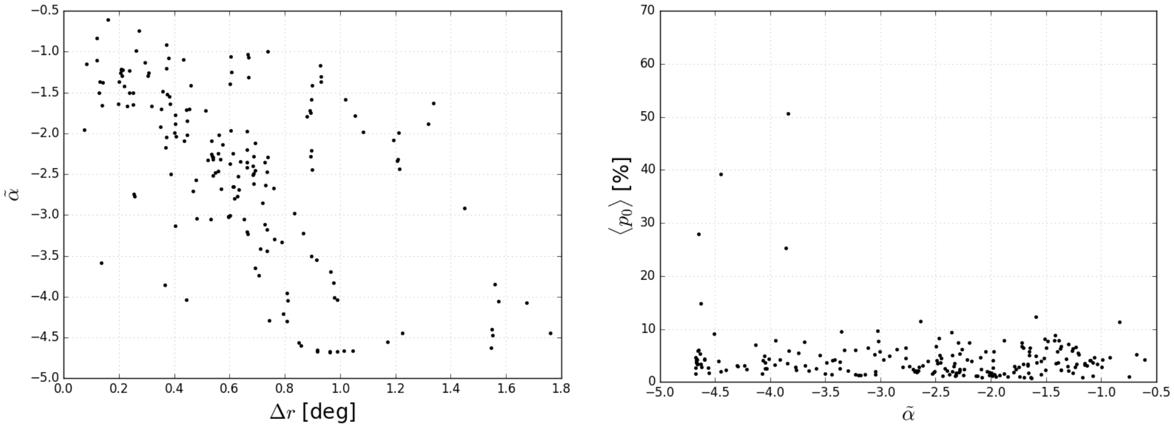

Figure 4.1: Left: Distribution of $\tilde{\alpha}$ as a function of distance from field centre for direct polarisation detections in our milli-Jy sample. Right: Distribution of $\langle p_0 \rangle$ as a function of $\tilde{\alpha}$.

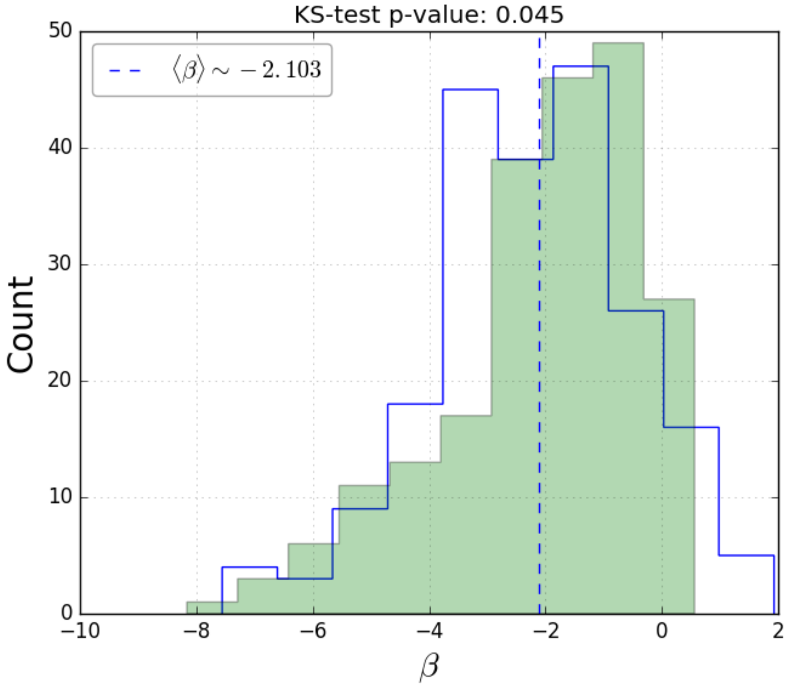

Figure 4.2: Distribution of β for direct polarisation detections in our milli-Jy sample. The open histogram represents the normal distribution with mean equal to $\langle \beta \rangle$ (vertical dashed line).

source fractions of ∼ 27, 33, 34, 16, 10, and 25% detected in DEEP1, DEEP2, DEEP3, DEEP5, DEEP6, and DEEP7, respectively. We exclude DEEP2off sources due to observed overpolarisation that could not be mitigated. This translates to an estimated average polarised source count of 30 ± 13 per square degree. It should be noted that this is not an accurate polarised source count due to the fact that we do not correct to true flux with the primary beam, but the value does serve as a good estimate. This is higher than the rate reported in the northern hemisphere NVSS sample (Condon et al., 1998) which includes radio sources down to 2.5 mJy at $\nu = 1.4$ GHz and a resolution of $45''$. Our study is of higher sensitivity, rms noise ~ 70 μJy/beam, and higher resolution (smoothed resolution of $\sim 14''$). The higher integrated polarised fluxes of lower resolution detections, due to fluxes averaged over the larger unresolved areas due to the larger beam, may have enhanced the detection rate in the NVSS (∼ 1 per square degree) (e.g Rudnick and Owen, 2014; Anderson et al., 2015). However, the higher sensitivity in this work has allowed us to detect more of the fainter sources that NVSS may have missed. Adjusting our sensitivity to match that of NVSS we find a detection rate of $19 \pm 8\%$. This discrepancy suggests that there may be other factors, such as those intrinsic to radio source populations in the different fields, that may be at play. Investigations of these dissimilarities should be the subject of future studies.

Polarised source densities at $P = 100$ μJy sensitivity and angular resolution $\sim 10''$ have been empirically predicted to be 32 ± 15 per square degree (Rudnick and Owen, 2014), in agreement with the value we find. We expect the polarised source density in this work to be slightly larger than the predicted value given that we have comparable flux limitations while our resolution of $14''$ is slightly larger. Rudnick and Owen (2014) derive polarised source number counts using a source catalog from VLA observations made at 1.4 GHz, at resolutions of 1.6 and $10''$, and sensitivity of $P = 14.5$ μJy. Their detections are made from image cube maps whose frequency channels are 10 MHz wide covering RF band 1265 - 2027 MHz. The authors detected 13 polarised sources out of 496 sources identified. They use a Monte Carlo approach to empirically derive a power law relating the source densities to polarised flux detection limits. They excluded sources that have low polarisation and high rotation measures as these are possibly spurious. In this work, we extract flux values along a single line of sight centred on the source ellipse as identified and characterised by our source finding analysis. The fluxes used to predict source detection rates at resolutions of $\sim 10''$ use the fluxes integrated over the entire area of sky subtended by the source and thus include more flux per source. A resolution bias does exists where detection rates from lower resolution integrated intensities tend to be higher than cases of higher resolution due to the larger flux density used to approximate the former. We do not observe significant discrepancies between our estimates and those of Rudnick and Owen (2014) despite differences in resolution.

4.2.2.2 Observed Faraday complexity

Faraday complexity is observed in a large sub-sample making up ∼ 49% of our sample and the sub-sample tended to have complex features detected at high significance. Some of these Faraday emission components result in “wiggle” structure observed along some lines of sight. Significant noise contribution to the Faraday spectrum can result in high ϕ_{peak} values at low signal to noise (e.g. Rudnick and Owen, 2014; Anderson et al., 2015). We find that for our direct polarised detections, the average ϕ_{peak} ($\langle\phi_{peak}\rangle$), is -19.9 ± 3.7 rad m^{-2}. The sample is composed largely of lines of sight with $\phi_{peak} < 400$ rad m^{-2} with a very small sub-population with $\phi_{peak} > 1000$ rad m^{-2}. Overall, the Faraday depths found in this work fall in the range found in other analyses at similar frequencies (e.g. Taylor et al., 2009; Law et al., 2011; O’Sullivan et al., 2012; Anderson et al., 2015, 2016). This high ϕ_{peak} sub-sample is undetected in Faraday synthesis (at the level of detection significance used in this work – we list some of these in Table A.1 where we list all sources measured below our threshold) which supports the notion that these spectra are due to noise-like emission components along the line of sight. These emission components may also be real but too faint for us to detect in Faraday synthesis, but that this small sub-population is actually detected in direct polarisation does motivate studies which probe faint polarisation with increased statistical significance by using methods such as stacking (e.g. Stil et al., 2014). Radio sources at these lowest polarisation fluxes and high ϕ_{peak} values can indicate dense magneto-ionic regions such as in starforming galaxies (e.g. Taylor et al., 2014) or features in the Galaxy's ISM.

We find evidence for variations of complex broadband polarisation features in spatially complex sources such as the object J0352-8022 (Figure 3.50). Our source finding analysis provides several distinct lines of sight through such sources and thus provides several probes of the magneto-ionic regions in these sources. With J0352-8022 as the example, we find evidence for several Faraday complex emission components along different lines of sight through the source indicating the presence of complex magneto-ionic structures within the source. Spatially complex radio sources such as radio lobes and jets have been found to be sites of spectropolarimetric complexity, displaying consistency with multiple component spectropolarimetric models, especially when spatially and spectrally resolved at GHz frequencies (e.g. O'Sullivan and Gabuzda, 2009; O'Sullivan et al., 2013; Anderson et al., 2018).

We find a mostly Faraday complex bright polarised sub-population made up of the 95th percentile of the $\tilde{T}$ distribution. We also identify a very small sub-population of these lines of sight that are consistent with Faraday simple classifications. Faraday complex behaviour is expected for bright polarised sources (e.g. O'Sullivan et al., 2012; Anderson et al., 2016) with repolarisation/depolarisation behaviour suggesting the presence of a additional emission components along the line of sight in the Galactic foreground, the inter-galactic medium, and/or intrinsic to the radio source. This then places doubt on these Faraday simple classifications and suggests more constraints, such as fitting of the $q, u,\ p$ spectra with multi-components spectropolarimetric models (e.g. Burn, 1966; Sokoloff et al., 1998; O'Sullivan et al., 2012; Horellou and Fletcher, 2014; Anderson et al., 2015, 2016; Anderson et al., 2018), in order to better describe the observed Faraday emission features.

Foreground rotation measure structure at angular scales of less than a square degree has been found to be insignificant (Stil et al., 2011). We thus expect a characteristic Faraday emission component with a low variance across the DEEP field that should be found as a distinct ϕ-component that is consistent among many lines of sight. Our ability to detect and resolve this component in Faraday depth space is limited by $\delta\phi = 51 \pm 10$ rad m^{-2} and also signal to noise. We thus explore the distribution of ϕ_{peak} with respect to T in search of evidence of ϕ_{gal} among the detected major components in our sample. Based on the Galactic foreground RM map of Oppermann et al. (2012), the average Galactic component value, $\langle\phi_{gal}\rangle$, in the DEEP field region is found to be 40.7 ± 0.4 rad m^{-2}. We find that the major ϕ-components that are in the range $\langle\phi_{gal}\rangle \pm \delta\phi$ are detected with the largest significance at the largest separations from $\langle\phi_{gal}\rangle$ (Figure 4.3). This suggests that the components we detect are less likely to be due to the Galactic foreground. This assertion is supported further by the distribution of ϕ_{peak} in the range $\phi_{peak} \pm \delta\phi/2$ where significantly fewer ϕ-components are detected as compared to outside of the range. The Oppermann et al. (2012) map is based on data taken at low resolution (with approximately one source per square degree in the northern and worse in the southern hemisphere), and is thus an under sampled estimator of the foreground RM. The value of 40 rad m^{-2} is likely due to one source in the vicinity of DEEP. On the scales of less than a few degrees (the scale of there DEEP fields) we expect variations between sources. If the RM is less than a few 10s it will be blended with low RM intrinsic source components.

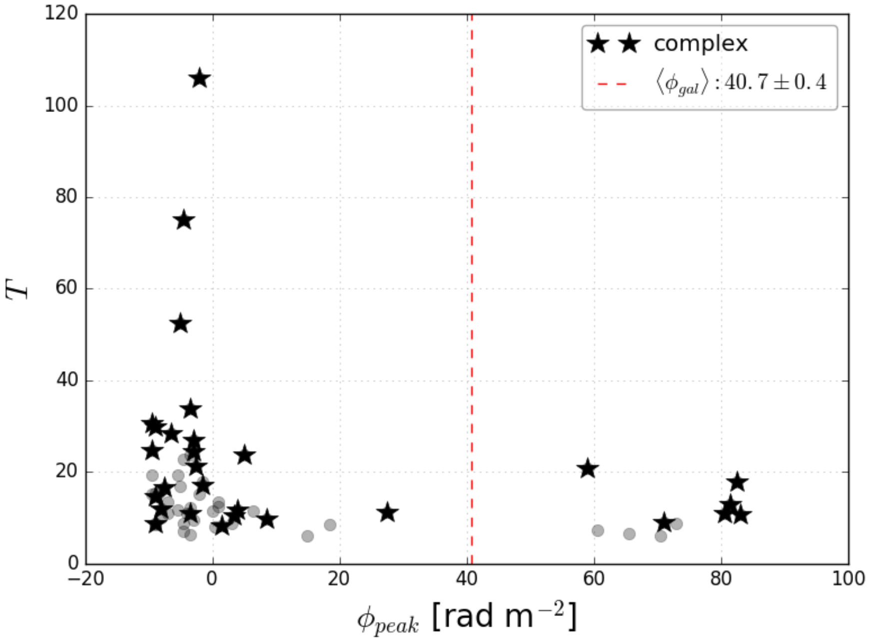

Figure 4.3: The signal to noise, T, of the major ϕ-components that are separated by no more than $\delta\phi$ from $\langle\phi_{gal}\rangle$ in the DEEP field.

Chapter 5

Conclusions

5.1 Summary and Conclusions

In Chapter 2, we have explored the properties of broadband linear polarization in two disk galaxies and four AGN powered sources in direct pointing mode with the KAT 7 array. The observations were made at the KAT 7 low band ($\nu_c = 1350$ MHz) and high band ($\nu_c = 1850$ MHz) with the mid band ($\nu_c = 1550$ MHz) discarded due to RFI. The synthesised beam at the low band was $\sim 4.9'$ and the same at the high band was $\sim 3.9'$. We detect linear polarisation down to ~ 2 mJy/beam and total intensities down to $\gtrsim 200$ mJy/beam. We employed the open-ended method of RM synthesis and RM clean (Burn, 1966; Brentjens and de Bruyn, 2005; Heald et al., 2009) which enabled us to resolve the Faraday depth components ($\delta\phi \sim 100$ rad m^{-2}) of the polarized emission along our line of sight. Our conclusions are summarised as follows:

i. The total intensity spectra that we were able to measure is in general agreement with previous studies. The one exception being the BL Lac source 0538-440 where our measured spectrum differs significantly from the literature. We attribute the discrepancy to inhomogeneity between our data and that of previous studies and also inhomogeneities between different studies which reported spectra at similar frequency ranges as those of the KAT 7 low and high bands.

ii. Our spectropolarimetric measurements show two major categories of objects: those that may have a single Faraday emission component and those that may have a composite Faraday structure that has more than one Faraday component. PKSB0407-658, PKS1934-638, NGC1097 and NGC1808 display a near featureless linear polarisation profile while the objects 0538-440 and 0240-231 display the opposite across the two KAT 7 bands. The simpler profiles of the first four objects suggest a single Faraday emission component in that their polarisation profiles are near constant functions of wavelength-squared – indicative of a spectropolarimetric profile emanating from a single Faraday depth. The other two objects display more complex Faraday spectra which is indicative of multiple emission components at different Faraday depths along the line of sight.

iii. Our RM synthesis results show that the four radio sources classified as Faraday simple have spectropolarimetric spectra that suggest emission from an unresolved narrow range of Faraday depths – i.e. Faraday thin. The two sources that are classified as complex have been found to have emission components over larger Faraday depth ranges which suggest Faraday thickness – indicative of complex magneto-ionic emission environments.

iv. The BL Lac source, 0538-440, and QSO, 0240-231, are the most polarized and most Faraday complex of our direct pointing sources. Our measurements support findings by O'Sullivan et al. (2012); Anderson et al. (2016); O'Sullivan et al. (2017) that Faraday complexity is expected in most polarized sources. The lower Faraday complexity found in the other less polarized sources may require more sensitive wide band and thus higher ϕ resolution studies to further tease out the properties that may be beyond our current efforts. Low polarisation sources may also have a significant degree of spectropolarimetric complexity that is beyond detection in studies with similar sensitivity and resolution limitations as ours. Our frequency coverage may also exclude sources that are highly depolarised at $\nu \sim 1-2$ GHz.

v. We determine the instrumental polarisation level in KAT 7 to have an upper limit of 0.07% in L-band. This is based on the polarisation level measured for the Faraday emission component found in the PKS1934-638 spectrum in this work – this source is unpolarised at the sensitivity and resolution of KAT 7 (e.g. Sault, 2003; Galluzzi et al., 2018).

Following the spectropolarimetric analysis of the six direct pointings with KAT 7, we further explored spectropolarimetric properties of various radio sources in the DEEP field area of sky observed with the initial 16 antenna MeerKAT array during the commissioning phase of the SKA precursor (Chapter 3). These observations are of better sensitivity ($\lesssim 100$ μJy/beam in linear polarisation, and $\lesssim 100$ μJy/beam in total intensity), wide field, and higher resolution ($\sim 14''$ in linear polarisation, and $\sim 6''$ in total intensity). The resolution in Faraday space is also improved as compared to the KAT 7 case, $\delta\phi \sim 50$ rad m^{-2}. Our conclusions are summarised as follows:

vi. Although most of the sources identified in the DEEP field observations are unresolved, we have found that our source finding method (using the AEGEAN source finder) results in multiple lines of sight through spatially complex sources. This provides different lines of sight that probe spatially different regions of these sources and thus provides spectra of different magneto-ionic regions. This suggests complex magneto-ionic arrangements that may show further structure when observed at high resolutions (e.g. Anderson et al., 2018).

vii. We have observed a significant number of polarised sources with significant complexity in the total intensity spectrum in the frequency range $\sim 810-1700$ MHz. This indicates a significant population of sources whose spectra deviate from the typical simple power law in synchrotron sources at $\nu \sim 1$ GHz. We also observe sources that display the expected spectral behaviour. Spectropolarimetric analysis on sources such as these will be further enriched with primary beam models, making it possible to make meaningful correlations between intrinsic source properties, such as the total intensity spectral index, and derived broad band spectropolarimetric properties, such as the polarised spectral index and Faraday complexity.

viii. We use the median polarisation degree of the undetected milli-Jy sources to estimate the upper limit of the instrumental polarisation level and find that this is 0.7%.

ix We find that polarised sources tend to be more spatially complex as compared to unpolarised sources. Polarised detections also tend to be steep with no detections showing spectra flatter than 0.5. This suggests a detection bias at the lower polarisations levels of flat spectrum compact sources.

x. We detected an average polarised source fraction of 24 ± 9%, which translates to an estimated average polarised source count of 30 ± 13 per square degree. This is not an accurate polarised source count due to uncorrected primary beam effects, but the value does serve as a good estimate to predictions (e.g. Rudnick and Owen, 2014).

xi. Our RM clean analysis excludes low signal to noise, large ϕ sources that are detected in direct polarisation. These sources are dubious detections, with the lowest direct detection significance, suggesting that they are either true but faint source detections or that their spectra are significantly noisy. The former scenario would indicate regions of relatively dense plasma or large field strengths of the large-scale magnetic field component somewhere along the line of sight.

xii. We find that our brightest polarised detections are also display the most Faraday complex behaviours, in accord with previous work. A small sub-population of Faraday simple sources is also found among the bright polarised detections. This may indicate complexity beyond the limits of detection in this work, as previous studies have shown that Faraday simple classifications can be made in cases where Faraday emission components are unresolved.

xiii. We find that the smoothly varying Galactic Faraday emission component in the DEEP field region is likely undetected in our RM clean analysis. Faraday emission components of our RM clean detections are rarely detected within the RMTF beam and those that are have low signal to noise.

5.2 Possible future work

The scope of the analysis presented in this work is limited, and we present some of the ways in which our findings can be enriched to better account for some of the spectropolarimetric properties that we, and others, have observed.

- The polarimetry measurements made in this work are subject to some variations, an example being the overpolarisation observed in the DEEP2off field observation, and the investigation and minimisation of these will be the subject of future work.

- We were limited by the lack of primary beam solutions during our analysis on MeerKAT commissioning observations. This limited our analysis of source properties, such as in the cases of the spectropolarimetric properties of steep versus flat spectrum sources, as they related to the true spectral index of the total intensity spectrum. We plan to enhance our analysis with better constraints on the primary beam as they become available in the near future.

- Theoretical constraints on spectropolarimetric parameters greatly aids in the interpretation of polarisation observations (e.g. Burn, 1966; Farnsworth et al., 2011; O'Sullivan et al., 2012; Sun et al., 2015; Anderson et al., 2016; Anderson et al., 2018; Pasetto et al., 2018) and we plan to extend our analysis to include model fitting of the observed polarisation spectra so as to enhance our conclusions.

- More sensitive observations will allow for the detection of fainter emission components and may support or disprove the detections of the high ϕ and low signal to noise components suggested by some of the lines of sight identified in this work. The full MeerKAT array and future survey projects such as MIGHTEE (MeerKAT International GHz Tiered Extragalactic Exploration) will be able to do this (Jarvis et al., 2017).

- An enrichment of our radio spectropolarimetric analysis with multi-wavelength studies of the properties of our radio sources may also provide some illumination regarding correlations between magneto-ionic properties of individual sources and other source properties such as those characterising source evolution at different cosmic times and different environmental effects especially for sources in extreme environments – e.g. peripheries and interiors of galaxy clusters in varying dynamical states (e.g. Feretti et al., 2012; Legodi, 2014; Sikhosana, 2016), galaxy groups, interacting galaxy environments, and also radio sources in cosmic voids.

- Depolarisation at large λ^2 is most severe as the sensitivity to Faraday complexity is proportional to λ_{min}^{-2} (Heald et al., 2009). Thus, broad band full polarisation observations that include higher frequencies and are also as continuous as possible can aid in detecting highly depolarised sources with the use of RM synthesis and also model fitting(e.g. Ideguchi et al., 2014; Sun et al., 2015; Anderson et al., 2016). A large λ^2 range is required as it has been shown that complex broad band behaviours are sometimes hidden and misleading best fitting models can be assumed when a narrow range of λ^2 is available (O'Sullivan et al., 2012; Gaensler et al., 2015; Brown et al., 2017).

Appendices

Appendix A

Appendices

A.1 Unpolarised sources

We have constructed a catalog of unpolarised sources in our mill-Jy sample and these are listed in Table A.1 – with column arrangement as in Table 3.3.

Table A.1: Catalog of UNPOLARISED sources (direct detections – see main text). [**], [*], and [A_{bm}] indicate units of [mJy/beam], [rad m^{-2}], and $14''$ beam area, respectively.

Source Name	RA [deg]	DEC [deg]	Δr [deg]	A_{fe} [A_{bm}]	$\tilde{\alpha}$	$\tilde{\alpha}_{c1}, \tilde{\alpha}_{c2}$	I_{peak} [**]	$\langle\sigma_{qu}\rangle$ [%]	β	$\langle p_0\rangle$ [%]	DF	$\lvert F\rvert_p$ [%]	ϕ_{peak} [*]	σ_ϕ [*]	T	$\tilde{T}$	Fid
J0408-80051	62.228	-80.853	0.462	0.23	-1.603	-2.891, -7.683	4.9	0.3	–	1.1	1	~ 1.3	~ -1039.0	–	5.7	3.8	–
J0400-80010	60.002	-80.173	0.757	0.24	-2.183	-3.221, -4.999	7.4	0.3	–	1.7	1	~ 1.2	~ -68.0	–	6.1	6.4	–
J0415-8043	63.903	-80.724	0.226	0.22	-0.633	-3.403, -8.601	2.2	0.7	–	2.3	1	~ 3.1	~ -23.5	–	6.1	4.4	–
J0411-8032	62.787	-80.549	0.216	0.25	-1.430	-12.758, -10.809	3.7	0.4	–	2.6	1	~ 3.0	~ -7.5	–	9.5	6.6	–
J0401-80031	60.344	-80.528	0.614	0.23	-2.180	-3.884, -4.375	1.9	1.0	–	2.6	1	~ 3.9	~ 613.0	–	5.2	2.3	–
J0401-81015	60.254	-81.261	0.971	0.64	-3.721	-8.708, -11.634	2.9	2.5	–	7.3	1	~ 6.4	~ -1881.5	–	5.2	4.7	–
J04018-8108	64.730	-81.134	0.642	0.54	-2.216	-8.186, -7.795	4.0	0.6	–	3.7	1	~ 2.9	~ 59.0	–	8.0	7.8	–
J04019-8107	64.758	-81.131	0.641	0.59	-2.053	-3.779, -5.134	2.4	0.8	–	3.2	1	~ 3.5	~ -1709.0	–	5.8	4.6	–
J0420-8027	65.013	-80.453	0.163	0.33	-0.757	-14.390, -13.661	2.5	0.5	–	3.1	1	~ 2.1	~ -843.0	–	4.9	6.1	–
J0433-8012	68.443	-80.201	0.792	0.24	-2.156	-2.472, -6.194	2.1	0.9	–	4.5	1	~ 3.7	~ -1744.5	–	5.2	4.7	–
J0430-8034	67.664	-80.568	0.595	0.27	-1.899	-3.403, -5.419	2.0	0.8	–	4.6	1	~ 4.5	~ -294.0	–	7.0	5.6	–
J0410-7949	62.615	-79.828	0.716	0.25	-2.356	-3.156, -5.506	1.7	1.4	–	5.0	1	~ 5.2	~ 1375.0	–	5.3	2.5	–
J0412-8043	63.243	-80.732	0.268	0.23	-1.657	-3.040, -6.205	1.8	1.0	–	5.2	1	~ 4.8	~ -399.0	–	6.9	5.0	–
J04025-8008	66.393	-80.134	0.536	0.40	-1.795	-3.400, -10.987	9.9	0.2	–	0.7	1	~ 0.9	~ -2.0	–	7.0	5.4	–
J0404-80028	61.044	-80.480	0.500	0.52	-1.639	-3.190, -4.560	1.4	1.2	–	4.5	1	~ 5.6	~ 1.0	–	6.1	4.4	–
J03051-8109	57.851	-81.157	1.188	0.32	-4.655	-3.572, -4.949	1.1	751538.4	–	2431146.2	1	$\sim nan$	~ -2000.0	–	nan	4.7	–
J0418-7957	64.609	-79.956	0.552	0.24	-1.863	-4.048, -3.854	1.9	0.9	–	2.8	1	~ 3.6	~ -715.0	–	5.0	3.0	–
J0419-8010	64.937	-80.181	0.350	0.23	-1.616	-13.859, -13.472	2.0	0.8	–	4.7	1	~ 3.6	~ -838.5	–	5.5	5.3	–
J03058-8103	59.617	-81.066	0.910	7.15	-2.708	-3.176, -7.760	1.4	3.0	–	11.3	1	~ 14.7	~ 1648.0	–	8.8	4.1	–
J0405-8101	61.276	-81.032	0.695	0.31	-2.412	-3.232, -12.068	1.9	1.2	–	4.5	1	~ 5.0	~ 807.0	–	5.3	4.1	–
J0421-8054	65.488	-80.909	0.469	0.23	-1.049	-9.117, -8.823	1.5	0.9	–	4.4	1	~ 3.1	~ 940.5	–	4.5	5.0	–
J0431-8039	67.946	-80.665	0.656	0.24	-2.219	-3.688, -5.787	2.5	0.9	–	5.2	1	~ 3.8	~ -1886.0	–	5.9	6.2	–
J0421-7928	65.412	-79.483	1.044	0.33	-4.026	-2.960, -8.014	4.2	1.5	–	2.3	1	~ 4.9	~ -683.0	–	5.0	4.9	–
J0414-8011	63.576	-80.194	0.317	0.29	-0.960	-3.641, -6.116	2.6	0.5	–	3.1	1	~ 2.3	~ 0.5	–	5.9	6.8	–
J0407-80017	61.992	-80.289	0.406	0.22	-1.556	-4.353, -5.072	2.3	0.7	–	1.9	1	~ 2.7	~ -920.5	–	5.1	2.1	–
J0430-8051	67.734	-80.861	0.695	0.25	-2.540	-6.883, -7.249	4.6	0.6	–	2.6	1	~ 2.2	~ 1384.5	–	5.5	5.0	–
J0421-7959	65.460	-79.998	0.554	0.23	-1.912	-3.631, -5.642	2.3	0.8	–	3.3	1	~ 3.3	~ 408.0	–	5.4	4.9	–
J0400-79054	60.071	-79.913	0.898	0.24	-2.471	-3.891, -5.964	3.8	0.7	–	2.1	1	~ 2.5	~ -72.5	–	5.4	3.2	–
J0411-8012	62.935	-80.206	0.350	0.22	-0.415	-12.020, -12.644	2.5	0.6	–	2.5	1	~ 2.6	~ 331.0	–	5.3	4.5	–
J0435-8045	68.943	-80.758	0.834	0.42	-2.801	-4.520, -5.650	2.6	1.2	–	5.4	1	~ 3.9	~ -189.5	–	4.5	5.7	–
J0420-8038	65.166	-80.646	0.232	0.38	-1.147	-5.421, -5.470	2.8	0.4	–	1.8	1	~ 1.5	~ 228.0	–	4.3	5.2	–
J0356-8040	59.054	-80.676	0.838	0.50	-2.818	-3.731, -6.551	5.2	0.6	–	2.9	1	~ 3.0	~ -28.5	–	7.5	7.1	–
J04022-8004	65.575	-80.072	0.497	1.11	-1.348	-6.137, -5.233	1.6	1.0	–	4.5	1	~ 4.4	~ -10.0	–	5.3	5.3	–
J0404-79056	61.066	-79.938	0.758	0.29	-2.689	-4.118, -5.549	6.1	0.4	–	1.8	1	~ 2.4	~ 3.0	–	7.8	5.6	–

... Continued on next page

Table A.1 – … *Continued from previous page*

Source Name	RA [deg]	DEC [deg]	Δr [deg]	A_{fe} [A_{bm}]	$\tilde{\alpha}$	$\tilde{\alpha}_{c1}, \tilde{\alpha}_{c2}$	I_{peak} [**]	$\langle\sigma_{qu}\rangle$ [%]	β	$\langle p_0\rangle$ [%]	DF	$\lvert F\rvert_p$ [%]	ϕ_{peak} [*]	σ_ϕ [*]	T	$\tilde{T}$	Fid
J0402-79051	60.654	-79.863	0.863	0.26	-2.935	-3.660, -4.926	1.9	2.1	–	7.2	1	~ 7.5	~ 1278.5	–	5.6	3.9	–
J0404-8101	61.229	-81.032	0.700	0.25	-2.554	-4.358, -4.909	4.7	0.5	–	3.1	1	~ 2.4	~ -25.5	–	6.6	7.8	–
J0414-8018	63.744	-80.310	0.198	0.22	-1.099	-5.401, -5.989	4.2	0.3	–	1.5	1	~ 1.1	~ 89.5	–	4.7	5.4	–
J0403-8103	60.796	-81.051	0.761	0.90	-2.421	-4.508, -5.011	1.5	1.4	–	2.7	1	~ 4.2	~ -1407.5	–	3.3	2.3	–
J04015-8105	63.880	-81.086	0.586	0.23	-2.280	-2.870, -8.160	2.0	1.2	–	5.9	1	~ 4.0	~ 667.5	–	4.9	5.9	–
J0418-8019	64.512	-80.325	0.190	0.22	-0.819	-4.344, -5.629	22.0	0.1	–	0.4	1	~ 0.3	~ -247.0	–	8.1	7.5	–
J0422-8050	65.634	-80.834	0.420	0.23	-1.814	-5.607, -5.725	2.7	0.6	–	2.9	1	~ 2.3	~ -1810.5	–	4.6	4.9	–
J0435-8126	68.820	-81.439	1.199	0.46	-4.670	-3.946, -4.332	7.2	3.3	–	10.8	1	~ 7.5	~ -158.5	–	3.9	6.9	–
J0419-8040	64.990	-80.681	0.236	0.26	-1.187	-3.024, -8.385	8.6	0.1	–	0.8	1	~ 0.9	~ -23.5	–	8.1	6.3	–
J0434-8122	68.738	-81.370	1.139	0.31	-4.613	-3.041, -6.053	3.7	3.9	–	13.2	1	~ 7.8	~ 1757.0	–	3.5	6.7	–
J0410-7954	62.642	-79.911	0.637	0.23	-0.960	-4.351, -5.303	1.6	1.0	–	4.1	1	~ 3.5	~ -813.0	–	4.8	4.5	–
J0434-7948	68.521	-79.804	1.031	0.52	-4.028	-4.321, -5.441	3.6	2.6	–	11.0	1	~ 7.8	~ -599.0	–	6.1	6.5	–
J0412-8130	63.045	-81.509	1.021	0.28	-3.845	-3.202, -7.119	2.3	3.9	–	14.9	1	~ 13.5	~ -576.0	–	7.2	4.8	–
J0408-80038	62.243	-80.636	0.329	0.23	-1.325	-11.435, -11.287	2.5	0.5	–	3.2	1	~ 3.1	~ -33.5	–	7.3	7.1	–
J0413-8056	63.357	-80.939	0.454	1.09	-1.887	-6.847, -6.788	1.2	1.7	–	8.0	1	~ 7.6	~ 816.0	–	5.5	4.0	–
J0400-79054	60.074	-79.911	0.899	2.22	-2.479	-4.780, -5.186	2.2	1.0	–	2.1	1	~ 3.8	~ -1990.5	–	4.6	2.5	–
J0409-80052	62.480	-80.870	0.450	0.23	-1.319	-3.811, -5.725	1.5	1.1	–	5.1	1	~ 4.3	~ -1488.5	–	5.3	5.4	–
J0413-8052	63.485	-80.872	0.384	0.44	-1.506	-5.723, -6.517	3.4	0.5	–	2.1	1	~ 1.8	~ -1868.0	–	4.8	5.6	–
J0404-80039	61.243	-80.655	0.488	0.23	-1.196	-3.019, -8.325	1.8	0.8	–	1.9	1	~ 3.1	~ 1786.0	–	5.3	2.6	–
J0414-8029	63.742	-80.485	0.056	0.89	-1.858	-3.331, -6.525	1.5	1.2	–	4.3	1	~ 4.9	~ 54.5	–	5.0	3.8	–
J0406-81017	61.589	-81.286	0.879	0.27	-3.384	-4.042, -5.589	5.2	0.8	–	3.8	1	~ 3.0	~ 1450.5	–	5.6	5.0	–
J0435-8026	68.921	-80.435	0.806	0.25	-2.812	-6.916, -6.303	3.2	1.0	–	3.3	1	~ 4.2	~ -1797.0	–	6.3	3.2	–
J0416-8020	64.095	-80.348	0.152	2.01	-0.816	-3.077, -6.887	2.1	0.5	–	1.3	1	~ 2.1	~ 244.5	–	4.9	2.4	–
J0427-8043	66.955	-80.722	0.521	0.30	-1.678	-2.823, -5.992	4.8	0.3	–	1.6	1	~ 1.6	~ -20.5	–	6.6	6.8	–
J04028-8003	67.152	-80.060	0.681	0.24	-2.303	-4.096, -5.540	2.7	0.8	–	0.9	1	~ 2.4	~ -1473.5	–	4.2	1.6	–
J0426-7949	66.698	-79.818	0.817	0.36	-2.792	-7.555, -7.588	5.0	0.6	–	2.8	1	~ 3.8	~ -26.0	–	9.6	6.6	–
J0427-8042	66.956	-80.712	0.517	0.56	-1.630	-3.568, -5.714	1.8	1.1	–	6.9	1	~ 6.2	~ -37.5	–	8.2	6.1	–
J0420-8042	65.003	-80.702	0.253	0.35	-0.901	-7.363, -7.031	2.0	0.7	–	2.7	1	~ 2.8	~ -323.0	–	5.3	4.4	–
J0417-7951	64.282	-79.858	0.643	0.30	-2.061	-3.141, -5.257	2.1	0.9	–	2.6	1	~ 3.1	~ -1167.5	–	4.3	2.9	–
J0426-8045	66.627	-80.754	0.488	0.22	-1.513	-6.364, -4.769	10.9	0.1	–	0.7	1	~ 0.5	~ -805.5	–	4.5	6.2	–
J0422-8030	65.556	-80.502	0.246	0.22	-1.130	-7.188, -6.670	6.4	0.2	–	0.9	1	~ 0.7	~ 1202.5	–	4.5	5.7	–
J0439-8015	69.822	-80.262	0.990	0.26	-3.759	-3.550, -4.839	3.2	1.9	–	8.9	1	~ 6.3	~ -958.0	–	5.6	6.2	–
J0423-7951	65.827	-79.852	0.714	0.48	-2.258	-6.294, -6.338	3.2	0.6	–	2.7	1	~ 2.0	~ -1633.0	–	4.1	5.5	–
J0406-80018	61.596	-80.314	0.452	0.25	-1.876	-8.204, -7.828	5.9	0.3	–	1.5	1	~ 1.4	~ 145.5	–	6.5	5.0	–
J04010-8100	62.679	-81.007	0.554	0.24	-2.015	-4.609, -4.448	1.8	1.0	–	1.8	1	~ 3.5	~ -27.5	–	4.6	2.7	–
J0412-8115	63.023	-81.254	0.772	0.80	-2.511	-3.035, -5.856	1.8	1.6	–	7.3	1	~ 6.6	~ -1415.5	–	5.8	4.5	–

… *Continued on next page*

Table A.1 – … *Continued from previous page*

Source Name	RA [deg]	DEC [deg]	Δr [deg]	A_{fe} [A_{bm}]	$\tilde{\alpha}$	$\tilde{\alpha}_{c1}, \tilde{\alpha}_{c2}$	I_{peak} [**]	$\langle \sigma_{qu} \rangle$ [%]	β	$\langle p_0 \rangle$ [%]	DF	$\|F\|_p$ [%]	ϕ_{peak} [*]	σ_ϕ [*]	T	$\tilde{T}$	Fid
J0400-8107	60.085	-81.121	0.888	0.52	-3.014	-4.060, -12.450	3.0	1.1	–	3.9	1	~ 4.5	~ 545.5	–	6.2	3.9	–
J0426-8053	66.647	-80.895	0.574	0.23	-1.800	-3.535, -5.377	6.3	0.3	–	1.3	1	~ 1.1	~ 312.5	–	6.2	5.2	–
J04023-8006	65.887	-80.107	0.498	0.22	-0.655	-3.677, -7.375	5.5	0.3	–	0.4	1	~ 1.1	~ 54.0	–	5.7	2.6	–
J0421-7928	65.399	-79.483	1.043	0.76	-4.029	-4.718, -5.135	4.5	1.5	–	3.3	1	~ 4.9	~ -743.5	–	5.5	3.8	–
J0419-8116	64.928	-81.282	0.794	0.24	-2.830	-7.084, -5.719	2.2	1.4	–	4.4	1	~ 4.4	~ -742.0	–	4.5	2.1	–
J0410-8020	62.505	-80.348	0.301	0.22	-1.254	-3.103, -9.790	1.4	1.0	–	2.7	1	~ 3.4	~ 260.5	–	4.3	3.1	–
J0415-7959	63.787	-79.995	0.508	0.24	-2.343	-2.851, -10.556	12.7	0.2	–	0.5	1	~ 0.5	~ 353.5	–	4.0	5.6	–
J0421-8026	65.299	-80.445	0.211	0.22	-0.802	-3.768, -5.333	2.3	0.5	–	2.1	1	~ 2.6	~ 459.0	–	6.0	4.3	–
J0413-8059	63.294	-80.997	0.512	0.23	-1.827	-4.568, -5.035	2.4	0.7	–	3.6	1	~ 2.6	~ 859.5	–	4.7	5.2	–
J0425-8046	66.429	-80.772	0.471	0.23	-1.714	-7.322, -6.970	4.3	0.4	–	1.4	1	~ 1.4	~ -668.5	–	5.1	2.9	–
J0414-8057	63.737	-80.960	0.463	0.23	-1.649	-3.769, -5.528	2.9	0.5	–	1.1	1	~ 1.7	~ 1818.5	–	4.1	2.8	–
J0408-80025	62.082	-80.431	0.336	0.22	-0.441	-7.616, -7.102	2.7	0.6	–	0.2	1	~ 1.9	~ -1157.0	–	4.3	1.3	–
J0408-79046	62.156	-79.779	0.791	0.43	-2.591	-6.009, -6.706	3.4	0.7	–	1.8	1	~ 2.4	~ -1999.5	–	4.4	3.9	–
J0411-7928	62.864	-79.477	1.044	0.28	-4.279	-3.309, -4.105	3.5	3.2	–	3.8	1	~ 8.3	~ 1813.5	–	5.4	2.6	–
J04031-8008	67.914	-80.139	0.740	0.23	-2.255	-8.425, -8.686	1.9	1.3	–	3.2	1	~ 5.6	~ -274.5	–	5.9	2.4	–
J04013-8006	63.465	-80.115	0.398	0.24	-1.455	-2.959, -6.299	4.1	0.4	–	1.4	1	~ 1.2	~ -573.5	–	4.5	4.1	–
J0353-8036	58.275	-80.607	0.956	0.28	-3.901	-3.002, -5.816	3.0	2.1	–	7.6	1	~ 7.3	~ -273.0	–	5.9	4.7	–
J04026-8004	66.611	-80.067	0.610	0.27	-1.924	-5.272, -6.784	2.2	0.8	–	2.7	1	~ 2.7	~ -1941.5	–	4.2	4.1	–
J0410-8046	62.630	-80.771	0.358	0.22	-0.994	-2.808, -3.990	7.2	0.2	–	0.9	1	~ 0.6	~ -118.5	–	4.9	6.6	–
J0406-80035	61.617	-80.585	0.412	0.24	-1.530	-3.446, -3.762	1.6	1.0	–	3.9	1	~ 3.5	~ 1642.5	–	4.5	4.6	–
J0406-80010	61.566	-80.182	0.526	0.23	-1.576	-3.980, -4.172	1.8	1.0	–	5.8	1	~ 8.2	~ -6.5	–	12.3	6.5	–
J03058-8103	59.627	-81.062	0.906	0.28	-3.275	-3.430, -5.901	5.8	0.7	–	3.7	1	~ 3.4	~ -385.5	–	7.8	5.9	–
J0419-8017	64.781	-80.296	0.236	0.22	-0.940	-6.826, -6.938	2.2	0.5	–	2.7	1	~ 2.3	~ 595.0	–	5.4	5.2	–
J04033-8003	68.437	-80.054	0.862	0.43	-2.845	-4.098, -6.142	5.1	0.6	–	2.4	1	~ 2.0	~ -410.5	–	4.8	5.5	–
J0413-8028	63.327	-80.480	0.124	0.22	-0.774	-4.211, -5.612	2.0	0.7	–	1.7	1	~ 2.4	~ -194.0	–	4.5	2.8	–
J0425-8014	66.263	-80.237	0.452	1.61	-1.425	-3.137, -6.605	1.5	1.1	–	6.5	1	~ 3.9	~ -558.5	–	4.6	6.7	–
J0428-8045	67.152	-80.762	0.566	0.23	-1.880	-3.981, -5.379	2.4	0.8	–	1.1	1	~ 2.9	~ -1580.5	–	4.6	1.4	–
J0430-8116	67.648	-81.280	0.964	0.26	-3.357	-4.072, -4.966	2.7	2.0	–	6.6	1	~ 7.9	~ 1648.5	–	6.7	2.7	–
J0433-8024	68.268	-80.409	0.702	0.24	-2.224	-3.098, -6.182	2.8	0.8	–	3.1	1	~ 2.8	~ 511.5	–	5.2	4.8	–
J0359-8036	59.940	-80.605	0.685	0.23	-2.102	-4.229, -5.130	3.0	0.6	–	2.7	1	~ 2.4	~ 615.0	–	5.2	4.8	–
J0427-8043	66.950	-80.719	0.519	0.75	-1.335	-3.505, -7.012	2.0	0.7	–	3.3	1	~ 2.5	~ -123.5	–	4.6	5.8	–
J0411-8029	62.839	-80.484	0.204	0.28	-1.230	26.217, -157.917	2.7	0.5	–	2.4	1	~ 1.8	~ 515.5	–	4.7	5.0	–
J0400-8107	60.082	-81.125	0.891	0.65	-3.260	-3.108, -6.788	4.7	0.8	–	4.2	1	~ 3.0	~ -448.5	–	5.7	5.9	–
J0414-8016	63.612	-80.268	0.244	0.22	-0.839	-3.001, -7.619	24.1	0.1	–	0.5	1	~ 0.4	~ -199.0	–	10.6	8.1	–
J0426-8044	66.745	-80.749	0.502	0.25	-1.669	-5.143, -5.309	4.1	0.4	–	0.6	1	~ 1.4	~ 1597.0	–	4.9	1.5	–
J0428-8057	67.115	-80.955	0.669	0.31	-2.048	-5.226, -5.502	2.2	0.7	–	2.2	1	~ 2.9	~ -1994.0	–	4.7	3.9	–

… *Continued on next page*

Table A.1 – … *Continued from previous page*

Source Name	RA [deg]	DEC [deg]	Δr [deg]	A_{fe} [A_{bm}]	$\tilde{\alpha}$	$\tilde{\alpha}_{c1}, \tilde{\alpha}_{c2}$	I_{peak} [**]	$\langle\sigma_{qu}\rangle$ [%]	β	$\langle p_0\rangle$ [%]	DF	$\lvert F\rvert_p$ [%]	ϕ_{peak} [*]	σ_ϕ [*]	T	$\tilde{T}$	Fid
J0418-7942	64.619	-79.712	0.793	0.31	-2.732	-3.109, -6.827	3.0	1.0	–	2.9	1	~ 3.5	~ 1334.5	–	4.9	2.5	–
J0423-7951	65.845	-79.855	0.713	0.60	-2.478	-4.287, -5.297	3.0	0.8	–	2.6	1	~ 2.8	~ -1963.0	–	4.9	3.8	–
J0421-8032	65.329	-80.543	0.212	0.42	-1.134	-3.054, -8.516	3.5	0.4	–	1.5	1	~ 1.6	~ 1002.0	–	5.4	4.4	–
J0356-8040	59.041	-80.672	0.840	0.66	-2.495	-5.952, -7.408	2.6	1.1	–	5.8	1	~ 4.5	~ -1037.5	–	5.9	5.1	–
J0410-7943	62.721	-79.721	0.812	0.32	-2.806	-4.101, -4.188	4.1	0.7	–	3.0	1	~ 2.6	~ -1957.0	–	5.5	4.4	–
J0413-7946	63.416	-79.773	0.228	0.56	-1.128	-6.836, -3.871	1.3	1.2	–	5.6	2	~ 5.3	~ -187.0	–	5.5	4.6	–
J0406-79039	61.739	-79.663	0.442	0.10	-1.798	-2.221, -4.142	2.1	0.7	–	2.7	2	~ 2.3	~ 1691.0	–	4.2	4.7	–
J0408-80025	62.080	-80.431	0.483	0.10	0.033	-3.205, -2.964	3.9	0.3	–	1.8	2	~ 1.4	~ 7.5	–	5.9	6.1	–
J0419-7914	64.843	-79.248	0.798	0.12	-4.049	-3.631, -2.559	2.5	2.1	–	5.5	2	~ 5.9	~ -1294.0	–	5.3	5.1	–
J0420-7927	65.194	-79.460	0.631	0.11	-1.839	-6.183, -5.592	7.5	0.2	–	1.1	2	~ 1.1	~ 88.0	–	8.4	5.9	–
J0411-7948	62.912	-79.805	0.210	0.13	-1.281	-2.395, -4.178	2.9	0.5	–	1.5	2	~ 1.8	~ -288.5	–	4.5	3.6	–
J0401-79040	60.410	-79.675	0.614	0.17	-2.935	-10.793, -5.930	2.6	0.9	–	4.7	2	~ 4.2	~ 506.0	–	6.4	5.5	–
J0410-8046	62.629	-80.771	0.781	0.11	-3.591	-3.552, -1.166	2.6	1.2	–	5.5	2	~ 5.2	~ 0.5	–	7.0	4.7	–
J0425-7914	66.262	-79.240	0.922	0.14	-4.387	-1.644, -2.730	7.4	0.7	–	3.2	2	~ 2.4	~ -122.5	–	6.0	5.1	–
J0419-8017	64.779	-80.296	0.383	0.10	-1.231	-2.693, 5.527	1.8	0.9	–	6.8	2	~ 3.3	~ 246.0	–	5.3	8.0	–
J0424-7938	66.030	-79.649	0.588	0.15	-2.790	-2.227, -4.733	9.6	0.3	–	1.7	2	~ 1.9	~ 153.0	–	12.0	8.0	–
J0422-8030	65.555	-80.502	0.624	0.11	-2.354	-5.783, -0.778	3.0	0.5	–	2.2	2	~ 2.0	~ -891.0	–	5.0	4.1	–
J0414-8041	63.617	-80.691	0.692	0.44	-3.859	-7.511, -2.301	2.7	1.7	–	6.7	2	~ 3.9	~ 1727.5	–	4.1	5.7	–
J0424-7939	66.002	-79.653	0.582	0.23	-2.719	-2.870, -4.630	15.6	0.1	–	1.2	2	~ 1.1	~ 3.0	–	12.8	8.5	–
J0359-7915	59.751	-79.261	0.983	0.16	-4.646	-7.282, -5.802	10.1	3.5	–	8.0	2	~ 4.6	~ -553.5	–	3.8	7.9	–
J0407-80017	61.990	-80.289	0.372	0.10	-1.917	-6.992, -0.609	2.2	0.6	–	2.6	2	~ 2.1	~ 1702.5	–	4.1	3.4	–
J0354-8023	58.515	-80.394	0.914	0.13	-4.671	-3.021, -5.285	11.8	1.6	–	6.3	2	~ 4.4	~ -73.0	–	7.9	7.9	–
J0411-8032	62.786	-80.549	0.557	0.14	-2.698	-10.753, -10.365	2.1	1.0	–	5.4	2	~ 5.0	~ 1661.0	–	6.8	5.1	–
J0403-79046	60.880	-79.767	0.494	0.22	-2.978	-2.651, -3.867	2.4	1.2	–	4.5	2	~ 4.5	~ -472.0	–	6.2	4.4	–
J0424-7914	66.249	-79.239	0.922	0.21	-4.530	-2.335, -2.405	6.0	1.2	–	4.3	2	~ 3.9	~ 76.0	–	7.2	6.0	–
J0415-7921	63.992	-79.352	0.658	0.11	-3.048	-6.083, -4.357	3.0	0.8	–	3.0	2	~ 2.9	~ -1048.0	–	4.9	5.3	–
J04023-8006	65.884	-80.107	0.449	0.11	-0.361	-7.739, -6.102	5.3	0.2	–	1.6	2	~ 1.3	~ -6.5	–	8.5	8.4	–
J0423-7951	65.842	-79.855	0.458	0.47	-2.176	-4.027, -2.264	4.6	0.5	–	2.9	2	~ 2.2	~ 68.0	–	7.5	7.1	–
J04021-8002	65.491	-80.047	0.372	1.99	-2.661	-4.234, -1.730	2.1	1.3	–	4.6	2	~ 4.3	~ -1998.5	–	4.8	4.0	–
J0424-7938	66.021	-79.650	0.586	0.13	-2.654	-0.963, -4.731	12.7	0.2	–	1.4	2	~ 1.0	~ -252.0	–	8.7	7.6	–
J0418-8032	64.721	-80.550	0.596	0.11	-2.873	-9.338, -8.786	2.0	1.1	–	7.6	2	~ 6.1	~ 1.0	–	7.9	7.3	–
J0425-8014	66.259	-80.234	0.550	1.21	-3.373	-1.890, -3.193	3.3	1.1	–	7.2	2	~ 5.7	~ 65.5	–	10.2	7.2	–
J0359-8036	59.939	-80.605	0.836	0.11	-4.555	-1.220, -7.662	2.3	2.3	–	8.5	2	~ 7.8	~ -1376.5	–	4.9	5.8	–
J0404-79027	61.163	-79.463	0.665	0.28	-3.123	-7.154, -4.303	2.5	1.1	–	5.2	2	~ 4.9	~ 49.5	–	6.2	4.9	–
J0411-8012	62.932	-80.206	0.219	0.10	-0.161	-3.386, -2.437	2.6	0.4	–	2.8	2	~ 2.2	~ -18.0	–	7.1	7.9	–
J0417-7917	64.468	-79.291	0.737	0.50	-4.245	-4.907, -3.480	2.4	1.8	–	2.2	2	~ 5.5	~ 562.5	–	4.4	2.5	–

… *Continued on next page*

Table A.1 – … *Continued from previous page*

Source Name	RA [deg]	DEC [deg]	Δr [deg]	A_{fe} [A_{bm}]	$\tilde{\alpha}$	$\tilde{\alpha}_{c1}, \tilde{\alpha}_{c2}$	I_{peak} [**]	$\langle\sigma_{qu}\rangle$ [%]	β	$\langle p_0\rangle$ [%]	DF	$\lvert F\rvert_p$ [%]	ϕ_{peak} [*]	σ_ϕ [*]	T	$\tilde{T}$	Fid
J04026-8003	66.608	-80.067	0.566	0.14	-2.598	-2.582, -1.740	2.3	0.9	–	5.4	2	~ 4.2	~ -1904.0	–	6.3	6.1	–
J0415-7912	63.854	-79.214	0.791	0.17	-4.578	-10.108, -7.347	7.6	0.8	–	2.8	2	~ 3.5	~ 70.0	–	7.7	7.9	–
J0411-8029	62.837	-80.484	0.492	0.16	-2.341	-3.203, 0.651	2.2	1.0	–	3.2	2	~ 3.6	~ -1580.0	–	4.8	4.4	–
J0406-80018	61.641	-80.311	0.428	0.14	-2.185	-2.395, -4.463	10.8	0.1	–	0.8	2	~ 0.7	~ -138.5	–	6.4	6.7	–
J0407-8003	61.882	-80.064	0.264	0.10	-0.529	-4.654, -3.704	2.0	0.5	–	3.0	2	~ 2.2	~ -1565.0	–	4.8	5.7	–
J0423-7929	65.956	-79.492	0.686	0.11	-4.071	-2.542, -2.586	2.3	2.3	–	7.0	2	~ 6.4	~ 1338.0	–	5.5	5.1	–
J0414-8011	63.574	-80.194	0.198	0.16	-0.909	-2.097, -3.849	2.8	0.4	–	3.3	2	~ 2.9	~ -15.5	–	9.0	7.2	–
J0417-7943	64.409	-79.731	0.326	0.11	-2.160	-38.524, -56.300	2.0	0.8	–	3.4	2	~ 2.9	~ 255.0	–	4.8	3.8	–
J0412-7946	63.076	-79.772	0.234	0.43	-1.344	-3.572, -4.069	2.2	0.6	–	4.6	2	~ 3.5	~ -18.0	–	7.0	7.4	–
J0410-7943	62.717	-79.721	0.301	0.18	-1.392	-10.198, -8.673	9.6	0.1	–	1.0	2	~ 0.9	~ 11.5	–	9.3	7.2	–
J0423-7948	65.870	-79.816	0.477	0.11	-2.067	-3.500, -3.242	2.3	0.7	–	2.9	2	~ 3.0	~ 342.0	–	5.8	3.4	–
J0417-7938	64.427	-79.647	0.400	0.12	-1.836	-2.871, -3.406	3.0	0.5	–	2.8	2	~ 1.9	~ 89.0	–	4.9	6.4	–
J0413-7949	63.335	-79.827	0.173	0.16	-1.110	-1.961, -3.850	2.6	0.5	–	3.7	2	~ 2.8	~ 90.5	–	7.2	8.5	–
J0425-8014	66.259	-80.250	0.556	0.56	-1.667	-3.554, -4.436	2.3	0.8	–	5.3	2	~ 5.0	~ -13.5	–	8.4	6.8	–
J0352-8022	58.183	-80.376	0.959	0.10	-4.687	-2.329, -4.836	9.9	4.1	–	17.5	2	~ 7.0	~ -151.0	–	5.2	7.1	–
J0423-7926	65.880	-79.446	0.714	0.28	-3.744	-3.207, -4.522	4.9	0.9	–	3.5	2	~ 3.0	~ 889.0	–	7.3	5.5	–
J0417-7915	64.336	-79.257	0.764	0.12	-3.243	-2.679, -7.022	2.8	0.9	–	3.8	2	~ 3.4	~ 922.0	–	5.0	5.0	–
J0420-7933	65.016	-79.559	0.529	0.10	-1.924	-4.154, -3.442	2.1	0.7	–	3.3	2	~ 2.5	~ -1051.0	–	4.7	5.2	–
J0423-7951	65.824	-79.852	0.456	0.34	-2.011	-3.434, -4.885	4.6	0.3	–	1.5	2	~ 1.5	~ 159.0	–	6.0	4.4	–
J0421-7922	65.416	-79.377	0.723	0.13	-3.617	-4.868, -4.550	2.7	1.2	–	3.0	2	~ 3.2	~ -1290.5	–	4.0	3.0	–
J0402-79051	60.651	-79.863	0.493	0.11	-2.007	-5.403, -1.920	3.7	0.4	–	2.3	2	~ 1.8	~ -1974.5	–	6.0	6.0	–
J0421-8032	65.327	-80.543	0.637	0.28	-3.584	-6.799, -2.805	2.0	1.8	–	3.6	2	~ 5.9	~ -1004.0	–	4.8	3.5	–
J04013-8006	63.462	-80.115	0.117	0.11	-1.105	-10.760, -9.666	4.9	0.3	–	1.9	2	~ 1.5	~ 1.0	–	7.9	7.1	–
J0414-8018	63.742	-80.310	0.317	0.10	-1.176	-1.923, -4.201	3.7	0.3	–	1.9	2	~ 1.9	~ 236.0	–	8.0	5.7	–
J0411-8028	62.774	-80.479	0.489	0.17	-2.153	-5.559, -3.816	2.4	0.7	–	3.6	2	~ 3.6	~ 6.0	–	6.9	5.8	–
J0411-7928	62.861	-79.477	0.530	0.11	-2.082	-8.319, -4.379	10.4	0.2	–	1.0	2	~ 0.9	~ 0.0	–	7.5	7.7	–
J0432-7944	68.024	-79.741	0.860	0.14	-4.594	-5.180, -3.141	12.3	0.5	–	1.4	2	~ 1.7	~ -532.0	–	5.8	6.5	–
J0419-8040	64.989	-80.681	0.734	0.15	-3.514	-26.009, -30.358	4.1	0.7	–	1.9	2	~ 2.9	~ 1459.5	–	5.9	4.8	–
J0410-7949	62.612	-79.829	0.216	0.12	-1.452	-8.497, -4.315	3.5	0.3	–	1.4	2	~ 1.5	~ -557.5	–	5.3	3.9	–
J0404-79020	61.243	-79.345	0.757	0.11	-4.215	-1.631, -6.007	2.4	2.3	–	10.0	2	~ 6.6	~ 1716.5	–	5.2	6.7	–
J0416-8025	64.067	-80.417	0.434	0.11	-1.811	-2.713, -3.108	1.8	0.7	–	5.0	2	~ 3.5	~ -5.0	–	5.4	7.6	–
J04028-8003	67.150	-80.060	0.659	0.11	-3.422	-7.914, -3.288	2.8	1.1	–	2.6	2	~ 3.8	~ 825.5	–	5.3	2.8	–
J04033-8003	68.435	-80.054	0.880	0.12	-4.631	-4.184, -4.374	4.5	2.1	–	10.0	2	~ 6.4	~ -215.0	–	5.4	7.3	–
J0355-7948	58.789	-79.809	0.824	0.11	-3.904	-119.508, -198.765	3.3	1.2	–	6.7	2	~ 3.8	~ 1512.0	–	5.4	5.8	–
J0358-7926	59.529	-79.441	0.883	0.11	-4.604	-1.681, -4.401	6.0	1.1	–	0.6	2	~ 3.7	~ 841.0	–	5.5	3.5	–
J04033-8003	68.430	-80.053	0.879	0.53	-4.617	-1.941, -2.447	4.0	2.1	–	6.8	2	~ 6.9	~ -16.0	–	5.0	4.8	–

… *Continued on next page*

Table A.1 – … *Continued from previous page*

Source Name	RA [deg]	DEC [deg]	Δr [deg]	A_{fe} [A_{bm}]	$\tilde{\alpha}$	$\tilde{\alpha}_{c1}, \tilde{\alpha}_{c2}$	I_{peak} [**]	$\langle \sigma_{qu} \rangle$ [%]	β	$\langle p_0 \rangle$ [%]	DF	$\lvert F \rvert_p$ [%]	ϕ_{peak} [*]	σ_ϕ [*]	T	$\tilde{T}$	Fid
J0410-7954	62.639	-79.911	0.154	0.10	0.563	-2.966, -3.317	2.4	0.5	–	2.2	2	~ 2.1	~ -1290.0	–	5.4	4.2	–
J04012-7908	63.065	-79.144	0.858	0.12	-4.416	-2.534, -1.914	2.9	1.9	–	4.1	2	~ 5.4	~ 1885.0	–	4.9	3.6	–
J0421-7959	65.458	-79.998	0.364	0.11	-1.801	-4.402, -5.489	2.7	0.5	–	1.6	2	~ 2.3	~ 1957.5	–	5.8	2.8	–
J0426-7949	66.708	-79.818	0.614	0.56	-3.352	-1.755, -3.852	3.4	1.0	–	5.3	2	~ 3.5	~ 3.0	–	5.5	8.1	–
J0400-79054	60.069	-79.913	0.580	0.10	-1.174	-6.739, -3.011	7.3	0.2	–	1.2	2	~ 1.1	~ 165.0	–	8.9	6.4	–
J0425-7914	66.272	-79.235	0.928	0.42	-4.614	-5.074, -2.853	3.1	3.5	–	11.4	2	~ 8.8	~ 449.5	–	5.1	5.4	–
J0419-7934	64.977	-79.571	0.516	0.11	-2.280	-3.834, -6.169	3.3	0.5	–	1.9	2	~ 2.2	~ 1885.5	–	5.2	3.6	–
J0417-7951	64.279	-79.858	0.214	0.16	-0.856	-4.575, -4.108	3.1	0.5	–	3.3	2	~ 2.4	~ -53.0	–	7.8	6.9	–
J0418-7957	64.606	-79.956	0.221	0.11	-1.289	-8.119, -6.840	2.5	0.4	–	2.7	2	~ 2.2	~ -369.0	–	5.7	6.9	–
J0411-8032	62.789	-80.549	0.469	0.17	-2.478	-2.662, -6.054	1.3	3.6	–	8.6	2off	~ 9.9	~ -349.0	–	4.5	3.7	–
J0345-8112	56.470	-81.210	0.816	0.15	-4.611	-7.494, -3.435	1.4	242.6	–	441.9	2off	~ 21.3	~ 1320.0	–	0.3	5.4	–
J0400-8107	60.088	-81.125	0.520	0.23	-2.144	-14.273, -21.523	6.5	0.6	–	3.6	2off	~ 1.9	~ -54.0	–	5.0	6.3	–
J03051-8109	57.854	-81.158	0.644	0.14	-3.437	-14.564, -20.252	2.4	5.2	–	22.6	2off	~ 9.2	~ -1769.5	–	4.2	4.5	–
J0401-81015	60.257	-81.262	0.658	0.53	-3.296	-2.611, -3.657	3.4	2.8	–	11.3	2off	~ 5.8	~ -388.0	–	4.3	5.3	–
J0408-80038	62.244	-80.636	0.376	0.15	-1.479	-2.752, -7.312	1.4	2.1	–	3.1	2off	~ 6.2	~ -1320.0	–	3.8	2.4	–
J0350-7942	57.522	-79.704	0.992	0.32	-4.585	-3.662, -5.909	3.4	120.3	–	343.5	2off	~ 12.0	~ 615.0	–	0.5	5.3	–
J0358-8039	59.511	-80.665	0.092	0.13	-1.269	-4.967, -6.290	1.6	2.2	–	7.5	2off	~ 5.1	~ 706.0	–	3.1	3.3	–
J0418-8019	64.513	-80.326	0.807	0.16	-2.936	-2.882, -8.266	4.1	1.8	–	4.7	2off	~ 4.1	~ 8.5	–	4.1	4.1	–
J0408-80025	62.083	-80.432	0.393	0.14	0.244	1.417, -12.290	3.3	1.2	–	5.9	2off	~ 2.9	~ -173.0	–	4.2	5.7	–
J03048-8004	57.031	-80.071	0.724	0.47	-2.942	-3.730, -8.999	1.5	5.0	–	23.8	2off	~ 13.2	~ -80.5	–	4.6	6.7	–
J0406-80018	61.643	-80.312	0.407	0.19	-1.698	-3.307, -7.456	6.9	0.5	–	3.5	2off	~ 2.1	~ -2.5	–	7.1	6.8	–
J0352-8022	58.189	-80.371	0.373	0.67	2.319	-6.468, -10.335	2.2	166.0	–	782.8	2off	~ 39.0	~ 26.0	–	5.1	11.4	–
J0404-79056	61.066	-79.939	0.693	0.17	-3.245	-4.738, -15.697	3.6	1.8	–	6.5	2off	~ 3.4	~ -756.5	–	3.5	4.5	–
J0400-8107	60.078	-81.126	0.521	0.34	-2.248	-3.787, 4.084	5.5	0.6	–	3.5	2off	~ 2.1	~ -11.5	–	4.8	6.5	–
J0342-8034	55.639	-80.579	0.704	0.14	-3.668	-4.155, -7.624	3.0	4.1	–	11.2	2off	~ 6.2	~ -376.0	–	3.2	3.2	–
J0413-8052	63.486	-80.873	0.630	0.31	-3.074	-54.910, -93.151	1.2	6.1	–	19.0	2off	~ 14.3	~ -759.5	–	3.7	3.9	–
J03059-8104	59.934	-81.075	0.469	0.14	-1.605	-4.866, -8.545	1.8	2.6	–	10.7	2off	~ 7.2	~ 271.5	–	4.0	4.7	–
J03052-8003	58.030	-80.065	0.629	0.17	-2.324	-5.788, -8.743	5.0	0.8	–	5.0	2off	~ 3.0	~ -18.0	–	5.7	6.4	–
J0356-8020	59.037	-80.348	0.298	0.14	-1.293	-3.543, -7.449	2.9	1.0	–	6.0	2off	~ 4.0	~ 7.0	–	6.1	5.8	–
J0400-80037	60.096	-80.621	0.029	0.51	-0.817	-2.635, -5.856	3.5	0.8	–	3.4	2off	~ 3.7	~ -66.0	–	6.2	5.1	–
J0359-8035	59.768	-80.590	0.032	1.20	-0.220	-11.407, -13.298	1.3	3.2	–	8.8	2off	~ 6.7	~ -345.0	–	3.1	3.4	–
J0345-8043	56.326	-80.726	0.599	0.13	-2.129	-2.754, -7.696	2.0	2.0	–	7.4	2off	~ 5.7	~ 79.0	–	4.1	4.9	–
J0355-7948	58.792	-79.809	0.820	0.15	-3.500	-2.843, -6.417	2.1	4.8	–	10.0	2off	~ 8.1	~ -1101.5	–	3.3	2.5	–
J0353-8036	58.276	-80.607	0.272	0.14	-1.401	-11.255, -14.810	6.2	0.5	–	3.1	2off	~ 2.8	~ -11.5	–	9.2	6.5	–
J0342-8035	55.647	-80.594	0.701	0.13	-3.272	-31.539, -47.618	2.4	6.0	–	14.2	2off	~ 11.1	~ -1782.0	–	4.0	3.7	–
J0405-8101	61.278	-81.032	0.477	0.21	-1.367	-25.007, -98.994	1.5	4.4	–	6.4	2off	~ 8.3	~ -1012.0	–	2.9	2.2	–

… *Continued on next page*

Table A.1 – … *Continued from previous page*

Source Name	RA [deg]	DEC [deg]	Δr [deg]	A_{fe} [A_{bm}]	$\tilde{\alpha}$	$\tilde{\alpha}_{c1}, \tilde{\alpha}_{c2}$	I_{peak} [**]	$\langle \sigma_{qu} \rangle$ [%]	β	$\langle p_0 \rangle$ [%]	DF	$\vert F \vert_p$ [%]	ϕ_{peak} [*]	σ_ϕ [*]	T	$\tilde{T}$	Fid
J0357-8043	59.334	-80.731	0.159	0.13	-1.218	-4.049, -6.061	1.6	1.7	–	4.6	2off	~ 4.5	~ -403.5	–	3.5	2.4	–
J0411-8028	62.777	-80.479	0.483	0.20	-1.718	-11.151, -13.027	1.6	2.6	–	17.4	2off	~ 8.1	~ 1035.0	–	4.4	7.4	–
J0345-8023	56.434	-80.388	0.619	0.23	-3.148	-6.415, -9.267	1.5	6.6	–	10.5	2off	~ 12.2	~ -1034.5	–	3.5	6.0	–
J03045-8001	56.364	-80.031	0.832	0.47	-4.552	-1.823, -4.372	1.3	29.5	–	111.0	2off	~ 21.7	~ -1777.0	–	1.6	3.7	–
J0400-80037	60.112	-80.622	0.032	0.48	-1.067	-4.074, -6.492	2.7	1.4	–	8.9	2off	~ 5.0	~ -0.5	–	5.0	7.1	–
J0347-8052	56.755	-80.881	0.582	0.14	-2.227	-61.590, -104.705	1.3	2.9	–	8.6	2off	~ 7.7	~ 590.5	–	3.7	2.3	–
J0402-79051	60.654	-79.864	0.752	0.17	-4.042	-1.769, -6.458	1.3	16.9	–	36.4	2off	~ 15.5	~ -1124.0	–	2.1	2.7	–
J0404-8101	61.231	-81.032	0.473	0.15	-1.872	-2.541, -5.265	4.0	0.7	–	3.7	2off	~ 2.4	~ 0.5	–	4.8	6.8	–
J0404-80039	61.244	-80.656	0.218	0.13	-0.407	-1.655, 2.924	1.6	2.2	–	11.3	2off	~ 4.9	~ -776.0	–	3.6	5.1	–
J0414-8018	63.745	-80.310	0.696	0.15	-2.657	-2.215, 2.818	1.0	5.9	–	28.5	2off	~ 19.2	~ 1702.0	–	5.1	5.0	–
J0414-8041	63.604	-80.697	0.602	0.42	-1.768	-16.255, -16.867	1.8	5.0	–	22.0	2off	~ 11.1	~ -869.5	–	3.7	4.0	–
J0355-8045	58.996	-80.753	0.212	0.13	-0.987	-12.193, -17.657	2.6	1.0	–	4.2	2off	~ 3.5	~ -83.5	–	4.6	4.3	–
J0400-8107	60.087	-81.122	0.516	0.54	-2.280	-37.149, -58.505	4.0	0.8	–	5.2	2off	~ 2.9	~ 8.5	–	4.7	6.3	–
J0407-80017	61.993	-80.289	0.464	0.15	-2.473	-4.817, -5.390	1.2	4.9	–	20.8	2off	~ 10.3	~ -1756.5	–	3.8	4.5	–
J0354-8052	58.558	-80.878	0.351	0.21	-1.545	-4.603, -5.498	1.9	2.1	–	9.2	2off	~ 6.2	~ -4.0	–	4.4	4.3	–
J04012-8109	63.050	-81.166	0.746	0.19	-3.619	-3.855, -7.194	7.8	1.1	–	6.1	2off	~ 2.2	~ 1175.0	–	4.0	7.5	–
J0345-8057	56.320	-80.950	0.675	0.18	-2.581	-16.879, -23.810	3.5	1.2	–	5.2	2off	~ 3.1	~ -4.5	–	3.4	5.2	–
J0359-8034	59.759	-80.572	0.045	0.13	-0.185	-3.746, -10.029	1.4	2.3	–	6.7	2off	~ 4.9	~ 357.5	–	2.9	3.7	–
J0419-8040	64.991	-80.682	0.824	0.20	-4.355	-3.995, -7.727	1.8	9.0	–	29.9	2off	~ 10.5	~ -462.0	–	1.9	4.5	–
J0410-8046	62.631	-80.772	0.466	0.14	-0.878	-6.207, -5.903	3.9	0.7	–	3.8	2off	~ 2.5	~ 11.0	–	5.2	5.6	–
J0406-81017	61.592	-81.287	0.729	0.15	-3.700	-3.114, -8.473	3.9	2.5	–	7.8	2off	~ 4.5	~ -8.0	–	4.0	6.7	–
J0401-80031	60.345	-80.529	0.101	0.14	-1.202	-11.117, -13.329	2.2	1.1	–	6.3	2off	~ 4.9	~ -15.0	–	5.7	6.0	–
J0408-80051	62.230	-80.853	0.444	0.14	-1.647	-3.637, -6.335	3.7	1.0	–	5.0	2off	~ 2.4	~ 1128.0	–	3.9	5.4	–
J0400-80037	60.073	-80.619	0.025	0.96	0.003	-2.363, -6.336	2.6	1.5	–	2.7	2off	~ 3.8	~ -686.5	–	3.5	2.2	–
J03051-8003	57.951	-80.061	0.639	0.20	-2.705	-1.675, -5.982	3.0	1.6	–	8.1	2off	~ 4.3	~ -1198.5	–	4.1	5.0	–
J0400-80037	60.116	-80.619	0.031	0.68	-0.989	-3.291, -4.270	2.7	1.5	–	6.9	2off	~ 3.3	~ 1339.5	–	3.4	4.9	–
J0403-8103	60.796	-81.052	0.466	0.67	-1.208	-0.782, -3.762	1.2	4.7	–	17.9	2off	~ 15.3	~ 1177.0	–	4.4	4.2	–
J0350-7941	57.500	-79.696	1.001	13.56	-4.549	-2.996, -6.155	1.1	66.3	–	141.4	2off	~ 27.4	~ 746.0	–	1.0	3.6	–
J0400-79054	60.071	-79.914	0.692	0.14	-1.437	-12.555, -16.984	3.9	0.8	–	4.7	2off	~ 3.0	~ -1.0	–	5.3	4.5	–
J0414-8041	63.619	-80.691	0.603	0.41	-2.328	-1.585, -6.841	1.4	3.3	–	7.2	2off	~ 9.4	~ -689.5	–	3.7	2.0	–
J0406-80010	61.567	-80.183	0.502	0.15	-1.690	-9.161, -9.950	1.5	2.7	–	8.1	2off	~ 8.9	~ -10.0	–	4.2	3.7	–
J0406-80018	61.597	-80.314	0.400	0.15	-1.853	-3.452, -7.299	3.5	0.8	–	4.4	2off	~ 2.7	~ 1378.0	–	4.2	5.2	–
J0359-8048	59.960	-80.812	0.206	0.15	-1.312	-66.698, -116.490	2.2	1.7	–	6.6	2off	~ 4.4	~ 740.0	–	3.5	3.3	–
J0400-80037	60.092	-80.618	0.027	1.31	-0.606	-6.865, -12.887	3.7	1.1	–	6.4	2off	~ 3.9	~ 9.5	–	5.6	6.1	–
J03048-8004	57.031	-80.069	0.726	1.15	-3.519	-5.481, -0.961	2.0	5.9	–	21.8	2off	~ 14.7	~ -1726.0	–	4.7	6.2	–
J0426-8045	66.623	-80.754	0.757	0.15	-3.476	-7.198, -6.447	6.8	0.4	–	2.0	3	~ 2.1	~ 173.5	–	7.4	5.9	–

… *Continued on next page*

Table A.1 – ... *Continued from previous page*

Source Name	RA [deg]	DEC [deg]	Δr [deg]	A_{fe} [A_{bm}]	$\tilde{\alpha}$	$\tilde{\alpha}_{c1}, \tilde{\alpha}_{c2}$	I_{peak} [**]	$\langle\sigma_{qu}\rangle$ [%]	β	$\langle p_0\rangle$ [%]	DF	$\|F\|_p$ [%]	ϕ_{peak} [*]	σ_ϕ [*]	T	$\tilde{T}$	Fid
J04023-8006	65.884	-80.107	0.123	0.14	-0.066	-1.043, -5.809	10.3	0.1	–	0.7	3	~ 0.4	~ 485.5	–	5.0	7.3	–
J0435-8045	68.948	-80.754	0.879	0.30	-4.651	-5.090, -4.576	5.9	1.9	–	5.8	3	~ 6.5	~ 1524.0	–	8.5	6.3	–
J0420-8038	65.163	-80.646	0.670	0.31	-3.471	-3.724, -3.293	2.1	1.7	–	6.1	3	~ 5.9	~ -1182.5	–	5.0	3.9	–
J04025-8008	66.390	-80.133	0.136	0.30	-1.404	-1.916, -5.145	14.9	0.1	–	0.5	3	~ 0.5	~ -40.5	–	7.8	6.3	–
J0433-7922	68.252	-79.370	0.725	0.15	-3.572	-4.747, -5.633	5.3	0.5	–	2.4	3	~ 2.3	~ -1236.5	–	6.5	7.8	–
J0414-8011	63.573	-80.194	0.498	0.21	-2.032	-2.512, -3.715	2.2	0.8	–	2.8	3	~ 3.2	~ -346.5	–	5.6	3.9	–
J0423-7951	65.842	-79.855	0.161	0.53	-1.587	-3.618, -4.519	6.4	0.2	–	0.6	3	~ 0.8	~ 1550.5	–	4.8	2.7	–
J0443-8011	70.871	-80.196	0.820	0.15	-3.997	-3.592, -2.721	3.1	1.2	–	6.7	3	~ 4.0	~ -633.5	–	5.2	8.2	–
J0421-8032	65.326	-80.543	0.565	0.32	-2.926	-2.842, -4.632	2.2	0.9	–	2.9	3	~ 3.3	~ 1825.5	–	4.8	3.7	–
J04031-8008	67.911	-80.139	0.320	0.15	-1.389	-4.170, -1.118	3.4	0.4	–	1.1	3	~ 1.3	~ 580.0	–	4.4	2.9	–
J0432-7921	68.229	-79.364	0.729	0.16	-3.770	-3.520, -2.851	3.5	0.8	–	2.6	3	~ 3.3	~ 308.5	–	5.3	3.9	–
J04028-8003	67.149	-80.060	0.169	0.14	-1.662	-10.617, -10.291	5.6	0.2	–	0.9	3	~ 0.8	~ -1780.5	–	4.6	4.5	–
J0410-7949	62.612	-79.828	0.658	0.17	-3.434	-2.371, -4.013	2.1	1.2	–	5.0	3	~ 4.5	~ 195.5	–	4.9	4.5	–
J0433-8024	68.265	-80.409	0.535	0.15	-2.180	-3.176, -3.094	3.7	0.4	–	2.6	3	~ 1.4	~ -196.5	–	4.4	5.9	–
J0429-7916	67.271	-79.281	0.743	0.37	-4.580	-6.720, -4.863	4.5	1.4	–	9.0	3	~ 6.6	~ 23.0	–	7.7	8.4	–
J0413-7946	63.416	-79.772	0.546	0.66	-2.389	-3.200, -4.945	1.4	1.5	–	3.7	3	~ 6.4	~ -537.0	–	5.1	2.9	–
J0421-7937	65.288	-79.625	0.411	0.15	-1.458	-6.511, -5.080	2.3	0.6	–	3.4	3	~ 2.4	~ 369.0	–	5.3	5.5	–
J0423-7926	65.852	-79.450	0.555	0.70	-2.777	-2.313, -1.716	3.6	0.8	–	3.9	3	~ 3.4	~ 289.0	–	7.1	5.6	–
J0433-7944	68.303	-79.737	0.448	0.14	-0.935	-7.468, -6.531	1.8	0.6	–	2.8	3	~ 2.8	~ -1318.5	–	5.8	4.9	–
J0436-7918	69.019	-79.315	0.847	0.21	-4.637	-2.428, -5.131	10.5	0.7	–	1.5	3	~ 2.2	~ -1914.0	–	5.7	5.8	–
J0410-7954	62.639	-79.910	0.634	0.15	-1.301	-3.634, -3.816	1.6	0.8	–	4.7	3	~ 2.8	~ -57.5	–	4.5	6.0	–
J0425-7914	66.253	-79.239	0.761	0.28	-2.935	-4.896, -3.920	10.4	0.2	–	1.5	3	~ 1.2	~ 8.5	–	8.6	5.3	–
J0423-7951	65.824	-79.851	0.166	0.37	-1.432	-6.491, -2.829	6.7	0.2	–	0.7	3	~ 0.7	~ -10.5	–	4.9	3.8	–
J0432-7944	68.026	-79.743	0.406	0.73	-2.189	-4.156, -3.545	12.0	0.1	–	0.8	3	~ 0.6	~ 86.5	–	5.8	6.2	–
J0425-7914	66.274	-79.234	0.766	0.52	-2.707	-11.078, -10.602	3.8	0.5	–	3.9	3	~ 2.9	~ 228.5	–	6.7	6.6	–
J0413-7946	63.415	-79.781	0.542	0.57	-2.812	-7.247, -6.508	1.9	1.3	–	8.0	3	~ 9.8	~ -20.5	–	11.3	6.9	–
J0404-79056	61.063	-79.938	0.904	0.20	-4.600	-1.099, -4.017	4.9	2.1	–	5.4	3	~ 6.2	~ -646.5	–	6.2	4.0	–
J0426-7949	66.709	-79.818	0.200	0.59	-1.398	-2.236, -4.050	4.9	0.3	–	1.3	3	~ 1.5	~ -42.5	–	7.8	5.0	–
J0423-7926	65.882	-79.445	0.559	0.23	-2.857	-3.333, -5.790	5.0	0.4	–	1.8	3	~ 1.9	~ -41.0	–	7.2	4.6	–
J0415-7921	63.994	-79.352	0.763	0.15	-3.676	-2.441, -5.000	2.7	1.3	–	6.0	3	~ 4.7	~ -308.5	–	5.2	5.7	–
J0411-8012	62.932	-80.206	0.605	0.15	-1.818	-9.340, -11.929	1.8	0.8	–	1.7	3	~ 3.0	~ 1861.0	–	4.8	2.3	–
J0425-8046	66.426	-80.771	0.772	0.16	-4.266	-2.418, -3.482	3.1	1.8	–	7.9	3	~ 4.8	~ -163.0	–	4.8	6.1	–
J0417-7938	64.428	-79.647	0.477	0.16	-2.392	-4.543, -2.090	3.2	0.6	–	3.0	3	~ 2.3	~ 163.5	–	5.6	4.6	–
J0419-7934	64.978	-79.571	0.484	0.15	-2.443	-3.452, -7.694	3.6	0.4	–	1.0	3	~ 1.6	~ 1606.5	–	4.5	2.2	–
J0414-8041	63.600	-80.696	0.825	0.48	-4.623	-3.054, -4.700	2.3	3.7	–	4.0	3	~ 7.8	~ -13.0	–	4.1	5.1	–
J0437-8016	69.459	-80.277	0.617	1.05	-2.902	-9.378, -8.945	3.4	0.6	–	3.4	3	~ 3.6	~ -36.0	–	8.4	5.7	–

... *Continued on next page*

Table A.1 – ... *Continued from previous page*

Source Name	RA [deg]	DEC [deg]	Δr [deg]	A_{fe} [A_{bm}]	$\tilde{\alpha}$	$\tilde{\alpha}_{c1}, \tilde{\alpha}_{c2}$	I_{peak} [**]	$\langle\sigma_{qu}\rangle$ [%]	β	$\langle p_0\rangle$ [%]	DF	$\lvert F\rvert_p$ [%]	ϕ_{peak} [*]	σ_ϕ [*]	T	$\tilde{T}$	Fid
J0435-7946	68.786	-79.777	0.500	0.14	-2.025	-8.789, -7.846	1.5	1.0	–	4.3	3	~ 4.3	~ -133.0	–	5.6	4.0	–
J0440-7947	70.020	-79.786	0.697	0.21	-4.604	-4.581, -2.846	4.0	2.5	–	10.2	3	~ 11.0	~ -32.5	–	10.9	5.3	–
J0428-7941	67.133	-79.689	0.349	0.14	-0.902	-1.655, -45.373	3.4	0.2	–	0.4	3	~ 1.0	~ 223.5	–	4.1	2.1	–
J0423-7929	65.957	-79.492	0.510	0.15	-2.841	-3.382, -5.808	3.7	0.5	–	1.9	3	~ 1.9	~ 19.5	–	4.6	4.2	–
J0420-8027	65.010	-80.453	0.499	0.27	-2.016	-6.646, -4.600	1.6	1.1	–	6.5	3	~ 4.6	~ -1165.5	–	5.0	5.9	–
J04037-8003	69.275	-80.064	0.529	0.15	-2.054	-2.868, -5.214	2.7	0.5	–	2.6	3	~ 1.9	~ 377.0	–	4.7	4.7	–
J0419-8040	64.987	-80.681	0.712	0.20	-3.214	-3.804, -4.238	4.9	0.5	–	1.7	3	~ 2.1	~ -900.0	–	5.8	3.7	–
J0431-8039	67.942	-80.665	0.724	0.16	-3.518	-11.680, -11.479	2.1	1.5	–	10.5	3	~ 6.8	~ -118.0	–	6.6	7.6	–
J0413-7949	63.336	-79.827	0.537	0.22	-2.579	-5.395, -3.756	2.0	0.9	–	6.0	3	~ 4.0	~ 110.5	–	5.3	6.8	–
J0418-8019	64.509	-80.325	0.439	0.15	-1.458	-3.737, -3.100	15.6	0.1	–	0.4	3	~ 0.3	~ 99.5	–	5.8	6.3	–
J0439-7933	69.813	-79.566	0.768	0.15	-4.496	-3.460, -6.108	2.3	2.6	–	6.3	3	~ 7.5	~ -1103.5	–	5.2	3.4	–
J0433-8012	68.440	-80.201	0.428	0.15	-1.419	-2.661, -5.643	3.0	0.5	–	3.2	3	~ 2.4	~ -61.5	–	7.1	6.8	–
J0426-8044	66.742	-80.749	0.753	0.18	-4.196	-3.180, -3.589	2.6	1.8	–	7.8	3	~ 4.8	~ -1557.0	–	4.6	5.6	–
J0423-7948	65.871	-79.815	0.196	0.15	-1.392	-2.771, -2.316	3.6	0.3	–	1.8	3	~ 1.2	~ -1132.0	–	4.5	5.5	–
J0427-8043	66.951	-80.722	0.732	0.25	-3.751	-8.539, -5.148	4.1	0.8	–	3.3	3	~ 3.7	~ 49.5	–	6.7	4.7	–
J04026-8003	66.608	-80.066	0.092	0.18	-1.405	-9.936, -9.112	3.9	0.3	–	1.5	3	~ 1.3	~ 1140.0	–	5.3	4.9	–
J0418-8032	64.719	-80.549	0.606	0.16	-2.943	-4.576, -3.897	2.4	1.0	–	2.3	3	~ 4.7	~ -767.5	–	6.2	3.6	–
J04031-8004	67.939	-80.077	0.304	0.15	-0.756	-3.658, -4.029	1.6	0.7	–	2.3	3	~ 2.5	~ -105.0	–	4.4	3.3	–
J0427-7943	66.978	-79.728	0.302	0.15	-1.709	-4.010, -4.627	4.1	0.3	–	1.0	3	~ 1.2	~ 1840.0	–	4.5	3.2	–
J0432-7922	68.242	-79.368	0.727	0.16	-3.572	-5.420, -2.671	3.8	0.7	–	1.5	3	~ 2.3	~ 388.5	–	4.7	3.2	–
J0420-7959	65.007	-79.998	0.214	0.18	-1.811	-4.656, -3.185	2.2	0.6	–	3.7	3	~ 2.2	~ 1113.5	–	4.3	5.9	–
J0424-7913	66.223	-79.232	0.768	0.47	-3.933	-2.774, -3.372	3.0	1.3	–	4.2	3	~ 4.5	~ 1203.5	–	5.6	6.0	–
J0421-8026	65.296	-80.444	0.472	0.15	-1.977	-5.251, -4.051	1.6	0.9	–	4.2	3	~ 3.7	~ 580.0	–	4.8	5.6	–
J0435-7945	68.787	-79.756	0.510	0.15	-2.823	-3.238, -3.025	2.0	1.2	–	5.7	3	~ 4.5	~ -599.0	–	5.4	5.5	–
J04025-8008	66.379	-80.139	0.141	0.15	-1.740	-3.373, -4.609	1.8	0.8	–	4.0	3	~ 2.8	~ 1861.0	–	4.5	4.5	–
J0417-7951	64.279	-79.857	0.371	0.21	-1.830	-4.291, -5.239	3.3	0.4	–	1.2	3	~ 1.3	~ 1947.5	–	3.6	3.3	–
J0431-8029	67.938	-80.494	0.571	11.52	-3.838	-2.479, -3.754	3.9	1.0	–	6.9	3	~ 6.9	~ 32.0	–	11.5	8.1	–
J0414-8016	63.609	-80.268	0.524	0.15	-1.743	-12.904, -13.173	18.3	0.1	–	0.5	3	~ 0.5	~ -57.0	–	9.4	6.0	–
J0418-7957	64.607	-79.955	0.288	0.16	-1.546	-6.323, -4.743	2.4	0.5	–	3.0	3	~ 2.0	~ 1941.5	–	4.6	6.2	–
J0412-7946	63.076	-79.771	0.601	0.48	-3.015	-7.468, -6.592	1.6	1.6	–	5.8	3	~ 6.0	~ -22.0	–	5.5	4.6	–
J0417-7917	64.475	-79.291	0.777	0.29	-4.260	-3.032, -5.536	2.8	1.7	–	6.1	3	~ 6.7	~ 1608.0	–	6.1	4.4	–
J0406-80018	61.640	-80.311	0.845	0.19	-4.584	-4.950, -5.454	5.9	1.0	–	5.8	3	~ 4.7	~ -173.5	–	7.4	7.4	–
J0422-8030	65.553	-80.501	0.515	0.15	-1.813	-3.961, -4.482	3.9	0.3	–	1.0	3	~ 1.3	~ 299.5	–	4.9	3.0	–
J0430-8034	67.661	-80.568	0.616	0.21	-2.954	-5.479, -4.211	2.5	1.0	–	1.6	3	~ 3.2	~ 494.0	–	4.2	3.0	–
J0425-7956	66.357	-79.949	0.055	0.14	-0.388	-3.536, -3.409	2.5	0.4	–	1.9	3	~ 1.5	~ 1116.0	–	4.8	4.9	–
J0421-7922	65.417	-79.377	0.640	0.16	-2.815	-21.200, -28.109	3.7	0.6	–	2.2	3	~ 1.9	~ 288.5	–	4.6	4.1	–

... *Continued on next page*

Table A.1 – … *Continued from previous page*

Source Name	RA [deg]	DEC [deg]	Δr [deg]	A_{fe} [A_{bm}]	$\tilde{\alpha}$	$\tilde{\alpha}_{c1}, \tilde{\alpha}_{c2}$	I_{peak} [**]	$\langle\sigma_{qu}\rangle$ [%]	β	$\langle p_0\rangle$ [%]	DF	$\|F\|_p$ [%]	ϕ_{peak} [*]	σ_ϕ [*]	T	$\tilde{T}$	Fid
J0430-7920	67.545	-79.341	0.699	0.15	-3.596	-4.600, -5.306	3.9	0.9	–	4.0	3	~ 3.4	~ -2000.0	–	6.1	3.9	–
J04013-8006	63.462	-80.115	0.493	0.16	-2.279	-4.158, -3.314	3.8	0.4	–	1.2	3	~ 1.5	~ 1617.0	–	4.5	3.0	–
J0439-8015	69.819	-80.262	0.667	0.15	-2.610	-10.725, -9.309	6.4	0.3	–	1.7	3	~ 1.6	~ -170.5	–	7.9	7.9	–
J0430-7943	67.648	-79.717	0.376	0.14	-2.015	-2.939, -5.355	2.2	0.7	–	4.5	3	~ 2.9	~ -865.0	–	5.2	6.5	–
J0424-7914	66.239	-79.237	0.763	0.61	-4.211	-3.023, -4.424	6.6	0.7	–	4.2	3	~ 2.6	~ 276.0	–	6.9	7.6	–
J0423-7926	65.897	-79.445	0.559	1.18	-2.569	-2.536, -4.841	2.7	1.3	–	9.6	3	~ 6.1	~ -87.0	–	6.0	7.5	–
J0426-7949	66.647	-79.821	0.193	0.32	-3.158	-4.453, -5.440	1.9	1.2	–	6.6	3	~ 4.6	~ 1856.5	–	5.5	6.9	–
J0431-7932	67.797	-79.546	0.532	0.16	-2.724	-3.086, -3.355	2.1	1.0	–	3.8	3	~ 3.4	~ 62.0	–	4.4	4.0	–
J0411-7928	62.862	-79.477	0.797	0.16	-3.893	-3.701, -3.504	6.5	0.5	–	1.8	3	~ 1.6	~ 710.5	–	4.9	4.5	–
J04022-8004	65.574	-80.073	0.136	0.58	-1.775	-3.370, -4.937	1.7	0.7	–	1.5	3	~ 2.7	~ -168.5	–	4.4	2.3	–
J0430-8036	67.743	-80.611	0.661	0.17	-3.254	-6.896, -3.697	14.6	0.2	–	1.2	3	~ 0.9	~ 76.0	–	7.8	7.8	–
J0419-8010	64.934	-80.181	0.289	0.15	-1.840	-4.503, -4.409	1.9	0.6	–	4.4	3	~ 2.9	~ -1209.5	–	4.9	6.2	–
J0410-7943	62.718	-79.721	0.680	0.25	-2.915	-4.442, -3.145	6.4	0.4	–	2.0	3	~ 1.6	~ -58.0	–	6.7	5.7	–
J0408-79046	62.153	-79.779	0.751	0.30	-3.655	-2.755, -4.524	4.1	0.7	–	2.7	3	~ 2.4	~ -916.5	–	4.7	4.0	–
J0424-7939	66.013	-79.655	0.348	2.69	-2.128	-5.588, -4.193	4.9	0.3	–	1.7	3	~ 1.5	~ -296.5	–	6.2	5.4	–
J0419-7914	64.845	-79.247	0.793	0.15	-3.774	-3.764, -3.196	3.0	1.1	–	2.8	3	~ 3.6	~ 1033.5	–	4.7	1.9	–
J0426-8053	66.644	-80.895	0.897	0.17	-4.606	-6.848, -5.317	3.8	2.3	–	9.5	3	~ 6.3	~ 780.0	–	5.7	6.2	–
J0421-7959	65.457	-79.998	0.136	0.15	-1.554	-3.256, -4.094	3.5	0.3	–	1.2	3	~ 1.2	~ 849.0	–	4.3	3.6	–
J0419-8017	64.778	-80.295	0.387	0.15	-1.348	-2.300, -4.114	1.9	0.7	–	4.4	3	~ 3.2	~ -388.0	–	5.6	6.5	–
J0415-7959	63.784	-79.994	0.427	0.15	-2.636	-6.620, -5.412	15.2	0.1	–	0.6	3	~ 0.5	~ 1021.5	–	5.5	4.8	–
J0410-8046	62.627	-80.771	0.979	0.17	-4.614	-5.203, -4.471	2.1	6.6	–	24.7	3	~ 9.2	~ 223.0	–	3.6	6.5	–
J0414-8018	63.742	-80.310	0.528	0.15	-2.205	-5.816, -4.058	3.0	0.5	–	1.9	3	~ 1.9	~ -532.0	–	4.8	4.1	–
J0417-7915	64.338	-79.256	0.819	0.17	-3.853	-4.593, -3.308	2.8	1.3	–	6.9	3	~ 4.7	~ 1857.5	–	6.0	6.0	–
J0435-8045	68.940	-80.757	0.882	0.37	-4.651	-2.406, -5.360	2.6	3.6	–	16.1	3	~ 7.3	~ -13.0	–	3.8	6.5	–
J04022-8004	65.566	-80.070	0.136	1.19	-1.709	-2.547, -5.272	1.5	1.0	–	4.5	3	~ 3.6	~ -698.0	–	4.6	4.8	–
J0420-7933	65.017	-79.559	0.492	0.15	-1.896	-3.375, -3.081	2.6	0.5	–	2.6	3	~ 1.5	~ -614.5	–	3.6	5.3	–
J0417-7943	64.410	-79.731	0.420	0.16	-1.932	-7.966, -7.826	1.8	0.8	–	2.9	3	~ 2.8	~ -1377.5	–	4.3	3.5	–
J0432-7944	68.024	-79.741	0.407	0.15	-2.098	-5.212, -4.624	30.0	0.0	–	0.4	3	~ 0.3	~ -100.0	–	8.4	8.9	–
J0417-8012	64.257	-80.209	0.400	0.20	-1.726	-5.567, -5.213	3.0	0.4	–	3.2	3	~ 3.6	~ -14.5	–	10.1	8.0	–
J0419-8116	64.932	-81.282	0.855	0.16	-1.356	-2.073, -2.459	5.2	0.4	–	1.9	5	~ 1.5	~ -243.5	–	5.7	5.6	–
J0418-8019	64.516	-80.325	0.467	0.16	-1.995	-2.901, -3.877	10.3	0.2	–	1.2	5	~ 1.1	~ -341.5	–	7.4	6.3	–
J0400-81023	60.100	-81.392	1.418	0.19	-3.422	-3.363, -4.024	2.3	2.6	–	3.7	5	~ 6.0	~ 1818.0	–	4.1	3.1	–
J03058-8103	59.628	-81.064	1.325	3.14	-3.208	-5.333, -5.215	5.6	1.0	–	4.7	5	~ 3.0	~ -311.0	–	5.7	7.5	–
J04025-8008	66.397	-80.134	0.386	0.35	-4.617	-1.520, -2.667	3.9	6.1	–	7.7	5	~ 11.1	~ 1286.5	–	4.7	3.8	–
J0422-8146	65.607	-81.771	1.292	0.25	-3.626	-2.923, -5.163	4.4	2.1	–	7.6	5	~ 7.9	~ -47.0	–	9.0	6.6	–
J0425-8129	66.351	-81.484	0.991	0.35	-2.110	-21.398, -22.983	4.1	0.7	–	3.8	5	~ 3.2	~ 57.0	–	7.2	8.5	–

… *Continued on next page*

Table A.1 – … *Continued from previous page*

Source Name	RA [deg]	DEC [deg]	Δr [deg]	A_{fe} [A_{bm}]	$\tilde{\alpha}$	$\tilde{\alpha}_{c1}, \tilde{\alpha}_{c2}$	I_{peak} [**]	$\langle \sigma_{qu} \rangle$ [%]	β	$\langle p_0 \rangle$ [%]	DF	$\lvert F \rvert_p$ [%]	ϕ_{peak} [*]	σ_ϕ [*]	T	$\tilde{T}$	Fid
J0401-81015	60.257	-81.261	1.326	0.59	-2.700	-1.378, -2.577	6.2	0.5	–	2.1	5	~ 1.7	~ -48.5	–	5.0	7.2	–
J0426-8129	66.550	-81.490	0.994	0.59	-2.760	-2.707, -5.598	9.2	0.4	–	1.7	5	~ 1.6	~ 91.0	–	6.5	5.2	–
J0419-8040	64.993	-80.681	0.392	0.20	-0.918	-3.868, -3.631	7.3	0.2	–	0.7	5	~ 0.8	~ -30.0	–	5.4	4.8	–
J0419-8111	64.857	-81.192	0.780	0.19	-1.689	-4.802, -2.489	1.8	1.6	–	6.0	5	~ 7.3	~ 1072.5	–	6.9	4.4	–
J0435-8110	68.812	-81.173	0.725	0.18	-3.289	-10.297, -5.590	2.0	3.1	–	7.2	5	~ 11.4	~ -1251.5	–	6.9	5.3	–
J0411-8029	62.843	-80.484	0.706	0.22	-2.548	-1.987, -6.658	2.1	1.9	–	3.6	5	~ 5.9	~ -174.0	–	4.9	2.8	–
J04018-8108	64.597	-81.149	0.763	0.17	-0.910	-3.996, -3.641	3.1	0.5	–	2.7	5	~ 2.7	~ 36.0	–	6.8	5.7	–
J0430-8034	67.668	-80.568	0.113	0.21	-2.957	-3.124, -2.350	2.1	3.7	–	14.9	5	~ 12.3	~ 656.5	–	6.8	7.7	–
J04010-8100	62.682	-81.007	0.875	0.17	-1.230	-3.197, -3.154	2.9	0.6	–	1.7	5	~ 2.0	~ 1374.5	–	4.0	3.3	–
J0401-81037	60.401	-81.628	1.535	0.62	-4.564	-4.975, -2.756	3.3	6.5	–	17.9	5	~ 10.2	~ -1223.0	–	3.8	5.1	–
J0428-8149	67.019	-81.824	1.324	0.29	-4.645	-1.342, 1.186	6.0	6.6	–	14.1	5	~ 9.5	~ -1113.0	–	4.6	6.2	–
J0422-8050	65.638	-80.834	0.412	0.16	-1.525	-1.554, -1.737	3.5	0.6	–	2.7	5	~ 2.2	~ 813.0	–	4.5	4.4	–
J0406-81017	61.593	-81.286	1.175	0.17	-1.993	-2.291, -3.442	11.9	0.2	–	1.1	5	~ 0.8	~ -1756.5	–	5.5	5.6	–
J0435-8045	68.947	-80.758	0.394	0.32	-3.874	-1.749, -3.574	3.0	3.4	–	14.8	5	~ 8.5	~ -1158.5	–	5.2	7.6	–
J0425-8046	66.433	-80.772	0.294	0.17	-1.652	-9.283, -10.049	4.6	0.4	–	2.9	5	~ 1.6	~ -545.5	–	5.0	7.0	–
J0431-8111	67.781	-81.189	0.697	0.33	-2.019	-4.906, -4.062	20.0	0.2	–	1.0	5	~ 0.5	~ 280.5	–	5.7	6.7	–
J0359-8036	59.944	-80.605	1.182	0.17	-3.590	-6.499, -6.566	3.0	2.3	–	7.9	5	~ 7.9	~ -1841.5	–	6.2	5.3	–
J0421-8054	65.492	-80.909	0.486	0.17	-0.435	-7.401, -7.905	2.1	0.7	–	3.0	5	~ 2.8	~ 286.5	–	4.9	4.8	–
J0428-8149	67.010	-81.822	1.322	0.34	-4.581	-2.845, -4.219	7.3	3.5	–	13.0	5	~ 8.5	~ -874.5	–	7.9	8.9	–
J0411-8028	62.779	-80.479	0.717	0.23	-1.928	-1.911, -3.776	2.5	1.0	–	4.1	5	~ 4.5	~ -95.0	–	6.0	3.7	–
J0418-8032	64.726	-80.550	0.397	0.17	-1.442	-15.180, -16.445	2.8	0.9	–	6.0	5	~ 4.7	~ -6.0	–	8.1	8.1	–
J0434-8122	68.741	-81.370	0.907	0.17	-2.729	-8.244, -8.500	8.7	0.5	–	2.4	5	~ 1.8	~ 2.5	–	7.2	8.3	–
J0430-8116	67.652	-81.280	0.785	0.16	-1.722	-2.747, -3.241	6.6	0.4	–	2.5	5	~ 1.5	~ -353.0	–	6.7	7.8	–
J0420-8042	65.007	-80.702	0.399	0.28	-0.805	-3.126, -5.613	2.0	1.1	–	3.7	5	~ 3.5	~ -322.5	–	4.3	3.5	–
J0400-8107	60.089	-81.121	1.282	0.56	-2.435	-14.071, -15.647	4.5	0.8	–	2.4	5	~ 2.7	~ 99.5	–	6.2	4.4	–
J04015-8105	63.884	-81.086	0.781	0.16	-1.096	-1.547, -3.219	3.7	0.5	–	1.7	5	~ 1.7	~ -1920.0	–	4.6	3.9	–
J0430-8036	67.741	-80.613	0.152	0.19	-2.872	-1.999, -3.631	14.4	0.3	–	1.1	5	~ 1.0	~ 134.5	–	5.8	5.8	–
J0413-8052	63.488	-80.872	0.695	0.34	-0.983	-1.828, -4.629	3.9	0.5	–	2.4	5	~ 2.6	~ -19.0	–	7.8	6.3	–
J04019-8107	64.828	-81.132	0.730	0.69	-0.871	-10.062, -9.607	2.4	1.1	–	6.4	5	~ 3.7	~ -124.5	–	5.3	6.2	–
J0413-8059	63.297	-80.997	0.790	0.16	-0.987	-5.976, -4.767	3.9	0.5	–	1.8	5	~ 1.7	~ -1807.0	–	4.9	4.1	–
J0426-8053	66.651	-80.895	0.402	0.17	-1.180	-1.617, -3.283	8.9	0.2	–	0.6	5	~ 0.6	~ 1762.0	–	4.4	3.3	–
J0408-81031	62.136	-81.527	1.288	1.17	-1.093	-3.862, 0.037	2.5	1.7	–	11.9	5	~ 7.4	~ -195.0	–	5.2	7.9	–
J0428-8126	67.215	-81.449	0.949	0.22	-1.890	-1.536, -2.887	2.1	1.2	–	4.7	5	~ 4.1	~ 1450.5	–	5.5	4.2	–
J0435-8057	68.887	-80.952	0.535	0.32	-3.145	-1.866, -3.400	22.4	0.3	–	1.5	5	~ 1.2	~ -3.0	–	10.2	8.9	–
J0424-8125	66.175	-81.426	0.938	0.23	-1.914	-5.494, -5.384	2.4	1.1	–	4.3	5	~ 3.4	~ -1671.0	–	4.2	4.2	–
J0409-80052	62.483	-80.870	0.836	0.16	-0.977	-1.592, -3.104	2.0	1.0	–	4.4	5	~ 3.9	~ 1772.0	–	5.5	5.1	–

… *Continued on next page*

Table A.1 – … *Continued from previous page*

Source Name	RA [deg]	DEC [deg]	Δr [deg]	A_{fe} [A_{bm}]	$\tilde{\alpha}$	$\tilde{\alpha}_{c1}, \tilde{\alpha}_{c2}$	I_{peak} [**]	$\langle \sigma_{qu} \rangle$ [%]	β	$\langle p_0 \rangle$ [%]	DF	$\lvert F \rvert_p$ [%]	ϕ_{peak} [*]	σ_ϕ [*]	T	$\tilde{T}$	Fid
J0424-8145	66.124	-81.754	1.263	0.18	-3.789	-12.387, -11.847	4.8	1.6	–	-0.8	5	~ 4.1	~ -1181.5	–	4.6	3.3	–
J0410-8142	62.700	-81.714	1.392	0.23	-3.757	-2.731, -3.172	5.5	1.4	–	1.0	5	~ 3.4	~ -1844.5	–	4.9	4.0	–
J0405-8101	61.279	-81.032	1.077	0.21	-1.757	-8.153, -8.739	2.6	1.0	–	5.1	5	~ 3.3	~ -14.5	–	4.9	6.2	–
J0417-8132	64.250	-81.542	1.134	0.17	-2.007	-3.660, -2.294	2.0	1.5	–	3.3	5	~ 5.7	~ 1203.0	–	5.7	2.6	–
J0408-80038	62.246	-80.636	0.810	0.17	-1.759	-6.544, -4.154	2.3	1.2	–	4.7	5	~ 4.5	~ 114.0	–	6.2	5.4	–
J0410-8046	62.633	-80.771	0.778	0.16	-0.959	-2.874, -4.011	6.8	0.2	–	0.8	5	~ 0.8	~ 785.0	–	4.6	3.4	–
J0430-8051	67.738	-80.861	0.375	0.17	-2.144	-11.407, -11.599	5.8	0.6	–	3.1	5	~ 2.1	~ -290.5	–	6.0	6.3	–
J0428-8057	67.119	-80.955	0.455	0.25	-1.429	-2.490, -2.837	3.5	0.7	–	2.6	5	~ 2.3	~ -1823.5	–	4.8	4.7	–
J0420-8135	65.221	-81.596	1.135	0.43	-2.903	-2.369, -5.000	8.4	0.5	–	2.4	5	~ 2.5	~ -31.0	–	8.3	8.7	–
J0413-8131	63.310	-81.531	1.190	0.22	-1.861	-1.508, -3.307	3.8	0.8	–	3.0	5	~ 3.0	~ -37.0	–	7.3	5.2	–
J0406-80018	61.599	-80.314	0.938	0.18	-4.441	-2.028, -2.353	3.0	4.5	–	11.3	5	~ 18.1	~ -1928.5	–	9.2	4.6	–
J0414-8115	63.504	-81.255	0.947	0.17	-1.278	-5.612, -2.709	3.1	0.8	–	2.5	5	~ 2.4	~ -592.0	–	5.3	3.8	–
J0435-8057	68.881	-80.955	0.536	0.40	-4.561	-3.007, -4.783	8.8	2.6	–	9.1	5	~ 5.7	~ 226.5	–	6.6	8.1	–
J04021-8102	65.397	-81.037	0.604	0.27	-0.983	-1.796, -4.069	1.9	1.1	–	3.6	5	~ 4.6	~ 328.0	–	5.4	3.8	–
J0421-8032	65.332	-80.543	0.297	0.34	-1.910	-4.904, -4.510	2.5	0.9	–	3.5	5	~ 3.5	~ -814.5	–	5.0	4.9	–
J0425-8129	66.366	-81.484	0.991	0.23	-2.071	-2.482, -5.393	3.6	0.7	–	1.9	5	~ 2.5	~ 37.0	–	5.2	4.7	–
J0418-8111	64.654	-81.187	0.790	0.16	0.553	-4.168, -2.073	4.0	0.4	–	1.7	5	~ 1.4	~ 1632.5	–	4.5	4.5	–
J04015-8106	63.813	-81.114	0.809	0.16	-1.134	-4.039, -5.044	1.8	1.1	–	4.5	5	~ 3.5	~ 485.0	–	4.9	4.6	–
J04015-8107	63.807	-81.129	0.822	0.16	-1.065	-4.907, -3.666	2.1	0.9	–	3.0	5	~ 2.6	~ 1565.0	–	3.9	3.4	–
J0414-8057	63.741	-80.960	0.712	0.16	-0.877	-1.590, -1.652	4.3	0.3	–	0.9	5	~ 1.3	~ -1520.0	–	5.0	2.9	–
J0435-8134	68.822	-81.573	1.106	0.63	-4.572	-5.629, -4.408	5.4	2.8	–	8.5	5	~ 6.7	~ 1834.5	–	5.0	8.9	–
J0429-8116	67.477	-81.269	0.771	0.24	-1.937	-4.449, -3.437	1.6	1.7	–	5.1	5	~ 7.0	~ 730.5	–	5.6	2.5	–
J0435-8134	68.837	-81.571	1.104	0.26	-4.545	-2.734, -4.308	4.1	3.2	–	5.3	5	~ 11.2	~ 735.0	–	8.1	5.8	–
J0427-8043	66.958	-80.722	0.224	0.26	-1.812	-2.748, -3.125	4.9	0.5	–	1.8	5	~ 2.1	~ -33.5	–	6.5	6.4	–
J04018-8109	64.574	-81.162	0.776	0.16	-0.895	-1.330, -5.091	2.5	0.6	–	1.7	5	~ 2.1	~ -286.0	–	4.4	3.0	–
J0422-8146	65.589	-81.770	1.291	0.70	-3.723	-2.754, -2.632	5.1	1.7	–	6.8	5	~ 4.7	~ -1970.0	–	6.0	8.1	–
J0410-8142	62.709	-81.712	1.390	0.17	-3.379	-1.942, -3.052	5.9	0.8	–	1.0	5	~ 2.1	~ 1952.0	–	4.2	4.2	–
J0416-8115	64.203	-81.266	0.894	0.18	-1.246	-6.407, -5.788	3.0	0.6	–	4.3	5	~ 4.2	~ -31.5	–	9.9	8.4	–
J04022-8105	65.727	-81.100	0.640	0.32	-1.321	-5.086, -1.354	1.9	1.1	–	4.0	5	~ 4.0	~ 489.5	–	5.1	4.2	–
J0426-8045	66.630	-80.754	0.266	0.16	-1.199	-2.143, -2.215	10.6	0.2	–	0.6	5	~ 0.5	~ -1172.5	–	4.3	4.5	–
J04021-8102	65.368	-81.040	0.609	0.21	-0.774	-1.835, -4.965	1.7	1.1	–	4.0	5	~ 3.9	~ -1104.0	–	4.1	4.0	–
J0420-8027	65.016	-80.453	0.351	0.29	-1.875	-3.044, -4.349	1.8	1.9	–	5.2	5	~ 6.4	~ 1385.5	–	4.6	4.1	–
J0414-8139	63.596	-81.666	1.287	0.35	-2.283	-5.473, -2.105	1.9	2.0	–	9.7	5	~ 7.7	~ -321.5	–	5.5	5.3	–
J0430-8036	67.749	-80.612	0.152	0.18	-2.924	-2.755, -3.898	14.3	0.3	–	1.2	5	~ 1.3	~ 126.0	–	7.7	5.8	–
J0415-8043	63.906	-80.724	0.570	0.16	-0.375	-2.864, -4.252	1.8	0.9	–	2.6	5	~ 3.3	~ 1836.5	–	5.1	3.1	–
J03058-8103	59.631	-81.062	1.324	0.18	-2.733	-2.919, -3.893	9.3	0.4	–	1.7	5	~ 1.5	~ 74.0	–	6.4	5.4	–

… *Continued on next page*

Table A.1 – … *Continued from previous page*

Source Name	RA [deg]	DEC [deg]	Δr [deg]	A_{fe} [A_{bm}]	$\tilde{\alpha}$	$\tilde{\alpha}_{c1}, \tilde{\alpha}_{c2}$	I_{peak} [**]	$\langle \sigma_{qu} \rangle$ [%]	β	$\langle p_0 \rangle$ [%]	DF	$\lvert F \rvert_p$ [%]	ϕ_{peak} [*]	σ_ϕ [*]	T	$\tilde{T}$	Fid
J04019-8107	64.833	-81.129	0.727	0.31	-1.155	-2.224, -5.956	3.3	0.7	–	3.5	5	~ 4.0	~ -36.5	–	9.2	6.1	–
J0408-81031	62.143	-81.523	1.284	0.24	-1.946	-5.185, -4.888	8.6	0.3	–	1.1	5	~ 1.4	~ -35.0	–	6.9	4.5	–
J0407-81040	61.855	-81.683	1.435	0.17	-4.102	-3.849, -3.621	3.6	2.2	–	3.3	5	~ 5.5	~ 1366.5	–	4.2	5.1	–
J0414-8016	63.616	-80.268	0.629	0.17	-2.300	-1.297, -1.191	10.9	0.2	–	1.2	5	~ 0.9	~ -92.5	–	5.4	5.9	–
J0400-80037	60.094	-80.617	1.157	1.19	-3.372	-2.705, -3.371	2.3	2.2	–	7.3	5	~ 9.4	~ -1407.5	–	7.2	4.6	–
J0434-8132	68.652	-81.539	1.066	0.24	-4.258	-2.726, -4.379	13.5	0.7	–	2.1	5	~ 2.4	~ 1561.0	–	6.5	7.8	–
J0406-81043	61.609	-81.728	1.493	0.37	-4.423	-2.901, -4.306	13.7	1.0	–	2.7	5	~ 2.7	~ 1457.0	–	6.6	6.0	–
J0406-80018	61.646	-80.311	0.931	0.21	-3.894	-1.856, -2.850	5.7	0.9	–	3.4	5	~ 4.7	~ -148.0	–	6.7	5.7	–
J0426-8044	66.749	-80.749	0.256	0.19	-1.541	-2.971, -0.958	4.1	0.5	–	1.4	5	~ 1.5	~ -1668.0	–	4.2	3.1	–
J0412-8115	63.036	-81.256	0.994	1.20	-1.087	-3.986, -6.478	3.2	0.6	–	1.2	5	~ 2.1	~ 279.0	–	4.9	2.3	–
J0408-80051	62.231	-80.853	0.866	0.16	-1.263	-1.814, -3.586	6.4	0.2	–	1.2	5	~ 0.9	~ 1674.0	–	5.0	5.3	–
J04019-8107	64.810	-81.129	0.729	0.37	-0.877	-2.766, -3.381	2.2	0.8	–	6.4	5	~ 4.2	~ -38.0	–	6.1	8.6	–
J0400-8107	60.086	-81.125	1.284	0.52	-2.390	-1.799, -2.755	8.2	0.4	–	1.6	5	~ 1.6	~ -19.5	–	6.6	5.6	–
J0407-81042	61.907	-81.707	1.450	0.17	-4.296	-3.553, -2.608	3.0	7.4	–	25.2	5	~ 11.6	~ -891.5	–	4.8	6.8	–
J0412-8130	63.049	-81.509	1.192	0.16	-1.739	-4.577, -3.500	7.3	0.3	–	1.3	5	~ 0.9	~ 503.5	–	4.5	6.5	–
J0403-8103	60.798	-81.051	1.152	0.78	-1.922	-3.141, -6.802	2.1	1.2	–	3.6	5	~ 3.6	~ -1039.0	–	4.3	4.6	–
J0414-8126	63.573	-81.436	1.089	0.16	-1.844	-6.262, -5.734	2.2	1.3	–	5.8	5	~ 5.8	~ -358.5	–	7.0	5.9	–
J0420-8038	65.169	-80.646	0.351	0.32	-1.406	-14.037, -13.559	2.7	0.9	–	2.0	5	~ 3.4	~ -75.0	–	5.4	2.9	–
J0408-81034	62.067	-81.567	1.325	0.17	-1.495	-3.595, -3.567	2.4	1.1	–	4.5	5	~ 4.5	~ 1262.5	–	6.2	4.6	–
J0358-8130	59.704	-81.510	1.536	0.18	-4.446	-1.955, -0.045	8.0	2.1	–	8.8	5	~ 3.5	~ -236.0	–	5.0	7.3	–
J0404-80048	61.184	-80.807	1.011	0.18	-1.984	-5.163, -3.431	8.4	0.3	–	1.1	5	~ 1.5	~ 7.5	–	7.5	4.9	–
J0414-8139	63.571	-81.664	1.287	0.33	-3.024	-9.636, -6.269	3.0	1.9	–	1.9	5	~ 4.9	~ -1013.0	–	4.3	3.1	–
J0413-8131	63.273	-81.529	1.191	0.28	-1.900	-1.746, -4.261	4.5	0.6	–	2.7	5	~ 2.2	~ 1850.0	–	4.8	5.3	–
J0356-8040	59.058	-80.675	1.329	0.49	-4.078	-2.706, -4.351	5.3	1.7	–	6.9	5	~ 6.6	~ -703.0	–	7.9	5.2	–
J04010-8107	62.685	-81.127	0.945	0.16	-1.334	-9.007, -14.022	1.8	1.2	–	0.8	5	~ 3.0	~ -67.5	–	3.3	1.6	–
J0358-8130	59.707	-81.512	1.537	0.19	-4.627	-4.555, -4.073	5.2	7.4	–	25.0	5	~ 15.0	~ -1476.5	–	7.0	6.0	–
J04019-8108	64.815	-81.136	0.735	6.05	3.034	-5.236, -3.798	1.1	6.0	–	9.6	5	~ 19.3	~ -1066.5	–	4.0	2.5	–
J0424-8145	66.132	-81.756	1.265	0.20	-4.125	-3.933, -2.670	3.9	2.0	–	2.3	5	~ 5.8	~ 1035.0	–	4.9	4.7	–
J0416-8133	64.100	-81.554	1.154	0.17	-2.417	-2.183, -5.462	2.3	1.4	–	1.1	5	~ 3.7	~ -1383.0	–	3.8	2.8	–
J0428-8045	67.156	-80.763	0.263	0.16	-2.017	-2.733, -3.253	2.2	1.3	–	5.8	5	~ 4.6	~ -1920.0	–	5.5	5.0	–
J04022-8105	65.703	-81.099	0.640	0.56	-1.330	-4.922, -5.511	2.1	1.3	–	7.9	5	~ 5.9	~ 1677.5	–	6.7	6.8	–
J0431-8039	67.949	-80.666	0.214	0.17	-2.729	-2.084, -2.991	2.1	1.7	–	0.2	5	~ 4.0	~ 319.0	–	3.4	2.1	–
J0414-8018	63.748	-80.310	0.593	0.17	-2.629	-16.016, -19.642	2.1	2.1	–	8.7	5	~ 7.3	~ 1841.5	–	6.7	5.0	–
J0425-8015	66.265	-80.252	0.286	0.24	-4.030	-3.390, -3.048	3.0	4.0	–	11.5	5	~ 11.5	~ -23.0	–	7.1	8.5	–
J0411-8032	62.791	-80.549	0.714	0.20	-1.936	-3.492, -2.168	2.3	1.2	–	3.8	5	~ 3.2	~ 860.5	–	4.4	3.6	–
J0435-8133	68.846	-81.566	1.099	0.69	-4.476	0.035, -13.235	3.7	3.8	–	8.2	5	~ 9.5	~ -1627.0	–	6.0	4.8	–

… *Continued on next page*

Table A.1 – … *Continued from previous page*

Source Name	RA [deg]	DEC [deg]	Δr [deg]	A_{fe} [A_{bm}]	$\tilde{\alpha}$	$\tilde{\alpha}_{c1}, \tilde{\alpha}_{c2}$	I_{peak} [**]	$\langle\sigma_{qu}\rangle$ [%]	β	$\langle p_0\rangle$ [%]	DF	$\lvert F\rvert_p$ [%]	ϕ_{peak} [*]	σ_ϕ [*]	T	$\tilde{T}$	Fid
J0422-8030	65.560	-80.502	0.257	0.16	-1.545	-10.636, -12.553	4.0	0.5	–	1.4	5	~ 1.3	~ -248.5	–	3.8	3.3	–
J0422-8146	65.561	-81.773	1.295	1.46	-2.483	-2.720, -9.854	1.5	2.3	–	13.9	5	~ 9.8	~ -35.5	–	5.4	8.1	–
J0403-81036	60.950	-81.612	1.467	0.21	-3.619	-3.947, -4.723	5.3	1.5	–	3.6	5	~ 3.3	~ 1861.0	–	5.0	5.2	–
J0412-8130	63.051	-81.509	0.543	0.11	-3.355	-6.858, -11.007	6.2	1.3	–	5.5	6	~ 5.1	~ 1459.0	–	7.2	6.2	–
J03059-8104	59.937	-81.075	0.681	0.10	-1.923	-7.238, -7.149	2.4	2.6	–	7.6	6	~ 9.1	~ -752.0	–	6.0	3.9	–
J0412-8050	63.064	-80.846	0.247	0.12	-3.071	-14.928, -16.338	2.9	2.8	–	13.3	6	~ 15.7	~ -1554.5	–	9.6	4.1	–
J0404-80039	61.246	-80.656	0.594	0.11	-1.753	-4.838, -8.323	2.1	2.5	–	9.3	6	~ 10.1	~ -1916.0	–	6.4	4.8	–
J0347-8126	56.951	-81.450	1.205	0.13	-4.635	-9.716, -12.729	4.2	6.0	–	12.5	6	~ 18.2	~ -336.0	–	7.0	4.2	–
J0352-8022	58.210	-80.379	1.162	0.31	-4.617	-5.403, -8.923	8.0	4.9	–	20.4	6	~ 22.2	~ 278.0	–	11.7	5.8	–
J0345-8057	56.321	-80.950	1.249	0.13	-4.401	-8.305, -13.479	5.5	3.6	–	10.3	6	~ 8.9	~ 1823.0	–	6.2	2.9	–
J0406-81017	61.594	-81.287	0.504	0.11	-2.680	-5.802, -11.317	13.1	0.5	–	2.1	6	~ 1.8	~ 1157.5	–	7.7	6.2	–
J0407-81042	61.964	-81.712	0.793	0.12	-3.614	-5.828, -12.615	7.3	1.6	–	4.8	6	~ 6.3	~ 1174.5	–	9.1	5.0	–
J0418-8019	64.515	-80.326	0.675	0.12	-4.573	-5.566, -11.164	6.4	3.3	–	3.0	6	~ 11.5	~ -761.0	–	8.0	3.4	–
J0345-8056	56.303	-80.950	1.252	1.54	-4.577	-5.454, -11.218	2.2	11.5	–	25.0	6	~ 23.0	~ -5.0	–	5.2	3.1	–
J0346-8127	56.516	-81.451	1.267	0.12	-4.497	-10.810, -13.236	2.8	6.1	–	11.7	6	~ 13.3	~ 351.0	–	4.5	3.4	–
J0408-80051	62.232	-80.853	0.356	0.10	-2.402	-20.432, -25.315	6.6	0.8	–	3.4	6	~ 3.1	~ 1176.5	–	6.9	3.2	–
J04018-8108	64.731	-81.134	0.151	0.18	-4.007	-5.844, -7.040	4.1	3.4	–	10.8	6	~ 10.9	~ -88.5	–	6.7	3.4	–
J0409-80052	62.484	-80.870	0.312	0.11	-2.382	-8.381, -14.812	1.9	3.1	–	10.9	6	~ 12.7	~ 1130.5	–	6.5	5.1	–
J0346-8119	56.545	-81.317	1.230	0.12	-4.144	-4.753, -6.591	2.7	5.3	–	18.1	6	~ 17.8	~ -521.5	–	6.3	4.8	–
J0406-80018	61.645	-80.312	0.811	0.15	-4.378	-8.037, -11.959	6.5	2.2	–	6.6	6	~ 5.3	~ 159.0	–	4.6	4.2	–
J0411-8028	62.779	-80.479	0.575	0.17	-3.797	-6.290, -3.208	2.0	5.4	–	10.6	6	~ 13.4	~ 499.0	–	4.9	2.6	–
J0347-8052	56.757	-80.881	1.191	0.11	-4.202	-8.806, -10.385	1.9	5.9	–	25.9	6	~ 21.7	~ -1577.0	–	6.1	5.5	–
J0408-81034	62.069	-81.567	0.659	0.11	-2.603	-12.944, -14.878	2.3	2.9	–	9.7	6	~ 10.8	~ -728.0	–	6.5	3.6	–
J0352-8130	58.016	-81.503	1.077	0.17	-4.111	-8.816, -10.017	15.8	0.9	–	4.1	6	~ 2.8	~ 328.0	–	7.1	6.1	–
J04023-8108	65.822	-81.136	0.275	0.55	-4.554	-4.170, -6.274	10.1	2.8	–	10.0	6	~ 6.6	~ 1596.5	–	8.1	4.1	–
J0414-8041	63.604	-80.692	0.327	1.28	-3.858	-7.798, -8.039	2.8	5.6	–	20.5	6	~ 21.0	~ -365.5	–	8.9	3.4	–
J0355-8045	58.998	-80.753	0.874	0.11	-3.006	-7.450, -8.271	2.7	2.6	–	9.6	6	~ 10.3	~ -1225.0	–	6.7	2.9	–
J03051-8109	57.856	-81.158	1.009	0.11	-3.720	-5.129, -11.462	4.2	3.1	–	10.5	6	~ 9.3	~ 1994.5	–	7.4	5.0	–
J0353-8116	58.287	-81.273	0.963	0.11	-3.008	-6.754, -10.568	2.5	3.4	–	11.7	6	~ 14.4	~ 1248.5	–	8.3	4.4	–
J0410-8046	62.633	-80.772	0.347	0.10	-2.311	-5.146, -11.973	8.7	0.6	–	1.5	6	~ 2.0	~ -228.0	–	5.9	3.9	–
J0400-81015	60.229	-81.261	0.678	0.34	-3.154	-7.041, -8.454	3.4	2.6	–	8.5	6	~ 9.0	~ -48.0	–	6.1	4.4	–
J0403-81036	60.952	-81.613	0.793	0.16	-3.904	-6.498, -8.860	5.6	1.4	–	2.1	6	~ 5.0	~ -102.0	–	5.0	3.7	–
J0403-81014	60.889	-81.243	0.578	0.16	-2.968	-5.364, -8.643	1.7	5.8	–	14.7	6	~ 22.3	~ -25.5	–	9.0	4.8	–
J0401-81037	60.405	-81.627	0.858	0.32	-4.268	-7.837, -10.087	2.9	6.6	–	24.0	6	~ 17.2	~ 1118.0	–	6.4	5.1	–
J04019-8107	64.763	-81.132	0.151	0.26	-4.211	-8.031, -14.501	2.2	6.0	–	7.7	6	~ 12.0	~ -481.5	–	3.9	3.9	–
J0352-8022	58.198	-80.378	1.164	0.31	-4.551	-4.504, -8.589	12.9	1.2	–	4.7	6	~ 5.4	~ -966.5	–	8.1	4.4	–

… *Continued on next page*

Table A.1 – … *Continued from previous page*

Source Name	RA [deg]	DEC [deg]	Δr [deg]	A_{fe} [A_{bm}]	$\tilde{\alpha}$	$\tilde{\alpha}_{c1}, \tilde{\alpha}_{c2}$	I_{peak} [**]	$\langle\sigma_{qu}\rangle$ [%]	β	$\langle p_0\rangle$ [%]	DF	$\lvert F\rvert_p$ [%]	ϕ_{peak} [*]	σ_ϕ [*]	T	$\tilde{T}$	Fid
J0407-81040	61.857	-81.683	0.775	0.12	-4.280	-4.530, -12.539	3.0	4.6	–	17.2	6	~ 18.9	~ 818.0	–	7.7	4.7	–
J0408-81031	62.141	-81.527	0.620	1.30	-3.843	-12.778, -15.854	1.7	6.5	–	26.4	6	~ 25.7	~ 651.0	–	6.4	5.2	–
J0414-8041	63.622	-80.690	0.327	0.30	-3.648	-5.283, -8.865	3.7	3.4	–	12.5	6	~ 11.7	~ 1866.0	–	8.8	3.5	–
J0412-8115	63.051	-81.259	0.321	0.52	-3.275	-6.315, -12.934	1.8	6.0	–	25.4	6	~ 21.8	~ -307.0	–	7.7	4.8	–
J0414-8041	63.603	-80.698	0.321	0.18	-3.955	-6.942, -8.561	3.2	3.7	–	12.1	6	~ 13.0	~ -1718.5	–	6.2	3.5	–
J0400-8107	60.091	-81.121	0.663	0.34	-2.070	-6.526, -9.331	8.4	0.9	–	5.9	6	~ 5.5	~ -53.5	–	18.3	6.9	–
J0356-8040	59.045	-80.674	0.896	0.49	-3.030	-8.769, -10.385	6.5	1.3	–	6.7	6	~ 6.7	~ -339.5	–	11.8	5.6	–
J0413-8059	63.298	-80.997	0.155	0.11	-2.747	-7.239, -9.073	2.6	2.1	–	6.0	6	~ 8.6	~ 944.5	–	6.4	3.8	–
J0407-81042	61.910	-81.707	0.792	0.11	-4.523	-6.143, -9.195	2.7	7.1	–	17.7	6	~ 24.7	~ -631.0	–	8.2	4.6	–
J04010-8100	62.683	-81.008	0.251	0.11	-2.660	-16.751, -18.848	2.5	3.0	–	9.8	6	~ 10.7	~ 779.0	–	7.0	4.4	–
J0410-8142	62.711	-81.713	0.751	0.14	-4.635	-7.705, -9.408	4.5	6.9	–	22.5	6	~ 21.6	~ -900.0	–	8.3	5.4	–
J0401-81026	60.297	-81.442	0.752	0.11	-3.088	-14.126, -16.139	2.6	2.9	–	11.2	6	~ 13.2	~ -863.5	–	7.4	4.7	–
J0359-8048	59.962	-80.812	0.709	0.11	-2.878	-6.174, -8.755	2.4	3.9	–	8.2	6	~ 11.1	~ 615.0	–	6.1	2.8	–
J04015-8105	63.885	-81.086	0.106	0.11	-2.910	-5.166, -7.628	2.2	4.3	–	9.4	6	~ 13.3	~ 465.5	–	6.9	3.9	–
J0351-8135	57.838	-81.584	1.137	0.16	-4.488	-7.373, -8.915	9.3	1.9	–	7.4	6	~ 7.8	~ -159.0	–	9.1	4.4	–
J0352-8022	58.186	-80.376	1.167	0.31	-4.238	-12.894, -15.820	12.9	1.3	–	6.3	6	~ 5.5	~ 254.0	–	11.3	6.1	–
J0406-81043	61.613	-81.730	0.833	0.17	-4.583	-14.509, -12.472	11.1	1.9	–	7.3	6	~ 6.4	~ -1697.0	–	8.2	5.5	–
J0401-81037	60.402	-81.629	0.860	0.56	-4.343	-14.510, -16.686	3.2	4.5	–	15.8	6	~ 15.4	~ -819.0	–	5.8	2.2	–
J04018-8108	64.740	-81.133	0.151	0.38	-4.217	-7.592, -10.872	4.2	3.8	–	15.1	6	~ 11.1	~ -1486.5	–	6.3	5.6	–
J0358-8117	59.640	-81.291	0.772	0.17	-3.154	-13.428, -15.468	1.9	5.4	–	16.4	6	~ 17.6	~ -1618.0	–	6.4	4.2	–
J0354-8052	58.560	-80.878	0.910	0.17	-3.265	-5.928, -11.399	2.5	3.6	–	6.2	6	~ 11.4	~ 1882.0	–	6.2	2.7	–
J0403-8103	60.794	-81.052	0.547	0.24	-3.067	-7.155, -11.112	3.3	2.9	–	11.6	6	~ 9.7	~ 437.5	–	6.7	4.9	–
J0413-8131	63.313	-81.531	0.551	0.15	-3.688	-5.905, -11.444	3.4	3.0	–	9.1	6	~ 9.0	~ -1012.0	–	5.2	3.6	–
J0400-81023	60.102	-81.393	0.751	0.13	-2.946	-8.884, -3.260	3.3	1.9	–	6.6	6	~ 9.5	~ -227.5	–	8.0	3.4	–
J0411-8032	62.791	-80.549	0.510	0.15	-3.300	-5.907, -9.663	2.3	4.0	–	9.2	6	~ 10.9	~ 882.0	–	4.8	4.3	–
J0400-8107	60.080	-81.126	0.665	0.36	-2.498	-5.042, -10.146	13.0	0.4	–	2.7	6	~ 2.5	~ -72.0	–	10.9	7.1	–
J0413-8052	63.488	-80.872	0.179	0.21	-2.945	-7.502, -9.700	2.8	2.3	–	8.0	6	~ 8.7	~ 1031.0	–	6.3	4.8	–
J0355-8147	58.767	-81.794	1.144	0.22	-4.631	-4.891, -9.880	30.7	1.1	–	3.4	6	~ 2.6	~ 466.0	–	6.6	6.7	–
J0405-80059	61.344	-80.999	0.460	0.10	-2.583	-6.985, -9.846	2.0	5.4	–	20.8	6	~ 17.5	~ 582.5	–	9.0	4.7	–
J0408-81031	62.119	-81.522	0.617	2.40	-4.218	-0.238, 13.537	1.6	18.8	–	84.6	6	~ 31.8	~ -296.5	–	4.1	5.0	–
J04018-8108	64.599	-81.150	0.157	0.12	-3.573	-14.323, -18.853	1.8	6.4	–	1.3	6	~ 17.2	~ -549.5	–	4.9	2.4	–
J0414-8016	63.614	-80.269	0.739	0.12	-4.429	-4.035, -3.049	8.3	1.9	–	5.9	6	~ 6.8	~ 764.0	–	7.2	5.3	–
J0403-8103	60.810	-81.052	0.545	0.49	-3.057	-7.526, -8.915	2.7	3.2	–	10.7	6	~ 8.7	~ -1279.0	–	5.0	5.5	–
J0410-8142	62.703	-81.715	0.753	0.16	-4.641	-5.045, -10.225	4.2	6.4	–	14.6	6	~ 17.6	~ -892.5	–	6.8	3.1	–
J0353-8036	58.278	-80.607	1.037	0.12	-3.793	-6.049, -8.434	6.0	1.8	–	2.4	6	~ 5.5	~ 1621.0	–	5.8	2.7	–
J0418-8111	64.656	-81.187	0.195	0.11	-2.273	-5.480, -15.846	2.6	3.6	–	7.8	6	~ 9.2	~ -233.5	–	4.4	4.5	–

… *Continued on next page*

Table A.1 – ... *Continued from previous page*

Source Name	RA [deg]	DEC [deg]	Δr [deg]	A_{fe} [A_{bm}]	$\tilde{\alpha}$	$\tilde{\alpha}_{c1}, \tilde{\alpha}_{c2}$	I_{peak} [**]	$\langle \sigma_{qu} \rangle$ [%]	β	$\langle p_0 \rangle$ [%]	DF	$\lvert F \rvert_p$ [%]	ϕ_{peak} [*]	σ_ϕ [*]	T	$\tilde{T}$	Fid
J0400-80010	60.004	-80.173	1.083	0.12	-4.325	-7.713, -9.482	4.7	3.3	–	6.9	6	~ 9.6	~ -355.0	–	5.3	4.4	–
J0408-80025	62.085	-80.432	0.670	0.11	-2.128	-9.431, -13.092	2.1	3.9	–	19.3	6	~ 12.4	~ 64.0	–	5.5	5.0	–
J04023-8108	65.814	-81.134	0.273	0.18	-4.442	-6.202, -10.663	13.6	0.9	–	3.3	6	~ 2.8	~ 667.5	–	5.2	7.5	–
J0414-8115	63.506	-81.255	0.282	0.11	-3.150	-3.888, -7.932	2.1	4.0	–	9.9	6	~ 15.2	~ -611.0	–	7.6	3.4	–
J0408-81031	62.145	-81.524	0.616	0.16	-3.043	-6.452, -14.014	8.0	1.0	–	5.2	6	~ 3.8	~ -253.5	–	7.8	6.7	–
J0404-80048	61.184	-80.808	0.527	0.11	-2.552	-5.054, -9.037	10.0	0.4	–	2.6	6	~ 2.3	~ -20.5	–	7.6	6.0	–
J03059-8105	59.928	-81.090	0.684	0.11	-2.042	-5.463, -5.947	2.4	2.3	–	2.1	6	~ 7.6	~ -1133.0	–	4.8	1.9	–
J0406-81043	61.611	-81.728	0.832	0.15	-4.563	-7.765, -7.428	13.2	2.0	–	4.3	6	~ 5.5	~ 1410.0	–	8.5	4.1	–
J0406-80018	61.598	-80.314	0.813	0.12	-4.437	-7.190, -7.910	3.2	4.6	–	0.2	6	~ 11.6	~ -1514.5	–	5.1	2.5	–
J0355-8135	58.754	-81.599	1.028	0.11	-3.772	-5.643, -9.068	4.9	3.0	–	10.3	6	~ 7.6	~ -1903.0	–	6.6	4.2	–
J0356-8040	59.067	-80.674	0.892	9.29	-2.292	-5.734, -10.493	3.2	1.7	–	9.2	6	~ 10.4	~ -35.5	–	11.3	4.4	–
J0413-8131	63.275	-81.529	0.551	0.21	-3.939	-5.045, -8.347	3.1	5.8	–	14.3	6	~ 14.4	~ 9.5	–	5.0	4.0	–
J0414-8057	63.742	-80.960	0.094	0.11	-2.787	-14.789, -14.360	2.8	2.9	–	7.8	6	~ 8.3	~ -1789.0	–	6.4	4.3	–
J0358-8130	59.706	-81.511	0.863	0.12	-3.602	-7.458, -10.572	13.1	0.9	–	2.0	6	~ 1.7	~ 1590.0	–	4.8	4.8	–
J0419-8040	64.993	-80.682	0.338	0.16	-3.870	-4.280, -8.046	4.2	3.4	–	7.1	6	~ 8.6	~ -1997.5	–	6.0	3.0	–
J0426-8045	66.630	-80.755	0.445	0.13	-4.614	-4.681, -9.141	4.1	6.9	–	8.3	6	~ 18.6	~ 1283.5	–	6.0	3.3	–
J0356-8040	59.057	-80.676	0.893	0.20	-2.890	-13.563, -17.216	10.6	0.6	–	3.2	6	~ 2.8	~ 71.5	–	8.3	6.3	–
J0359-8036	59.944	-80.606	0.798	0.11	-2.837	-5.685, -15.725	4.8	1.2	–	3.9	6	~ 3.7	~ -1531.0	–	4.6	4.5	–
J0405-8101	61.280	-81.033	0.470	0.15	-3.003	-13.869, -12.651	3.4	1.9	–	9.5	6	~ 6.7	~ 1586.5	–	5.3	5.3	–
J0408-80038	62.246	-80.636	0.488	0.11	-3.098	-5.656, -8.589	2.5	2.8	–	6.9	6	~ 12.3	~ 1418.5	–	6.7	3.4	–
J03058-8103	59.632	-81.063	0.728	0.11	-2.468	-6.940, -7.663	16.3	0.4	–	1.6	6	~ 1.5	~ -1336.5	–	8.3	5.4	–
J0413-8052	63.499	-80.872	0.178	1.86	-2.722	-7.227, -8.840	1.5	4.1	–	12.4	6	~ 12.4	~ 1289.0	–	4.9	3.5	–
J0355-8120	58.815	-81.344	0.907	0.42	-3.216	-5.002, -9.325	1.7	5.1	–	23.3	6	~ 24.8	~ -208.0	–	8.3	4.9	–
J0358-8130	59.709	-81.513	0.864	0.12	-3.683	-8.223, -10.370	9.4	1.4	–	6.7	6	~ 5.8	~ -43.5	–	11.6	5.5	–
J04023-8108	65.798	-81.136	0.271	2.48	-4.587	-8.654, -11.443	6.7	4.7	–	11.8	6	~ 17.0	~ -28.0	–	9.5	4.5	–
J0348-8120	57.003	-81.335	1.166	0.11	-3.966	-7.238, -19.861	2.8	3.6	–	9.7	6	~ 12.1	~ -307.0	–	5.8	3.5	–
J0419-8116	64.933	-81.283	0.300	0.12	-3.923	-7.598, -12.733	2.6	6.8	–	22.9	6	~ 19.2	~ 698.5	–	7.1	5.9	–
J0357-8043	59.336	-80.731	0.830	0.11	-2.905	-7.367, -9.666	2.0	3.6	–	15.2	6	~ 12.7	~ 336.0	–	6.0	4.3	–
J0412-8115	63.029	-81.255	0.320	0.76	-3.150	-7.411, -10.544	2.7	2.2	–	8.8	6	~ 8.8	~ -1154.5	–	5.4	4.5	–
J0400-80037	60.120	-80.620	0.766	0.50	-2.916	-5.089, -9.811	3.3	2.4	–	10.8	6	~ 6.9	~ 158.5	–	5.4	5.3	–
J0401-81015	60.259	-81.262	0.674	0.53	-2.663	-7.682, -10.596	9.4	0.7	–	3.1	6	~ 2.6	~ -670.5	–	7.4	5.0	–
J0401-80031	60.347	-80.529	0.788	0.11	-3.547	-5.075, -11.664	2.5	5.2	–	22.0	6	~ 19.2	~ 1728.0	–	8.0	4.1	–
J0354-8023	58.519	-80.394	1.111	0.14	-4.502	-7.513, -11.857	15.0	1.2	–	5.2	6	~ 3.4	~ 1408.5	–	7.0	6.1	–
J04023-8107	65.803	-81.131	0.269	0.46	-4.492	-15.102, -17.716	5.6	3.9	–	16.5	6	~ 18.6	~ -1.5	–	12.7	6.4	–
J0406-81017	61.590	-81.287	0.227	0.17	-4.125	-7.723, -9.697	6.5	0.4	–	0.7	7	~ 1.4	~ 1539.5	–	4.8	3.7	–
J0411-8012	62.935	-80.207	1.327	0.15	-1.023	-4.686, -7.749	1.4	0.6	–	1.6	7	~ 2.6	~ 1799.5	–	4.8	2.7	–

... *Continued on next page*

Table A.1 – ... *Continued from previous page*

Source Name	RA [deg]	DEC [deg]	Δr [deg]	A_{fe} [A_{bm}]	$\tilde{\alpha}$	$\tilde{\alpha}_{c1}, \tilde{\alpha}_{c2}$	I_{peak} [**]	$\langle\sigma_{qu}\rangle$ [%]	β	$\langle p_0\rangle$ [%]	DF	$\|F\|_p$ [%]	ϕ_{peak} [*]	σ_ϕ [*]	T	$\tilde{T}$	Fid
J0355-7950	58.759	-79.848	1.693	0.24	-3.679	-4.688, -10.317	1.9	1.3	–	5.5	7	~ 5.9	~ -354.5	–	6.5	3.8	–
J03058-8103	59.638	-81.062	0.489	3.23	-2.552	-3.259, -2.671	6.6	0.2	–	1.4	7	~ 1.4	~ -108.0	–	8.9	5.3	–
J0422-8030	65.557	-80.502	1.219	0.16	-3.554	-5.473, -9.073	3.4	0.6	–	2.6	7	~ 2.2	~ 1300.0	–	5.5	4.7	–
J03048-8004	57.021	-80.076	1.564	1.69	-2.539	-5.940, -6.245	1.9	1.6	–	9.7	7	~ 8.1	~ 24.0	–	6.6	6.7	–
J0345-8043	56.325	-80.726	1.065	0.16	-3.950	-5.932, -9.242	2.5	1.0	–	4.2	7	~ 3.5	~ 663.5	–	5.2	3.9	–
J0406-80018	61.615	-80.313	1.190	0.42	-1.254	-11.409, -13.728	2.7	0.4	–	1.7	7	~ 1.7	~ -5.0	–	5.3	3.8	–
J0426-8045	66.627	-80.755	1.135	0.16	-4.633	-7.770, -12.952	3.9	1.6	–	4.7	7	~ 4.8	~ 1253.0	–	5.2	3.5	–
J03051-8109	57.852	-81.158	0.594	0.16	-4.636	-15.808, -19.345	2.5	1.8	–	5.7	7	~ 4.9	~ -1077.0	–	4.2	4.7	–
J0410-7943	62.721	-79.722	1.798	0.25	-4.211	-4.504, -3.840	4.3	0.7	–	1.7	7	~ 2.7	~ -818.0	–	5.4	3.0	–
J0359-8048	59.959	-80.812	0.709	0.16	-2.229	-6.600, -8.868	2.1	0.5	–	3.7	7	~ 2.6	~ -42.5	–	6.1	6.6	–
J0406-80035	61.617	-80.586	0.918	0.15	-1.688	-4.875, -12.489	2.1	0.6	–	2.6	7	~ 2.3	~ 641.0	–	5.6	4.5	–
J03052-8003	58.030	-80.064	1.515	0.20	-3.154	-6.465, -6.840	8.7	0.2	–	0.9	7	~ 1.0	~ 13.0	–	6.6	6.0	–
J0414-8016	63.612	-80.269	1.295	0.15	-1.778	-5.022, -12.383	16.3	0.1	–	0.5	7	~ 0.5	~ -4.0	–	12.0	9.4	–
J0354-8023	58.517	-80.394	1.177	0.17	-2.469	-4.810, -11.562	31.3	0.1	–	0.7	7	~ 0.4	~ -18.5	–	13.8	12.1	–
J0416-7948	64.205	-79.816	1.758	0.18	-4.573	-7.283, -9.338	10.8	0.3	–	2.2	7	~ 1.6	~ -84.0	–	6.8	7.7	–
J03051-8003	57.951	-80.060	1.523	0.24	-3.269	-4.946, -10.606	5.5	0.3	–	2.2	7	~ 2.1	~ 11.5	–	8.4	5.7	–
J0345-8023	56.434	-80.387	1.330	0.25	-4.052	-4.150, -11.597	2.1	1.0	–	3.8	7	~ 4.5	~ 782.0	–	4.9	4.6	–
J0401-81015	60.254	-81.262	0.268	0.60	-3.978	-33.507, -50.065	4.8	0.5	–	2.5	7	~ 2.0	~ -1589.0	–	5.2	7.9	–
J0404-79056	61.066	-79.939	1.561	0.17	-2.709	-4.963, -10.527	8.4	0.2	–	0.9	7	~ 1.0	~ -25.0	–	7.8	5.5	–
J0356-8040	59.037	-80.677	0.881	11.49	-1.628	-3.757, -9.939	4.3	0.3	–	1.8	7	~ 1.6	~ -166.5	–	9.2	5.6	–
J0418-8033	64.723	-80.550	1.107	0.16	-2.767	-4.128, -12.272	1.9	0.7	–	3.8	7	~ 3.8	~ -11.5	–	6.7	6.6	–
J04012-8109	63.048	-81.166	0.447	0.20	-3.745	-4.410, -13.622	15.6	0.1	–	1.1	7	~ 1.0	~ -4.5	–	9.6	7.0	–
J0417-8012	64.261	-80.210	1.386	0.22	-2.552	-4.981, -10.621	1.8	0.7	–	4.3	7	~ 3.7	~ -7.0	–	7.1	6.0	–
J0413-8052	63.485	-80.873	0.728	0.34	-2.666	-5.678, -9.915	2.5	0.6	–	3.2	7	~ 2.7	~ 55.0	–	5.7	5.7	–
J0355-7948	58.792	-79.809	1.731	0.16	-2.846	-4.962, -16.174	3.5	0.4	–	2.8	7	~ 2.0	~ -1675.0	–	6.0	7.1	–
J04013-8006	63.465	-80.116	1.436	0.16	-2.452	-6.422, -9.604	3.0	0.4	–	1.5	7	~ 1.7	~ 510.5	–	4.9	2.8	–
J0408-80038	62.243	-80.636	0.882	0.16	-1.818	-4.795, -11.889	2.6	0.5	–	3.5	7	~ 4.1	~ -28.0	–	13.9	6.9	–
J03045-8001	56.364	-80.031	1.650	0.57	-4.599	-6.209, -7.520	2.4	2.1	–	13.1	7	~ 5.4	~ 667.0	–	4.1	5.7	–
J0415-7959	63.787	-79.995	1.566	0.16	-3.722	-53.367, -82.051	9.3	0.2	–	1.2	7	~ 1.0	~ 1601.5	–	5.5	5.0	–
J0345-8056	56.319	-80.950	0.910	0.22	-4.498	-5.272, -11.241	4.4	0.8	–	2.9	7	~ 3.9	~ 1371.0	–	7.5	5.1	–
J04018-8108	64.730	-81.134	0.662	0.42	-4.588	-11.210, -11.513	2.6	2.3	–	6.9	7	~ 6.5	~ -29.5	–	5.2	5.6	–
J0425-8015	66.261	-80.253	1.493	0.24	-4.631	-7.194, -9.124	2.4	2.3	–	6.9	7	~ 6.7	~ -20.5	–	4.2	7.6	–
J0413-8059	63.294	-80.997	0.606	0.16	-3.111	-7.163, -10.363	1.8	0.9	–	4.5	7	~ 4.5	~ -1174.0	–	6.3	4.6	–
J0400-8107	60.085	-81.121	0.407	0.54	-3.100	-4.120, -17.936	6.0	0.3	–	1.9	7	~ 1.4	~ -896.5	–	6.6	5.0	–
J0350-7942	57.500	-79.702	1.890	9.46	-4.615	-9.639, -11.689	3.4	1.9	–	6.4	7	~ 6.8	~ -154.0	–	6.2	7.9	–
J0359-8034	59.758	-80.572	0.950	0.15	-1.789	-4.484, -12.399	1.8	0.5	–	0.9	7	~ 2.0	~ -174.5	–	4.7	2.0	–

... *Continued on next page*

Table A.1 – … *Continued from previous page*

Source Name	RA [deg]	DEC [deg]	Δr [deg]	A_{fe} [A_{bm}]	$\tilde{\alpha}$	$\tilde{\alpha}_{c1}, \tilde{\alpha}_{c2}$	I_{peak} [**]	$\langle\sigma_{qu}\rangle$ [%]	β	$\langle p_0\rangle$ [%]	DF	$\lvert F\rvert_p$ [%]	ϕ_{peak} [*]	σ_ϕ [*]	T	$\tilde{T}$	Fid
J0342-8034	55.639	-80.579	1.250	0.17	-4.649	-4.969, -12.122	4.0	1.9	–	7.5	7	~ 5.2	~ 93.0	–	5.3	5.8	–
J0419-8040	64.990	-80.682	1.018	0.20	-3.000	-5.632, -9.762	4.7	0.3	–	1.1	7	~ 1.4	~ -1884.5	–	5.7	3.7	–
J03058-8103	59.616	-81.066	0.487	6.66	-2.746	-11.982, -14.857	3.3	0.5	–	2.0	7	~ 2.1	~ -404.5	–	6.2	3.4	–
J0400-79054	60.071	-79.914	1.594	0.16	-1.805	-8.685, -11.607	6.7	0.2	–	0.9	7	~ 0.8	~ 864.5	–	6.8	5.3	–
J0404-80039	61.243	-80.656	0.844	0.15	-1.206	-4.039, -11.370	2.3	0.4	–	2.3	7	~ 1.8	~ -1078.0	–	5.9	5.2	–
J0411-8029	62.839	-80.485	1.052	0.21	-2.011	-4.785, -10.617	2.3	0.5	–	3.1	7	~ 1.9	~ -1476.5	–	5.2	6.6	–
J04023-8108	65.810	-81.134	0.803	0.21	-4.649	-10.064, -12.183	9.1	1.2	–	4.0	7	~ 3.5	~ -1604.5	–	5.1	6.6	–
J0358-8130	59.701	-81.510	0.203	0.18	-4.676	-5.530, -5.565	5.1	4.8	–	22.4	7	~ 6.4	~ -1455.0	–	3.3	6.4	–
J04023-8107	65.800	-81.131	0.803	0.74	-4.675	-5.202, -10.419	4.6	1.9	–	5.0	7	~ 5.2	~ 1481.5	–	4.2	6.4	–
J0359-8036	59.941	-80.606	0.911	0.15	-1.695	-4.569, -12.915	5.9	0.1	–	1.0	7	~ 0.8	~ 3.5	–	6.5	7.3	–
J0425-8013	66.266	-80.232	1.512	0.25	-4.631	-5.151, -13.299	5.3	1.1	–	2.2	7	~ 2.7	~ -1730.0	–	4.2	5.3	–
J0404-80024	61.188	-80.410	1.091	0.15	-1.588	-4.175, -10.925	1.7	0.8	–	3.3	7	~ 3.1	~ -582.0	–	6.0	3.7	–
J0407-80017	61.993	-80.289	1.219	0.15	-2.142	-5.647, -9.880	2.5	0.4	–	1.1	7	~ 2.1	~ 708.5	–	6.0	2.0	–
J0408-80051	62.228	-80.853	0.671	0.15	-2.182	-4.788, -12.519	5.6	0.2	–	1.0	7	~ 0.8	~ 330.0	–	5.0	4.9	–
J0357-8043	59.333	-80.731	0.815	0.15	-2.187	-4.062, -10.729	2.2	0.5	–	2.7	7	~ 2.9	~ 447.0	–	6.9	5.0	–
J04025-8008	66.394	-80.134	1.607	0.34	-4.632	-4.764, -10.941	4.2	2.2	–	9.8	7	~ 5.1	~ -1702.0	–	4.2	4.2	–
J0400-79049	60.090	-79.818	1.690	0.18	-3.111	-5.054, -9.670	23.8	0.1	–	0.7	7	~ 0.7	~ -101.0	–	14.3	8.4	–
J04023-8006	65.887	-80.108	1.589	0.16	-4.012	-4.451, -13.851	2.1	1.2	–	5.4	7	~ 4.3	~ -801.5	–	4.6	3.8	–
J0408-80025	62.082	-80.432	1.080	0.15	-0.800	-4.470, -12.220	3.0	0.6	–	1.4	7	~ 1.9	~ -1035.5	–	6.6	2.7	–
J0401-80031	60.344	-80.529	0.978	0.15	-1.980	-5.730, -9.380	3.6	0.3	–	1.5	7	~ 1.4	~ -527.0	–	5.9	4.2	–
J03058-8103	59.654	-81.064	0.486	2.73	-2.011	-4.129, -14.590	1.6	0.9	–	4.1	7	~ 3.2	~ -60.0	–	4.6	4.9	–
J0411-8032	62.788	-80.549	0.988	0.19	-2.010	-9.525, -12.701	2.9	0.4	–	2.4	7	~ 2.7	~ -0.5	–	9.5	5.1	–
J0358-8039	59.510	-80.664	0.870	0.15	-2.259	-5.584, -10.162	1.7	0.6	–	4.4	7	~ 3.2	~ -1407.0	–	5.9	6.2	–
J0406-80018	61.596	-80.314	1.189	0.16	-2.061	-4.924, -12.380	7.8	0.2	–	1.4	7	~ 1.5	~ 9.0	–	13.4	7.4	–
J0352-7946	58.231	-79.779	1.782	0.16	-4.412	-8.267, -10.048	2.6	1.5	–	5.9	7	~ 5.0	~ 0.5	–	5.2	5.5	–
J0350-7942	57.522	-79.704	1.886	0.37	-4.652	-18.128, -24.031	6.9	0.9	–	2.4	7	~ 4.0	~ -165.0	–	7.0	7.9	–
J0413-8028	63.327	-80.480	1.079	0.15	-2.057	-3.778, -14.246	1.6	0.8	–	3.6	7	~ 2.9	~ 456.5	–	5.0	4.7	–
J0403-8103	60.793	-81.051	0.451	0.50	-2.542	-7.440, -10.831	1.9	0.8	–	4.4	7	~ 3.7	~ -1821.0	–	5.8	4.1	–
J0414-8018	63.744	-80.311	1.262	0.15	-2.211	-5.278, -10.585	3.1	0.3	–	1.5	7	~ 1.5	~ -1668.5	–	5.2	4.8	–
J0408-79046	62.155	-79.780	1.729	0.31	-3.451	-10.816, -12.737	4.3	0.5	–	2.1	7	~ 2.1	~ -1379.5	–	5.8	3.8	–
J04021-8002	65.483	-80.046	1.616	0.91	-4.377	-8.708, -10.010	1.6	2.6	–	11.2	7	~ 8.2	~ 519.5	–	4.7	5.2	–
J03056-8000	59.209	-80.012	1.518	0.17	-2.794	-5.111, -11.086	2.0	0.7	–	3.4	7	~ 2.7	~ -658.0	–	4.9	3.8	–
J0414-8011	63.576	-80.195	1.365	0.21	-2.060	-5.053, -11.859	1.8	0.7	–	3.2	7	~ 2.4	~ -1688.5	–	4.7	4.9	–
J0400-79049	60.108	-79.820	1.687	2.97	-3.436	-5.195, -12.181	2.3	0.9	–	3.4	7	~ 3.8	~ 141.5	–	5.1	3.9	–
J0426-8053	66.647	-80.896	1.045	0.17	-4.645	-5.238, -9.829	2.5	6.2	–	18.7	7	~ 13.3	~ -305.5	–	5.3	5.7	–
J0414-8057	63.738	-80.960	0.676	0.15	-3.209	-4.582, -12.996	2.2	0.8	–	2.4	7	~ 3.4	~ -892.5	–	5.6	3.3	–

… *Continued on next page*

Table A.1 – … *Continued from previous page*

Source Name	RA [deg]	DEC [deg]	Δr [deg]	A_{fe} [A_{bm}]	$\tilde{\alpha}$	$\tilde{\alpha}_{c1}, \tilde{\alpha}_{c2}$	I_{peak} [**]	$\langle \sigma_{qu} \rangle$ [%]	β	$\langle p_0 \rangle$ [%]	DF	$\vert F \vert_p$ [%]	ϕ_{peak} [*]	σ_ϕ [*]	T	$\tilde{T}$	Fid
J0402-79051	60.654	-79.864	1.638	0.17	-2.976	-4.849, -12.526	3.0	0.6	–	2.3	7	~ 2.5	~ 1026.0	–	6.2	2.7	–
J0405-8101	61.277	-81.032	0.469	0.22	-2.253	-4.557, -8.579	2.3	0.8	–	3.6	7	~ 2.9	~ -454.0	–	5.5	5.4	–
J0416-8021	64.099	-80.350	1.245	1.01	-2.372	-4.905, -12.292	1.2	1.1	–	6.5	7	~ 4.6	~ 748.5	–	5.4	5.9	–
J0359-8035	59.826	-80.594	0.926	8.18	-1.576	-5.474, -9.868	1.0	1.3	–	6.7	7	~ 5.3	~ 616.5	–	5.5	4.3	–
J0353-8036	58.275	-80.607	0.993	0.16	-2.492	-4.701, -10.669	8.2	0.2	–	1.4	7	~ 1.2	~ -18.5	–	10.0	8.0	–
J0418-8019	64.513	-80.326	1.293	0.15	-2.188	-9.309, -9.657	12.0	0.1	–	0.6	7	~ 0.5	~ -4.5	–	7.1	6.3	–
J0356-8020	59.036	-80.348	1.196	0.15	-2.129	-6.417, -10.546	4.5	0.3	–	2.1	7	~ 2.0	~ 34.5	–	9.7	5.9	–
J03048-8004	57.030	-80.070	1.569	0.83	-3.952	-4.941, -10.717	3.0	0.9	–	3.2	7	~ 3.5	~ 1055.5	–	5.4	5.0	–
J0412-8050	63.060	-80.846	0.721	0.17	-2.425	-8.363, -10.645	2.4	0.5	–	1.1	7	~ 2.0	~ 1460.0	–	4.6	3.6	–
J0355-8045	58.995	-80.752	0.813	0.15	-2.151	-5.746, -9.968	2.8	0.4	–	2.3	7	~ 1.8	~ -3.0	–	5.7	6.6	–
J0410-8046	62.630	-80.772	0.767	0.15	-1.553	-4.576, -13.505	6.2	0.1	–	0.4	7	~ 0.6	~ 281.5	–	5.3	2.0	–
J03058-8103	59.627	-81.063	0.489	0.16	-2.656	-21.811, -31.592	10.6	0.1	–	0.6	7	~ 0.8	~ -123.5	–	8.0	3.1	–
J0354-8052	58.556	-80.877	0.732	0.22	-2.597	-4.599, -12.831	2.0	0.7	–	3.9	7	~ 3.2	~ -29.5	–	5.9	4.8	–

A.2 Faraday Detections

The following tables list the detected Faraday emission components of the bright polarised sub-population (Table A.2) and the faint sub-population (Table A.3) as defined in Sections 3.6.2 and 3.6.3.

A.2.1 Bright Faraday detections

Table A.2: Catalog of ϕ-components of the bright sub-population of Faraday source detections.

Name	RA [deg]	DEC [deg]	Field	T	$\|F_i\|$	ϕ_i [rad m^{-2}]
J0412-8110	63.046	-81.169	DEEP1			
				28.3	0.0309	-34.5
				12.8	0.0140	-128.5
				8.7	0.0095	71.5
				8.2	0.0090	-140.0
J0414-8041	63.611	-80.693	DEEP1			
				11.3	0.0242	6.5
				10.7	0.0228	-17.0
				10.1	0.0215	71.0
				8.4	0.0179	122.0
J0414-8041	63.618	-80.690	DEEP1			
				9.3	0.0186	82.0
				9.0	0.0180	-2.5
J0425-8013	66.265	-80.231	DEEP1			
				45.5	0.0391	-23.0
				19.9	0.0171	-123.0
				17.7	0.0152	73.5
				12.8	0.0110	107.5
				11.8	0.0102	-21.5
J04023-8108	65.810	-81.134	DEEP1			
				45.6	0.0392	-35.0
				20.3	0.0175	-146.5
				19.3	0.0166	-22.5
				14.3	0.0123	-47.0
				12.9	0.0111	-200.0
J0431-8029	67.939	-80.490	DEEP1			
				35.0	0.0205	-34.0
				15.3	0.0089	-17.5
				14.2	0.0083	-42.5
				11.6	0.0068	-146.0
				10.9	0.0064	-190.5
J0414-8041	63.602	-80.697	DEEP1			
				34.2	0.0775	-9.0
				11.3	0.0257	87.0
				9.0	0.0203	-102.5
				8.7	0.0198	110.0
J0414-8041	63.608	-80.695	DEEP1			

... Continued on next page

Table A.2 – ... *Continued from previous page*

Name	RA [deg]	DEC [deg]	Field	T	$\lvert F_i \rvert$	ϕ_i [rad m^{-2}]
				35.8	0.0762	-9.0
				11.9	0.0254	75.5
				11.3	0.0241	15.5
				10.9	0.0231	-107.5
				10.4	0.0220	120.0
J0425-8013	66.263	-80.231	DEEP2			
				26.5	0.0299	-19.0
				10.5	0.0118	-121.0
				8.7	0.0097	-80.5
				8.2	0.0092	157.5
J0416-7948	64.202	-79.816	DEEP2			
				17.6	0.0057	109.0
				17.2	0.0055	-16.0
				16.0	0.0051	-53.5
J0424-7926	66.007	-79.436	DEEP2			
				13.0	0.0066	81.5
				10.2	0.0051	142.0
				9.5	0.0048	21.0
				8.5	0.0043	-134.0
J0416-7948	64.196	-79.813	DEEP2			
				130.5	0.0274	-14.0
				24.5	0.0051	103.5
				22.1	0.0046	-114.5
J0421-7928	65.409	-79.483	DEEP2			
				17.9	0.0186	-10.5
J0400-79049	60.087	-79.817	DEEP2			
				22.4	0.0089	-77.0
				20.5	0.0082	1.0
				18.1	0.0072	-56.0
				15.6	0.0062	-124.0
				14.1	0.0056	-85.5
				11.1	0.0044	127.5
J0418-8019	64.510	-80.325	DEEP2			
				23.1	0.0114	-4.5
J0356-8040	59.055	-80.676	DEEP2off			
				26.0	0.0401	-9.5
J0354-8023	58.517	-80.394	DEEP2off			
				35.4	0.0282	-9.0
				15.5	0.0124	-40.5
J0352-8022	58.168	-80.376	DEEP2off			
				26.5	0.0145	-55.0
				25.5	0.0139	-7.0

... *Continued on next page*

Table A.2 – ... *Continued from previous page*

Name	RA [deg]	DEC [deg]	Field	T	$\|F_i\|$	ϕ_i [rad m^{-2}]
				17.1	0.0094	-16.0
J0352-8022	58.155	-80.375	DEEP2off			
				52.9	0.0130	-53.0
				50.1	0.0123	-6.0
				34.2	0.0084	-14.5
J0352-8022	58.197	-80.378	DEEP2off			
				23.2	0.0249	-4.0
				14.0	0.0150	-57.5
				10.8	0.0116	149.5
J0425-8013	66.262	-80.231	DEEP3			
				54.4	0.0303	-19.0
				16.0	0.0089	6.5
				11.7	0.0065	-137.5
				11.4	0.0064	-28.5
J0425-8015	66.258	-80.252	DEEP3			
				10.1	0.0135	12.0
				9.4	0.0126	-25.0
J0424-7926	66.008	-79.436	DEEP3			
				51.1	0.0149	-17.0
				21.5	0.0063	11.5
				17.8	0.0052	-363.5
				15.8	0.0046	-73.5
				14.1	0.0041	92.0
J0431-8029	67.936	-80.490	DEEP3			
				43.8	0.0199	-33.0
				19.0	0.0086	43.0
				12.8	0.0058	78.0
				11.3	0.0051	-56.5
J0416-7948	64.196	-79.813	DEEP3			
				85.4	0.0231	-19.5
				18.6	0.0050	-41.0
				18.1	0.0049	-171.0
J0440-7946	70.064	-79.778	DEEP3			
				14.1	0.0166	38.0
				13.3	0.0157	-44.5
				10.8	0.0127	-18.5
J0425-7952	66.332	-79.874	DEEP3			
				86.0	0.0785	-29.0
				17.9	0.0163	11.5
J0425-7952	66.321	-79.870	DEEP3			
				63.6	0.0614	-29.0
				14.9	0.0144	121.0

... *Continued on next page*

Table A.2 – … *Continued from previous page*

Name	RA [deg]	DEC [deg]	Field	T	$\|F_i\|$	ϕ_i [rad m^{-2}]
				12.4	0.0120	20.5
J04021-8002	65.470	-80.043	DEEP3			
				38.7	0.0791	-23.5
J0400-8107	60.087	-81.124	DEEP6			
				19.9	0.0346	-3.0
				15.2	0.0265	-346.5
				14.3	0.0248	-309.0
				13.6	0.0236	47.5
				11.5	0.0200	-345.5
				11.4	0.0197	46.0
				10.5	0.0183	271.5
				10.3	0.0178	314.0
				10.1	0.0175	-673.0
				9.8	0.0171	361.5
				9.5	0.0164	88.5
				9.4	0.0163	-440.0
J0352-8022	58.157	-80.375	DEEP6			
				13.0	0.0133	-142.0
				11.1	0.0113	-106.5
				9.4	0.0097	-53.5
				9.2	0.0094	-175.0
J0410-8153	62.664	-81.892	DEEP6			
J0404-8101	61.234	-81.032	DEEP6			
				9.2	0.0237	-22.0
J0400-8107	60.091	-81.126	DEEP6			
				8.9	0.0163	-10.0
				8.3	0.0151	-170.5
J0412-8110	63.051	-81.169	DEEP6			
				37.6	0.0463	-31.0
				21.6	0.0265	323.0
				21.0	0.0258	290.0
				20.6	0.0253	-2.0
				19.4	0.0239	-46.0
				18.0	0.0222	-11.5
				17.3	0.0213	367.5
				16.8	0.0206	-381.5
				16.5	0.0203	643.0
				16.2	0.0200	21.0
				15.7	0.0194	-336.5
				15.2	0.0187	53.0
J0338-8123	54.642	-81.396	DEEP6			
J03058-8103	59.616	-81.062	DEEP6			
				19.1	0.0730	59.0

… *Continued on next page*

Table A.2 – … *Continued from previous page*

Name	RA [deg]	DEC [deg]	Field	T	$\|F_i\|$	ϕ_i [rad m^{-2}]
				18.4	0.0703	-27.5
				17.1	0.0654	71.5
				17.0	0.0649	36.0
				16.1	0.0614	-286.5
				14.5	0.0553	-312.0
				13.8	0.0527	-273.5
				13.6	0.0519	353.0
				11.9	0.0453	404.0
				11.2	0.0429	43.0
				11.1	0.0424	8.0
				10.6	0.0404	99.0
J0435-8057	68.875	-80.951	DEEP5			
				28.2	0.0082	-1.0
				23.5	0.0068	-76.5
				20.6	0.0060	57.0
				19.0	0.0055	-174.5
				18.7	0.0054	171.0
				18.2	0.0053	-69.5
				14.6	0.0042	133.5
				14.1	0.0041	-85.5
J0435-8126	68.823	-81.440	DEEP5			
				42.9	0.0500	-38.5
				14.2	0.0166	19.5
J0435-8126	68.796	-81.442	DEEP5			
				31.2	0.0323	-38.5
				10.2	0.0106	28.0
J0435-8053	68.872	-80.888	DEEP5			
				12.5	0.0092	-53.5
				11.3	0.0083	-81.5
				9.5	0.0070	170.0
				9.0	0.0066	-171.5
				8.4	0.0062	-127.5
				8.1	0.0060	3.5
J0410-8153	62.660	-81.891	DEEP5			
				15.7	0.0077	62.0
				14.8	0.0072	-57.5
				13.6	0.0067	120.5
				13.1	0.0064	47.0
				12.1	0.0059	-168.0
				11.8	0.0057	75.0
				10.0	0.0049	168.0
				9.4	0.0046	-122.0
				8.6	0.0042	-48.5
J04023-8108	65.813	-81.134	DEEP5			
				93.7	0.0356	-34.5
				40.4	0.0153	33.0
				24.1	0.0091	118.5

… *Continued on next page*

Table A.2 – … *Continued from previous page*

Name	RA [deg]	DEC [deg]	Field	T	$\|F_i\|$	ϕ_i [rad m^{-2}]
				22.4	0.0085	72.0
J0412-8110	63.049	-81.169	DEEP5			
				54.7	0.0296	-32.0
				15.8	0.0085	-101.5
				11.8	0.0064	-51.0
				10.8	0.0058	26.0
J04023-8107	65.804	-81.131	DEEP5			
				39.6	0.0329	-35.0
				25.1	0.0209	27.0
				17.2	0.0143	36.5
				16.6	0.0138	10.5
				15.4	0.0128	47.0
J04023-8108	65.820	-81.136	DEEP5			
				59.2	0.0405	-36.0
				31.8	0.0217	33.5
				15.4	0.0105	65.5
				14.7	0.0100	-149.0
J0352-8022	58.210	-80.379	DEEP7			
				29.0	0.0204	-35.5
				19.2	0.0135	-49.5
				18.4	0.0129	-24.5
				14.4	0.0101	-210.0
				13.5	0.0095	-89.0
				13.0	0.0091	-346.0
				11.6	0.0081	-263.5
J0352-8022	58.154	-80.375	DEEP7			
				80.2	0.0078	-7.0
				56.4	0.0055	-158.5
				36.7	0.0036	-122.0
				34.5	0.0034	-170.5
				31.0	0.0030	-53.5
				30.4	0.0030	77.5
J0406-80010	61.567	-80.183	DEEP7			
J0356-8040	59.054	-80.676	DEEP7			
				28.6	0.0188	-17.5
				11.1	0.0073	-124.0
				9.9	0.0065	-161.5
				8.3	0.0055	79.5
J0414-8041	63.603	-80.697	DEEP7			
				20.7	0.0550	-5.5
J0400-80037	60.088	-80.618	DEEP7			
				24.9	0.0380	-11.0
				12.3	0.0188	-20.5

… *Continued on next page*

Table A.2 – … *Continued from previous page*

Name	RA [deg]	DEC [deg]	Field	T	$\lvert F_i \rvert$	ϕ_i [rad m^{-2}]
				11.5	0.0176	7.5
J0400-80037	60.095	-80.621	DEEP7			
				46.5	0.0695	-12.5
				14.6	0.0219	101.0
				9.4	0.0141	-131.5

A.2.2 Faint Faraday detections

Table A.3: Catalog of ϕ-components of the faint sub-population of Faraday source detections.

Name	RA [deg]	DEC [deg]	Field	T	$\lvert F_i \rvert$	ϕ_i [rad m^{-2}]
J0406-80018	61.643	-80.311	DEEP1			
				12.0	0.0129	-108.5
				10.9	0.0116	-14.5
				8.0	0.0086	89.0
J0426-7949	66.693	-79.818	DEEP2			
				11.5	0.0202	27.0
				9.0	0.0159	75.0
J0359-8010	60.000	-80.173	DEEP2			
				11.4	0.0110	-9.0
				10.9	0.0104	-88.0
				8.2	0.0079	-79.5
J0414-8016	63.612	-80.269	DEEP2off			
				10.6	0.0257	-7.0
				8.5	0.0205	-30.0
J04012-8109	63.052	-81.166	DEEP6			
				19.0	0.0191	-64.5
				17.8	0.0178	-321.0
				17.0	0.0171	-82.0
				16.6	0.0167	-49.5
				16.2	0.0162	284.0
				15.6	0.0156	-367.5
				13.9	0.0140	-684.5
				13.3	0.0133	-646.5
				13.0	0.0130	-358.5
				12.7	0.0128	306.0
				12.2	0.0122	-619.5
				12.1	0.0121	272.0
				11.6	0.0116	7.5
J0425-8013	66.267	-80.231	DEEP6			

… *Continued on next page*

Table A.3 – … *Continued from previous page*

Name	RA [deg]	DEC [deg]	Field	T	$\lvert F_i \rvert$	ϕ_i [rad m^{-2}]
				9.0	0.6050	1916.0
				8.3	0.5553	1890.5
J0345-8112	56.472	-81.210	DEEP6			
				8.5	0.1596	195.5
				8.3	0.1546	-452.5
				8.2	0.1530	-43.5
J0410-8153	62.663	-81.894	DEEP5			
				9.1	0.0358	-81.5
				8.9	0.0349	-114.0
J0414-8041	63.610	-80.694	DEEP7			
				16.5	0.0441	-13.0
				8.0	0.0214	-144.0
J0400-79049	60.090	-79.818	DEEP7			
				13.6	0.0062	-100.5
				11.5	0.0053	-70.5

Bibliography

I. Agudo, C. Thum, H. Wiesemeyer, and T. P. Krichbaum. A 3.5 mm Polarimetric Survey of Radio-loud Active Galactic Nuclei. *ApJS*, 189:1–14, July 2010. doi: 10.1088/0067-0049/189/1/1.

C. S. Anderson, B. M. Gaensler, I. J. Feain, and T. M. O. Franzen. Broadband radio polarimetry and faraday rotation of 563 extragalactic radio sources. *The Astrophysical Journal*, 815(1):49, 2015. URL `http://stacks.iop.org/0004-637X/815/i=1/a=49`.

C. S. Anderson, B. M. Gaensler, and I. J. Feain. A study of broadband faraday rotation and polarization behavior over 1.3–10 ghz in 36 discrete radio sources. *The Astrophysical Journal*, 825(1):59, 2016. URL `http://stacks.iop.org/0004-637X/825/i=1/a=59`.

C. S. Anderson, B. M. Gaensler, G. H. Heald, S. P. O'Sullivan, J. F. Kaczmarek, and I. J. Feain. Broadband Radio Polarimetry of Fornax A. I. Depolarized Patches Generated by Advected Thermal Material from NGC 1316. *ApJ*, 855:41, March 2018. doi: 10.3847/1538-4357/aaaec0.

I Andruchow, G. E. Romero, and S. A. Cellone. Polarization microvariability of BL Lacertae objects. *Astronomy and Astrophysics*, 442(1):97–107, oct 2005. ISSN 0004-6361. doi: 10.1051/0004-6361:20053325. URL `http://www.edpsciences.org/10.1051/0004-6361:20053325`.

T. G. Arshakian, R. Stepanov, R. Beck, M. Krause, and D. Sokoloff. Modeling the total and polarized emission in evolving galaxies: "Spotty" magnetic structures. *Astronomische Nachrichten*, 332:524, June 2011. doi: 10.1002/asna.201111551.

Tigran G. Arshakian and Rainer Beck. Optimum frequency band for radio polarization observations. *Monthly Notices of the Royal Astronomical Society*, 418(4):2336–2342, 2011. ISSN 00358711. doi: 10.1111/j.1365-2966.2011.19623.x.

K. M. B. Asad, L. V. E. Koopmans, V. Jelić, A. Ghosh, F. B. Abdalla, M. A. Brentjens, A. G. de Bruyn, B. Ciardi, B. K. Gehlot, I. T. Iliev, M. Mevius, V. N. Pandey, S. Yatawatta, and S. Zaroubi. Polarization leakage in epoch of reionization windows - II. Primary beam model and direction-dependent calibration. *MNRAS*, 462:4482–4494, November 2016. doi: 10.1093/mnras/stw1863.

K. A. Assaf, P. J. Diamond, A. M. S. Richards, and M. D. Gray. Polarization morphology of SiO masers in the circumstellar envelope of the asymptotic giant branch star R Cassiopeiae. *MNRAS*, 431:1077–1089, May 2013. doi: 10.1093/mnras/stt242.

J. K. Banfield, S. J. George, A. R. Taylor, J. M. Stil, R. Kothes, and D. Scott. Polarized Radio Sources: A Study of Luminosity, Redshift, and Infrared Colors. *ApJ*, 733:69, May 2011. doi: 10.1088/0004-637X/733/1/69.

R. A. Battye, I. W. A. Browne, M. W. Peel, N. J. Jackson, and C. Dickinson. Statistical properties of polarized radio sources at high frequency and their impact on cosmic microwave background polarization measurements. *MNRAS*, 413:132–148, May 2011. doi: 10.1111/j.1365-2966.2010.18115.x.

R. Beck. The Role of Magnetic Fields in Spiral Galaxies. *a&Ss*, 289:293–302, 2004. doi: 10.1007/978-3-662-44625-6_18. URL http://adsabs.harvard.edu/abs/2004Ap{&}SS.289..293B{%}5Cnpapers2://publication/doi/10.1023/B:ASTR.0000014957.31590.50.

R. Beck. Magnetic Fields in Galaxies. *Space Sci Rev*, 166:215–230, May 2012. doi: 10.1007/s11214-011-9782-z.

R. Beck. Magnetic fields in the nearby spiral galaxy IC 342: A multi-frequency radio polarization study. *A&A*, 578:A93, June 2015. doi: 10.1051/0004-6361/201425572.

R. Beck and B. M. Gaensler. Observations of magnetic fields in the Milky Way and in nearby galaxies with a Square Kilometre Array. *New Astronomy Reviews*, 48:1289–1304, December 2004. doi: 10.1016/j.newar.2004.09.013.

R. Beck and R. Wielebinski. *Magnetic Fields in Galaxies*, volume 5, chapter 13, page 641. Springer, Dordrecht, 2013. doi: 10.1007/978-94-007-5612-0_13.

R. Beck, C. L. Carilli, M. A. Holdaway, and U. Klein. Multifrequency observations of the radio continuum emission from NGC 253. 1: Magnetic fields and rotation measures in the bar and halo. *A&A*, 292:409–424, December 1994.

R. Beck, M. Ehle, V. Shoutenkov, A. Shukurov, and D. Sokoloff. Magnetic field as a tracer of sheared gas flow in barred galaxies. *Nature*, 397(6717):324–327, 1999. ISSN 00280836. doi: 10.1038/16861. URL http://adsabs.harvard.edu/abs/1999Natur.397..324B.

R Beck, V Shoutenkov, M Ehle, J. I. Harnett, R. F. Haynes, A Shukurov, D. D. Sokoloff, and M Thierbach. Magnetic fields in barred galaxies. *Astronomy and Astrophysics*, 391(1):83–102, aug 2002. ISSN 0004-6361. doi: 10.1051/0004-6361:20020642. URL http://www.edpsciences.org/10.1051/0004-6361:20020642.

R. Beck, A. Fletcher, A. Shukurov, A. Snodin, D. D. Sokoloff, M. Ehle, D. Moss, and V. Shoutenkov. Magnetic fields in barred galaxies. *Astronomy and Astrophysics*, 444(3):739–765, dec 2005. ISSN 0004-6361. doi: 10.1051/0004-6361:20053556. URL http://adsabs.harvard.edu/abs/2005A{&}A...444..739Bhttp://www.edpsciences.org/10.1051/0004-6361:20053556.

R. Beck, P. Frick, R. Stepanov, and D. Sokoloff. Recognizing magnetic structures by present and future radio telescopes with Faraday rotation measure synthesis. *Astronomy & Astrophysics*, 543(3):A113, 2012. ISSN 0004-6361. doi: 10.1051/0004-6361/201219094.

Rainer Beck. Magnetic fields in spiral galaxies. *The Astronomy and Astrophysics Review*, 24(1):507–528, sep 2015. ISSN 00386308. doi: 10.1007/s00159-015-0084-4. URL http://arxiv.org/pdf/1509.04522v1.pdfhttp://arxiv.org/abs/1509.04522http://dx.doi.org/10.1007/978-3-662-44625-6{_}18http://link.springer.com/10.1007/978-3-662-44625-6{_}18http://link.springer.com/10.1007/s00159-015-0084-4.

Rainer Beck, Axel Brandenburg, David Moss, Anvar Shukurov, and Dmitry Sokoloff. GALACTIC MAGNETISM: Recent Developments and Perspectives. *Annual Review of Astronomy and Astrophysics*, 34(1):155–206, 1996. ISSN 0066-4146. doi: 10.1146/annurev.astro.34.1.155.

M. L. Bernet, F. Miniati, and S. J. Lilly. The Interpretation of Rotation Measures in the Presence of Inhomogeneous Foreground Screens. *ApJ*, 761:144, December 2012. doi: 10.1088/0004-637X/761/2/144.

D. C.-J. Bock, M. I. Large, and E. M. Sadler. SUMSS: A Wide-Field Radio Imaging Survey of the Southern Sky. I. Science Goals, Survey Design, and Instrumentation. *AJ*, 117:1578–1593, March 1999. doi: 10.1086/300786.

Axel Brandenburg and Kandaswamy Subramanian. Astrophysical magnetic fields and nonlinear dynamo theory. *arXiv preprint: astro-ph/0405052*, 2004. doi: 10.1016/j.physrep.2005.06.005. URL http://arxiv.org/abs/astro-ph/0405052http://dx.doi.org/10.1016/j.physrep.2005.06.005.

R Braun, G Heald, and R Beck. The Westerbork SINGS survey III. Global magnetic field topology. *arXiv preprint arXiv:1002.1776*, 42:1–19, 2010. ISSN 0004-6361. doi: 10.1051/0004-6361/200913375. URL http://arxiv.org/abs/1002.1776.

M. a. Brentjens and a. G. de Bruyn. Faraday Rotation Measure Synthesis. *Astronomy and Astrophysics*, 441(3):1217–1228, jul 2005. ISSN 0004-6361. doi: 10.1051/0004-6361:20052990. URL http://arxiv.org/abs/astro-ph/0507349{%}5Cnhttp://www.edpsciences.org/10.1051/0004-6361:20052990http://arxiv.org/abs/astro-ph/0507349http://dx.doi.org/10.1051/0004-6361:20052990.

D. S. Briggs. High Fidelity Interferometric Imaging: Robust Weighting and NNLS Deconvolution. In *American Astronomical Society Meeting Abstracts*, volume 27 of *Bulletin of the American Astronomical Society*, page 1444, December 1995.

S. Brown. Internal POSSUM Report #9: Assess Complexity of RM Synthesis Spectrum. Technical report, 2011.

S. Brown, B. Bergerud, A. Costa, B. M. Gaensler, J. Isbell, D. LaRocca, R. Norris, C. Purcell, L. Rudnick, and X. Sun. Classifying Complex Faraday Spectra with Convolutional Neural Networks. *ArXiv e-prints*, November 2017.

B. J. Burn. On the Depolarization of Discrete Radio Sources by Faraday Dispersion. *Monthly Notices of the Royal Astronomical Society*, 133(1):67–83, jul 1966. ISSN 0035-8711. doi: 10.1093/mnras/133.1.67. URL https://academic.oup.com/mnras/article-lookup/doi/10.1093/mnras/133.1.67.

C. Carignan, B. S. Frank, K. M. Hess, D. M. Lucero, T. H. Randriamampandry, S. Goedhart, and S. S. Passmoor. Kat-7 Science Verification: Using H I Observations of Ngc 3109 To Understand Its Kinematics and Mass Distribution. *Aj*, 146(3):48, 2013. ISSN 0004-6256. doi: 10.1088/0004-6256/146/3/48. URL http://stacks.iop.org/1538-3881/146/i=3/a=48.

C. Carilli. Square Kilometre Array key science: a progressive retrospective. *Advancing Astrophysics with the Square Kilometre Array (AASKA14)*, art. 171, April 2015.

C. L. Carilli and S. Rawlings. Motivation, key science projects, standards and assumptions. *New Astronomy Reviews*, 48:979–984, December 2004. doi: 10.1016/j.newar.2004.09.001.

L. Chamandy, a. Shukurov, and K. Subramanian. Magnetic spiral arms and galactic outflows. *Monthly Notices of the Royal Astronomical Society: Letters*, 446(1):L6–L10, 2014a. ISSN 1745-3925. doi: 10.1093/mnrasl/slu156. URL http://mnrasl.oxfordjournals.org/cgi/doi/10.1093/mnrasl/slu156.

L. Chamandy, A. Shukurov, and A. R. Taylor. Statistical Tests of Galactic Dynamo Theory. *ApJ*, 833:43, December 2016. doi: 10.3847/1538-4357/833/1/43.

Luke Chamandy, Anvar Shukurov, Kandaswamy Subramanian, and Katherine Stoker. Non-linear galactic dynamos: A toolbox. *Monthly Notices of the Royal Astronomical Society*, 443(3):1867–1880, 2014b. ISSN 13652966. doi: 10.1093/mnras/stu1274.

L. Chen. Curvature of the Spectral Energy Distributions of Blazars. *ApJ*, 788:179, June 2014. doi: 10.1088/0004-637X/788/2/179.

K. T. Chyży and R. Buta. Strong magnetic spiral pattern in a ringed galaxy NGC 4736. In M. Bureau, E. Athanassoula, and B. Barbuy, editors, *Formation and Evolution of Galaxy Bulges*, volume 245 of *IAU Symposium*, pages 133–134, July 2008. doi: 10.1017/S174392130801747X.

B. G. Clark. An efficient implementation of the algorithm 'CLEAN'. *A&A*, 89:377, September 1980.

J J Condon, G. Helou, D. B. Sanders, and B T Soifer. A 1.425 GHz Atlas of the IRAS Bright Galaxy Sample, Part II. *The Astrophysical Journal Supplement Series*, 103(8):81, mar 1996. ISSN 0067-0049. doi: 10.1086/192270. URL `http://adsabs.harvard.edu/doi/10.1086/192270`.

J J Condon, W D Cotton, E W Greisen, Q F Yin, Richard A Perley, G B Taylor, and J J Broderick. The NRAO VLA Sky Survey. *The Astronomical Journal*, 115(5):1693–1716, may 1998. ISSN 00046256. doi: 10.1086/300337. URL `http://adsabs.harvard.edu/abs/2002yCat.8065....0C{%}5Cnpapers2://publication/doi/10.1086/300337http://stacks.iop.org/1538-3881/115/i=5/a=1693`.

M. Dahlem, S. Aalto, U. Klein, R. Booth, U Mebold, R Wielebinski, and H. Lesch. A comprehensive study of the peculiar spiral galaxy NGC 1808. I - Radio Continuum and CO line Observations. *Astronomy and Astrophysics (ISSN 0004-6361)*, 240:237–246, 1990. URL `http://adsabs.harvard.edu/cgi-bin/nph-data{_}query?bibcode=1993A{&}A...268...14K{&}link{_}type=ABSTRACT{%}5Cnpapers://71bd6ab0-03a5-4df8-b2de-61475e95cc8f/Paper/p6123{%}5Cnhttp://adsabs.harvard.edu/cgi-bin/nph-data{_}query?bibcode=1993A{%}26A...268...14K{&}link{_}type=ABSTRA`.

D Dallacasa, M Bondi, W Alef, and F Mantovani. European VLBI Network dual frequency observations of CSS–GPS candidates. *Astronomy and Astrophysics Supplement Series*, 129(2):219–236, apr 1998. ISSN 0365-0138. doi: 10.1051/aas:1998183. URL `http://aas.aanda.org/10.1051/aas:1998183`.

F. de Gasperin, H. T. Intema, and D. A. Frail. A radio spectral index map and catalogue at 147-1400 MHz covering 80 per cent of the sky. *MNRAS*, 474:5008–5022, March 2018. doi: 10.1093/mnras/stx3125.

R. H. Dicke, P. J. E. Peebles, P. G. Roll, and D. T. Wilkinson. Cosmic Black-Body Radiation. *ApJ*, 142: 414–419, July 1965. doi: 10.1086/148306.

J. W. Dreher, C. L. Carilli, and R. A. Perley. The Faraday rotation of Cygnus A - Magnetic fields in cluster gas. *ApJ*, 316:611–625, May 1987. doi: 10.1086/165229.

P G Edwards and S J Tingay. New candidate GHz peaked spectrum and compact. *Astronomy*, 106:91–106, 2004. doi: 10.1051/0004-6361.

W. Eichendorf and M. Reinhardt. Polarization properties of extragalactic radio sources. *Astrophysics and Space Science*, 61(1):153–167, mar 1979. ISSN 0004-640X. doi: 10.1007/BF00645799. URL `http://cdsads.u-strasbg.fr/cgi-bin/nph-bib{_}query?1979Ap{&}SS..61..153E{&}db{_}key=AST{&}nosetcookie=1http://link.springer.com/10.1007/BF00645799`.

P. Esquej, A. Alonso-Herrero, O. González-Martín, S. F. Hönig, A. Hernán-Caballero, P. Roche, C. Ramos Almeida, R. E. Mason, T. Díaz-Santos, N. A. Levenson, I. Aretxaga, J. M. Rodríguez Espinosa, and C. Packham. NUCLEAR STAR FORMATION ACTIVITY AND BLACK HOLE ACCRETION IN NEARBY SEYFERT GALAXIES. *The Astrophysical Journal*, 780(1):86, dec 2013. ISSN 0004-637X. doi: 10.1088/0004-637X/780/1/86. URL `http://stacks.iop.org/0004-637X/780/i=1/a=86?key=crossref.fb67e2413da6c2ac1ba2f91527126ad3`.

B. L. Fanaroff and J. M. Riley. The morphology of extragalactic radio sources of high and low luminosity. *MNRAS*, 167:31P–36P, May 1974. doi: 10.1093/mnras/167.1.31P.

C Fanti, F Pozzi, R Fanti, S A Baum, C P O'Dea, M Bremer, D Dallacasa, H Falcke, T de Graauw, A Marecki, G Miley, H Rottgering, R T Schilizzi, I Snellen, R E Spencer, and C Stanghellini. ISO observations of a sample of Compact Steep Spectrum and GHz Peaked Spectrum radio galaxies. *A&A*, 358:499–513, 2000. ISSN 00046361. URL `http://adsabs.harvard.edu/abs/2000A{%}26A...358..499F`.

R. Fanti, C. Fanti, R. T. Schilizzi, R. E. Spencer, Nan Rendong, P. Parma, W. J. M. van Breugel, and T. Venturi. On the nature of compact steep spectrum radio sources. *A&A*, 231:333–346, May 1990.

J. S. Farnes. Constraining Direction-Dependent Instrumental Polarisation: A New Technique for Polarisation Angle Calibration. *ArXiv e-prints*, July 2014.

D. Farnsworth, L. Rudnick, and S. Brown. Integrated Polarization of Sources at $\lambda \sim 1$ m and New Rotation Measure Ambiguities. *AJ*, 141:191, June 2011. doi: 10.1088/0004-6256/141/6/191.

C. I. Fassett, I. R. King, C. A. Nypaver, and B. J. Thomson. Temporal Evolution of S-Band Circular Polarization Ratios of Kilometer-Scale Craters on the Lunar Maria. *Journal of Geophysical Research (Planets)*, 123:3133–3143, December 2018. doi: 10.1029/2018JE005741.

C. Fendt, R. Beck, H. Lesch, and N. Neininger. Large-field optical polarimetry of NGC 891, 5907 and 7331. Selecting the intrinsic polarising mechanism. *A&A*, 308:713–722, April 1996.

L. Feretti, G. Giovannini, F. Govoni, and M. Murgia. Clusters of galaxies: observational properties of the diffuse radio emission. *Astronomy and Astrophysics Reviews*, 20:54, May 2012. doi: 10.1007/s00159-012-0054-z.

A. Fletcher, R. Beck, A. Shukurov, E. M. Berkhuijsen, and C. Horellou. Magnetic fields and spiral arms in the galaxy M51. *MNRAS*, 412:2396–2416, April 2011. doi: 10.1111/j.1365-2966.2010.18065.x.

Andrew Fletcher. Magnetic fields in nearby galaxies. 438:14, 2010. URL http://arxiv.org/abs/1104.2427.

A. R. Foley, T. Alberts, R. P. Armstrong, A. Barta, E. F. Bauermeister, and Bester et al. Engineering and science highlights of the KAT-7 radio telescope. *MNRAS*, 460:1664–1679, August 2016. doi: 10.1093/mnras/stw1040.

B. Gaensler, I. Agudo, T. Akahori, J. Banfield, R. Beck, E. Carretti, J. Farnes, M. Haverkorn, G. Heald, D. Jones, T. Landecker, S. A. Mao, R. Norris, S. O'Sullivan, L. Rudnick, D. Schnitzeler, N. Seymour, and X. Sun. Broadband Polarimetry with the Square Kilometre Array: A Unique Astrophysical Probe. *Advancing Astrophysics with the Square Kilometre Array (AASKA14)*, art. 103, April 2015.

E. Galliano, D. Alloin, E. Pantin, G. L. Granato, P. Delva, L. Silva, P. O. Lagage, and P. Panuzzo. Extremely massive young clusters in NGC 1365. *Astronomy and Astrophysics*, 492:3–22, 2008. ISSN 0004-6361. doi: 10.1051/0004-6361:20077621. URL http://adsabs.harvard.edu/abs/2008A{%}26A...492....3G.

V. Galluzzi, M. Massardi, and A. et. al. Bonaldi. Characterization of polarimetric and total intensity behaviour of a complete sample of PACO radio sources in the radio bands. *MNRAS*, 475:1306–1322, March 2018. doi: 10.1093/mnras/stx3216.

S. Ganesh. *Wavelets in the Astronomical Context*. Physical Research Laboratory Abstract, 2003.

F.~F. Gardner and J.~B. Whiteoak. The Polarization of Cosmic Radio Waves. *Annual Review of Astronomy and Astrophysics*, 4(1):245–+, sep 1966. ISSN 0066-4146. doi: 10.1146/annurev.aa.04.090166.001333. URL http://www.annualreviews.org/doi/10.1146/annurev.aa.04.090166.001333http://adsabs.harvard.edu/abs/1966ARA{&}A...4..245G.

S. J. George, J. M. Stil, and B. W. Keller. Detection Thresholds and Bias Correction in Polarized Intensity. *Publications of the Astronomical Society of Australia*, 29:214–220, October 2012. doi: 10.1071/AS11027.

M. Gerin, F. Combes, and N. Nakai. A molecular ring in the nucleus of the barred spiral galaxy NGC 1097. *A&A*, 203:44–50, September 1988.

O. González-Martín, J. M. Rodríguez-Espinosa, T. Díaz-Santos, C. Packham, a. Alonso-Herrero, P. Esquej, C. Ramos Almeida, R. Mason, and C. Telesco. Dust in active galactic nuclei. *Astronomy & Astrophysics*, 553:A35, 2013. ISSN 0004-6361. doi: 10.1051/0004-6361/201220382. URL http://adsabs.harvard.edu/abs/2013A{&}A...553A..35G.

O. Gressel, D. Elstner, U. Ziegler, and G. Rüdiger. Direct simulations of a supernova-driven galactic dynamo. *A&A*, 486:L35–L38, August 2008a. doi: 10.1051/0004-6361:200810195.

O. Gressel, U. Ziegler, D. Elstner, and G. Rüdiger. Dynamo coefficients from local simulations of the turbulent ISM. *Astronomische Nachrichten*, 329:619, July 2008b. doi: 10.1002/asna.200811005.

C. A. Hales, B. M. Gaensler, R. Norris, and E. Middelberg. Deep Imaging of the Radio Sky in Total Intensity and Linear Polarization. In *American Astronomical Society Meeting Abstracts #221*, volume 221 of *American Astronomical Society Meeting Abstracts*, page 420.05, January 2013.

M. Hanasz, K. Otmianowska-Mazur, G. Kowal, and H. Lesch. Cosmic-ray-driven dynamo in galactic disks. A parameter study. *A&A*, 498:335–346, May 2009. doi: 10.1051/0004-6361/200810279.

P. J. Hancock, T. Murphy, B. M. Gaensler, A. Hopkins, and J. R. Curran. Compact continuum source finding for next generation radio surveys. *MNRAS*, 422:1812–1824, May 2012. doi: 10.1111/j.1365-2966.2012.20768.x.

P. J. Hancock, C. M. Trott, and N. Hurley-Walker. Source Finding in the Era of the SKA (Precursors): Aegean 2.0. *Publications of the Astronomical Society of Australia*, 35:e011, March 2018. doi: 10.1017/pasa.2018.3.

G. Heald, R. Braun, and R. Edmonds. The Westerbork SINGS survey. *Astronomy and Astrophysics*, 503(2): 409–435, aug 2009. ISSN 0004-6361. doi: 10.1051/0004-6361/200912240. URL `http://adsabs.harvard.edu/abs/2009A{&}A...503..409Hhttp://www.aanda.org/10.1051/0004-6361/200912240`.

George Heald. The Faraday rotation measure synthesis technique. *Proceedings of the International Astronomical Union*, 4(259):591, nov 2008. ISSN 1743-9213. doi: 10.1017/S1743921309031421. URL `http://www.journals.cambridge.org/abstract{_}S1743921309031421`.

George Heald, Rainer Beck, W. J. G. de Blok, Ralf-Juergen Dettmar, Andrew Fletcher, Bryan Gaensler, Marijke Haverkorn, Volker Heesen, Cathy Horellou, Marita Krause, Sui Ann Mao, Niels Oppermann, Anna Scaife, Dmitry Sokoloff, Jeroen Stil, Fatemeh Tabatabaei, Keitaro Takahashi, Russ Taylor, and Anna Williams. Magnetic Field Tomography in Nearby Galaxies with the Square Kilometre Array. In *Advancing Astrophysics with the Square Kilometre Array June*, page 11, jan 2015. URL `http://arxiv.org/abs/1501.00408http://arxiv.org/abs/1501.0408`.

V. Heesen, R. Beck, M. Krause, and R.-J. Dettmar. Cosmic rays and the magnetic field in the nearby starburst galaxy NGC 253. I. The distribution and transport of cosmic rays. *A&A*, 494:563–577, February 2009a. doi: 10.1051/0004-6361:200810543.

V. Heesen, M. Krause, R. Beck, and R.-J. Dettmar. Cosmic rays and the magnetic field in the nearby starburst galaxy NGC 253. II. The magnetic field structure. *A&A*, 506:1123–1135, November 2009b. doi: 10.1051/0004-6361/200911698.

A. Hewitt and G. Burbidge. A new optical catalog of Quasi-Stellar Objects. In *A new optical catalog of QSO (1989)*, 1989.

J. A. Högbom. Aperture Synthesis with a Non-Regular Distribution of Interferometer Baselines. *A&AS*, 15: 417, June 1974.

A. M. Hopkins, M. T. Whiting, N. Seymour, K. E. Chow, R. P. Norris, L. Bonavera, R. Breton, D. Carbone, C. Ferrari, T. M. O. Franzen, H. Garsden, J. González-Nuevo, C. A. Hales, P. J. Hancock, G. Heald, D. Herranz, M. Huynh, R. J. Jurek, M. López-Caniego, M. Massardi, N. Mohan, S. Molinari, E. Orrù, R. Paladino, M. Pestalozzi, R. Pizzo, D. Rafferty, H. J. A. Röttgering, L. Rudnick, E. Schisano, A. Shulevski, J. Swinbank, R. Taylor, and A. J. van der Horst. The ASKAP/EMU Source Finding Data Challenge. *Publications of the Astronomical Society of Australia*, 32:e037, October 2015. doi: 10.1017/pasa.2015.37.

C. Horellou and a. Fletcher. Magnetic field tomography, helical magnetic fields and Faraday depolarization. *Monthly Notices of the Royal Astronomical Society*, 441(3):2049–2057, 2014. ISSN 0035-8711. doi: 10.1093/mnras/stu701. URL `http://mnras.oxfordjournals.org/cgi/doi/10.1093/mnras/stu701`.

E. Hummel, H. Lesch, R. Wielebinski, and R. Schlickeiser. The radio halo of NGC 4631: Ordered magnetic fields far above the plane. *A&A*, 197:L29–L31, May 1988.

M. T. Huynh, A. Hopkins, R. Norris, P. Hancock, T. Murphy, R. Jurek, and M. Whiting. The Completeness and Reliability of Threshold and False-discovery Rate Source Extraction Algorithms for Compact Continuum Sources. *Publications of the Astronomical Society of Australia*, 29:229–243, December 2012. doi: 10.1071/AS11026.

Shinsuke Ideguchi, Yuichi Tashiro, Takuya Akahori, Keitaro Takahashi, and Dongsu Ryu. Faraday Dispersion Functions of Galaxies. *The Astrophysical Journal*, 792(1):51, 2014. ISSN 1538-4357. doi: 10.1088/0004-637X/792/1/51. URL `http://stacks.iop.org/0004-637X/792/i=1/a=51?key=crossref.93074eea4f620fbe6be962d59fcd2aa1`.

C. D. Impey and S. Tapia. New blazars discovered by polarimetry. *ApJ*, 333:666–672, October 1988. doi: 10.1086/166775.

P. Jagannathan, S. Bhatnagar, U. Rau, and A. R. Taylor. Direction-dependent Corrections in Polarimetric Radio Imaging. I. Characterizing the Effects of the Primary Beam on Full-Stokes Imaging. *AJ*, 154:56, August 2017. doi: 10.3847/1538-3881/aa77f8.

Karl G. Jansky. Directional studies of atmospherics at high frequencies. In *Preceedings of The Institude of Radio Engineers*, volume 20, 1932.

Karl G. Jansky. Electrical disturbances apparently of extraterrestrial origin. In *Preceedings of The Institude of Radio Engineers*, volume 21, 1933.

M. J. Jarvis, A. R. Taylor, I. Agudo, J. R. Allison, R. P. Deane, B. Frank, N. Gupta, I. Heywood, N. Maddox, K. McAlpine, M. G. Santos, A. M. M. Scaife, M. Vaccari, J. T. L. Zwart, E. Adams, D. J. Bacon, A. J. Baker, B. A. Bassett, P. N. Best, R. Beswick, S. Blyth, M. L. Brown, M. Bruggen, M. Cluver, S. Colafranceso, G. Cotter, C. Cress, R. Dave, C. Ferrari, M. J. Hardcastle, C. Hale, I. Harrison, P. W. Hatfield, H.-R. Klockner, S. Kolwa, E. Malefahlo, T. Marubini, T. Mauch, K. Moodley, R. Morganti, R. Norris, J. A. Peters, I. Prandoni, M. Prescott, S. Oliver, N. Oozeer, H. J. A. Rottgering, N. Seymour, C. Simpson, O. Smirnov, D. J. B. Smith, K. Spekkens, J. Stil, C. Tasse, K. van der Heyden, I. H. Whittam, and W. L. WIlliams. The MeerKAT International GHz Tiered Extragalactic Exploration (MIGHTEE) Survey. *ArXiv e-prints*, September 2017.

Shubhendu Joardar, Somak Bhattacharyya, Ashit Baran Bhattacharya, and Chira R. Datta. Radio Astronomy and Super-Synthesis: a Survey. *Progress In Electromagnetics Research B*, 22:73–102, 2010. ISSN 19376472. doi: 10.2528/PIERB10032105.

R. Kato and J. Soda. Probing circular polarization in stochastic gravitational wave background with pulsar timing arrays. *Physical Review D*, 93(6):062003, March 2016. doi: 10.1103/PhysRevD.93.062003.

Ulrich Klein and Andrew Fletcher. *Galactic and Intergalactic Magnetic Fields*. Springer International Publishing, Cham, 2015. ISBN 978-3-319-08941-6. doi: 10.1007/978-3-319-08942-3. URL `http://link.springer.com/10.1007/978-3-319-08942-3`.

F. Krause, K. H. Radler, and G. Rudiger, editors. *The cosmic dynamo: proceedings of the 157th Symposium of the International Astronomical Union held in Potsdam, F.R.G., September 7-11, 1992.*, volume 157 of *IAU Symposium*, 1993.

M. Krause. Magnetic Fields and Star Formation in Spiral Galaxies. In *Revista Mexicana de Astronomia y Astrofisica Conference Series*, volume 36 of *Revista Mexicana de Astronomia y Astrofisica Conference Series*, pages 25–29, August 2009.

M. Krause. Magnetic fields and halos in spiral galaxies. *ArXiv e-prints*, January 2014.

H Kuehr, A Witzel, I I K Pauliny-Toth, and U Nauber. A catalogue of extragalactic radio sources having flux densities greater than 1 Jy at 5 GHz. *Astronomy and Astrophysics*, 45:367, 1981. ISSN 0365-0138.

Brian C. Lacki. Interpreting the low-frequency radio spectra of starburst galaxies: a pudding of strömgren spheres. *Monthly Notices of the Royal Astronomical Society*, 431(4):3003–3024, 2013. doi: 10.1093/mnras/stt349. URL http://dx.doi.org/10.1093/mnras/stt349.

C. J. Law, B. M. Gaensler, G. C. Bower, D. C. Backer, A. Bauermeister, S. Croft, R. Forster, C. Gutierrez-Kraybill, L. Harvey-Smith, C. Heiles, C. Hull, G. Keating, D. MacMahon, D. Whysong, P. K. G. Williams, and M. Wright. Spectropolarimetry with the Allen Telescope Array: Faraday Rotation Toward Bright Polarized Radio Galaxies. *ApJ*, 728:57, February 2011. doi: 10.1088/0004-637X/728/1/57.

Letjatji Legodi. Multi-colour analysis of galaxy clusters with radio halos and/or relics. Master of science, University of Cape Town, Faculty of Science, Astronomy Department, 2014.

J. L. B. Line, B. McKinley, J. Rasti, M. Bhardwaj, R. B. Wayth, R. L. Webster, D. Ung, D. Emrich, L. Horsley, A. Beardsley, B. Crosse, T. M. O. Franzen, B. M. Gaensler, M. Johnston-Hollitt, D. L. Kaplan, D. Kenney, M. F. Morales, D. Pallot, K. Steele, S. J. Tingay, C. M. Trott, M. Walker, A. Williams, and C. Wu. In situ measurement of MWA primary beam variation using ORBCOMM. *ArXiv e-prints*, August 2018.

M. L. Lister, K. I. Kellermann, and I. I. K. Pauliny-Toth. The Diverse Properties of GPS Sources. In E. Ros, R. W. Porcas, A. P. Lobanov, and J. A. Zensus, editors, *Proceedings of the 6th EVN Symposium*, page 135, June 2002.

Y.-Q. Lou and Z. Fan. Fast and Slow Density Waves in Magnetized Spiral Galaxies. *ApJ*, 493:102–120, January 1998. doi: 10.1086/305114.

T. Mauch, T. Murphy, H. J. Buttery, J. Curran, R. W. Hunstead, B. Piestrzynski, J. G. Robertson, and E. M. Sadler. SUMSS: a wide-field radio imaging survey of the southern sky - II. The source catalogue. *MNRAS*, 342:1117–1130, July 2003. doi: 10.1046/j.1365-8711.2003.06605.x.

Tom Mauch. Meerkat ar1 / 1.5 continuum imaging report. Technical report, Square Kilometre Array - South Africa, July 2016. `tmauch@ska.ac.za`.

Tom Mauch. The deep meerkat mosaic. Technical report, Square Kilometre Array - South Africa, August 2017. `tmauch@ska.ac.za` for technical questions; `fernando@ska.ac.za` for questions regarding the use of these data.

J P Mcmullin, B Waters, D Schiebel, W Young, and K Golap. CASA Architecture and Applications. *Astronomical Data Analysis Software and Systems XVI*, 376:127, 2007. ISSN 1050-3390.

D. Mesa, C. Baccigalupi, G. De Zotti, L. Gregorini, K.-H. Mack, M. Vigotti, and U. Klein. Polarization properties of extragalactic radio sources and their contribution to microwave polarization fluctuations. *A&A*, 396:463–471, December 2002. doi: 10.1051/0004-6361:20021392.

B. Y. Mills. The Molonglo Observatory synthesis telescope. *Proceedings of the Astronomical Society of Australia*, 4:156–159, 1981. doi: 10.1017/S1323358000016222.

N. Mohan and D. Rafferty. PyBDSF: Python Blob Detection and Source Finder. Astrophysics Source Code Library, February 2015.

D. Moss. The relation between magnetic and gas arms in spiral galaxies. *MNRAS*, 297:860–866, July 1998. doi: 10.1046/j.1365-8711.1998.01580.x.

D. Moss, D. Sokoloff, R. Beck, and M. Krause. Galactic winds and the symmetry properties of galactic magnetic fields. *A&A*, 512:A61, March 2010. doi: 10.1051/0004-6361/200913509.

D. Moss, R. Stepanov, T. G. Arshakian, R. Beck, M. Krause, and D. Sokoloff. Multiscale magnetic fields in spiral galaxies: evolution and reversals. *Astronomy & Astrophysics*, 537:A68, 2012. ISSN 0004-6361. doi: 10.1051/0004-6361/201118122.

D. Moss, R. Beck, D. Sokoloff, R. Stepanov, M. Krause, and T. G. Arshakian. The relation between magnetic and material arms in models for spiral galaxies. *A&A*, 556:A147, August 2013. doi: 10.1051/0004-6361/201321296.

D. Moss, R. Stepanov, M. Krause, R. Beck, and D. Sokoloff. The formation of regular interarm magnetic fields in spiral galaxies. *A&A*, 578:A94, June 2015. doi: 10.1051/0004-6361/201526145.

C. P. O'Dea, S. A. Baum, and C. Stanghellini. What are the gigahertz peaked-spectrum radio sources? *ApJ*, 380:66–77, October 1991. doi: 10.1086/170562.

Christopher P. O'Dea. The Compact Steep-Spectrum and Gigahertz Peaked-Spectrum Radio Sources. *Publications of the Astronomical Society of the Pacific*, 110(747):493–532, 1998a. ISSN 0004-6280. doi: 10.1086/316162. URL `http://www.jstor.org/stable/10.1086/316162{%}5Cnhttp://labs.adsabs.harvard.edu/adsabs/abs/1998PASP..110..493O/`.

Christopher P. O'Dea. The Compact Steep-Spectrum and Gigahertz Peaked-Spectrum Radio Sources. *Publications of the Astronomical Society of the Pacific*, 110(747):493–532, 1998b. ISSN 0004-6280. doi: 10.1086/316162. URL `http://www.jstor.org/stable/10.1086/316162{%}5Cnhttp://labs.adsabs.harvard.edu/adsabs/abs/1998PASP..110..493O/`.

N. Oppermann, H. Junklewitz, and et. al. Robbers. An improved map of the Galactic Faraday sky. *A&A*, 542:A93, June 2012. doi: 10.1051/0004-6361/201118526.

N. Oppermann, H. Junklewitz, M. Greiner, T. a. Enßlin, T. Akahori, E. Carretti, B. M. Gaensler, a. Goobar, L. Harvey-Smith, M. Johnston-Hollitt, L. Pratley, D. H. F. M. Schnitzeler, J. M. Stil, and V. Vacca. Estimating Extragalactic Faraday Rotation. *Astronomy & Astrophysics*, 118(2):1–33, 2014. ISSN 14320746. doi: 10.1051/0004-6361/201423995.

S. P. O'Sullivan and D. C. Gabuzda. Three-dimensional magnetic field structure of six parsec-scale active galactic nuclei jets. *MNRAS*, 393:429–456, February 2009. doi: 10.1111/j.1365-2966.2008.14213.x.

S. P. O'Sullivan, S. Brown, T. Robishaw, D. H. F. M. Schnitzeler, N. M. McClure-Griffiths, I. J. Feain, A. R. Taylor, B. M. Gaensler, T. L. Landecker, L. Harvey-Smith, and E. Carretti. Complex Faraday depth structure of active galactic nuclei as revealed by broad-band radio polarimetry. *MNRAS*, 421:3300–3315, April 2012. doi: 10.1111/j.1365-2966.2012.20554.x.

S. P. O'Sullivan, N. M. McClure-Griffiths, I. J. Feain, B. M. Gaensler, and R. J. Sault. Broad-band radio circular polarization spectrum of the relativistic jet in PKS B2126-158. *MNRAS*, 435:311–319, October 2013. doi: 10.1093/mnras/stt1298.

S. P. O'Sullivan, B. M. Gaensler, M. A. Lara-López, S. van Velzen, J. K. Banfield, and J. S. Farnes. The Magnetic Field and Polarization Properties of Radio Galaxies in Different Accretion States. *ApJ*, 806:83, June 2015. doi: 10.1088/0004-637X/806/1/83.

S. P. O'Sullivan, C. R. Purcell, C. S. Anderson, J. S. Farnes, X. H. Sun, and B. M. Gaensler. Broad-band, radio spectro-polarimetric study of 100 radiative-mode and jet-mode AGN. *MNRAS*, 469:4034–4062, August 2017. doi: 10.1093/mnras/stx1133.

Z. Paragi, L. Godfrey, C. Reynolds, M. J. Rioja, A. Deller, B. Zhang, L. Gurvits, M. Bietenholz, A. Szomoru, H. E. Bignall, P. Boven, P. Charlot, R. Dodson, S. Frey, and M. A. et al. Garrett. Very Long Baseline Interferometry with the SKA. *Advancing Astrophysics with the Square Kilometre Array (AASKA14)*, art. 143, April 2015.

A. Pasetto, A. Kraus, K.-H. Mack, G. Bruni, and C. Carrasco-González. A possible link between high rotation measure and CSS-GPS sources. *Astronomische Nachrichten*, 337:91, February 2016. doi: 10.1002/asna.201512271.

A. Pasetto, C. Carrasco-González, S. O'Sullivan, A. Basu, G. Bruni, A. Kraus, S. Curiel, and K.-H. Mack. Broadband radio spectro-polarimetric observations of high Faraday rotation measure AGN. *ArXiv e-prints*, January 2018.

A. A. Penzias and R. W. Wilson. A Measurement of Excess Antenna Temperature at 4080 Mc/s. *ApJ*, 142: 419–421, July 1965. doi: 10.1086/148307.

L. K. Pollack, G. B. Taylor, and R. T. Zavala. VLBI Polarimetry of 177 Sources from the Caltech-Jodrell Bank Flat-Spectrum Survey. *ApJ*, 589:733–751, June 2003. doi: 10.1086/374712.

Urvashi Rau, Sanjay Bhatnagar, Maxim A. Voronkov, and Tim J. Cornwell. Advances in calibration and imaging techniques in radio interferometry. *Proceedings of the IEEE*, 97(8):1472–1481, 2009. ISSN 00189219. doi: 10.1109/JPROC.2009.2014853.

Grote Reber. Cosmic static. *Preceedings of The Institude of Radio Engineers*, 28:68–70, 1940.

Grote Reber. Cosmic static. *Astrophysical Journal*, 100:279–287, 1944.

A. Refregier. Shapelets - I. A method for image analysis. *MNRAS*, 338:35–47, January 2003. doi: 10.1046/j.1365-8711.2003.05901.x.

S. O. Rice. Mathematical Analysis of Random Noise-Conclusion. *Bell Systems Tech. J., Volume 24, p. 46-156*, 24:46–156, 1945.

J. G. Robertson. The Most and Other Radio Telescopes. *Australian Journal of Physics*, 44:729, 1991. doi: 10.1071/PH910729.

G. E. Romero, S. A. Cellone, and J. A. Combi. Two-Color Photometry with High Temporal Resolution of the Extremely Variable Blazar PKS 0537-441. *AJ*, 120:1192–1197, September 2000. doi: 10.1086/301526.

G. E. Romero, S. A. Cellone, J. A. Combi, and I. Andruchow. Optical microvariability of EGRET blazars. *A&A*, 390:431–438, August 2002. doi: 10.1051/0004-6361:20020743.

L. Rudnick and F. N. Owen. The Distribution of Polarized Radio Sources >15 μJy in GOODS-N. *ApJ*, 785:45, April 2014. doi: 10.1088/0004-637X/785/1/45.

A Ruzmaikin, A., Anvar Shukurov, and D D Sokoloff. *Magnetic fields of galaxies*, volume 50. Kluwer Academic Publishers, Moscow, 133 edition, 1988. ISBN 90-277-2450-4. doi: 10.1080/03091929008219869. URL http://adsabs.harvard.edu/abs/1988ASSL..133.....R.

A. P. Sarma, T. H. Troland, R. M. Crutcher, and D. A. Roberts. Circular Polarization in water masers - VLA Zeeman Effect Observations. In *American Astronomical Society Meeting Abstracts #198*, volume 33 of *Bulletin of the American Astronomical Society*, page 874, May 2001.

R. J. Sault. ATCA flux density scale at 12mm. Technical Report AT/39.3/124, ATNF, 2003.

Riccardo Scarpa and Renato Falomo. Are high polarization quasars and BL Lacertae objects really different ? A study of the optical spectral properties. *Astron. Astrophys.*, 325:109–123, 1997. ISSN 00046361.

S. M. Scarrott, D. Ward-Thompson, and R. F. Warren-Smith. Evidence for a spiral magnetic field configuration in the galaxy M51. *MNRAS*, 224:299–305, January 1987. doi: 10.1093/mnras/224.2.299.

D. H. F. M. Schnitzeler, J. K. Banfield, and K. J. Lee. Polarization signatures of unresolved radio sources. *MNRAS*, 450:3579–3596, July 2015. doi: 10.1093/mnras/stv708.

Chandreyee Sengupta and Ramesh Balasubramanyam. H I content in galaxies in loose groups. *Monthly Notices of the Royal Astronomical Society*, 369(1):360–368, jun 2006. ISSN 00358711. doi: 10.1111/j.1365-2966.2006.10307.x. URL `https://academic.oup.com/mnras/article-lookup/doi/10.1111/j.1365-2966.2006.10307.x`.

Sinenhlanhla Sikhosana. Giant radio halos and relics in actpol clusters. Master of science, University of KwaZulu-Natal, Faculty of Science, School of Mathematics, Statistics and Computer Science, 2016.

J F L Simmons and B G Stewart. Point and interval estimation of the true unbiased degree of linear polarization in the presence of low signal-to-noise ratios. *Astronomy & Astrophysics*, 142:100, 1985. ISSN 0004-6361. URL `http://adsabs.harvard.edu/cgi-bin/nph-data{_}query?bibcode=1985A{%}2526A...142..100S{&}link{_}type=ABSTRACT{%}5Cnpapers://ee00755c-a478-4d4e-a50b-ef01ee7b9957/Paper/p9994`.

M. Soida, R. Beck, M. Urbanik, and J. Braine. Magnetic fields in the absence of spiral density waves - NGC 4414. *A&A*, 394:47–57, October 2002. doi: 10.1051/0004-6361:20021100.

M. Soida, M. Krause, R.-J. Dettmar, and M. Urbanik. The large scale magnetic field structure of the spiral galaxy NGC 5775. *A&A*, 531:A127, July 2011. doi: 10.1051/0004-6361/200810763.

D D Sokoloff, a a Bykov, a Shukurov, E M Berkhuijsen, R Beck, and a D Poezd. Depolarization and Faraday effects in galaxies. *Monthly Notices of the Royal Astronomical Society*, 299:189, 1998. ISSN 0035-8711. doi: 10.1046/j.1365-8711.1999.02161.x. URL `http://adsabs.harvard.edu/cgi-bin/nph-data{_}query?bibcode=1998MNRAS.299..189S{&}link{_}type=ABSTRACT{%}5Cnpapers2://publication/doi/10.1046/j.1365-8711.1998.01782.x`.

C. Stanghellini, C. P. O'Dea, D. Dallacasa, S. A. Baum, R. Fanti, and C. Fanti. A complete sample of GHz-peaked-spectrum radio sources and its radio properties. *A&AS*, 131(2):303–315, 1998. ISSN 0365-0138. doi: 10.1051/aas:1998270. URL `http://adsabs.harvard.edu/abs/1998A{%}26AS..131..303S`.

C Stanghellini, C P O'Dea, D Dallacasa, P Cassaro, S A Baum, R Fanti, and C Fanti. Extended emission around GPS radio sources. *Astronomy & Astrophysics*, 443(3):891–902, 2005. ISSN 00046361. doi: 10.1051/0004-6361:20042226.

J.-L. Starck, F. Murtagh, and A. Bijaoui. *Image Processing and Data Analysis: The Multiscale Approach*. Cambridge University Press, New York, NY, USA, 1998. ISBN 0-521-59914-8.

J. M. Stil, M. Krause, R. Beck, and A. R. Taylor. the Integrated Polarization of Spiral Galaxy Disks. *The Astrophysical Journal*, 693(2):1392–1403, 2009. ISSN 0004-637X. doi: 10.1088/0004-637X/693/2/1392. URL `http://stacks.iop.org/0004-637X/693/i=2/a=1392?key=crossref.6ba564d5a205903f2a9a1fed2edf45f8`.

J. M. Stil, M. Krause, L. Mitchell, R. Beck, and A. R. Taylor. The integrated polarization of spiral galaxies. In K. G. Strassmeier, A. G. Kosovichev, and J. E. Beckman, editors, *Cosmic Magnetic Fields: From Planets, to Stars and Galaxies*, volume 259 of *IAU Symposium*, pages 543–544, April 2009. doi: 10.1017/S174392130903124X.

J. M. Stil, A. R. Taylor, and C. Sunstrum. Structure in the Rotation Measure Sky. *The Astrophysical Journal*, 726(1):4, 2011. ISSN 0004-637X. doi: 10.1088/0004-637X/726/1/4. URL `http://stacks.iop.org/0004-637X/726/i=1/a=4?key=crossref.a8490f553f64a6f9aafcbf2d660fe0f0`.

J. M. Stil, B. W. Keller, S. J. George, and A. R. Taylor. Degree of Polarization and Source Counts of Faint Radio Sources from Stacking Polarized Intensity. *ApJ*, 787:99, June 2014. doi: 10.1088/0004-637X/787/2/99.

Thaisa Storchi-Bergmann, Michael Eracleous, Maria Teresa Ruiz, Mario Livio, Andrew S. Wilson, and Alexei V. Filippenko. Evidence for a Precessing Accretion Disk in the Nucleus of NGC 1097. *The Astrophysical Journal*, 489(1):87–93, nov 1997. ISSN 0004-637X. doi: 10.1086/304783. URL `http://stacks.iop.org/0004-637X/489/i=1/a=87`.

R. Subrahmanyan, R. D. Ekers, L. Saripalli, and E. M. Sadler. ATLBS: the Australia Telescope Low-Brightness Survey. *MNRAS*, 402:2792–2806, March 2010. doi: 10.1111/j.1365-2966.2009.16105.x.

X. H. Sun and W. Reich. Polarisation properties of Milky-Way-like galaxies. *Astron. Astrophys.*, 543:A127, 2012. ISSN 0004-6361. doi: 10.1051/0004-6361/201218802. URL `http://www.aanda.org/10.1051/0004-6361/201218802`.

X H Sun, L Rudnick, Takuya Akahori, C S Anderson, M R Bell, J D Bray, J S Farnes, S Ideguchi, K Kumazaki, T. O'Brien, S. P. O'Sullivan, A M M Scaife, R Stepanov, J Stil, K Takahashi, R J Van Weeren, and M Wolleben. COMPARISON OF ALGORITHMS FOR DETERMINATION OF ROTATION MEASURE AND FARADAY STRUCTURE. I. 1100–1400 MHZ. *The Astronomical Journal*, 149(2):60, jan 2015. ISSN 1538-3881. doi: 10.1088/0004-6256/149/2/60. URL `http://dx.doi.org/10.1088/0004-6256/149/2/60http://stacks.iop.org/1538-3881/149/i=2/a=60?key=crossref.5ea97678d2b2099cf2db91f30cb06e42`.

G. C. Surpi, G. E. Romero, and H. Vucetich. The Gravitational Microlensing Scenario for PKS 0537-441. *RMxAA*, 32:153–159, October 1996.

Tacconi-Garman. Sub-arcsecond 2.2micro imaging of the starburst galaxy NGC1808: infrared observations of super star clusters. *AJ*, 112(3):918, sep 1996. ISSN 00046256. doi: 10.1086/118065. URL `http://adsabs.harvard.edu/cgi-bin/bib{_}query?1996AJ....112..918T`.

a. R. Taylor, J. M. Stil, and C. Sunstrum. A Rotation Measure Image of the Sky. *The Astrophysical Journal*, 702:1230–1236, 2009. ISSN 0004-637X. doi: 10.1088/0004-637X/702/2/1230.

A. R. Taylor, S. Bhatnagar, J. Condon, D. A. Green, J. M. Stil, P. Jagannathan, N. Kantharia, R. Kothes, R. Perley, J. Wall, and T. Willis. The deep full-stokes radio sky. In *Astronomical Society of India Conference Series*, volume 13 of *Astronomical Society of India Conference Series*, pages 99–104, 2014.

G. B. Taylor, C. L. Carilli, and R. A. Perley, editors. *Synthesis Imaging in Radio Astronomy II*, volume 180 of *Astronomical Society of the Pacific Conference Series*, 1999.

G. B. Taylor, S. E. Healey, J. F. Helmboldt, S. Tremblay, C. D. Fassnacht, R. C. Walker, L. O. Sjouwerman, T. J. Pearson, A. C. S. Readhead, L. Weintraub, N. Gehrels, R. W. Romani, P. F. Michelson, R. D. Blandford, and G. Cotter. Characteristics of EGRET Blazars in the VLBA Imaging and Polarimetry Survey (VIPS). *ApJ*, 671:1355–1364, December 2007. doi: 10.1086/523264.

R. Taylor, I. Agudo, T. Akahori, R. Beck, B. Gaensler, G. Heald, M. Johnston-Hollitt, M. Langer, L. Rudnick, A. Scaife, D. Schleicher, J. Stil, and D. Ryu. SKA Deep Polarization and Cosmic Magnetism. *Advancing Astrophysics with the Square Kilometre Array (AASKA14)*, art. 113, April 2015.

A. R. Thompson, J. M. Moran, and G. W. Swenson, Jr. *Interferometry and Synthesis in Radio Astronomy, 3rd Edition*. 2017. doi: 10.1007/978-3-319-44431-4.

Steven J Tingay. ATCA Monitoring Observations of 202 Compact Radio Sources in Support of the VSOP AGN Survey. *Publications of the Astronomical Society of Japan*, 55:351–384, 2003. ISSN 00046264.

I. Torniainen, M. Tornikoski, H. Teräsranta, M. F. Aller, and H. D. Aller. Long term variability of gigahertz-peaked spectrum sources and candidates. *A&A*, 435:839–856, June 2005. doi: 10.1051/0004-6361:20041886.

M. Tornikoski, I. Jussila, P. Johansson, M. Lainela, and E. Valtaoja. Radio Spectra and Variability of Gigahertz-Peaked Spectrum Radio Sources and Candidates. *AJ*, 121:1306–1318, March 2001. doi: 10.1086/319417.

M. Tucci, E. Carretti, S. Cecchini, L. Nicastro, R. Fabbri, B. M. Gaensler, J. M. Dickey, and N. M. McClure-Griffiths. Polarization Angular Spectra of Galactic Synchrotron Emission on Arcminute Scales. *ApJ*, 579: 607–615, November 2002. doi: 10.1086/342793.

A. K. Tzioumis et al. VLBI observations at 2.3 GHz of the compact galaxy 1934-638. *AJ*, 98:36–43, July 1989. doi: 10.1086/115124.

M.-P. Véron-Cetty and P Véron. NGC1808: a nearby galaxy with a faint Seyfert nucleus. *Astronomy and Astrophysics*, 145:425, 1985. URL `http://adsabs.harvard.edu/abs/1985A{%}26A...145..425V`.

M.-P. Véron-Cetty and P. Véron. A catalogue of quasars and active nuclei: 12th edition. *Astronomy and Astrophysics*, 455(2):773–777, aug 2006. ISSN 0004-6361. doi: 10.1051/0004-6361:20065177. URL `http://adsabs.harvard.edu/abs/2010A{&}A...518A..10Vhttp://www.aanda.org/10.1051/0004-6361/201014188http://www.aanda.org/10.1051/0004-6361:20065177`.

W. Vlemmings, P. J. Diamond, and H. J. van Langevelde. Circular polarization of circumstellar water masers around S Per. *A&A*, 375:L1–L4, August 2001. doi: 10.1051/0004-6361:20010890.

B. Vollmer, M. Soida, R. Beck, A. Chung, M. Urbanik, K. T. Chyży, K. Otmianowska-Mazur, and J. D. P. Kenney. Large-scale radio continuum properties of 19 Virgo cluster galaxies. The influence of tidal interactions, ram pressure stripping, and accreting gas envelopes. *A&A*, 553:A116, May 2013. doi: 10.1051/0004-6361/201321163.

T. Mauch W. D. Cotton, J. J. Condon. The ionosphere at l band: Meerkat. OBIT DEVELOPMENT MEMO SERIES 59, NRAO, SARAO, September 2018.

J. A. Högbom W. N. Christiansen. *Radio Telescopes*. Cambridge University Press, 2 edition, 1985.

E. M. Waldram, R. C. Bolton, J. M. Riley, and G. G. Pooley. 9C spectral-index distributions and source-count estimates from 15 to 93 GHz - a re-assessment. *MNRAS*, 473:1317–1324, January 2018. doi: 10.1093/mnras/stx2368.

J. F. C. Wardle and P. P. Kronberg. The linear polarization of quasi-stellar radio sources at 3.71 and 11.1 centimeters. *ApJ*, 194:249–255, December 1974. doi: 10.1086/153240.

W. D. Watson and H. W. Wyld. The Relationship between the Circular Polarization and the Magnetic Field for Astrophysical Masers with Weak Zeeman Splitting. *The Astrophysical Journal Letters*, 558:L55–L58, September 2001. doi: 10.1086/323513.

Y. Xu, P. P. Kronberg, S. Habib, and Q. W. Dufton. A Faraday Rotation Search for Magnetic Fields in Large-scale Structure. *ApJ*, 637:19–26, January 2006. doi: 10.1086/498336.